

Copyright  
by  
Reeshidev Bansal  
2007

The Dissertation Committee for Reeshidev Bansal  
certifies that this is the approved version of the following dissertation:

**Seismic characterization of naturally fractured  
reservoirs**

Committee:

---

Mrinal K. Sen, Supervisor

---

Paul L. Stoffa

---

Stephen P. Grand

---

Nathan L. Bangs

---

Robert H. Tatham

---

Robert J. Ferguson

**Seismic characterization of naturally fractured  
reservoirs**

**by**

**Reeshidev Bansal, B.S., M.S.**

**DISSERTATION**

Presented to the Faculty of the Graduate School of  
The University of Texas at Austin  
in Partial Fulfillment  
of the Requirements  
for the Degree of

**DOCTOR OF PHILOSOPHY**

THE UNIVERSITY OF TEXAS AT AUSTIN

May 2007

**To my parents**

*Shree Mahiman Tulsian and Smt. Kiran devi*

## Acknowledgments

I would like to express my deepest gratitude to my advisor Dr. Mrinal K. Sen for bearing me all these years. I would stop by his office unannounced whenever I would be struggling with my research, and he was always there to help me out. He has been a constant source for inspiration, encouragement and support during my graduate studies. I would also like to thank Dr. Nathan Bangs, Dr. Robert Ferguson, Dr. Steve Grand, Dr. Paul Stoffa and Dr. Robert Tatham for serving in my committee. Thanks to Dr. Matthias Imhof, my MS supervisor, for his continuous support and encouragement.

Many thanks to Carmen Teresa Gomez and Paresh Patel for proof-reading part of this dissertation. I sincerely wish to thank my friends and colleagues: Saurabh Agrawal, Chandan Kumar, Banit agrawal, Sanjeev Kumar, Dhananjay Kumar, Imtiaz Ahmed, Sanjay Sood, Sanjeev Rajput, Samarjeet Chakraborty, Manish Niranjana, Anubhavi Mukharjee, Russell Young, Tiancong Hong, Armando Sena, Ajit Barnwal, Rupesh Barnwal, Jonas De Basabe, Paresh Patel, Chunlei Chu, Samkil Sil, Irina Filina.

I would also like to thank my former colleagues from Virginia Tech: Shailendra Mahapatra, Ethan Nowak, Stephanie Nowak, Dhananjay Mishra, Arvind Sharma, Joy Mukherjee, Arijit Paul, Ali Yawar and Akbar Rizvi.

I also thank Mark Wiederspahn, Kevin Johnson and John Gerboc for

their technical support; Phillip Guerrero, Susan Beaubien; Judy Sansom, Dr. Katherine Ellins, Jan Everett, Lisa Gahagan, Patricia E Ganey-Curry and Nancy Hard and Miriam Pashby for their administrative help.

Finally, I would like to thank my parents and family for being there when I needed them most. This work could not have been completed without their continuous love and support.

# Seismic characterization of naturally fractured reservoirs

Publication No. \_\_\_\_\_

Reeshidev Bansal, Ph.D.  
The University of Texas at Austin, 2007

Supervisor: Mrinal K. Sen

Many hydrocarbon reservoirs have sufficient porosity but low permeability (for example, tight gas sands and coal beds). However, such reservoirs are often naturally fractured. The fracture patterns in these reservoirs can control flow and transport properties, and therefore, play an important role in drilling production wells.

On the scale of seismic wavelengths, closely spaced parallel fractures behave like an anisotropic media, which precludes the response of individual fractures in the seismic data. There are a number of fracture parameters which are needed to fully characterize a fractured reservoir. However, seismic data may reveal only certain fracture parameters and those are fracture orientation, crack density and fracture infill.

Most of the widely used fracture characterization methods such as S-wave splitting analysis or amplitude vs. offset and azimuth (AVOA) analysis

fail to render desired results in laterally varying media. I have conducted a systematic study of the response of fractured reservoirs with laterally varying elastic and fracture properties, and I have developed a scheme to invert for the fracture parameters.

I have implemented a 3D finite-difference method to generate multicomponent synthetic seismic data in general anisotropic media. I applied the finite-difference algorithm in both Standard and Rotated Staggered grids. Standard Staggered grid is used for media having symmetry up to orthorhombic (isotropic, transversely isotropic, and orthorhombic), whereas Rotated Staggered grid is implemented for monoclinic and triclinic media. I have also developed an efficient and accurate ray-bending algorithm to compute seismic traveltimes in 3D anisotropic media.

AVOA analysis is equivalent to the first-order Born approximation. However, AVOA analysis can be applied only in a laterally uniform medium, whereas the Born-approximation does not pose any restriction on the subsurface structure. I have developed an inversion scheme based on a ray-Born approximation to invert for the fracture parameters. Best results are achieved when both vertical and horizontal components of the seismic data are inverted simultaneously. I have also developed an efficient positivity constraint which forbids the inverted fracture parameters to be negative in value. I have implemented the inversion scheme in the frequency domain and I show, using various numerical examples, that all frequency samples up to the Nyquist are not required to achieve desired inversion results.



# Table of Contents

<b>Acknowledgments</b>	<b>v</b>
<b>Abstract</b>	<b>vii</b>
<b>List of Tables</b>	<b>xii</b>
<b>List of Figures</b>	<b>xiii</b>
<b>Chapter 1. Introduction</b>	<b>1</b>
1.1 Introduction . . . . .	1
1.2 Motivation . . . . .	5
1.3 Equivalent media theories for cracks and fractures . . . . .	6
1.3.1 Linear slip theory . . . . .	9
1.3.2 Rotationally invariant fractures . . . . .	12
1.3.3 Hudson’s model for aligned penny-shaped cracks . . . . .	14
1.3.4 Comparison of Hudson’s and Linear-Slip model and significance of fracture parameters . . . . .	15
1.3.5 Fluid indicator for cracks and fractures . . . . .	20
1.4 HTI and VTI media . . . . .	20
1.5 Conventional methods of estimation of fracture parameters . . . . .	28
1.5.1 S-wave splitting . . . . .	28
1.5.2 P-wave NMO and AVOA analysis . . . . .	33
1.5.3 Linearized Born inversion of fracture parameters . . . . .	35
1.6 Objectives and Organization . . . . .	38
<b>Chapter 2. Finite-difference modeling in anisotropic media: An S-wave splitting study in fractured reservoirs</b>	<b>39</b>
2.1 Introduction . . . . .	39
2.2 Modeling Algorithm . . . . .	43

2.2.1	Governing equations . . . . .	43
2.2.2	Sources and seismograms . . . . .	44
2.3	Staggered grid finite-difference implementation . . . . .	45
2.4	Examples . . . . .	52
2.4.1	Homogeneous anisotropic media . . . . .	52
2.4.2	Comparison between synthetic seismograms generated by finite-difference method and reflectivity algorithm . . . . .	59
2.4.3	Seismic data generated for a complex subsurface model . . . . .	66
2.5	Shear-wave splitting study . . . . .	69
2.5.1	Background medium and source type . . . . .	69
2.5.2	Dipping rotationally invariant fractures . . . . .	71
2.5.3	Two rotationally invariant vertical fracture sets . . . . .	76
2.5.4	Dipping corrugated fractures . . . . .	77
2.6	Discussion . . . . .	81
<b>Chapter 3. Ray bending in anisotropic media</b>		<b>83</b>
3.1	Introduction . . . . .	83
3.2	Methodology of ray bending . . . . .	89
3.3	Estimation of Group Velocity . . . . .	91
3.3.1	Weak TI media . . . . .	91
3.3.2	Strong TI media . . . . .	96
3.3.3	Arbitrary anisotropy . . . . .	103
3.4	Interpolation of Traveltime . . . . .	106
3.5	Ray Tracing Examples . . . . .	109
3.6	Discussion . . . . .	115
<b>Chapter 4. Ray-Born inversion for fracture parameters</b>		<b>117</b>
4.1	Introduction . . . . .	117
4.2	Methodology . . . . .	119
4.2.1	The linearized forward problem . . . . .	119
4.2.2	Inversion scheme . . . . .	123
4.3	Implementation of inversion . . . . .	124
4.3.1	Applied constraint . . . . .	128

4.3.2	Inversion using single component of seismic data . . . .	142
4.3.3	Sensitivity of the inversion to the frequency content in the data . . . . .	151
4.3.4	Application of inversion on a finite-difference generated dataset . . . . .	161
4.4	Discussion and conclusions . . . . .	167
<b>Chapter 5.</b>	<b>Summary and Future Work</b>	<b>170</b>
5.1	Summary . . . . .	170
5.2	Future work . . . . .	172
<b>Appendices</b>		<b>177</b>
<b>Appendix A.</b>	<b>Phase and group velocity calculation</b>	<b>178</b>
<b>Appendix B.</b>	<b>Thomsen’s model of fractured porous media</b>	<b>180</b>
<b>Appendix C.</b>	<b>Hyperbolic interpolation of traveltimes</b>	<b>183</b>
<b>Appendix D.</b>	<b>Derivation of some of the formulas used in chapter</b>	
	<b>4</b>	<b>185</b>
D.1	Derivation of equation 4.13 . . . . .	185
D.2	Derivation of $L^q$ for vertical fractures (equation 4.16) . . . . .	186
<b>Appendix E.</b>	<b>A useful asymptotic approximation of Born inte-</b>	
	<b>gral</b>	<b>187</b>
<b>Bibliography</b>		<b>196</b>
<b>Vita</b>		<b>209</b>

## List of Tables

1.1	In this table, most common cases of anisotropy due to presence of the vertical fractures are listed. . . . .	13
1.2	Summary of relationships of fracture weaknesses with microfracture properties in Linear-slip model and Hudson's model for natural fractures in hydrocarbon reservoirs (adapted from Shaw and Sen, 2006). . . . .	18
1.3	Four most widely used approaches to estimate the fracture parameters are listed: Note that other than Born inversion none of these methods directly solves for normal- and tangential-weaknesses $\Delta_N$ and $\Delta_T$ which define the stiffness matrix of a fractured medium (equation 1.9). . . . .	37
2.1	Relevant elastic parameters of the three-layered model. . . . .	59
2.2	Relevant elastic parameters of the background subsurface model. . . . .	70

## List of Figures

1.1	Maps of intersecting fractures on bedding surface of Rico Formation, southeastern Utah (Olson and Pollard, 1989): Linear slip theory suggests that each fracture set can be treated individually without taking into account any interaction between different fracture sets; i.e., compliances of each fracture set can be estimated, independently, by equation 1.5. Compliances of each fracture set and background medium add up to give the equivalent compliance of the fractured rock (equation 1.7). . .	11
1.2	$\Delta_N$ and $\Delta_T$ in isotropic host rock for different values of fracture density $e$ and $V_S/V_P$ : $\Delta_N$ is plotted for completely dry fractures using equation 1.16. Notice that $\Delta_N$ exceeds the value of 1 for small $V_S/V_P$ and high crack density $e$ . Also notice that for same values of $V_S/V_P$ and $e$ , $\Delta_T$ has much smaller value than $\Delta_N$ . .	17
1.3	Phase velocity surfaces in a fractured medium: Background medium is isotropic with one set of vertical fractures oriented perpendicular to $x$ -direction. Crack density $e$ of the fractures is 8%. Notice that P-wave and SV-wave velocities are different for dry and fluid-filled fractures. . . . .	18
1.4	The phase velocity surfaces in an isotropic medium with two sets of vertical fractures embedded in it; angle between the fracture sets is 30°. The crack densities of the fracture sets are 6% and 8%. Notice that velocities of all three modes (P-, S1-, S2-waves) are different for dry and fluid-filled fractures. . . . .	19
1.5	(a) VTI and (b) HTI models: VTI media are typically formed due to layering of sand-shale sequence or due to the intrinsic anisotropy of the sedimentary rocks (mostly shale) while HTI media are mostly formed due to the presence of rotationally invariant vertical fractures in an isotropic host rock. . . . .	23
1.6	Group velocity surfaces in Green River shale for (a) P- and (b) SV-waves: Notice that the group velocity surfaces are symmetrical about vertical axis. Colorbar shows the polarization of particles with respect to the slowness direction. . . . .	24
1.7	Group velocity surfaces in an HTI medium for (a) P- and (b) SV-waves: The medium has one set of <b>fluid-filled</b> vertical fractures perpendicular $x$ -axis. Notice that group velocity surfaces also symmetrical about $x$ -axis. Colorbar shows the polarization of particles with respect to the slowness direction. . . . .	25

1.8	Group velocity surfaces in an HTI medium (dry fractures) for (a) P- and (b) SV-waves: The medium has one set of <b>dry</b> vertical fractures perpendicular $x$ -axis. Notice that group velocity surfaces also symmetrical about $x$ -axis. Colorbar shows the polarization of particles with respect to the slowness direction. . . . .	26
1.9	Variation of reflection coefficients with angles of incidence and azimuth: (a) dry fractures, (b) one set of fluid-filled fractures, and (c) a VTI medium. Notice that there is a significant difference in the reflection coefficients between the cases when the fractures are dry and fluid-filled. Also notice that there is no change in the reflection coefficients with azimuth when the bottom layer is a VTI medium. . . . .	27
1.10	The subsurface contains two fractured layers. In case the orientations of fractures are different in these layers, pure shear modes $S^{\parallel}$ and $S^{\perp}$ entering second layer from first layer will, again, split into pure modes. This makes analysis of the S-wave data very challenging. In coarse layer-stripping, the goal is to remove or null the effects of first layer while analysing the reflections from the bottom of second layer (Thomsen et al., 1999).	31
1.11	(a) Equal-area projection of the upper hemisphere of directions representing polarizations of qS1 (solid bars) and qS2 (broken bars) as seen by the horizontal instruments, after propagating through parallel vertical cracks striking east-west. The position of each polarization pair is determined by the angle of incidence $\theta$ and azimuth $\phi$ , such that the center point corresponds to vertical propagation. (b) Schematic profile showing the raypath angles at geophones 1, 2 and 3 mapped on the projection (a). The inner circle marks the theoretical shear-wave window (angles smaller than the critical angle) at about $35^{\circ}$ for plane waves at a horizontal free surface (MacBeth and Crampin, 1991). . . . .	32
2.1	Discretization scheme in a standard staggered grid (SSG) scheme in 2D: There are four different grids staggered to each other. Notice that stiffness tensor $c_{ijkl}$ and $\sigma_{xz}$ are not defined at the same locations which necessitates the interpolation of some components of $c_{ijkl}$ . Similarly, buoyancy $b$ and particle velocity components $v_i$ are not defined at the same grid nodes which requires the interpolation of $b$ . $v_{x,z}$ also needs to be interpolated if the medium has symmetry lower than orthorhombic. . . . .	50

2.2	Discretization scheme in a rotated staggered grid (RSG) scheme in 2D: There are only two different grids staggered to each other. All components of stress tensor $\sigma_{ij}$ and stiffness tensor $c_{ijkl}$ are collocated. Hence, no interpolation of $c_{ijkl}$ is required to estimate $\sigma_{ij}$ after each time step. $b$ still needs to be interpolated to estimate particle velocity components $v_i$ . No interpolation of any spatial derivative of particle velocity $v_{i,j}$ is needed in any kind of anisotropic media. . . . .	51
2.3	A snapshot of $x$ -component of particle velocity $v_x$ after 650 time steps (650 ms) in Green River Shale with the symmetry axis in $x$ -direction: Wave propagation was simulated using SSG scheme. The model is a homogeneous block with 450 grid points (grid spacing 10 m) in all the directions. Both P- and SV-waves were generated by an explosion source. Group velocity surfaces (dashed) were superimposed on top of wavefronts. Triplications in SV-wave can be observed in the symmetry planes ( $xy$ and $xz$ ). 55	55
2.4	A snapshot of $x$ -component of particle velocity $v_x$ after 650 time steps (650 ms) in an orthorhombic medium: Wave propagation was simulated in SSG. All three types of waves qP, qS1 and qS2 were generated by an explosion. Group velocity surfaces (dashed) were superimposed on the wavefronts. . . . .	56
2.5	A snapshot of $x$ -component of particle velocity $v_x$ after 650 time steps (650 ms) in Green River shale with symmetry axis rotated by $30^\circ$ about $y$ -direction: Wave propagation was simulated in RSG. Due to the rotated symmetry axis, wavefront is also rotated in $xz$ -plane. $zx$ -plane is the symmetry plane of the medium where group velocity surface (dashed) has been superimposed on the wavefronts. . . . .	57
2.6	A snapshot of $x$ -component of particle velocity $v_x$ after 575 time steps (575 ms) in a triclinic medium: Wave propagation was simulated in RSG. All three types of waves qP, qS1 and qS2 were generated due to the explosion. . . . .	58
2.7	Three-layered model used to generate seismic data using both the finite-difference method and the reflectivity method. The model has three flat layers. The middle layer has one set of fluid-filled vertical fractures normal to $x$ -direction. . . . .	60
2.8	Seismic data generated using finite-difference method (a) $x$ -component of particle motion, and (b) $y$ -component of particle motion: PP is the reflected P-wave from top of second layer, PS is the converted S-wave (P-to-S) from top of second layer, PPPP is the reflected P-wave from bottom of the second layer and the PPSS is the converted S-wave (P-to-S) from bottom of the second layer. . . . .	61

2.9	Comparison between the seismic data generated by the finite-difference method and by the reflectivity method at two azimuths and offsets: (a) At azimuth $16^\circ$ and offset 1080 m, and (b) at azimuth $21^\circ$ and offset 1120 m. . . . .	62
2.10	Comparison between the $x$ -component of seismic data generated by the finite-difference method and by the reflectivity method for a whole seismic line: The line is 400 m away from the source in $y$ -direction. The traces plotted in blue and red were generated by the finite-difference and the reflectivity methods, respectively.	63
2.11	Comparison between the $y$ -component of seismic data generated by the finite-difference method and by the reflectivity method for a whole seismic line: The line is 400 m away from the source in $y$ -direction. The traces plotted in blue and red were generated by the finite-difference and the reflectivity methods, respectively.	64
2.12	Comparison between the $z$ -component of seismic data generated by the finite-difference method and by the reflectivity method for a whole seismic line: The line is 400 m away from the source in $y$ -direction. The traces plotted in blue and red were generated by the finite-difference and the reflectivity methods, respectively.	65
2.13	3D model used to generate synthetic seismograms: Layer 1 is isotropic, layer 2 has VTI symmetry, layer 3 has one set of dry fractures, layer 4 has orthorhombic symmetry, and basement is isotropic. . . . .	67
2.14	Shot gathers generated for model shown in figure 2.13: (a) $x$ -component of velocity $v_x$ in inline direction, (b) $y$ -component of velocity $v_y$ in inline direction, (c) $v_x$ in crossline direction, and (d) $v_y$ in crossline direction. . . . .	68
2.15	Subsurface model used to demonstrate shear wave splitting: In all the experiments, background model remains same. Only the number of fracture sets and fracture orientation changes. A plane-wave source is used. Source is polarized at $45^\circ$ from $x$ -axis. Source and receivers are placed at each grid location. .	70
2.16	Seismic sections generated using a plane-wave source: (a) $x$ -component of the particle motion ( $S^\perp$ ), and (b) $y$ -component of the particle motion ( $S^\parallel$ ). There is one set of dry vertical fractures in the middle layer of the subsurface model (figure 2.15) with increasing crack density from left to right of the model. Notice that arrival time of $S^\perp$ is increasing with increasing fracture density. . . . .	72



2.17	Seismic sections generated using a plane-wave source for one set of dry and fluid-filled fractures: Fractures are dipping $60^\circ$ with vertical. (a) $x$ -component of velocity ( $v_x$ or $S^\perp$ ) for dry fractures, (b) $y$ -component of velocity ( $v_y$ or $S^\parallel$ ) for dry fractures, (c) $x$ -component of velocity ( $v_x$ or $S^\perp$ ) for fluid-filled fractures, and (d) $y$ -component of velocity ( $v_y$ or $S^\parallel$ ) for fluid-filled fractures. Notice that for dry fractures $S^\parallel$ is traveling faster than $S^\perp$ and opposite is true for fluid-filled fractures. . . . .	74
2.18	Time-difference between $S^\perp$ and $S^\parallel$ for both dry and fluid-filled fractures: Time-difference is the largest when the fractures are vertical. As the dip of the fractures is increased, time-difference for fluid-filled fractures starts decreasing and after certain angle, $S^\parallel$ becomes faster and $S^\perp$ becomes slower. For dry fractures, $S^\perp$ and $S^\parallel$ always remain faster and slower, respectively, but the time-difference between the two starts decreasing after a certain dip. . . . .	75
2.19	S-wave seismic sections for two dry vertical fracture sets making an angle of $30^\circ$ : (a) $x$ -component of velocity $v_x$ , (b) $y$ -component of velocity $v_y$ , (c) faster $S1$ mode, and (d) slower $S2$ mode. Notice the arrival at about 1.5 s is reflected from the bottom of the fractured layer. S-wave splitting is evident. . . .	78
2.20	Time-difference between $S2$ and $S1$ waves reflected from the bottom of the fractured layer (two sets of intersecting fractures): Notice that the time-difference for both dry and fluid-filled fractures stays same for all angles. With the angle between the two fracture sets increasing, time-difference is decreasing. After a certain angle pure faster $S1$ becomes slower and pure slower $S2$ becomes faster. . . . .	79
2.21	Time-difference between $S^\perp$ and $S^\parallel$ reflected from the bottom of the fractured layer containing corrugated fractures: Notice that, unlike the case of rotationally variant fractures, vertical dry and fluid-filled fractures have different time-difference. Moreover, dry and fluid-filled fractures show different time-difference as the fractures dip is increased. Dry horizontal fractures, unlike fluid-filled fractures, do not show any shear-wave splitting. . . .	80
3.1	Initial-value ray tracing in Marmousi model. . . . .	85
3.2	An example of wavefront construction technique in a depth-dependent velocity model: Notice that the extra rays are inserted after certain times to maintain the ray density. . . . .	86

3.3	The solution of two-point ray tracing by the bending method: The initial guessed raypath is iterated until final solution is attained. . . . .	87
3.4	Comparison of group velocity computed with Fourier expansion (equation 3.6) and the exact group velocity in Taylor sandstone: For P- and SH-waves, the approximate curves closely follow the exact curves of velocity. But for SV-wave, approximate group velocity curve deviates from the exact velocity curve, especially at the oblique angles. . . . .	92
3.5	The angle $\psi$ between a ray and symmetry axis can be expressed in terms of the azimuth $\phi$ and the incidence angle $\beta$ of the ray with vertical and the tilt $\theta$ of the symmetry axis with vertical. . . . .	93
3.6	P- and SV-waves group velocities calculated using equations 3.6 and 3.7 for a TTI medium (Dog Creek shale rotated by $45^\circ$ about $y$ -axis) with azimuth $\phi$ and incidence angle $\beta$ of the group velocity vector (Figure 3.5): (a) Group velocities for P-wave, (b) Difference between the exact and the Fourier expansion group velocities for P-wave. (c) Group velocities for SV-wave, and (d) Difference between the exact and the Fourier expansion group velocities for SV-wave. Notice that velocities are varying both with $\beta$ and $\phi$ . . . . .	95
3.7	Comparison between the exact group velocity, group velocity computed by the Fourier expansion (equation 3.6), and the group velocity derived by search scheme for P-, SV-, and SH-waves in Green River shale: Notice that for P-wave, Fourier expansion solution is deviating from exact group velocity trend at oblique angles. For SV-wave, the Fourier expansion solution completely fails to predict the right group velocity at oblique angles. Search scheme is predicting the group velocity precisely for all three modes. For SV-wave, we get one of the three solutions at triplication. . . . .	100
3.8	Phase and Group angles in Green River shale for P-, SV- and SH-waves: Notice that for SV-wave, three different phase angles have the same group angle which causes the triplication in group velocity surface. The search scheme solves for only one of the phase angles associated with a group direction. Hence, the search scheme yields only one of the branches of the triplication in figure 3.7. . . . .	101

3.9	Comparison between the exact group velocity and the group velocity computed by search scheme for SV-wave in Taylor sandstone: In the absence of triplication, the search scheme accurately reproduces the whole group velocity curve. Exact group velocity curve was computed by constant increment in phase angle, but we can see that group velocity vectors are unevenly distributed due to focusing and defocusing of the energy. This is not the case in group velocity curve produced by the search scheme. . . . .	102
3.10	Phase (a) and group (b) velocity surfaces of the orthorhombic medium which was used as the test model to invert group velocities using search scheme: Thomsen-style anisotropic parameters are $\alpha_0 = 3000$ m/s, $\beta_0 = 2000$ m/s, $\varepsilon^{(1)} = 0.25$ , $\varepsilon^{(2)} = 0.15$ , $\delta^{(1)} = 0.05$ , $\delta^{(2)} = -0.1$ , $\delta^{(3)} = 0.15$ , $\gamma^{(1)} = 0.28$ , $\gamma^{(2)} = 0.15$ . . .	104
3.11	Comparison between the exact and the group velocities computed by search scheme at various azimuths: Exact group velocity curves for $30^\circ$ and $60^\circ$ were not calculated due to the non-planar phase vector. Notice the problems in estimation of group velocity close to S-wave singularity at oblique azimuth $60^\circ$ .	105
3.12	Traveltimes estimated with brute force scheme (Faria and Stoffa, 1994b) in a VTI medium with (a) and without (b) hyperbolic interpolation. . . . .	108
3.13	Relative absolute error (%) caused by hyperbolic interpolation for a VTI medium with vertical velocity $\alpha_0$ gradually increasing with depth. . . . .	109
3.14	Raypaths for (a) P-, SV-, and SH-waves in a smoothly varying HTI media (equation 3.17) with symmetry axis in $x_1$ -direction: Initial raypaths were guessed as a straight line joining source and receivers. Most of the results converged in about 40 iterations. Raypaths for equivalent isotropic medium are also displayed. . . . .	111
3.15	Traveltime of P-, SV-, and SH-waves in HTI model. Traveltimes in equivalent isotropic medium are also displayed. . . . .	112
3.16	The subsurface model with TI thrust sheet embedded into an isotropic background: The thrust sheet is divided into four TI blocs with varying angle of axis of symmetry with respect to the vertical axis. . . . .	113
3.17	(a) Traveltime computed by two-point ray tracing and interpolation, (b) Absolute relative difference in traveltime computed by ray bending scheme and by method proposed Kumar et al. (2004). . . . .	114

3.18	Traveltime for the thrustsheet model (figure 3.16) in 3D: The model is not varying in $y$ -direction. . . . .	115
4.1	(a) Plot of $f(m)$ against $m$ : Notice that as the $m$ goes below zero, $f(m)$ increases rapidly. (b) Plot of $df(m)/dm$ against $m$ : As $m$ goes below zero, the absolute value of $df(m)/dm$ increases rapidly which indicates that $f(m)$ is increasing sharply as $m$ turns more negative. . . . .	131
4.2	Input model parameters: (a) $\Delta_N$ and (b) $\Delta_T$ . Note that the first layer does not have any fractures, and hence $\Delta_N = 0$ and $\Delta_T = 0$ . The middle and bottom layers have one set of vertical fractures oriented normal to the $x$ -direction. . . . .	135
4.3	(a) Vertical and (b) horizontal components of the data (shot gather) for the model shown in figure 4.2. The shot is located at the $x$ -location of 230 m. All the scattering modes (PP, PS, SS, SP) were incorporated in the modeling. . . . .	136
4.4	Inverted model parameters without using any constraints in the error function: (a) $\Delta_N$ and (b) $\Delta_T$ . Notice that at several locations $\Delta_N$ and $\Delta_T$ are less than zero which is not physically possible. Moreover, the inverted model values are not close to the input model values (figure 4.2). . . . .	137
4.5	Inverted model parameters with constraint function $f(\mathbf{m})$ (equation 4.22) added in the error function: (a) $\Delta_N$ and (b) $\Delta_T$ . Notice that $\Delta_N$ and $\Delta_T$ are no longer less than zero at any location. Moreover, the values of the inverted model parameters are closer to the values of the input model parameters (figure 4.2). . . . .	138
4.6	Subsurface model with laterally varying fracture parameters: (a) $\Delta_N$ and (b) $\Delta_T$ . The top layer does not have any fractures, the middle layer has one set of vertical fractures oriented normal to the $x$ -direction with smoothly varying fracture parameters. The bottom layer also has one set of vertical fractures oriented normal to the $x$ -direction with constant $\Delta_N$ and $\Delta_T$ . . . . .	139
4.7	(a) Vertical and (b) horizontal components of the data (shot gather) for the model shown in figure 4.6. The shot is located at the $x$ -location of 230 m. All the scattering modes (PP, PS, SS, SP) were incorporated in the modeling. . . . .	140
4.8	Inverted model parameters for the subsurface model displayed in figure 4.6: (a) $\Delta_N$ and (b) $\Delta_T$ . Notice that the inverted $\Delta_N$ and $\Delta_T$ values are very close to the original $\Delta_N$ and $\Delta_T$ . The constraint function was not used in the inversion. . . . .	141

4.9	Inverted model parameters (a) $\Delta_N$ and (b) $\Delta_T$ using only vertical component seismic data: Note that the inversion results have deteriorated compared to the inversion results when both of the components of the data are inverted simultaneously (figure 4.5). However, the syncline layer has been imaged in both the sections. . . . .	144
4.10	Inverted model parameters (a) $\Delta_N$ and (b) $\Delta_T$ using only horizontal component seismic data: Notice that the inversion results have deteriorated compared to the inversion results when both of the components of the data are inverted (figure 4.5); the values of $\Delta_N$ and $\Delta_T$ have been overestimated in second layer. . . . .	145
4.11	Diagonal elements of the covariance matrices of $\Delta_N$ and $\Delta_T$ in the region of interest when the vertical and horizontal components of the data are inverted simultaneously. . . . .	146
4.12	Diagonal elements of the covariance matrices of $\Delta_N$ and $\Delta_T$ in the region of interest when only the vertical component data is inverted. The covariances have increased many fold compared to the case when both of the components of the data are inverted simultaneously. . . . .	147
4.13	Diagonal elements of the covariance matrices of $\Delta_N$ and $\Delta_T$ in the region of interest when only the horizontal component data is inverted. The covariances are larger compared to the case when both of the components are inverted simultaneously. However, the covariances are smaller than those from the case in which only the vertical component is inverted. . . . .	148
4.14	Inverted model parameters (a) $\Delta_N$ and (b) $\Delta_T$ using only the vertical component data for the subsurface model shown in figure 4.6. The inverted values are slightly deteriorated when compared to those values inverted from both of the components of the data simultaneously. . . . .	149
4.15	Inverted model parameters (a) $\Delta_N$ and (b) $\Delta_T$ using only horizontal component data for the subsurface model shown in figure 4.6. The inverted values are slightly deteriorated when compared to those values inverted from both of the components of the data simultaneously. . . . .	150
4.16	Amplitude spectrum of a 40 Hz Ricker wavelet: Notice that beyond 130 Hz, the amplitude spectrum is zero. . . . .	153
4.17	Inverted (a) $\Delta_N$ and (b) $\Delta_T$ using every other frequency sample up to 130 Hz: Source pulse is a 40 Hz Ricker wavelet. Notice that the results are very similar to the results shown in figure 4.5 which was generated using all of the frequency samples up to the Nyquist. . . . .	154

4.18	Inverted (a) $\Delta_N$ and (b) $\Delta_T$ using every third frequency sample up to 130 Hz: Source pulse is a 40 Hz Ricker wavelet. Notice that the results are very similar to the results shown in figure 4.5 which was generated using all of the frequency samples up to the Nyquist. . . . .	155
4.19	Inverted (a) $\Delta_N$ and (b) $\Delta_T$ using only every fourth frequency sample up to 130 Hz: Source wavelet is a 40 Hz Ricker wavelet. Notice that the inverted results have slightly deteriorated when compared to the results shown in figure 4.5. . . . .	156
4.20	Amplitude spectrum of a 30 Hz Ricker wavelet: Notice that beyond 96 Hz, the amplitude spectrum is zero. . . . .	157
4.21	Inverted (a) $\Delta_N$ and (b) $\Delta_T$ using every frequency sample up to 96 Hz: Source pulse is a 30 Hz Ricker wavelet. Notice that the spatial resolution of the inverted models has gone down. . . . .	158
4.22	Inverted (a) $\Delta_N$ and (b) $\Delta_T$ using every other frequency sample up to 96 Hz: Source pulse is a 30 Hz Ricker wavelet. Notice that the spatial resolution has further gone down. Moreover, $\Delta_N$ and $\Delta_T$ values have been overestimated for the second layer. . . . .	159
4.23	Inverted (a) $\Delta_N$ and (b) $\Delta_T$ using every third frequency sample up to 96 Hz: Source pulse is a 30 Hz Ricker wavelet; the results have worsened when compared to the results shown in figure 4.21. . . . .	160
4.24	Subsurface model used to generate finite-difference data: (a) $\Delta_N$ and (b) $\Delta_T$ . The top layer does not have any fractures. The bottom layer has one set of vertical fractures oriented normal to the $x$ -direction. $\Delta_N$ and $\Delta_T$ are smoothly increasing from the left to the right in the model. . . . .	163
4.25	One of the shot gathers generated by 3D finite-difference code: (a) Vertical component (b) Horizontal component. The direct waves have been muted out. The source type is a vertical force. Hence, in addition to the PP and the PS arrivals, the SS arrival is also present. . . . .	164
4.26	Comparison between finite-difference data (red) and ray-Born generated data: (a) Vertical component (b) Horizontal component. There is a reasonable match between these two data sets. . . . .	165
4.27	Inverted model parameters (a) $\Delta_N$ (b) $\Delta_T$ : The general trend in $\Delta_N$ and $\Delta_T$ has been recovered. At a few locations, the values of $\Delta_N$ and $\Delta_T$ are less than zero which can be avoided by setting a larger value for multiplier $\epsilon$ . However, this may cause over estimation of $\Delta_N$ and $\Delta_T$ at other locations. . . . .	166

5.1	Comparison between the exact $\tau$ - $p$ curve and $\tau$ - $p$ curves generated by using the $q(p)$ given in equations 5.1 and 5.2 which I call approximation1 and approximation2, respectively. . . . .	176
E.1	A typical subsurface with a number of layers ( $l_1, l_2, \dots, l_n$ ). . .	191
E.2	Subsurface model used to generate synthetic seismic data. A vertical force was used as the source. A single line of receivers was used to collect the data. First layer is isotropic while second and third layers have one set of vertical fractures oriented normal to $x$ -direction. . . . .	191
E.3	Seismic sections generated for model shown in figure E.2: (a) Vertical component generated without asymptotic expansion, (b) Vertical component generated after applying asymptotic expansion, (c) Horizontal component generated without asymptotic expansion, and (d) Horizontal component generated after applying asymptotic expansion. . . . .	192
E.4	Comparison between the synthetic data generated with and without asymptotic approximation of equation 4.10: (a) Vertical component, (b) Horizontal component. Notice that the synthetics are in excellent match. . . . .	193
E.5	A three layer model used to demonstrate the inversion by asymptotic approximation: First layer does not have any fractures in it. Layer 2 has one set of vertical fractures oriented normal to $x$ -direction with $\Delta_N = 0.3$ and $\Delta_T = 0.1$ . Layer 3 also has one set of vertical fractures oriented normal to $x$ -direction with $\Delta_N = 0.5$ and $\Delta_T = 0.2$ . . . . .	194
E.6	Inverted models $\Delta_N$ and $\Delta_T$ for top of (a) layer 2 (flat layer) and (b) layer 3 (syncline) of the model shown in figure E.6. Notice that the inversion results are much better when multiple shots are used. . . . .	195

# Chapter 1

## Introduction

### 1.1 Introduction

Recognition of fractures or fracture networks in a hydrocarbon reservoir could be the key to its economic viability. The literature is full of examples where understanding of fracture patterns helped save the potential reservoirs from being abandoned (e.g., Aguilera, 1995; Nelson, 2001). Sometimes, the hydrocarbon recovery is completely dependent on the exploitation of the natural fracture networks in a reservoir. Typical examples are *tight gas* reservoirs and *coalbed methane* reservoirs.

Rocks in tight gas reservoirs are often characterized by sufficient porosity, but they have very low matrix permeability ( $\leq 0.1$  mD) which might render gas production unprofitable. This type of reservoir, however, is often fractured (Neves et al., 2003). These fractures provide the necessary open channels for the flow of gas, and they may control the permeability of the reservoir (Bansal, 2003). A high density of naturally occurring fractures has been recognized as a controlling factor for commercial success of production wells (e.g., Neves et al., 2003).

Coal has negligible matrix porosity and permeability. Reservoir gases



are not contained in granular pores; instead they are absorbed on the surface of the coal. Although coal has an impermeable matrix, it has an anisotropic fabric of natural fractures known as cleats. The cleat system is composed of two orthogonal sets of fractures known as face cleats and butt cleats (e.g., Laubach et al., 1998). Exploitation of this cleat system is crucial for commercial production of gas from the coalbed methane reservoirs (Shuck et al., 1996).

Nelson (2001) lists the following reasons to understand the fracture patterns in a reservoir: (1) Early assessment of reservoir's potential, (2) Optimization of well locations and paths, (3) Accurate prediction of field rates and recovery, and (4) Economic depletion of field.

To characterize the fractures, it is important to understand them. The following are the two definitions of fractures given by two prominent geologists, pioneers in fracture study:

*“A natural fracture is a macroscopic planar discontinuity that results from stresses that exceed the rupture strength of the rock”* (Stearns, 1994).

*“A reservoir fracture is a naturally occurring macroscopic planar discontinuity in rock due to a deformation or physical diagenesis”* (Nelson, 2001).

Fractures can be either man-made (e.g., hydraulic fractures, cracks developed while drilling) or naturally occurring in the reservoirs. For exploration purposes, detection of naturally occurring fractures are preferred which are proven conduit for oil and gas in low-porosity reservoirs (Aguilera, 1998).

There are six main fracture parameters which might be relevant to a reservoir geophysicist:

1. **Fracture orientation:** Fracture orientation may control the direction of fluid flow in a reservoir and are taken into account in the derivation of equivalent stiffness matrix (section 1.3) for the fractured media.
2. **Fracture spacing:** Fracture spacing or fracture density may be a major factor while planning the location of the production wells in the field. Drilling many wells on the same fracture network may lead to over production and quick depletion of a reservoir. Fracture spacing is related to fracture density (crack density), a parameter often used by geophysicists in describing fractures. However, exact estimate of fracture spacing cannot be made from crack density.
3. **Fracture aperture:** Fracture permeability is proportional to the cube of fracture aperture (Laubach, 2003). Typical fracture aperture may vary from 0.06 mm to 3 cm depending on the lithology and compaction. In general, fracture aperture decreases with depth. Fracture apertures, measured on outcrops, are not considered to be reliable enough to predict the permeability in the subsurface. Fracture aperture measured from core is also not considered to be very reliable because the core is not under the same stress and strain conditions as it was originally in the subsurface (Aguilera, 1998). I have not found any reference where the

in-situ stresses and strain condition is simulated to measure the exact aperture from the core.

4. **Fracture area:** Fractures could be either infinitely extensive or could terminate into another fracture or bed rock. Well data or core data cannot be used to determine the fracture area. This is a fundamental problem in fracture analysis and only direct observation, so far, seems to be a promising method to solve this problem.
5. **Fracture porosity:** Fracture porosities are mostly secondary porosities. Most of the fractures are considered to be only a conduit to the hydrocarbon flow because of their low porosities which vary from 0.01 to 10% (Aguilera, 1998).
6. **Fracture morphology:** According to Nelson (2001) Fracture morphology can be considered as open, deformed, mineral-filled, or vuggy. Open fractures that are uncemented might have a positive effect on oil flow but a negative effect on water or gas flow due to coning (Aguilera, 1998). These fractures tend to close as reservoirs are depleted due to increase in normal stress condition. Mineral-filled fractures could be either partially mineralized or completely mineralized. Partially mineralized fractures might provide a better conduit for hydrocarbon flow because they remain open while reservoirs are depleted. Completely mineralized fractures are not very useful for hydrocarbon production. Hence, recognition of these completely mineralized fractures is important to avoid overly optimistic

estimates of hydrocarbon recovery from reservoirs.

## 1.2 Motivation

In the past, detection of the fracture network in the subsurface has been a very difficult task due to the lack of direct observation. Many times, a reservoir is first developed and then the role of the fracture network is realized by observing the discrepancies between the observed and the expected production from the wells, instead of direct observations of fracture porosity, size, and connectivity (e.g., Aguilera, 1998; Laubach, 2003).

Fractures can be detected by direct core observation from a wellbore. However, it may sometimes be very difficult to maintain core integrity while drilling. Drilling may introduce artificial fractures in the core which might be confused with the natural fractures. There are, however, logging tools available now, which can give better core samples and can image fractures in borehole walls. These tools can provide correct but insufficient data to image fracture networks on a regional scale. Moreover, most of the fractures in the subsurface are nearly vertical which is corroborated by the success of horizontal or directional production wells in naturally fractured reservoirs (Aguilera, 1995). Hence, there are very slim chances of intercepting vertical fractures with a vertical well. This situation becomes worse in the case of large fractures (Laubach, 2003).

Surface seismic data can also be used to detect fracture patterns in the subsurface. Aligned fractures or fracture swarms behave as anisotropic

media in the seismic frequency band. There are several examples in literature where surface seismic data were successfully used to detect fracture patterns in a reservoir (e.g., Hall and Kendall, 2003; Shen et al., 2002; Shuck et al., 1996). However, surface seismic data may not be sufficient for detecting large regional fractures. Moreover, the shape of fractures and spacing between them cannot be appraised by surface seismic due to limitations of equivalent media theories (section 1.3). Further, seismic data can reveal only certain parameters which are called fracture parameters by the seismologists. Moreover, most of the conventional seismic methods are limited to laterally homogeneous media (section 1.5). Much of my dissertation research is aimed at extending the existing seismic methods to laterally varying media to invert for fracture parameters that are resolvable from seismic data (namely, fracture orientation, crack density and fracture infill).

In this chapter, I will review some of the popular equivalent or effective media theories for cracks and fractures, I will explain the differences between the HTI and VTI media, and I will give an overview of the conventional methods of estimation of fracture parameters. Finally, I will outline my research objectives and describe the organization of the rest of my dissertation chapters.

### **1.3 Equivalent media theories for cracks and fractures**

In continuum mechanics a hypothesis is made that, if a real material with its atomic and molecular structure is replaced by an equivalent model continuum, which remains a continuum no matter how much it is subdivided,

the macroscopic mechanical properties of the material remain unchanged. This is called the continuum hypothesis (e.g., Christensen, 1979; Hudson, 1991). This hypothesis works as long as the scale of observation is much larger than the scale-length of the molecular structure.

In a similar way, micro fractures, pores and other heterogeneities with uniform statistical distributions can be replaced by an **equivalent** or **effective** medium provided that the scale of the observation is much larger than the scale of the heterogeneities. The replacement of the inhomogeneous media with an equivalent continuum might make the material anisotropic. In exploration seismology, this approach is favored due for reasons. First, the wave equation for the homogeneous anisotropic media is easier to deal with than the wave equation for the inhomogeneous media. Second, the scale of the observation, or seismic wavelengths, is much larger than the scale length of the heterogeneities present in the subsurface (Hudson, 1991).

The concept of equivalent media clearly implies that, if the stress, strain or displacements are measured on a large enough scale, the values obtained and the relationship between them will be that of homogeneous continuum (e.g., Christensen, 1979). This implies some kind of spatial averaging process. For instance, the average stress and strain would be defined as

$$\bar{\sigma}_{ij} = \frac{1}{V} \int_V \sigma_{ij} dV, \quad (1.1)$$

and

$$\bar{\varepsilon}_{ij} = \frac{1}{V} \int_V \varepsilon_{ij} dV, \quad (1.2)$$

where  $V$  is the region large compared to the scale of the heterogeneities in the region  $V$ . Similarly, other quantities such as the average stiffness tensor of the material  $\bar{c}_{ijkl}$  can be used to relate the average stress and strain as

$$\bar{\sigma}_{ij} = \bar{c}_{ijkl}\bar{\epsilon}_{ij}. \quad (1.3)$$

One may construct a laboratory test (Hudson, 1991) or a mathematical model (Grechka, 2003) by isolating  $V$  and imposing a static average stress and measuring average strain in order to measure the average stiffness tensor. Although no one has yet tried any laboratory measurements of average stress and strain to yield overall average stiffness tensor (to the best of my knowledge), many analytical solutions for average stiffness tensor have been derived using various approaches.

Based on the averaging of the stress and strain, Backus (1962) derived expressions for an equivalent stiffness tensor for a stack of homogeneous, isotropic flat layers. Eshelby (1957), first, gave an analytical solution for the stress and strain inside an ellipsoidal inclusion in an unbounded homogeneous material for a static stress at infinity. Ellipsoid is a very versatile shape because it can accommodate most kinds of heterogeneities ranging from spherical inclusions to flat cracks. This model became instantly popular and Cheng (1978) extended this model to derive the equivalent elastic properties of a cracked isotropic host rock which turned out to be transversely isotropic. This model was valid for only small concentration of the cracks and, unlike Hudson's model (section 1.3.3), could handle a range of defined aspect ratios of the cracks. Due

to its limited applicability in the presence of multiple sets of cracks, this theory is not taken into consideration here.

The most widely accepted equivalent media theories for fractured rocks were given by Hudson (1980) for penny-shaped cracks and Schoenberg and Douma (1988) for parallel planar discontinuities. Thomsen (1995) corrected for anisotropy caused by fluid-flow between cracks and spherical (equant) pores. Grechka (2003) numerically solved the wave equation for average stress and strain in an inhomogeneous media for given boundary conditions in order to estimate an average stiffness tensor of the material.

### 1.3.1 Linear slip theory

A perfectly welded interface requires that both the tractions and displacements be continuous across the interface (e.g., Aki and Richards, 2002, p. 128). An imperfectly welded interface requires that only traction be continuous, and the displacement field is not continuous across the interface (e.g., Schoenberg, 1980; Aki and Richards, 2002, p. 39). These imperfect bonding surfaces can be called fractures (Schoenberg, 1980). Let this small vector difference in displacement be  $[u_i]$ . If there are a number of thin parallel fractures, the traction  $\sigma_{ij}n_j$  applied on the face of fractures and extra slip across the fractures per unit length in the direction of fracture normal is related by the following linear relationship (Schoenberg and Douma, 1988):

$$n_j \frac{\partial u_i}{\partial x_i} = Z_{ij} \sigma_{jk} n_k, \quad (1.4)$$



where  $n_j$  is the fracture normal,  $\sigma_{jk}$  is the second-order stress tensor, and  $Z_{ij}$  is defined as **fracture system compliance tensor** which is symmetric and non-negative.  $Z_{ij}$  depends on fracture orientation, fracture density (or crack density, see section 1.3.3), fracture infill (fractures are fluid-filled or dry), and fracture corrugation (e.g., Schoenberg and Douma (1988); Kachanov (1992)). Schoenberg and Sayers (1995) derived an analytical expression relating second-order fracture system compliance tensor  $Z_{ij}$  to fourth-order excess fracture compliance tensor  $s_{ijkl_f}$  which can be written as

$$s_{ijkl_f} = \frac{1}{4}(Z_{ik}n_l n_j + Z_{jk}n_l n_i + Z_{il}n_k n_j + Z_{jl}n_k n_i). \quad (1.5)$$

Schoenberg and Sayers (1995) also showed that equivalent compliance  $s_{ijkl}$  of a fractured medium is given by a summation of unfractured background medium compliance  $s_{ijkl_b}$  and the excess fracture compliances  $s_{ijkl_f}$ ; i.e.,

$$s_{ijkl} = s_{ijkl_b} + s_{ijkl_f}. \quad (1.6)$$

Schoenberg and Sayers (1995) and Schoenberg and Helbig (1997) assumed that more than one set of intersecting parallel fractures in the same background, do not affect the compliance of each other (figure 1.1). Moreover, equivalent compliance of the medium can be given by summing the individual fracture compliance to the background compliance; i.e.,

$$s_{ijkl} = s_{ijkl_b} + \sum_m s_{ijkl_f}^{(m)}, \quad (1.7)$$

where  $s_{ijkl_f}^{(m)}$  is the compliance of  $m^{th}$  fracture set. It should be noted that all fracture compliance tensors for different fracture sets and the background compliance tensor should be transformed into common coordinate system before

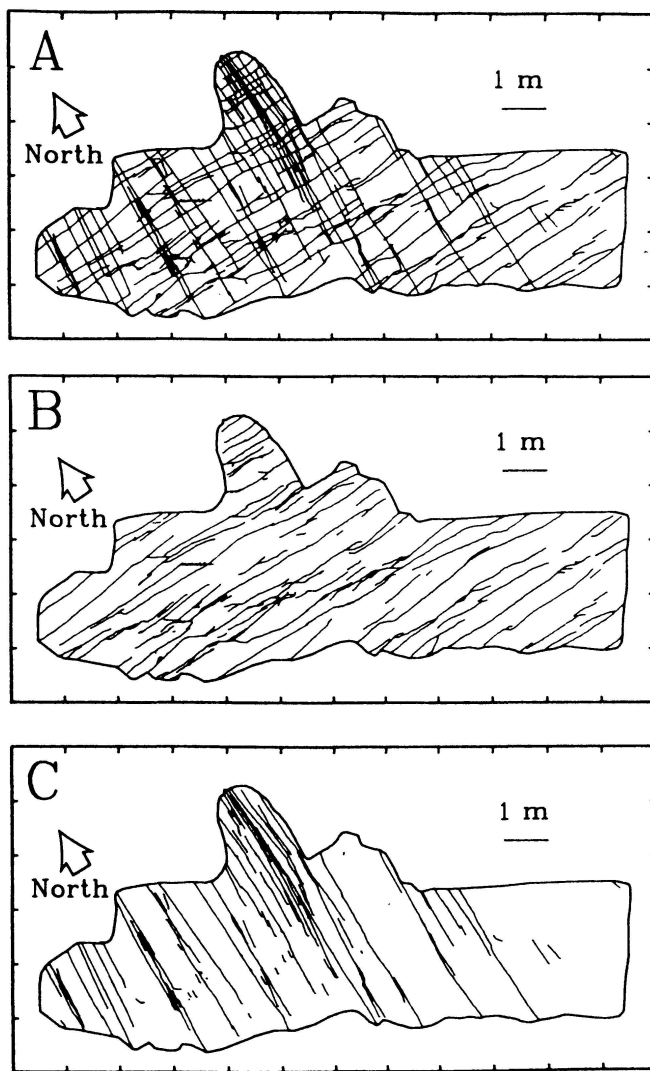


Figure 1.1: Maps of intersecting fractures on bedding surface of Rico Formation, southeastern Utah (Olson and Pollard, 1989): Linear slip theory suggests that each fracture set can be treated individually without taking into account any interaction between different fracture sets; i.e., compliances of each fracture set can be estimated, independently, by equation 1.5. Compliances of each fracture set and background medium add up to give the equivalent compliance of the fractured rock (equation 1.7).

adding them. Moreover, only compliances add up to yield an equivalent compliance tensor of a fractured rock, and the stiffness tensor should be calculated by inverting the compliance tensor (Schoenberg and Douma, 1988).

### 1.3.2 Rotationally invariant fractures

If properties of a parallel fracture set remain unchanged while they are rotated about their normal  $n_i$ , they are called **rotationally invariant fractures** (Schoenberg and Sayers, 1995). The fracture system compliance tensor  $Z_{ij}$  of these types of fractures should satisfy the following condition:

$$Z_{ij} = Z_N n_i n_j + Z_T (\delta_{ij} - n_i n_j) = Z_T \delta_{ij} + (Z_N - Z_T) n_i n_j. \quad (1.8)$$

If there is one set of vertical rotationally invariant fractures embedded in an isotropic background with a normal parallel to the  $x$ -axis, equations 1.6, 1.5 and 1.8 yield the following equivalent stiffness matrix  $\tilde{\mathbf{c}}$  of the fractured medium is given as

$$\tilde{\mathbf{c}} = \mathbf{c}_b - \begin{pmatrix} M\Delta_N & \lambda\Delta_N & \lambda\Delta_N & 0 & 0 & 0 \\ \lambda\Delta_N & r\Delta_N & r\Delta_N & 0 & 0 & 0 \\ \lambda\Delta_N & r\Delta_N & r\Delta_N & 0 & 0 & 0 \\ 0 & 0 & 0 & 0 & 0 & 0 \\ 0 & 0 & 0 & 0 & \mu\Delta_T & 0 \\ 0 & 0 & 0 & 0 & 0 & \mu\Delta_T \end{pmatrix}, \quad (1.9)$$

where  $\mathbf{c}_b$  is the stiffness matrix of the isotropic background,  $\lambda$  and  $\mu$  are the elastic Lamé's coefficients of the background,  $M = \lambda + 2\mu$ ,  $r = \frac{\lambda^2}{M}$ ,  $\Delta_N = \frac{Z_N M}{1 + Z_N M}$ , and  $\Delta_T = \frac{Z_T \mu}{1 + Z_T \mu}$ . The stiffness matrix  $\tilde{\mathbf{c}}$  suggests that the equivalent

medium is transversely isotropic with a horizontal symmetry axis (HTI, see section 1.4). The dimensionless quantities  $\Delta_N$  and  $\Delta_T$  are called the **normal and tangential weaknesses** (Schoenberg and Douma, 1988), respectively. The weaknesses vary from zero to one, with the zero value corresponding to the unfractured medium and the unity corresponding to the highly fractured medium. *It should be noted that P-wave velocity vanishes across the fractures for  $\Delta_N = 1$ , and S-wave velocity vanishes for  $\Delta_T = 1$ .*

In the case of multiple sets of fractures in the background, fracture compliances should be added to obtain the equivalent compliance of the media. It can be verified that increasing the number of fracture sets lowers the symmetry of the media. Table 1.1 summarizes the most common cases of anisotropy caused by the presence of the fractures (Bakulin et al., 2000a; Bakulin et al., 2000b; Bakulin et al., 2000c).

<b>Special cases of anisotropy caused by presence of the vertical fracture</b>		
<i>Background</i>	<i>Number of fracture sets</i>	<i>Equivalent Media</i>
Isotropic	1	HTI
Isotropic	2 (orthogonal)	Orthorhombic
Isotropic	2 (Non-orthogonal)	Monoclinic
VTI	1	Orthorhombic
Isotropic	$> 1$ ( $Z_N = Z_T$ ; any angle of intersection)	Orthorhombic

Table 1.1: In this table, most common cases of anisotropy due to presence of the vertical fractures are listed.

### 1.3.3 Hudson's model for aligned penny-shaped cracks

Hudson (1980, 1981) derived an analytical expression for the stiffness tensor for aligned and randomly oriented flat (penny-shaped) microcracks (where one of the semi-axes of the ellipsoidal cracks is much smaller than other two axes), with semimajor axis  $a$  and semiminor axis  $c$ , embedded in an isotropic background. The main assumptions for this formula to be valid are that (1) concentration of the cracks in the subsurface is very dilute, and (2) the radii or semimajor axes of the cracks are very small. To put this condition in the condensed form,  $e = \nu \langle a^3 \rangle \ll 1$ , where  $\nu$  is the number of cracks per unit volume; i.e.,  $\nu = N/V$ , and  $\langle \rangle$  denotes volume averaging. Parameter  $e$  was defined by Hudson as **crack density**. Hudson (1980) also assumed that concentration of the cracks in the background medium is homogeneous; cracks are evenly distributed, which is a very reasonable assumption in the case of dilute concentration of cracks.

If the cracks are aligned in the  $x$ -direction, then in condensed indices notation (Hudson, 1981):

$$\tilde{\mathbf{c}} = \mathbf{c}_b - \frac{e}{\mu} \begin{pmatrix} M^2 U_{11} & \lambda M U_{11} & \lambda M U_{11} & 0 & 0 & 0 \\ \lambda M U_{11} & \lambda^2 U_{11} & \lambda^2 U_{11} & 0 & 0 & 0 \\ \lambda M U_{11} & \lambda^2 U_{11} & \lambda^2 U_{11} & 0 & 0 & 0 \\ 0 & 0 & 0 & 0 & 0 & 0 \\ 0 & 0 & 0 & 0 & \mu^2 U_{33} & 0 \\ 0 & 0 & 0 & 0 & 0 & \mu^2 U_{33} \end{pmatrix} + O(e^2), \quad (1.10)$$

where  $\mathbf{c}_b$  is the stiffness matrix of the isotropic background,  $U_{11}$  and  $U_{33}$  are dimensionless quantities that depend on the boundary conditions of the crack

faces, fracture infill, direction of cracks (Hudson, 1981), and  $M = \lambda + 2\mu$ . It should be noted that, yet again, equivalent stiffness matrix  $\tilde{\mathbf{c}}$  represents an HTI medium. Assad et al. (1993) verified the Hudson's theory by a physical model study. They reported that the Hudson's theory was in agreement with the lab measurement for crack densities less than or equal to 7%.

#### 1.3.4 Comparison of Hudson's and Linear-Slip model and significance of fracture parameters

Schoenberg and Douma (1988) noticed that elastic stiffness matrices for fractures (equation 1.9) and microcracks (equation 1.10) have the same structure, and become identical if the following relationships are fulfilled:

$$\Delta_N = \frac{(\lambda + 2\mu)}{\mu} U_{11}, \quad (1.11)$$

$$\Delta_T = U_{33}e. \quad (1.12)$$

The two approaches are completely different for distinct types of cracks or fractures (Linear Slip theory assumes fractures to be planar discontinuities whereas Hudson (1980) treats the cracks as flat ellipsoidal inclusions), but they give the same elastic stiffness matrix  $\tilde{\mathbf{c}}$ . This observation suggests that **it is impossible to distinguish the type of the discontinuity (cracks and fractures) from seismic data; both cracks and fractures will have identical signatures on the seismic data.**

Hudson (1981) gave expressions for  $U_{11}$  and  $U_{33}$  for different types of infill materials in cracks. In case of a weak solid inclusion with elastic coefficients

$k'$  and  $\mu'$  (Schoenberg and Douma, 1988),

$$\Delta_N = \frac{4e}{3g(1-g)\left[1 + \frac{1}{\pi g(1-g)}\left(\frac{k'+4/3\mu'}{\mu}\right)\left(\frac{a}{c}\right)\right]}, \quad (1.13)$$

and

$$\Delta_T = \frac{16e}{3(3-2g)\left[1 + \frac{4}{\pi(3-2g)}\left(\frac{\mu'}{\mu}\right)\left(\frac{a}{c}\right)\right]}. \quad (1.14)$$

The parameter  $g$  is defined as

$$g = \frac{\mu}{\lambda + 2\mu} = \frac{V_S^2}{V_P^2}. \quad (1.15)$$

For dry (gas-filled) cracks both elastic coefficients of infill material vanish ( $k' = \mu' = 0$ ), yielding

$$\Delta_N = \frac{4e}{3g(1-g)}, \quad (1.16)$$

and

$$\Delta_T = \frac{16e}{3(3-2g)}. \quad (1.17)$$

If the cracks are filled with fluid, the shear modulus goes to zero ( $\mu' = 0$ ), but the bulk modulus  $k'$  for water or oil is almost equal to the shear modulus  $\mu$  of the medium. Hence, for very flat cracks (very small  $c/a$ ),  $[(k + 4/3\mu')/\mu](a/c) \gg 1$  and  $\Delta_N$  goes to zero. However, tangential weakness  $\Delta_T$  remains unchanged:

$$\Delta_N = 0, \quad (1.18)$$

$$\Delta_T = \frac{16e}{3(3-2g)}. \quad (1.19)$$

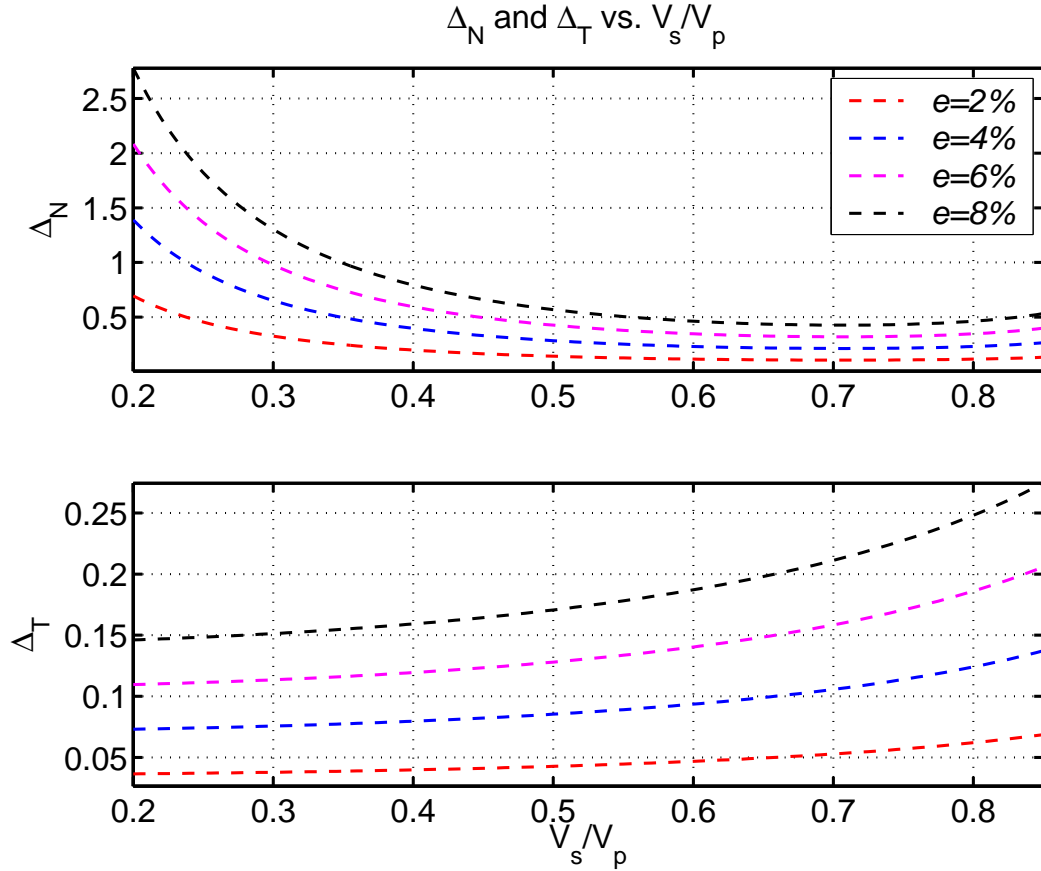


Figure 1.2:  $\Delta_N$  and  $\Delta_T$  in isotropic host rock for different values of fracture density  $e$  and  $V_S/V_P$ :  $\Delta_N$  is plotted for completely dry fractures using equation 1.16. Notice that  $\Delta_N$  exceeds the value of 1 for small  $V_S/V_P$  and high crack density  $e$ . Also notice that for same values of  $V_S/V_P$  and  $e$ ,  $\Delta_T$  has much smaller value than  $\Delta_N$ .

Table 1.2 summarizes the relationships of fracture weaknesses with microfracture properties in Linear-slip model and Hudson's model. Figure 1.2 shows  $\Delta_N$  and  $\Delta_T$  for different values of fracture density  $e$  and  $V_S/V_P$  for dry cracks. Notice that  $\Delta_N$  exceeds the value of 1 for small  $V_S/V_P$  and high crack density  $e$ . Also notice that for same values of  $V_S/V_P$  and  $e$ ,  $\Delta_T$  has much



Fracture parameters	Linear-slip model (Schoenberg and Sayers, 1995)	Thin, penny-shaped, aligned cracks (Hudson, 1980)
Normal weakness, $\Delta_N$	$\frac{(\lambda+2\mu)Z_N}{1+(\lambda+2\mu)Z_N}$	$\frac{4e}{3g(1-g)}$ (dry), 0 (fluid-filled)
Tangential weakness, $\Delta_T$	$\frac{\mu Z_N}{1+\mu Z_T}$	$\frac{4e}{3g(1-g)}$ (dry), $\frac{16e}{3(3-2g)}$ (fluid-filled)
Fluid indicator $\approx g \frac{\Delta_N}{\Delta_T}$	$\frac{Z_N}{Z_T}$	$\frac{7}{8} \left(1 + \frac{5\zeta^a}{2\pi f^b}\right)^{-1}$

<sup>a</sup> $\zeta$  represents the ratio of incompressibility of the inclusion fluid and the rock matrix.  
<sup>b</sup> $f$  is the aspect ratio of the cracks.

Table 1.2: Summary of relationships of fracture weaknesses with microfracture properties in Linear-slip model and Hudson’s model for natural fractures in hydrocarbon reservoirs (adapted from Shaw and Sen, 2006).

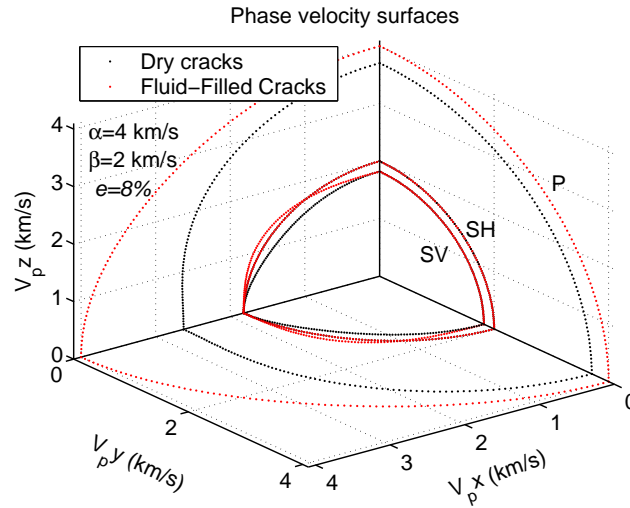


Figure 1.3: Phase velocity surfaces in a fractured medium: Background medium is isotropic with one set of vertical fractures oriented perpendicular to  $x$ -direction. Crack density  $e$  of the fractures is 8%. Notice that P-wave and SV-wave velocities are different for dry and fluid-filled fractures.

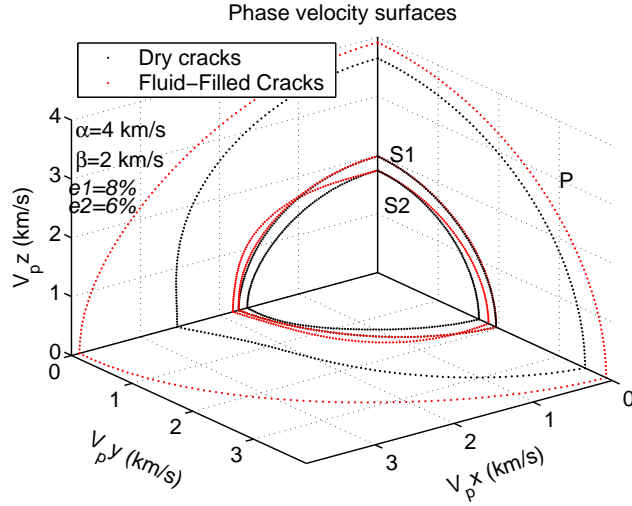


Figure 1.4: The phase velocity surfaces in an isotropic medium with two sets of vertical fractures embedded in it; angle between the fracture sets is  $30^\circ$ . The crack densities of the fracture sets are 6% and 8%. Notice that velocities of all three modes (P-, S1-, S2-waves) are different for dry and fluid-filled fractures.

smaller value than  $\Delta_N$ .

Figure 1.3 shows the phase velocity surfaces in a fractured medium. Background medium is isotropic with one set of vertical fractures oriented perpendicular to  $x$ -direction. Crack density  $e$  of the fractures is 8%. Notice the anisotropic behavior of all three modes (P-, SV- and SH-waves). Moreover, P- and SV-wave velocities are significantly different in case of dry and fluid-filled fractures. Appendix A explains how phase velocity surfaces in anisotropic media are calculated. Figure 1.4 shows the phase velocity surfaces in an isotropic medium with two sets of vertical fractures embedded in it. The crack densities of the fracture sets are 6% and 8%. Angle between the fracture sets is  $30^\circ$ . This type of medium falls into monoclinic symmetry (Table 1.1). There is a

more detailed discussion on this type of medium in chapter 2.

### 1.3.5 Fluid indicator for cracks and fractures

Schoenberg and Sayers (1995) suggested that the ratio  $Z_N/Z_T$  (section 1.3.2) could be indicator of the **fluid type** in fractures. This ratio is obtained as

$$\frac{Z_N}{Z_T} = g \frac{\Delta_N(1 - \Delta_T)}{\Delta_T(1 - \Delta_N)}. \quad (1.20)$$

For fluid-filled cracks normal weakness vanishes to zero ( $\Delta_N = 0$ ), and hence, the ratio  $Z_N/Z_T$  goes to zero. However, this is not always the case (Thomsen, 1995). This issue is discussed in detail in appendix B.

In the limit of small weaknesses ( $\Delta_N \ll 1$  and  $\Delta_T \ll 1$ ), above equation reduces to

$$\frac{Z_N}{Z_T} \approx g \frac{\Delta_N}{\Delta_T}. \quad (1.21)$$

Substituting the values of  $\Delta_N$  and  $\Delta_T$  from equations 1.16 and 1.17 into equation 1.21, we get

$$\frac{Z_N}{Z_T} \approx \frac{3 - 2g}{4(1 - g)} = 1 - \sigma/2. \quad (1.22)$$

For whole range of poisson's ratio  $\sigma$  from 0 to 0.5,  $Z_N/Z_T$  varies from 1 to 0.75.

## 1.4 HTI and VTI media

A transversely isotropic (TI) medium has a single axis of rotational symmetry. All seismic signatures in such media depend on the angle between

the propagation direction and the symmetry axis. TI media can have either a vertical axis of symmetry (VTI) or a horizontal axis of symmetry (HTI). A VTI medium is generally found in thin sand-shale sequences (figure 1.5(a)). Thin sand or shale bands are much thinner than the seismic wavelength. Hence, the whole sequence of sand-shale beds acts like a VTI medium to seismic waves (Backus, 1962). HTI media are mostly found in the subsurfaces with vertical parallel fractures (figure 1.5(b)). Both VTI and HTI media have 5 independent elastic coefficients and are given as follows:

$$\mathbf{c}^{(\text{VTI})} = \begin{pmatrix} c_{11} & c_{11} - 2c_{66} & c_{13} & 0 & 0 & 0 \\ c_{11} - 2c_{66} & c_{11} & c_{13} & 0 & 0 & 0 \\ c_{13} & c_{13}c_{33} & 0 & 0 & 0 & 0 \\ 0 & 0 & 0 & c_{44} & 0 & 0 \\ 0 & 0 & 0 & 0 & c_{44} & 0 \\ 0 & 0 & 0 & 0 & 0 & c_{66} \end{pmatrix}, \quad (1.23)$$

and

$$\mathbf{c}^{(\text{HTI})} = \begin{pmatrix} c_{11} & c_{13} & c_{13} & 0 & 0 & 0 \\ c_{13} & c_{33} & c_{33} - 2c_{44} & 0 & 0 & 0 \\ c_{13} & c_{33} - 2c_{44} & c_{33} & 0 & 0 & 0 \\ 0 & 0 & 0 & c_{44} & 0 & 0 \\ 0 & 0 & 0 & 0 & c_{66} & 0 \\ 0 & 0 & 0 & 0 & 0 & c_{66} \end{pmatrix}. \quad (1.24)$$

Although the general HTI media depends on five independent elastic coefficients, equivalent stiffness matrix  $\tilde{\mathbf{c}}$  of a fractured medium with one set of vertical fractures is defined by only four independent elastic parameters:  $\lambda$ ,  $\mu$ , and dimensionless quantities  $\Delta_N$  and  $\Delta_T$  (equation 1.9). Hence, it can be shown that the stiffness coefficients should satisfy the following condition

(Schoenberg and Sayers, 1995):

$$c_{11}c_{33} - c_{13}^2 = 2c_{44}(c_{11} + c_{13}). \quad (1.25)$$

Figure 1.6 shows the group velocity surfaces (or wavefronts since the medium is homogeneous) for P- and SV-waves in a VTI medium (Green River shale) with the Thomsen parameters (Thomsen, 1986)  $\alpha_0 = 3.292 \text{ km/s}$ ,  $\beta_0 = 1.768 \text{ km/s}$ ,  $\varepsilon = 0.195$ ,  $\delta = -0.220$ ,  $\gamma = 0.180$ . Notice that the group velocity surfaces are symmetrical about vertical axis. Colorbar shows the polarization of particles with respect to the slowness direction. Figure 1.7 shows the group velocity surfaces for an HTI medium made of one set of vertical fluid-filled fractures perpendicular to  $x$ -axis embedded in an isotropic background. Crack density  $e$  of the fracture set is 8% and the background P- and S-wave velocities are  $4 \text{ km/s}$  and  $2 \text{ km/s}$ , respectively. Notice that the group velocity surfaces are now symmetrical about  $x$ -axis. Figure 1.8 shows the group velocity surfaces when the fractures are dry; rest of the parameters were kept the same as in the previous case. Notice the change in the particle polarization and the change in the group velocity surfaces due to the change in the fracture infill (fluid-infill to dry). Appendix A explains how the group and phase velocity surfaces in anisotropic media are calculated. Figure 1.9 shows the variation in reflection coefficients with angles of incidence and azimuth in HTI and VTI media. The top layer is isotropic with P- and S-wave velocities of  $2.75 \text{ km/s}$  and  $1.25 \text{ km/s}$ , respectively. Density of the isotropic medium is  $1.5 \text{ g/cc}$ . (a) The bottom layer has one set of dry fractures. Crack density  $e$  is 8%. Medium P-wave and S-wave velocities are  $4 \text{ km/s}$  and  $2 \text{ km/s}$ , respectively. Medium density is  $2.075 \text{ g/cc}$ ,

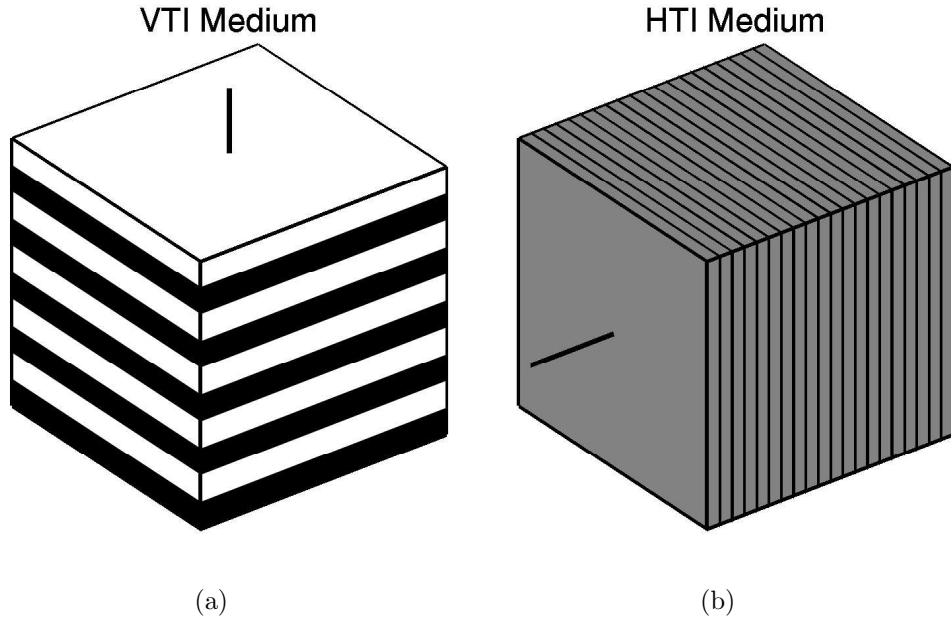
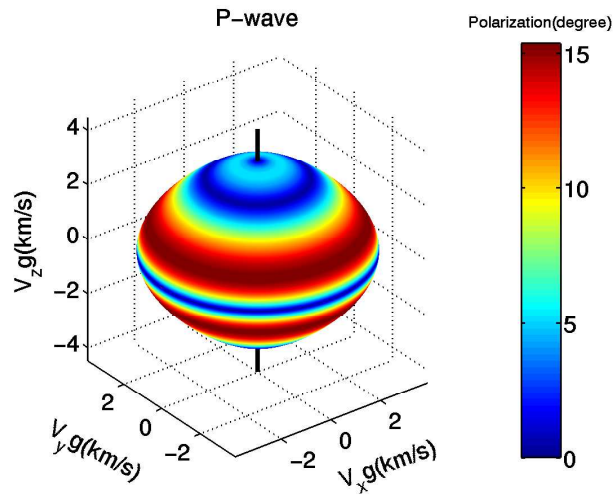
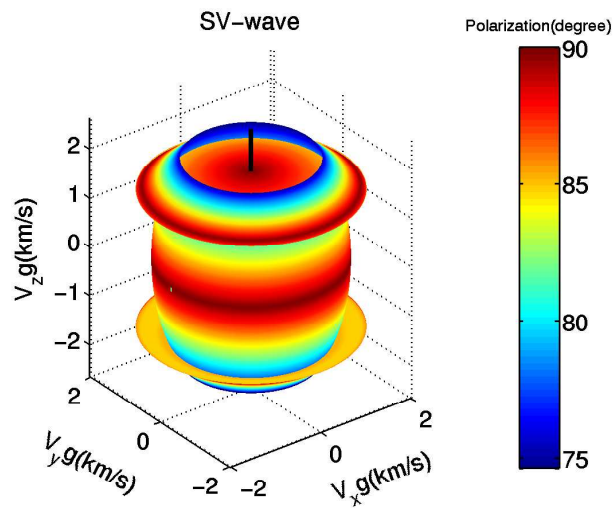


Figure 1.5: (a) VTI and (b) HTI models: VTI media are typically formed due to layering of sand-shale sequence or due to the intrinsic anisotropy of the sedimentary rocks (mostly shale) while HTI media are mostly formed due to the presence of rotationally invariant vertical fractures in an isotropic host rock.

(b) Bottom layer has one set of fluid-fill fractures. The rest of the parameters are kept the same as in the previous case, and (c) Bottom layer is a VTI medium (Taylor sandstone) with the Thomsen parameters (Thomsen, 1986)  $\alpha_0 = 3.368 \text{ km/s}$ ,  $\beta_0 = 1.829 \text{ km/s}$ ,  $\varepsilon = 0.110$ ,  $\delta = -0.035$ ,  $\gamma = 0.255$ . Notice the variation in the reflection coefficients with azimuth when the bottom layer is fractured (HTI medium). Moreover, there is a significant difference in the reflection coefficients between the cases when the fractures are dry and fluid-filled, especially at large incidence angles.

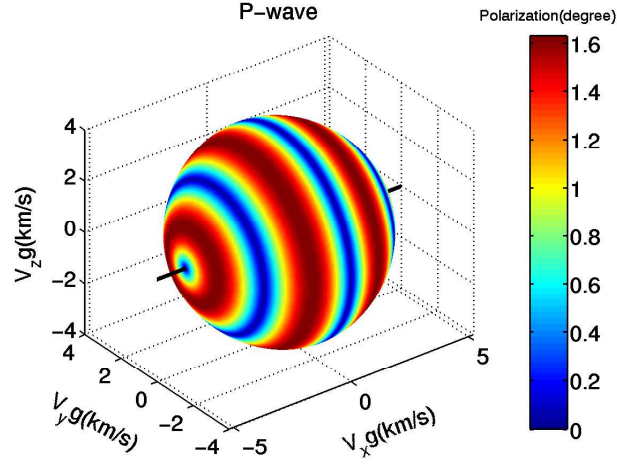


(a)

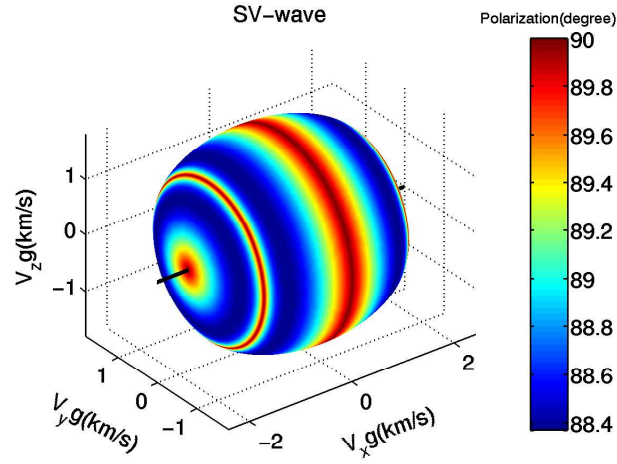


(b)

Figure 1.6: Group velocity surfaces in Green River shale for (a) P- and (b) SV-waves: Notice that the group velocity surfaces are symmetrical about vertical axis. Colorbar shows the polarization of particles with respect to the slowness direction.



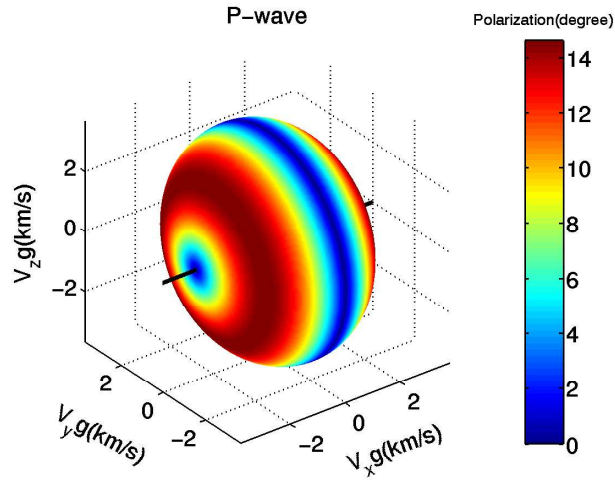
(a)



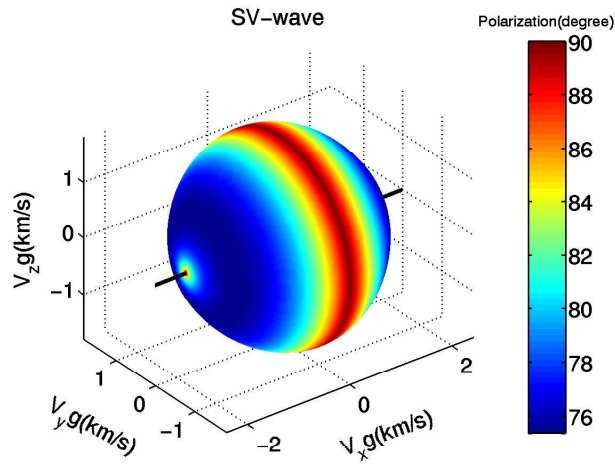
(b)

Figure 1.7: Group velocity surfaces in an HTI medium for (a) P- and (b) SV-waves: The medium has one set of **fluid-filled** vertical fractures perpendicular  $x$ -axis. Notice that group velocity surfaces also symmetrical about  $x$ -axis. Colorbar shows the polarization of particles with respect to the slowness direction.





(a)



(b)

Figure 1.8: Group velocity surfaces in an HTI medium (dry fractures) for (a) P- and (b) SV-waves: The medium has one set of **dry** vertical fractures perpendicular  $x$ -axis. Notice that group velocity surfaces also symmetrical about  $x$ -axis. Colorbar shows the polarization of particles with respect to the slowness direction.

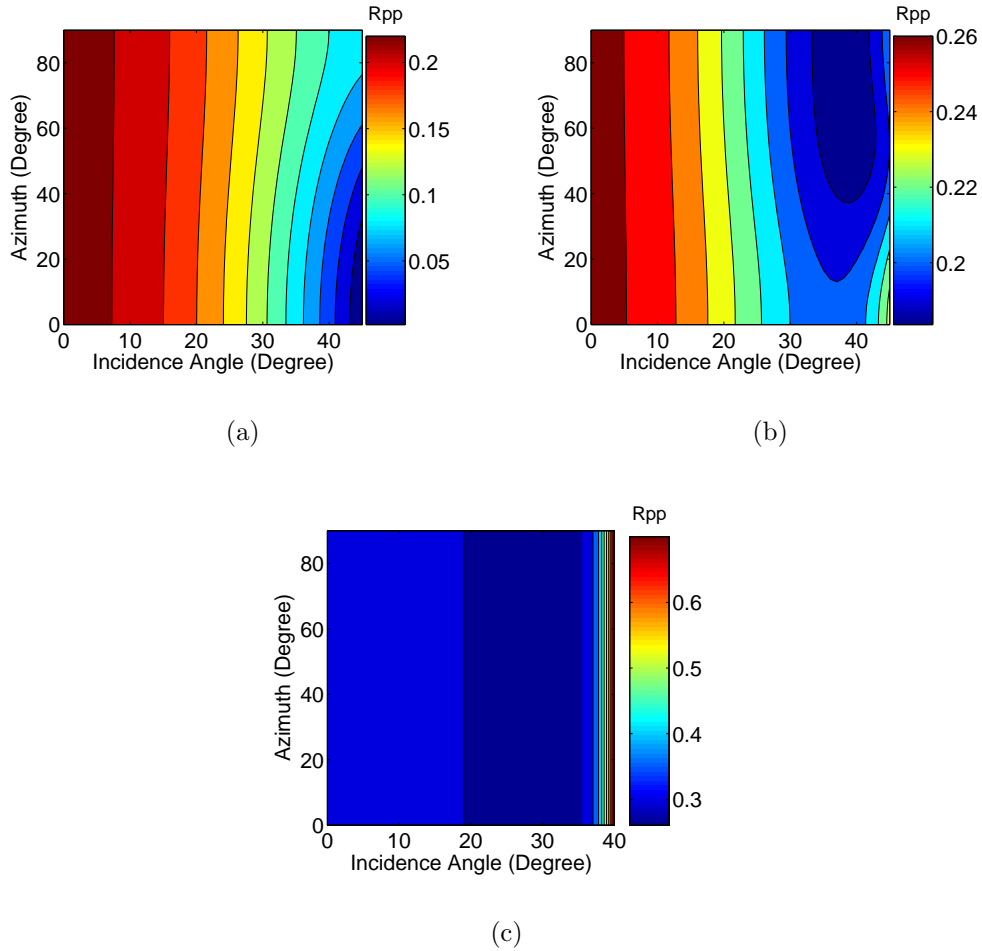


Figure 1.9: Variation of reflection coefficients with angles of incidence and azimuth: (a) dry fractures, (b) one set of fluid-filled fractures, and (c) a VTI medium. Notice that there is a significant difference in the reflection coefficients between the cases when the fractures are dry and fluid-filled. Also notice that there is no change in the reflection coefficients with azimuth when the bottom layer is a VTI medium.

## 1.5 Conventional methods of estimation of fracture parameters

The fracture parameters that can be estimated using seismic data are (1) orientation of the fractures or cracks, (2) crack or fracture density, and (3) fracture infill (dry or fluid-filled). As mentioned earlier, equivalent media theory does not carry information on the shape of the cracks or the fractures in the media. Hence, I do not expect to differentiate between the cracks and fractures from the seismic data.

A number of techniques have evolved in the last two decades to estimate the fracture parameters using seismic data, mainly using VSP and surface seismic data. I realize that these techniques can be grouped into three broad categories: S-wave splitting, P-wave NMO and AVOA analysis, and linearized Born inversion for fracture parameters.

### 1.5.1 S-wave splitting

Let us assume that the subsurface has parallel vertical fractures striking parallel to  $y$ -direction. Stiffness matrix of this type of medium is given by equation 1.9. S-wave propagating in a direction parallel to the fractures (say,  $z$ -direction which is vertical in this case) will be polarized into directions perpendicular to the fractures ( $x$ -direction) and parallel to the fractures ( $y$ -direction). S-wave velocity polarized parallel to the fractures ( $S^{\parallel}$ ) is given by  $\sqrt{\mu/\rho}$ , whereas velocity of S-wave polarized perpendicular to the fractures ( $S^{\perp}$ ) is given by  $\sqrt{\mu(1 - \Delta_T)/\rho}$  (these solutions are derived from Christoffel

equation; see appendix A).<sup>†</sup> It is obvious that the S-wave polarized perpendicular to the fractures travels slower than the S-wave polarized parallel to the fractures. This phenomenon is called S-wave splitting. This property of the S-wave has been exploited extensively in exploration seismology to detect fracture orientation and density. Note that the vertically traveling S-waves do not carry information on the fracture infill; velocities of the vertically traveling S-waves are affected only by  $\mu$  and  $\mu(1 - \Delta_T)$ . So the only “fracture parameter” that affects the S-wave velocities is tangential weakness  $\Delta_T$ . However, the tangential weakness is immune to the fracture infill (equations 1.17 and 1.19). This limitation on S-wave data, however, did not discourage the geophysicists, and a number of approaches were proposed and used to determine the fracture orientation and crack density using S-wave splitting.

An underlying idea in most of the approaches is to estimate the time difference between S-wave arrivals  $S^{\parallel}$  and  $S^{\perp}$ , and polarization of the faster S-wave  $S^{\parallel}$ . A number of rotation schemes to separate the fast and the slow S-waves was suggested by various researchers. Some of the most popular techniques are Alford rotation (Alford, 1986), Igel and Crampin rotation technique (Igel and Crampin, 1990), and configuration of propagator matrix between two geophones levels (used only in VSP) (Neville, 1986). A comprehensive review of all these methods can be found in MacBeth and Crampin (1991).

---

<sup>†</sup>S-waves traveling parallel and perpendicular to the fractures are only denoted as  $S^{\parallel}$  and  $S^{\perp}$  as they are pure shear modes (particle motions are orthogonal to the propagation direction of wave). In anisotropic media, pure modes (longitudinal or shear) rarely exist, and the waves are normally denoted as qP, qS1 and qS2 (q stands for quasi).

Alford rotation is the most widely used technique for rotation of S-wave data. Alford (1986) proposed a technique that includes rotating, in a synchronic way, source and geophone by linearly combining the two polarizations. This is equivalent to rotating the medium and keeping source and receiver at their original orientations. This method is applicable only for  $2C \times 2C$  (two source components, two receiver components). S-wave zero-offset data are needed as input for this technique. However, stacked data are used as surrogate to the zero-offset data; although in anisotropic media, zero-offset data are not equivalent to the stacked data. Four different configurations of the stacked data are used: (1) sources oriented inline and receivers crossline, (2) sources oriented inline and receivers inline, (3) sources oriented crossline and receivers crossline, and (4) sources oriented crossline and receivers inline. This configures a  $2 \times 2$  data matrix; a tensor rotation by angle  $\theta$  is applied until the energy is focused onto the principal diagonal stacks and the energy detected on the off-diagonal stacks (inline source recorded on crossline receivers and vice versa) is minimal. The final rotation angle  $\theta$  is the orientation of the fractures. The time delay between  $S^{\parallel}$  and  $S^{\perp}$  (in fact, these stacked data are not pure  $S^{\parallel}$  and  $S^{\perp}$ ; most of the contribution in the stacked data comes from qS1 and qS2) is found by observing the time shift between events on each of the principal diagonals or by cross-correlating which yields the fracture density in the media. A homogeneous medium is assumed between the source and the receiver positions, and it works only for a single anisotropic layer. **Coarse-layer stripping techniques** (e.g., Winterstein and Meadows,

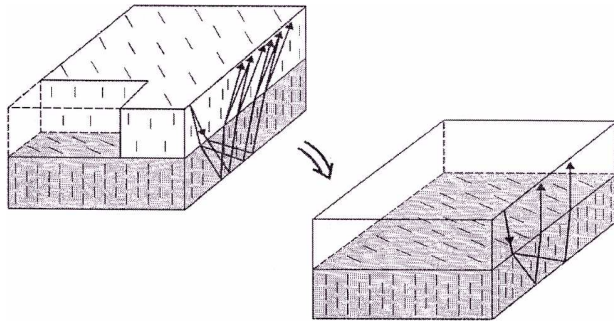


Figure 1.10: The subsurface contains two fractured layers. In case the orientations of fractures are different in these layers, pure shear modes  $S^{\parallel}$  and  $S^{\perp}$  entering second layer from first layer will, again, split into pure modes. This makes analysis of the S-wave data very challenging. In coarse layer-stripping, the goal is to remove or null the effects of first layer while analysing the reflections from the bottom of second layer (Thomsen et al., 1999).

1991; Thomsen et al., 1999) are used to extend the application of Alford to a layered media with a fracture set with a different azimuth in each layer.

Winterstein and Meadows (1991) reported that the subsurface rarely has only one fractured layer; instead, many fractured layers with varying fracture orientations are common. Alford rotation or any other rotation technique is applicable in case of a single fractured layer. The problem is that each pure shear mode splits into two modes as it enters the layers with a different orientation of fractures (different orientation of symmetry axis; see figure 1.10). To deal with this problem **coarse-layer stripping techniques** was introduced by Winterstein and Meadows (1991), and was modified by Thomsen et al. (1999). The idea behind the layer stripping is simple; first rotate and find the time-difference between  $S^{\parallel}$  and  $S^{\perp}$  for the arrivals from the bottom of the first

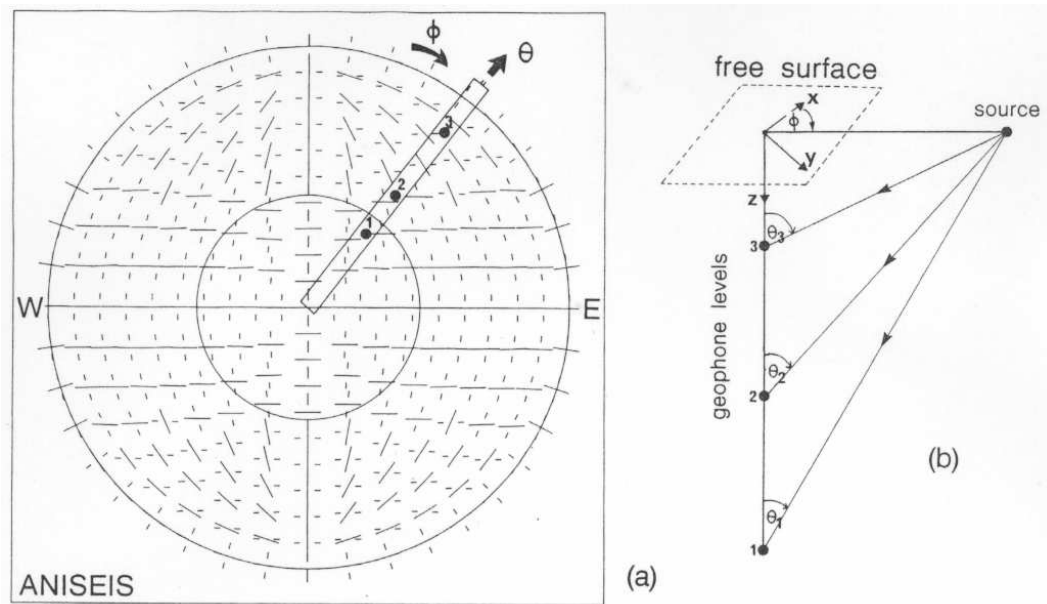


Figure 1.11: (a) Equal-area projection of the upper hemisphere of directions representing polarizations of qS1 (solid bars) and qS2 (broken bars) as seen by the horizontal instruments, after propagating through parallel vertical cracks striking east-west. The position of each polarization pair is determined by the angle of incidence  $\theta$  and azimuth  $\phi$ , such that the center point corresponds to vertical propagation. (b) Schematic profile showing the raypath angles at geophones 1, 2 and 3 mapped on the projection (a). The inner circle marks the theoretical shear-wave window (angles smaller than the critical angle) at about  $35^\circ$  for plane waves at a horizontal free surface (MacBeth and Crampin, 1991).

fractured layer, then subtract the one- or two-way time (depending on whether the data is VSP or surface seismic) from the arrivals from the bottom of next fractured layer and correct for dispersion and attenuation caused by the first fractured layer. The procedure is repeated for subsequent fractured layers.

The main drawbacks of most of the rotation techniques and layer stripping are that they rely on the orthogonality of the split S-waves (qS1 and qS2)

particle motion at the receiver location which is not always the case. In an azimuthally anisotropic media (e.g., HTI), the group direction (ray direction) deviates significantly from the phase direction. Split S-waves particle motions are orthogonal only for the same phase direction; these arrivals at the geophone may belong to the different phase directions, and hence, may not be orthogonal to each other. Unorthogonality of the split S-waves are illustrated in figure 1.11. Notice that beyond incidence angle of  $35^\circ$ , polarizations of qS1 and qS2 are significantly non-orthogonal.

Moreover, the amount of S-wave splitting in the data is dependent on the thickness of the fractured layer. In a very thin fractured layer, it might be very difficult to do any quantitative analysis on split S-wave arrivals. Many times the slow S-wave wavelet completely rides over the fast S-wave that makes it impossible to find the time-difference between these two arrivals. Moreover, S-wave signals are significantly distorted by the free surface which might make it very difficult to do any meaningful interpretation of the data.

### 1.5.2 P-wave NMO and AVOA analysis

P-wave NMO velocity in the horizontal plane of an HTI medium is elliptic in nature and is controlled by P-wave vertical velocity, fracture azimuth and one of the Thomsen-style parameters<sup>§</sup>  $\delta^{(V)}$  (e.g., Tsvankin, 1997a). P-wave

---

<sup>§</sup>Tsvankin (1997a) proposed ‘Thomsen-style’ parameters for HTI media. These parameters are very similar to the parameters given by Thomsen (1986) for VTI media. Like Thomsen parameters, Thomsen-style parameters are a set of five variables, namely  $\epsilon^{(V)}$ ,  $\delta^{(V)}$ ,  $\gamma^{(V)}$ ,  $V_{Pvert}$ ,  $V_{S\perp vert}$ . These parameters, like Thomsen parameters, are a very handy



NMO analysis at a minimum of three different azimuths can be inverted for these parameters. Another Thomsen-style parameter  $\varepsilon^{(V)}$  can be estimated by NMO analysis of dipping events (Contreras et al., 1999). These Thomsen-style parameters, in turn, can be used to estimate normal and tangential weaknesses  $\Delta_N$  and  $\Delta_T$ . Rüger (1997) derived an analytical expression for the P-wave AVO gradient for isotropic-HTI interface. The AVO gradient term  $B$  is composed of azimuthally invariant isotropic term  $B^{iso}$  and anisotropic term  $B^{ani}$  dependent on azimuthal angle  $\phi$  (angle between fracture-normal and CMP line), and is given as  $B = B^{iso} + B^{ani} \cos^2 \phi$ . Rüger and Tsvankin (1997) showed that AVO analysis at well separated multiazimuth data can reveal the fracture parameters.

The same approach with some modifications can be applied in the presence of more than one set of fractures with *weak* anisotropy approximation (Bakulin et al., 2000a; Bakulin et al., 2000b; Bakulin et al., 2000c). In addition to P-wave NMO analysis, converted split S-wave NMO analysis is also required in case of lower order of symmetry (Table 1.1); converted S-wave NMO velocity for flat reflectors, like P-wave NMO velocity, turns out to be elliptical in horizontal plane (Bakulin et al., 2000a), and can be inverted for additional anisotropic parameters (lower order of anisotropic media are defined by more elastic coefficients). Since the presence of higher number of parallel fracture sets lowers down the symmetry of the media, they also require more

---

tool to visualize the relationships between horizontal and vertical P- and S-wave velocities and strength of anisotropy. Moreover, these parameters are directly related to the fracture parameters  $\Delta_N$  and  $\Delta_T$  (Bakulin et al., 2000a).

parameters for an inversion, which requires solving more equations.

### 1.5.3 Linearized Born inversion of fracture parameters

Shaw and Sen (2006) introduced the direct inversion of wide-azimuth P-wave AVOA data to invert the fracture parameters  $\Delta_N$  and  $\Delta_T$ . They derived the following expression

$$\mathbf{R}_{PP}^{obs}(i, \phi) - \mathbf{R}_{PP}^{iso}(i) = \delta\mathbf{R}_{PP} = \mathbf{G}\mathbf{M}, \quad (1.26)$$

where  $i$  is the incidence angle,  $\phi$  is survey azimuth,  $\mathbf{R}_{PP}^{obs}$  represents the observed PP-reflection coefficients, and  $\mathbf{R}_{PP}^{iso}$  is the PP-reflection coefficient without the fractures in the medium.  $\mathbf{G}$  is the sensitivity matrix and  $\mathbf{M}$  is the model vector which is given as  $\mathbf{M} = [\Delta_N, \Delta_T]^T$ . Shaw and Sen (2006) derived analytic expressions for the elements of the matrix  $\mathbf{G}$  using first-order Born approximation, which depend on  $i$ ,  $\phi$ , and  $g = V_S^2/V_P^2$ .

Least squares solution of Equation 1.26 can be written as

$$\mathbf{M} = [\mathbf{G}^T\mathbf{G}]^{-1}\mathbf{G}^T\delta\mathbf{R}_{PP}. \quad (1.27)$$

If information on the isotropic medium in which the fractures are embedded and the fracture orientation are known a priori, or estimated by conventional methods (e.g., well log data, NMO velocity, or conventional AVO analysis),  $\delta\mathbf{R}_{PP}$  and  $\mathbf{G}$  can be computed. Once  $\delta\mathbf{R}_{PP}$  and  $\mathbf{G}$  are known, equation 1.27 can be used to estimate  $\mathbf{M} = [\Delta_N, \Delta_T]^T$ . Finally,  $\Delta_N$  and  $\Delta_T$  can reveal the crack density and the fluid-type in the fractures (equations 1.17 and 1.21).

The main limitation of this scheme is that it is applicable only for laterally homogeneous media. Further, the information on the isotropic background is needed as a priori. Table 1.3 summarizes all the conventional approaches to estimate the fracture parameters.

Summary of various fracture-parameters estimation approaches			
<i>Method</i>	<i>Data</i>	<i>Procedure</i>	<i>Estimated Parameters</i>
S-wave Splitting layer stripping	2C × 2C stacked S-wave surface or VSP data	estimating the time-difference between $S^{\parallel}$ and $S^{\perp}$ , estimation of orientation of $S^{\parallel}$	<b>Crack density</b> $e$ which is given as $e \approx \frac{T_{S^{\perp}} - T_{S^{\parallel}}}{T_{S^{\parallel}}}$ . <b>fractures orientation</b> $\phi$ .
Azimuthal P-wave NMO Analysis	P-wave CMP data at minimum of three azimuths	P-wave NMO velocity is estimated at three different azimuths and $V_{nmo}^2 = \alpha^2 \frac{1+2\delta^{(V)}}{1+2\delta^{(V)} \sin^2 \phi}$ is solved for vertical P-wave velocity $\alpha$ , azimuth $\phi$ and $\delta^{(V)}$	<b>fractures orientation</b> $\phi$ . Combining with AVOA analysis, Thomsen's parameter $\gamma$ can be extracted, which is related to <b>crack density</b> $e$ through <i>weak</i> anisotropy approximation.
AVOA Analysis	true amplitude preserved P-wave data at minimum of three azimuths	AVO gradient is given as $B = B^{iso} + B^{ani} \cos^2 \phi$ . This equation is solved for $B^{iso}$ , $B^{ani}$ and azimuth $\phi$	<b>Fractures orientation</b> $\phi$ ( $B$ is either most positive or most negative in direction of fracture-normal; i.e., when $\phi = 0$ . Some kind of modeling might be needed to resolve ambiguous $\phi$ ). Combining with P-wave NMO analysis, $\gamma^{(V)}$ can be extracted <sup>a</sup> which is related to <b>crack density</b> $e$ through <i>weak</i> anisotropy approximation <sup>b</sup> .
Linearized Born inversion	multi-azimuth P-wave data	$\mathbf{M} = [\mathbf{G}^T \mathbf{G}]^{-1} \mathbf{G}^T \delta \mathbf{R}_{PP}$	Normal weakness $\Delta_N$ and tangential weakness $\Delta_T$

<sup>a</sup>in case of gas-filled fractures, measurable azimuthal variation in AVO gradient is not possible at small angle of incidence (Rüger and Tsvankin, 1997) which may inhibit the estimation of  $\gamma$ .

<sup>b</sup> $B^{ani}$  is given by a combination of  $\delta^{(V)}$  and  $\gamma$ . Thus a direct estimate of  $\gamma$  from AVOA analysis is not possible. However, in case of tight formation with no equant porosity and thin **fluid-filled** cracks,  $\delta^{(V)} = \gamma$  which facilitate the direct estimation of  $\gamma$  from AVOA.

Table 1.3: Four most widely used approaches to estimate the fracture parameters are listed: Note that other than Born inversion none of these methods directly solves for normal- and tangential-weaknesses  $\Delta_N$  and  $\Delta_T$  which define the stiffness matrix of a fractured medium (equation 1.9).

## 1.6 Objectives and Organization

The main objective of my dissertation is to develop a new inversion algorithm that can invert for fracture weaknesses  $\Delta_N$  and  $\Delta_T$  in laterally varying media. My inversion scheme is based on ray-Born approximation and uses both vertical and horizontal components of seismic data. I have also developed a 3D forward modeling algorithm to generate synthetic data and ray-bending algorithm to compute traveltimes in general anisotropic media.

In chapter 2, 3D finite-difference modeling in general anisotropic media is explained. I study shear-wave splitting for a number of cases (e.g., fracture dip, angle between the fracture etc.) using finite-difference modeling scheme. Chapter 3 deals with ray-bending in 3D general anisotropic media. To accomplish ray-bending in general anisotropic media, a new method based on a search scheme is introduced to estimate the group velocity in a given group direction. For practical application to modeling and migration, I employed a hyperbolic interpolation scheme resulting in an efficient method for travel-time computation in finely gridded models. Chapter 4 focuses on the ray-Born inversion for fracture parameters in laterally varying media. Chapter 5 summarizes the research and highlights the scope of future research.

## Chapter 2

# Finite-difference modeling in anisotropic media: An S-wave splitting study in fractured reservoirs

### 2.1 Introduction

Accurate numerical simulation of wave propagation is essential for understanding the behavior of elastic waves in the subsurface. Synthetic data provide the forward model for inverse problems, they help the interpretation of field real seismic data, and they help to determine the lithology of the subsurface by attribute analysis. In addition to exploration seismologists, earthquake seismologists also routinely use synthetic seismic data to characterize the type and location of earthquakes.

Over the years, a number of methods have been developed to generate synthetic seismograms, with each method having its own advantages and disadvantages. Kennett (1983) popularized reflection-matrix method to generate seismic data in a stratified isotropic medium. This technique can account for all kinds of waves (e.g., direct, surface waves, multiples) and is reasonably cpu-efficient. These advantages encouraged others to use it for full waveform inversion as a tool to generate forward models at each iteration (e.g., Sen and Stoffa, 1991). Booth and Crampin (1983) and Fryer and Frazer (1984) extended the

reflectivity method to general anisotropic media. However, the generation of synthetic seismograms using this method in azimuthally anisotropic media is computationally intensive.

The second category of techniques are the asymptotic or ray-tracing methods. The asymptotic algorithms are very efficient computationally, but they cannot account for all types of seismic waves. Although this type of technique can handle complex media, there are problems in the presence of shadow zones and at caustics which precludes its wider application. An excellent overview of these schemes can be found in Carcione et al. (2002).

The third category of methods is called integral-equation methods where the wavefield is represented in an integral form and an analytical expression of the Green's function is sought. An overview of these schemes can be found in De Hoop (1995). Although most of the schemes in this category can account for all kinds of waves, their application in complex structures becomes tedious. However, these methods can be used to study wave propagation in a specific type of medium such as in a cracked or fractured medium (e.g., Liu et al., 1997).

Finally, there are methods that numerically solve the wave equation, which are sometimes called direct methods. These techniques can account for all kinds of waves and can handle complex subsurfaces. There are a number of numerical schemes that can solve the wave equation such as the finite-element method, the pseudo-spectral method, and the finite-difference method. All of these schemes have their own advantages and disadvantages. The finite-

element method can handle irregular grids and boundaries. Serón et al. (1996) and Padovani et al. (1994) give a good description of this scheme. The pseudo-spectral methods use Fourier and Chebychev differential operators to estimate the spatial derivatives. This scheme has been used by a number of geophysicists to model wave propagation (e.g., Fornberg, 1988; Carcione, 1994; Tessmer and Kosloff, 1994).

Finally, there are a number of finite-difference schemes available to simulate wave propagation. Kelly et al. (1976) showed how to generate synthetic seismic data using a finite-difference scheme in 2D acoustic media. Virieux (1984, 1986) introduced a staggered grid scheme to simulate wave propagation in 2D elastic media with a velocity-stress formulation. Levander (1988) used fourth-order spatial derivatives to generate synthetic seismograms using a finite-difference scheme in 2D elastic media. Faria and Stoffa (1994a) implemented a finite-difference scheme in 2D transversely isotropic media.

Although it was fairly straightforward to extend these 2D applications to 3D, it was not implemented in 3D right away due to lack of enough computational power. The advent of fast and cluster-based computers in the mid-1990s prompted the implementation in 3D. Graves (1996) and Dong and McMechan (1995) applied the standard staggered grid finite-difference scheme in 3D for isotropic and anisotropic media, respectively. Igel et al. (1995) derived dispersion relationships in general anisotropic media for the standard staggered grid scheme in 3D. They also pointed out that some components of the strain tensor will need to be interpolated to simulate wave propagation in



general anisotropic media, which would introduce additional numerical errors in a finite-difference scheme. Saenger et al. (2000) and Saenger and Bohlen (2004) introduced a modified staggered grid scheme in which a rotated staggered grid was used to simulate wave propagation in large contrast as well as in general anisotropic media. Moczo et al. (2002) introduced wave propagation in 3D isotropic heterogeneous medium utilizing volume harmonic and arithmetic averaging of elastic parameters and density.

Ramos-Martínez et al. (2000) generated synthetic seismograms in fractured media using eighth-order spatial-derivatives to study shear-wave splitting arising from the presence of cracks in the subsurface. To generate zero-offset S-wave data, they used a plane-wave shear source. They also used a standard staggered grid scheme to generate seismic data in all types of anisotropy. They derived equivalent medium using the approach given by Hudson (1980).

This chapter has two parts. In the first part, I review the finite-difference modeling in both conventional and modified staggered grids and show some examples of forward modeling. I also show a comparison between the finite-difference generated synthetic seismograms and the reflectivity method generated synthetic seismograms in an azimuthally anisotropic medium. In the second part, I use my finite-difference program to generate synthetic data in fractured media and observe the splitting pattern in various scenarios: namely, one set of rotationally invariant dipping fractures, two non-orthogonal vertical fractures and one set of corrugated dipping fractures. I observe the effects on S-wave splitting of the dip, the fracture infill (dry or

fluid-filled) and the angle between the fractures .

## 2.2 Modeling Algorithm

### 2.2.1 Governing equations

For small deformations, the equation of motion is given as (Aki and Richards, 2002, p. 18)

$$\rho \ddot{u}_i = \sigma_{ij,j} + f_i, \quad (2.1)$$

and the constitutive relationship (Hooke's law) for general anisotropic media is written as

$$\sigma_{ij} = c_{ijkl} \varepsilon_{kl}, \quad (2.2)$$

where  $u_i$  is the particle displacement vector,  $\sigma_{ij}$  is the second-order stress tensor,  $\varepsilon_{kl}$  is the strain tensor, body force  $f_i$  is the vector per unit volume that represents the source,  $\rho$  is the density, and  $c_{ijkl}$  is the fourth-order elastic stiffness tensor, which summarizes the elastic properties of the medium. A dot over a variable denotes differentiation with respect to time. Equations 2.1 can also be rewritten as

$$\dot{v}_i = b[\sigma_{ij,j} + f_i], \quad (2.3)$$

where  $v_i$  is the particle velocity and  $b = 1/\rho$  is the buoyancy. By taking the time-derivative of equation 2.2, and using the relation  $\varepsilon_{kl} = 1/2(u_{k,l} + u_{l,k})$  we get

$$\dot{\sigma}_{ij} = c_{ijkl} v_{k,l}. \quad (2.4)$$

Equations 2.3 and 2.4 are linear first-order coupled partial differential

equations for particle velocity and stress. These equations can be solved directly using a finite-difference algorithm.

Time and spatial derivatives of the quantities in equations 2.3 and 2.4 are performed using a Taylor series expansion. Any order of the Taylor series expansion in time and space can be performed. Higher order Taylor series in time and space yields more accurate results (Marfurt, 1984), at the cost of greater computational expense. Second- and fourth-order expansions in time and space, respectively, are mostly preferred due to their balance of accuracy and computation time (Levander, 1988). A detailed overview of numerical implementation of velocity-stress formulation in 3D isotropic media can be found in Graves (1996) and Minkoff (2002).

### 2.2.2 Sources and seismograms

Finite-difference schemes can handle numerous types of sources. For example, the unidirectional point source  $f_i$  acting in volume  $V$  can be represented as

$$f_i = Fw(t)s_i\delta(\mathbf{x} - \mathbf{x}_s), \quad (2.5)$$

where  $F$  is the magnitude of the force,  $w(t)$  is the source wavelet,  $s_i$  is the source orientation and  $\mathbf{x}_s$  is the location of the force. In the same way, generalized moment tensor  $m_{ij}$  acting within volume  $V$  can be written as

$$m_{ij} = M_{ij}w(t)\delta(\mathbf{x} - \mathbf{x}_s), \quad (2.6)$$

where  $M_{ij}$  is the moment amplitude matrix. A source represented in the form of a moment tensor first needs to be transformed into the equivalent distributed

body forces before it can be introduced into the velocity-stress formulation (equations 2.3 and 2.4). A very good description of its implementation can be found in Frankel (1993) and Graves (1996).

A seismogram can represent either particle velocity  $v$  or pressure  $p$ . If the receiver is oriented in the direction  $r_k$  where  $r_k r_k = 1$ , the particle velocity can be found as

$$v = v_k r_k = v_1 r_1 + v_2 r_2 + v_3 r_3. \quad (2.7)$$

The pressure seismogram can be represented as

$$p = -\frac{1}{3}\sigma_{kk} = -\frac{1}{3}[\sigma_{11} + \sigma_{22} + \sigma_{33}]. \quad (2.8)$$

### 2.3 Staggered grid finite-difference implementation

To implement the finite-difference scheme, all the quantities ( $c_{ijkl}$ ,  $b$ ,  $\sigma_{ij}$ ,  $u_i$ ) in equations 2.3 and 2.4 need to be discretized. I will review two types of discretization schemes: the conventional or standard staggered scheme (SSG) and the rotated staggered scheme (RSG). The main advantage of using a staggered grid is that the differential operators are centered at the same point in both space and time which enables the calculation of the derivative at half the grid size. Moreover, velocity and stress can be updated in time independent of each other.

Virieux (1984, 1986) first described SSG for isotropic medium in 2D. Figure 2.1 shows the discretization in a staggered grid scheme in 2D. Notice that there are four individual grids overlapping each other. In 3D there are

seven individual grids. Parameters are stored in the following manner: Normal stresses are stored as  $\sigma_{xx}(x_i, y_i, z_i)$ ,  $\sigma_{yy}(x_i, y_i, z_i)$ , and  $\sigma_{zz}(x_i, y_i, z_i)$ , where  $i$  represents grid number. Notice that all the normal stresses are stored on the same grids. Particle velocities are stored as  $v_x(x_i + h/2, y_i, z_i)$ ,  $v_y(x_i, y_i + h/2, z_i)$ , and  $v_z(x_i, y_i, z_i + h/2)$ , where  $h$  represents the grid size (for the sake of simplicity, I assume that the grid size in all directions is the same). Notice that all the particle velocity components are stored on three different grids.

Off-diagonal stress terms are stored as  $\sigma_{xy}(x_i + h/2, y_i + h/2, z_i)$ ,  $\sigma_{xz}(x_i + h/2, y_i, z_i + h/2)$ , and  $\sigma_{yz}(x_i, y_i + h/2, z_i + h/2)$ . Notice that all the shear stress components are stored on three different grids. The stiffness tensor and the buoyancy are stored as  $c_{ijkl}(x_i, y_i, z_i)$  and  $b(x_i, y_i, z_i)$ , respectively. This requires the interpolation of  $b$  and some components of  $c_{ijkl}$ .  $b$  is interpolated at the grids where the particle velocity components are defined. For instance,  $b(x_i + h/2, y_i, z_i)$  can be calculated as

$$b(x_i + h/2, y_i, z_i) = \frac{1}{2}[b(x_i, y_i, z_i) + b(x_{i+1}, y_i, z_i)]. \quad (2.9)$$

In the same way, the components of the  $c_{ijkl}$  which are needed to estimate the shear stress components need to be interpolated at the grids where the shear stress components are defined. For example,  $c_{1313}(x_i + h/2, y_i + h/2, z_i)$  can be estimated as (Graves, 1996)

$$c_{1313}(x_i + h/2, y_i + h/2, z_i) = 4 \left[ \frac{1}{c_{1313}(x_i, y_i, z_i)} + \frac{1}{c_{1313}(x_{i+1}, y_i, z_i)} + \frac{1}{c_{1313}(x_i, y_{i+1}, z_i)} + \frac{1}{c_{1313}(x_{i+1}, y_{i+1}, z_i)} \right]^{-1}. \quad (2.10)$$

Notice that the staggered grid scheme, discussed above, will also need the interpolation of the components of  $v_{i,j}$  if the medium has symmetry lower than orthorhombic. To demonstrate this need, let us write down equation 2.4 for an orthorhombic medium in condensed indices:

$$\begin{pmatrix} \dot{\sigma}_{xx} \\ \dot{\sigma}_{yy} \\ \dot{\sigma}_{zz} \\ \dot{\sigma}_{yz} \\ \dot{\sigma}_{xz} \\ \dot{\sigma}_{xy} \end{pmatrix} = \begin{pmatrix} c_{11} & c_{12} & c_{13} & 0 & 0 & 0 \\ c_{12} & c_{22} & c_{23} & 0 & 0 & 0 \\ c_{13} & c_{23} & c_{33} & 0 & 0 & 0 \\ 0 & 0 & 0 & c_{44} & 0 & 0 \\ 0 & 0 & 0 & 0 & c_{55} & 0 \\ 0 & 0 & 0 & 0 & 0 & c_{66} \end{pmatrix} \begin{pmatrix} v_{x,x} \\ v_{y,y} \\ v_{z,z} \\ v_{y,z} + v_{z,y} \\ v_{x,z} + v_{z,x} \\ v_{x,y} + v_{y,x} \end{pmatrix}. \quad (2.11)$$

Notice that  $\dot{\sigma}_{i,i}$  ( $i = 1, 2, 3$ ) are dependent only on  $v_{i,i}$  while  $\dot{\sigma}_{i,j}$  ( $i \neq j$ ) are controlled only by  $v_{i,j}$  ( $i \neq j$ ). This is true for any medium with symmetry higher or equal to orthorhombic medium (for example, isotropic, HTI, VTI). In the standard staggered grid scheme (SSG),  $\sigma_{i,i}$  and  $v_{i,i}$  are defined at the same location and so are  $\sigma_{i,j}$  and  $v_{i,j}$  (figure 2.1). Thus, to evaluate equation 2.11 no interpolation of any component of  $v_{i,i}$  and  $v_{i,j}$  is necessary.

Now, let us write down the equation 2.4 for a monoclinic medium:

$$\begin{pmatrix} \dot{\sigma}_{xx} \\ \dot{\sigma}_{yy} \\ \dot{\sigma}_{zz} \\ \dot{\sigma}_{yz} \\ \dot{\sigma}_{xz} \\ \dot{\sigma}_{xy} \end{pmatrix} = \begin{pmatrix} c_{11} & c_{12} & c_{13} & 0 & c_{15} & 0 \\ c_{12} & c_{22} & c_{23} & 0 & c_{25} & 0 \\ c_{13} & c_{23} & c_{33} & 0 & c_{36} & 0 \\ 0 & 0 & 0 & c_{44} & 0 & c_{46} \\ c_{15} & c_{25} & c_{35} & 0 & c_{55} & 0 \\ 0 & 0 & 0 & c_{46} & 0 & c_{66} \end{pmatrix} \begin{pmatrix} v_{x,x} \\ v_{y,y} \\ v_{z,z} \\ v_{y,z} + v_{z,y} \\ v_{x,z} + v_{z,x} \\ v_{x,y} + v_{y,x} \end{pmatrix}. \quad (2.12)$$

Notice that  $\dot{\sigma}_{i,i}$  and  $\dot{\sigma}_{i,j}$  are no longer exclusively dependent on  $v_{i,i}$  and  $v_{i,j}$ ,

respectively. For instance,  $\dot{\sigma}_{xx} = c_{11}v_{x,x} + c_{12}v_{y,y} + c_{13}v_{z,z} + c_{15}(v_{x,z} + v_{z,x})$ . However, in the SSG scheme,  $\sigma_{xx}$ ,  $v_{x,z}$  and  $v_{z,x}$  are not defined at the same grid locations which will necessitate the interpolation of  $v_{x,z}$  and  $v_{z,x}$  at the next grid location where  $\sigma_{xx}$  is defined. Similarly, some other components of  $v_{i,i}$  and  $v_{i,j}$  need to be interpolated to evaluate equation 2.12. This interpolation introduces additional numerical errors in the estimation of the wavefield. In fact, in the case of a triclinic medium, all the components of  $v_{i,i}$  and  $v_{i,j}$  need to be interpolated. This will likely introduce a considerable amount of numerical error in the computation.

To compute synthetic seismograms in monoclinic or triclinic media, a better grid discretization is needed. To circumvent this problem, another discretization scheme called rotated staggered grid (RSG) was proposed by Saenger et al. (2000). Figure 2.2 shows the RSG in 2D. The medium is divided into rectangular or square grids. There are only two staggered grids in either 2D or 3D. All the components of the stresses are stored as  $\sigma_{xx}(x_i, y_i, z_i)$ ,  $\sigma_{yy}(x_i, y_i, z_i)$ ,  $\sigma_{zz}(x_i, y_i, z_i)$ ,  $\sigma_{xy}(x_i, y_i, z_i)$ ,  $\sigma_{xz}(x_i, y_i, z_i)$ , and  $\sigma_{yz}(x_i, y_i, z_i)$ . All the velocity components are stored as  $v_x(x_i + h/2, y_i + h/2, z_i + h/2)$ ,  $v_y(x_i + h/2, y_i + h/2, z_i + h/2)$ , and  $v_z(x_i + h/2, y_i + h/2, z_i + h/2)$ . All the medium properties are stored as  $c_{ijkl}(x_i, y_i, z_i)$  and  $b(x_i, y_i, z_i)$ . The spatial derivatives are evaluated along the diagonals of the grids and then projected back to the sides of the grids. An excellent description can be found in Saenger et al. (2000). Since all of the components of  $\sigma_{ij}$  and  $v_{i,j}$  are positioned at the same location, wave propagation can be simulated in any kind of anisotropic medium

without interpolation of any components of  $v_{i,j}$ . Moreover, there is no need for interpolation of any component of  $c_{ijkl}$  using RSG which, unlike SSG, does not introduce any numerical error in a high contrast medium. However, buoyancy  $b(x_i, y_i, z_i)$  still needs to be interpolated on the grids where the components of particle velocity are stored. For instance,  $b(x_i + h/2, y_i + h/2, z_i + h/2)$  can be estimated as

$$\begin{aligned}
b(x_i + h/2, y_i + h/2, z_i + h/2) = & \frac{1}{8} [b(x_i, y_i, z_i) + b(x_{i+1}, y_i, z_i) + b(x_i, y_{i+1}, z_i) \\
& + b(x_i, y_i, z_{i+1}) + b(x_{i+1} + y_{i+1}, z_i) \\
& + b(x_{i+1}, y_i, z_{i+1}) + b(x_i, y_{i+1}, z + i + 1) \\
& + b(x_{i+1}, y_{i+1}, z_{i+1})]. \tag{2.13}
\end{aligned}$$

The RSG scheme, however, requires the additional estimation of some of the spatial derivatives which makes it computationally more expensive than SSG schemes. Therefore, I used SSG for media having symmetry higher than or equal to orthorhombic and RSG for media with monoclinic or triclinic symmetry.

The grid size is an important parameter in any finite-difference scheme. A large grid size allows for the computation of large models, but a very large grid size tends to push the numerical dispersion in the computation beyond acceptable limits (e.g., Marfurt, 1984). Furthermore, a small grid size requires small time-steps in computation to avoid numerical instability. Small time-steps increase the number of time-steps to be computed, which should be avoided in any finite-difference scheme as it takes a long time to compute each



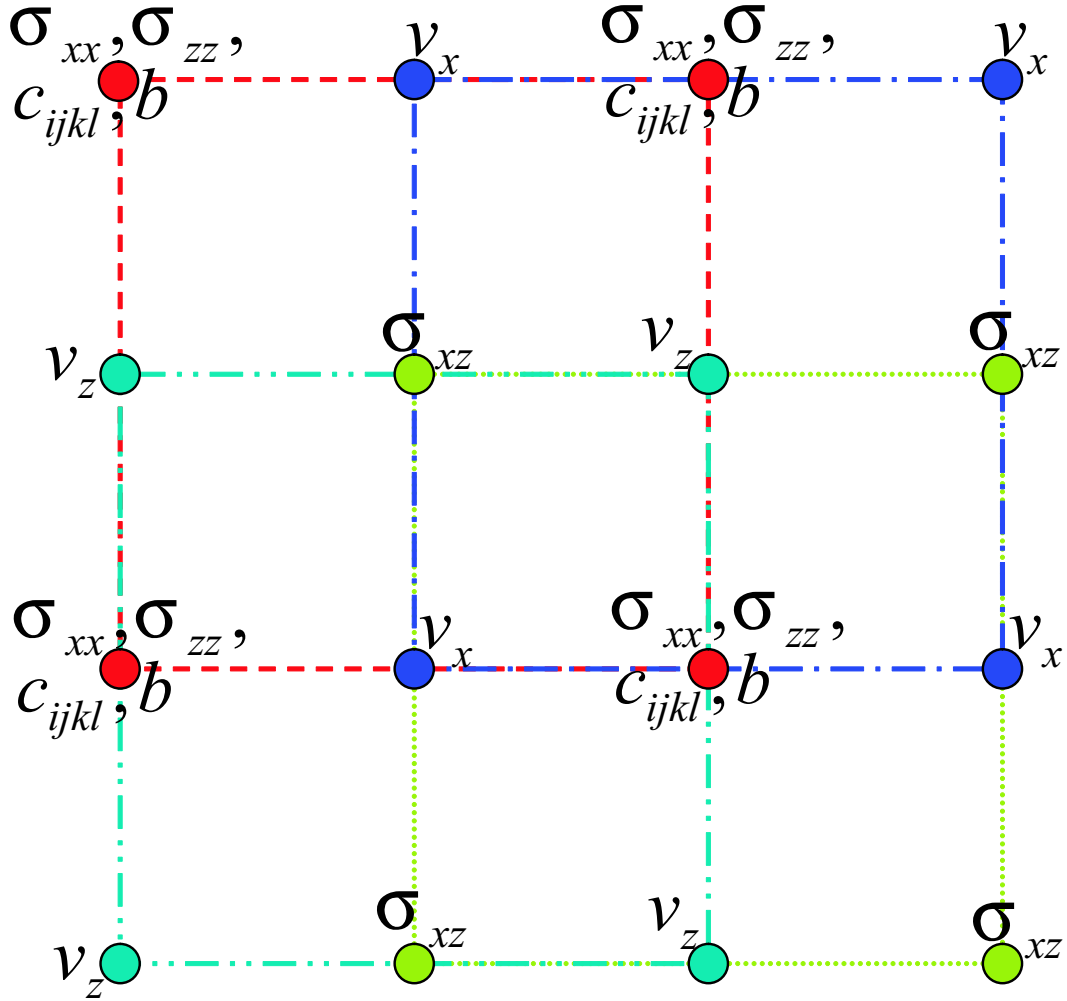


Figure 2.1: Discretization scheme in a standard staggered grid (SSG) scheme in 2D: There are four different grids staggered to each other. Notice that stiffness tensor  $c_{ijkl}$  and  $\sigma_{xz}$  are not defined at the same locations which necessitates the interpolation of some components of  $c_{ijkl}$ . Similarly, buoyancy  $b$  and particle velocity components  $v_i$  are not defined at the same grid nodes which requires the interpolation of  $b$ .  $v_{x,z}$  also needs to be interpolated if the medium has symmetry lower than orthorhombic.

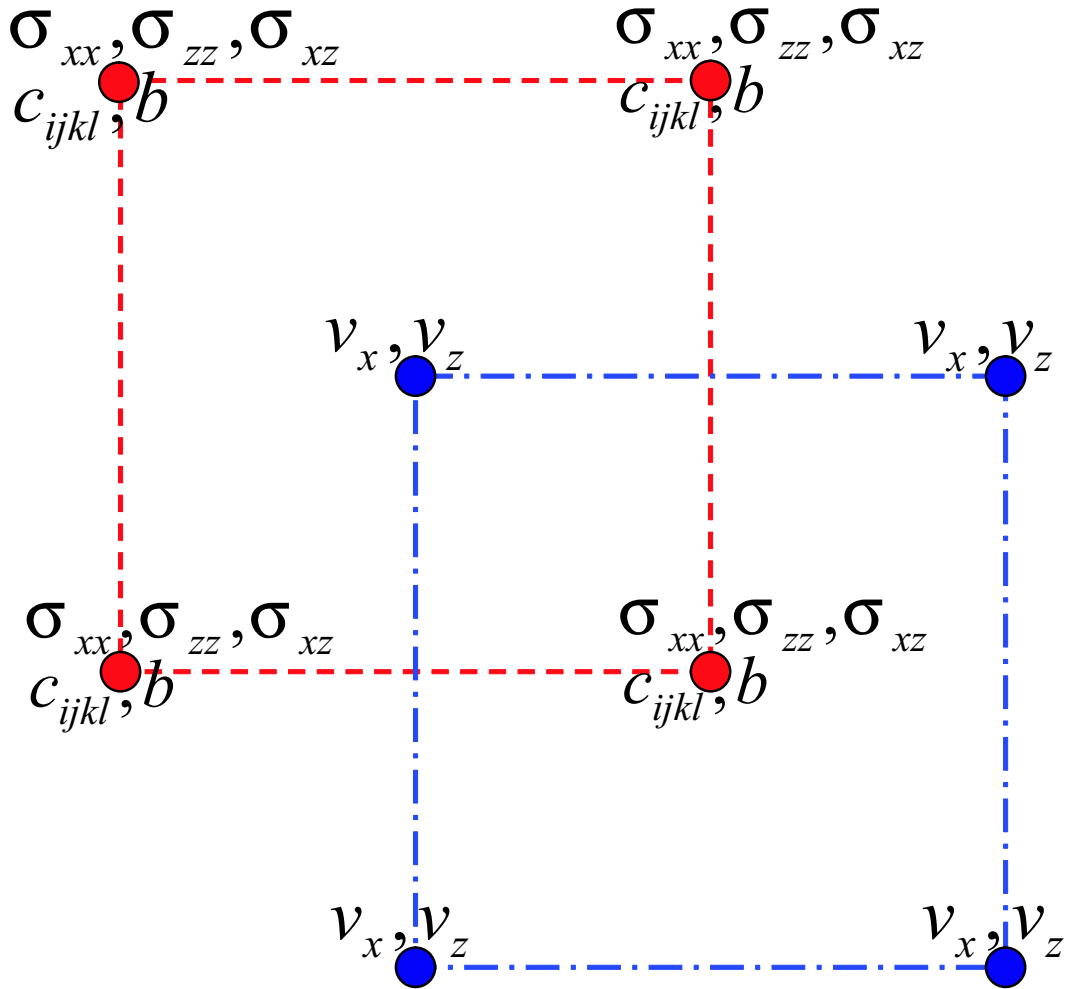


Figure 2.2: Discretization scheme in a rotated staggered grid (RSG) scheme in 2D: There are only two different grids staggered to each other. All components of stress tensor  $\sigma_{ij}$  and stiffness tensor  $c_{ijkl}$  are collocated. Hence, no interpolation of  $c_{ijkl}$  is required to estimate  $\sigma_{ij}$  after each time step.  $b$  still needs to be interpolated to estimate particle velocity components  $v_i$ . No interpolation of any spatial derivative of particle velocity  $v_{i,j}$  is needed in any kind of anisotropic media.

time-step. Details of numerical stability and dispersion for SSG scheme are very well explained in Marfurt (1984), and Moczo et al. (2000). Saenger et al. (2000) and Saenger and Bohlen (2004) give detailed overview of dispersion relationships and numerical stability conditions for RSG schemes.

## 2.4 Examples

### 2.4.1 Homogeneous anisotropic media

I simulated wave propagation in four different types of homogeneous anisotropic medium with symmetries HTI, orthorhombic, monoclinic and triclinic. In all the modeling examples, the source wavelet used is a Gaussian (Sheriff, 2002, p. 158) with a dominant frequency of 15 Hz. The source type in all the examples is an explosion and is injected in form of moment tensor  $m_{ij}$  ( $m_{11} = m_{22} = m_{33}$  and  $m_{ij} = 0$  if  $i \neq j$ ). The source is placed exactly at the centre of the model. All the homogeneous models have 450 grid points with equal grid spacing of 10 m in all three directions. Time interval of 1 ms was used in all the cases.

As an HTI example, I used Green River shale (Thomsen, 1986) with the symmetry axis in the  $x$ -direction. The generic Thomsen parameters of Green River shale are given as  $\alpha_0 = 3292$  m/s,  $\beta_0 = 1768$  m/s,  $\varepsilon = 0.195$ ,  $\delta = -0.220$ , and  $\gamma = 0.180$ . The density  $\rho$  of the medium is  $2.075$  g/cm<sup>3</sup>. Wave propagation was simulated using SSG scheme. Figure 2.3 shows a snapshot of the  $x$ -component of the particle velocity  $v_x$  after 650 time steps (650 ms). Notice that the wavelet is changed from the Gaussian to its 2nd derivative Ricker be-

cause the source type is in form of the moment tensor  $m_{ij}$  ( $m_{11} = m_{22} = m_{33}$  and  $m_{ij} = 0$  if  $i \neq j$ ). On top of the wavefronts, I have also superimposed the group-velocity contours. To match the group-velocity surfaces with the wavefronts, group velocity surfaces were multiplied with a suitable multiplier. Notice that there is a very good match between the wavefronts and the group velocity surfaces in all three planes. Unlike in isotropic media, both P- and SV-waves were generated due to an explosion source. In the  $yz$ -plane, which is an isotropic plane, wavefronts are spherical while in the  $xz$ - and  $xy$ -plane, which are symmetry planes, wavefronts are non-spherical. Due to strong anisotropy, triplications in SV-wave can also be observed. Moreover, even though a Gaussian wavelet was used as a source wavelet, resultant particle velocity wavelet is its second derivative Ricker wavelet. The reason is that the particle velocity is a function of second derivative of the moment tensor (Aki and Richards, 2002, p. 111, eq. 4.97).

Next, I simulated wave propagation in an orthorhombic medium using SSG scheme. The orthorhombic medium is defined by the following Thomsen-style parameters introduced by Tsvankin (1997b):  $\alpha_0 = 3000$  m/s,  $\beta_0 = 1500$  m/s,  $\varepsilon^{(1)} = 0.2$ ,  $\varepsilon^{(2)} = 0.45$ ,  $\delta^{(1)} = -0.1$ ,  $\delta^{(2)} = 0.2$ ,  $\delta^{(3)} = -0.15$ ,  $\gamma^{(1)} = 0.28$ ,  $\gamma^{(2)} = 0.15$ . Figure 2.4 shows a snapshot of  $v_x$  after 650 time steps (650 ms). All three types of waves qP, qS1 and qS2 were generated due to the explosion. The group velocity surfaces were superimposed on the wavefronts and there is an excellent match between them.

A tilted transversely isotropic (TTI) medium was used to simulate wave

propagation using the RSG scheme. The medium is Green River shale, which was rotated about the  $y$ -axis by  $30^\circ$  anti-clockwise. The resultant medium is equivalent to a monoclinic medium. The stiffness matrix of the medium has the same shape as written in equation 2.12. Figure 2.5 shows the snapshot of  $v_x$  after 650 time steps (650 ms). Notice that due to the rotation of the symmetry axis, wavefronts are also rotated in the  $xz$ -plane. Only P- and SV-wave were generated by the explosion source because the medium is inherently TI. The group velocity surfaces were superimposed only on the  $xz$ -plane as it is the only symmetry plane of all three planes. In other planes, group and phase velocity vectors are not confined to the same planes, which makes the estimation of group velocity surface in the plane impossible.

Next, wave propagation in a triclinic medium was simulated. The elastic constants of the medium are as follows (the factor of  $10^9$  is omitted):  $c_{11} = 10.0$ ,  $c_{12} = 3.5$ ,  $c_{13} = 2.5$ ,  $c_{14} = -5.0$ ,  $c_{15} = 0.1$ ,  $c_{16} = 0.3$ ,  $c_{22} = 8.0$ ,  $c_{23} = 1.5$ ,  $c_{24} = 0.2$ ,  $c_{25} = -0.1$ ,  $c_{26} = -0.15$ ,  $c_{33} = 6.0$ ,  $c_{34} = 1.0$ ,  $c_{35} = 0.4$ ,  $c_{36} = 0.24$ ,  $c_{44} = 5.0$ ,  $c_{45} = 0.35$ ,  $c_{46} = 0.525$ ,  $c_{55} = 4.0$ ,  $c_{56} = -1.0$ ,  $c_{66} = 3.0$ . Figure 2.6 shows  $v_x$  after 575 time steps (575 ms). All three types of waves (qP, qS1, and qS2) are generated from an explosion source.

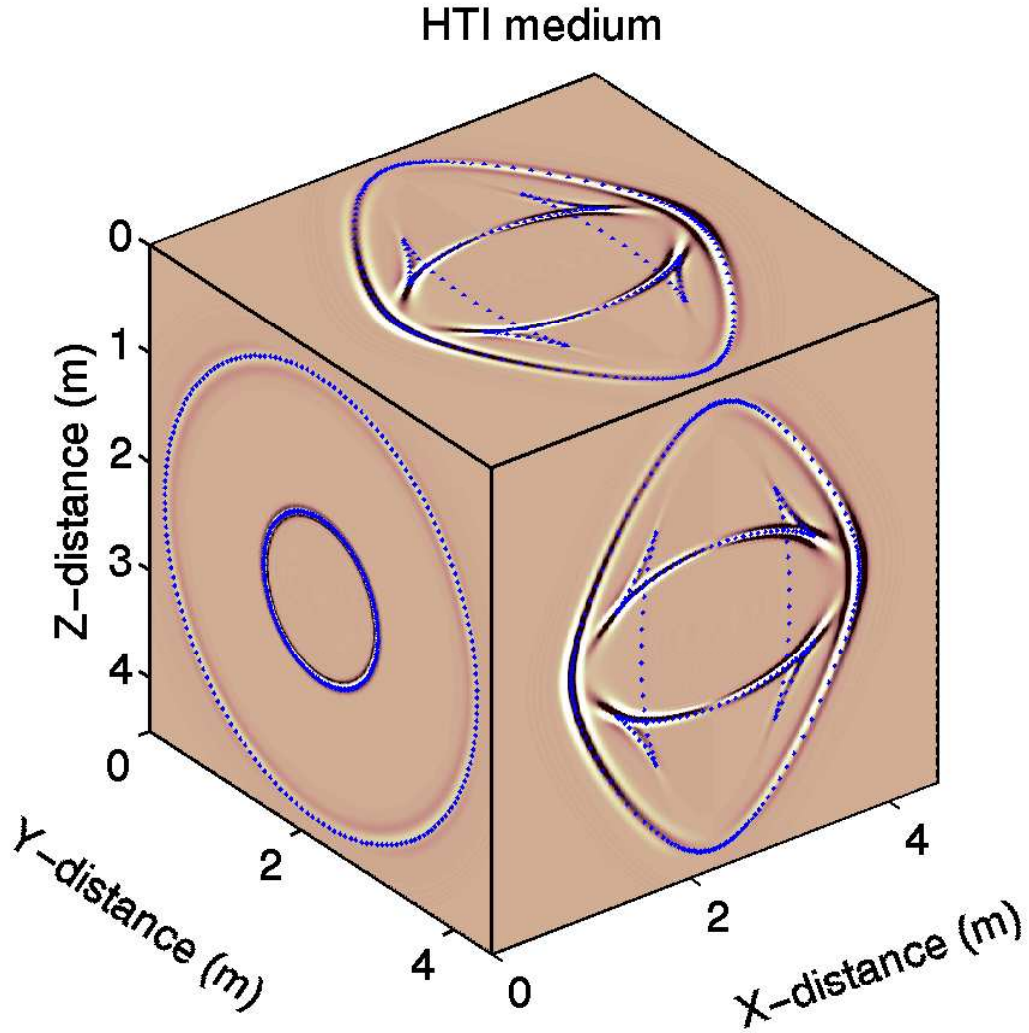


Figure 2.3: A snapshot of  $x$ -component of particle velocity  $v_x$  after 650 time steps (650 ms) in Green River Shale with the symmetry axis in  $x$ -direction: Wave propagation was simulated using SSG scheme. The model is a homogeneous block with 450 grid points (grid spacing 10 m) in all the directions. Both P- and SV-waves were generated by an explosion source. Group velocity surfaces (dashed) were superimposed on top of wavefronts. Triplications in SV-wave can be observed in the symmetry planes ( $xy$  and  $xz$ ).

### Orthorhombic medium

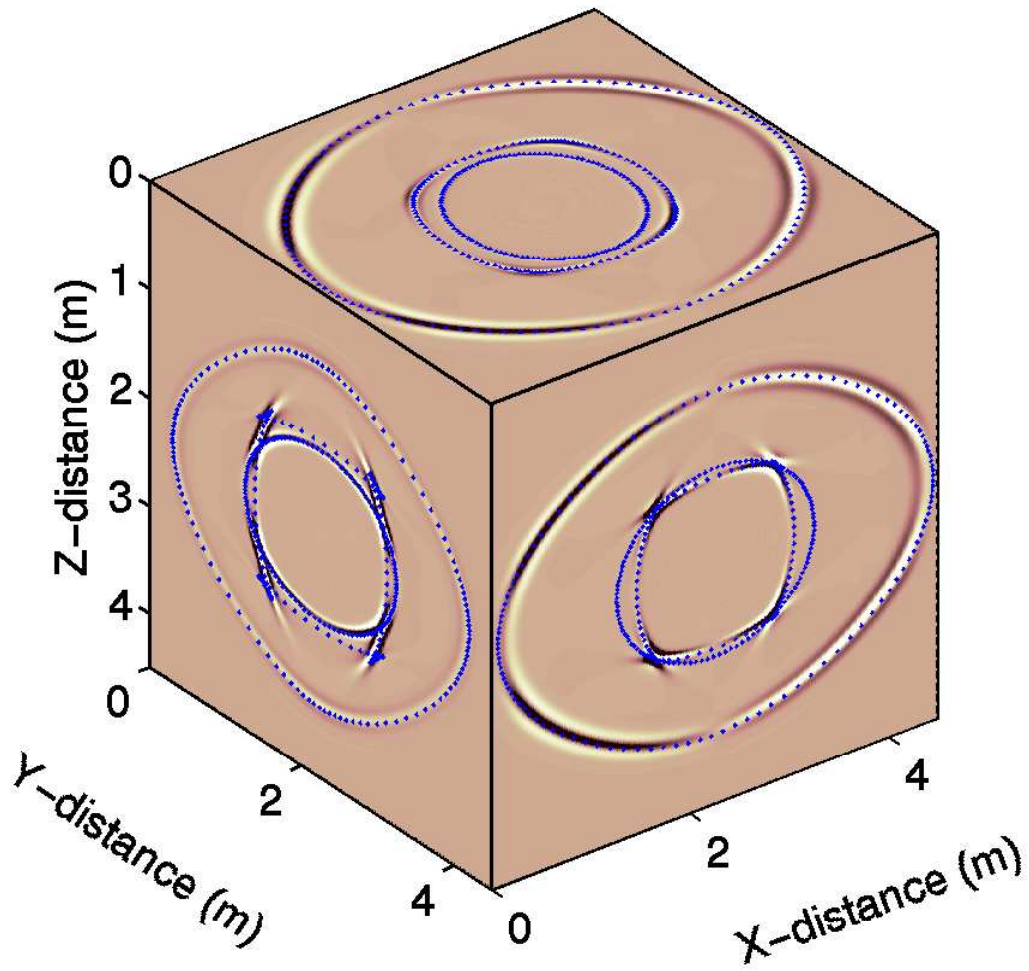


Figure 2.4: A snapshot of  $x$ -component of particle velocity  $v_x$  after 650 time steps (650 ms) in an orthorhombic medium: Wave propagation was simulated in SSG. All three types of waves qP, qS1 and qS2 were generated by an explosion. Group velocity surfaces (dashed) were superimposed on the wavefronts.

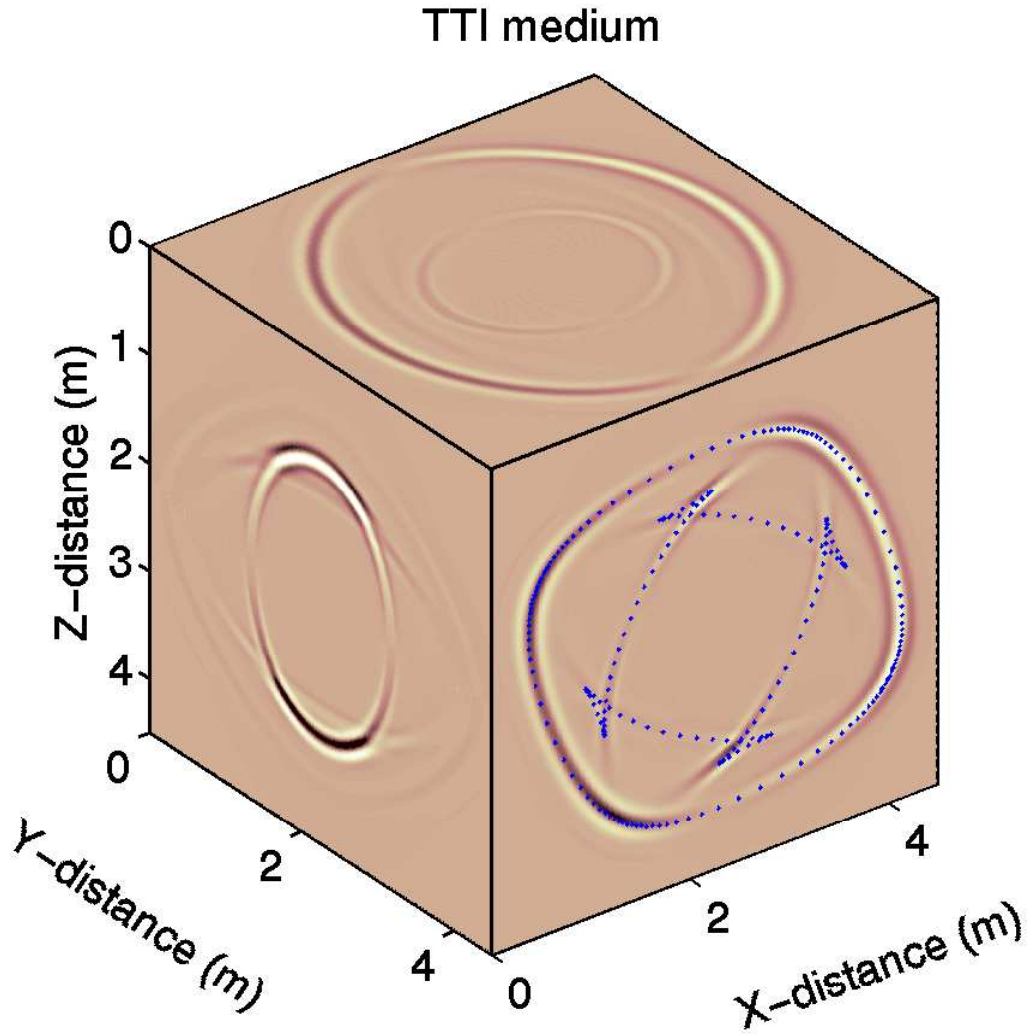


Figure 2.5: A snapshot of  $x$ -component of particle velocity  $v_x$  after 650 time steps (650 ms) in Green River shale with symmetry axis rotated by  $30^\circ$  about  $y$ -direction: Wave propagation was simulated in RSG. Due to the rotated symmetry axis, wavefront is also rotated in  $xz$ -plane.  $zx$ -plane is the symmetry plane of the medium where group velocity surface (dashed) has been superimposed on the wavefronts.



### Triclinic medium

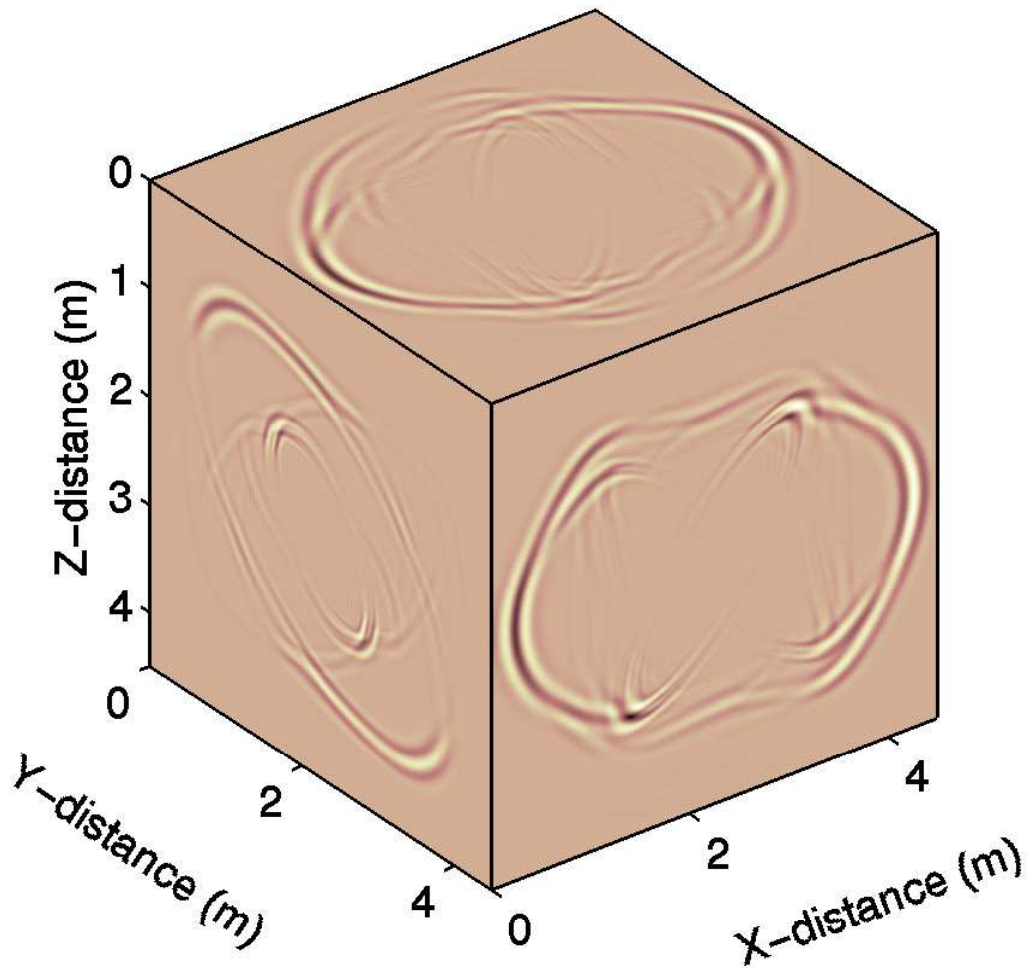


Figure 2.6: A snapshot of  $x$ -component of particle velocity  $v_x$  after 575 time steps (575 ms) in a triclinic medium: Wave propagation was simulated in RSG. All three types of waves qP, qS1 and qS2 were generated due to the explosion.

### 2.4.2 Comparison between synthetic seismograms generated by finite-difference method and reflectivity algorithm

In this section, I show comparison between the seismic data generated by the finite-difference method and by the reflectivity algorithm (Mallick and Frazer, 1990a; Mallick and Frazer, 1990b) for an azimuthally anisotropic medium. A three-layered model was used for comparison. Figure 2.7 shows the model. The top and the bottom layers are isotropic whereas the middle layer has one set of fluid-filled vertical fractures oriented normal to the  $x$ -direction with crack density of 7%. The rest of the elastic properties of the model are tabulated in table 2.1. The source wavelet used is a Gaussian (Sheriff, 2002)

Thickness (m)	$V_p$ (m/s)	$V_s$ (m/s)	Density (g/cm <sup>3</sup> )
710	3000	2000	1.3
1300	4100	2300	2.5
$\infty$	5200	3200	3.5

Table 2.1: Relevant elastic parameters of the three-layered model.

with a dominant frequency of 15 Hz. The source type is an explosion. A number of receiver lines were collected in both the  $x$ - and  $y$ -directions.

Figures 2.8(a) and 2.8(b) show the  $x$ - and  $y$ -components, respectively, of the synthetic seismic data generated by the finite-difference method. This seismic line is 400 m away from the source in the  $y$ -direction. Notice the time difference in the event PPSS in the  $x$ - and  $y$ -components. PPSS is the converted S-wave (P-to-S) which was reflected from the bottom of the fractured layer. While traveling through a fractured reservoir, PPSS is polarized perpen-

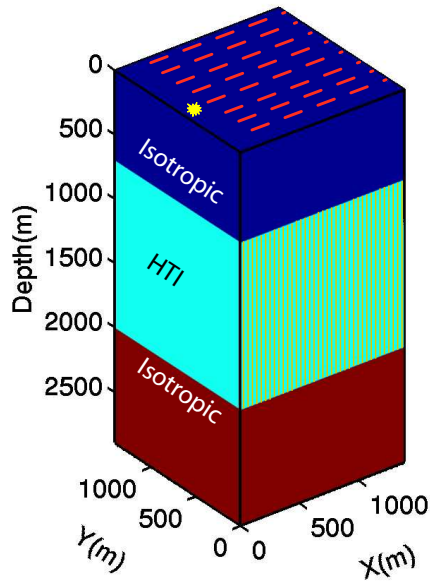


Figure 2.7: Three-layered model used to generate seismic data using both the finite-difference method and the reflectivity method. The model has three flat layers. The middle layer has one set of fluid-filled vertical fractures normal to  $x$ -direction.

dicular and quasi-parallel (at near-offset it is almost parallel) to the fractures, which are recorded as the slower  $x$ -component and the faster  $y$ -component, respectively.

Figure 2.9 shows a comparison between the seismic data generated by the finite-difference method and by the reflectivity algorithm for all three components at two azimuths and offsets. Notice that there is an excellent match between the two sets of synthetics. Figures 2.10, 2.11, and 2.12 show the comparison between the seismic data generated by these two methods for an entire seismic line.

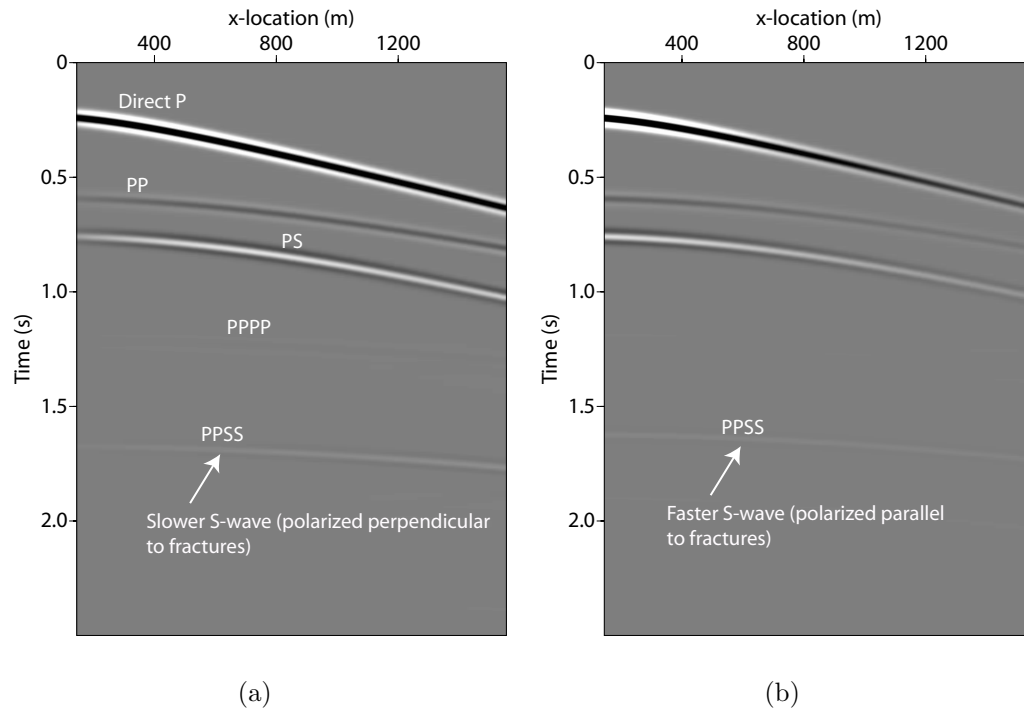
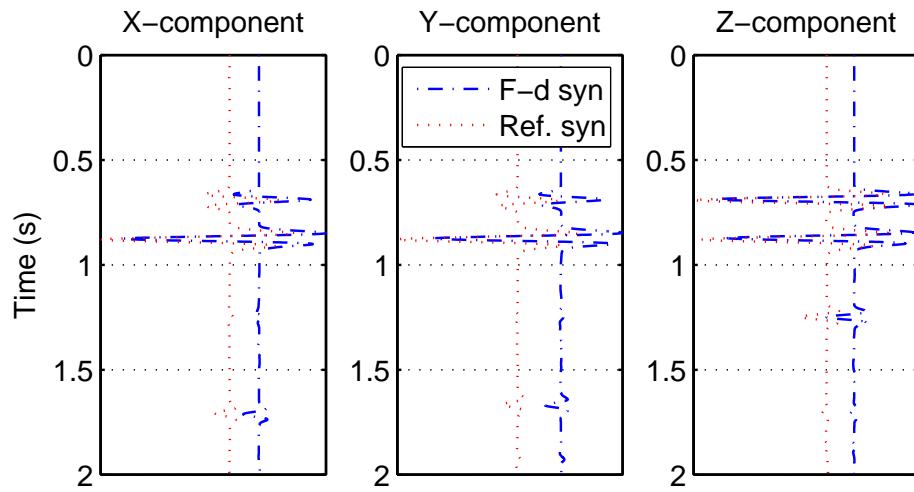
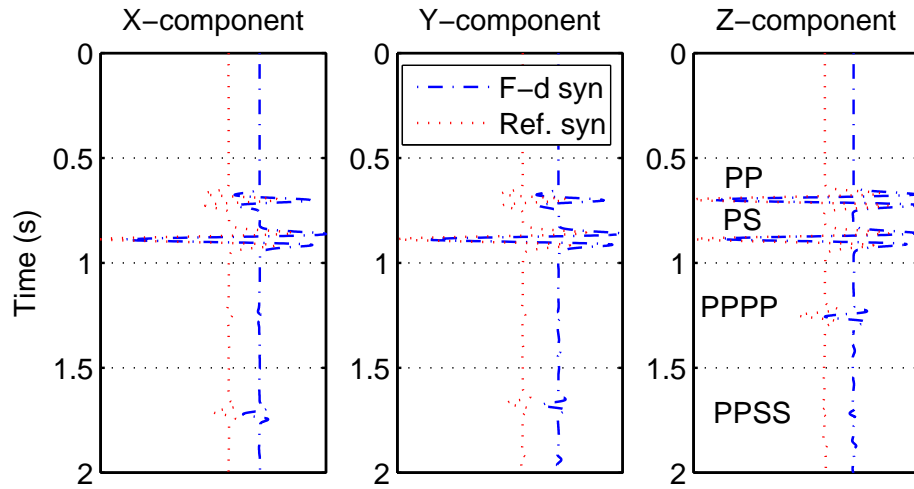


Figure 2.8: Seismic data generated using finite-difference method (a)  $x$ -component of particle motion, and (b)  $y$ -component of particle motion: PP is the reflected P-wave from top of second layer, PS is the converted S-wave (P-to-S) from top of second layer, PPPP is the reflected P-wave from bottom of the second layer and the PPSS is the converted S-wave (P-to-S) from bottom of the second layer.



(a)



(b)

Figure 2.9: Comparison between the seismic data generated by the finite-difference method and by the reflectivity method at two azimuths and offsets: (a) At azimuth  $16^\circ$  and offset 1080 m, and (b) at azimuth  $21^\circ$  and offset 1120 m.

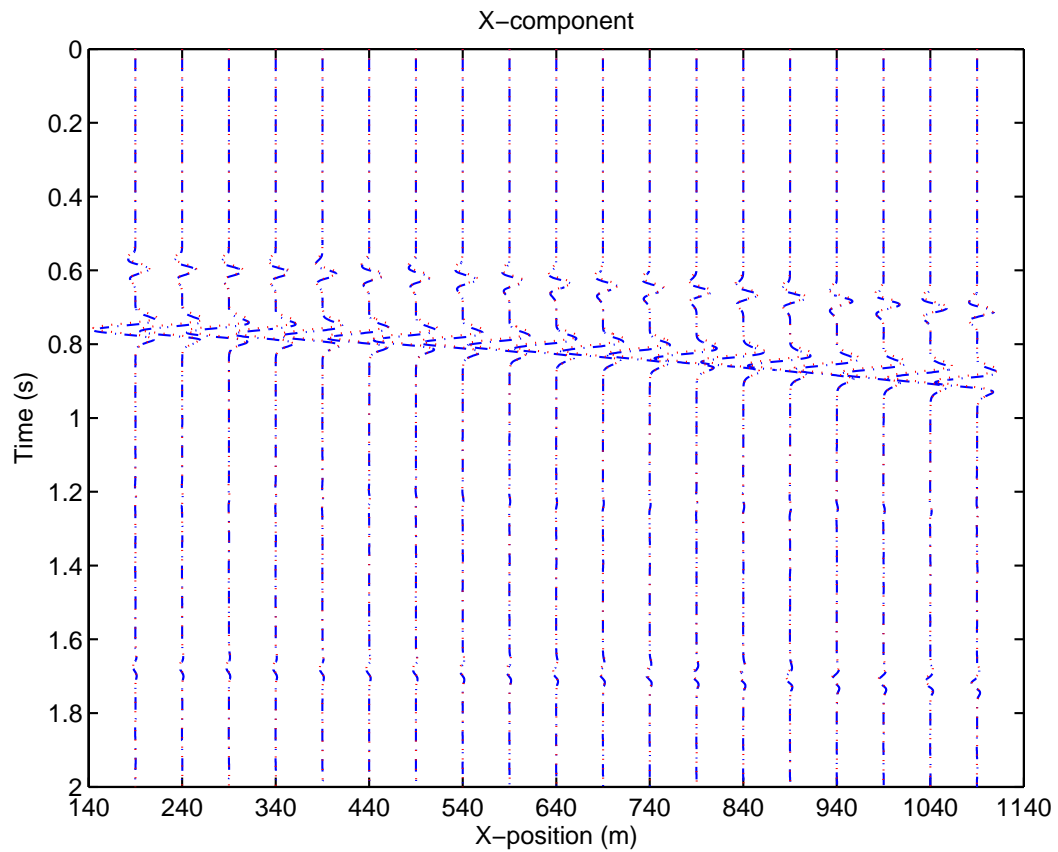


Figure 2.10: Comparison between the  $x$ -component of seismic data generated by the finite-difference method and by the reflectivity method for a whole seismic line: The line is 400 m away from the source in  $y$ -direction. The traces plotted in blue and red were generated by the finite-difference and the reflectivity methods, respectively.

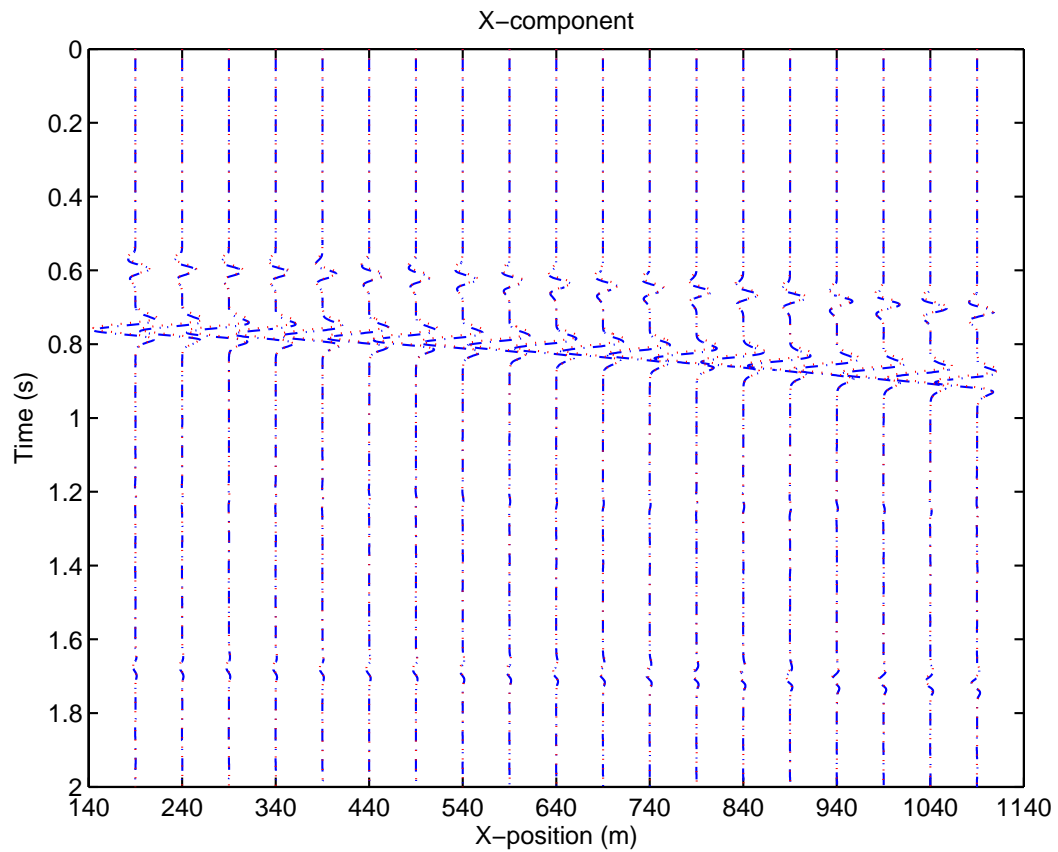


Figure 2.11: Comparison between the  $y$ -component of seismic data generated by the finite-difference method and by the reflectivity method for a whole seismic line: The line is 400 m away from the source in  $y$ -direction. The traces plotted in blue and red were generated by the finite-difference and the reflectivity methods, respectively.

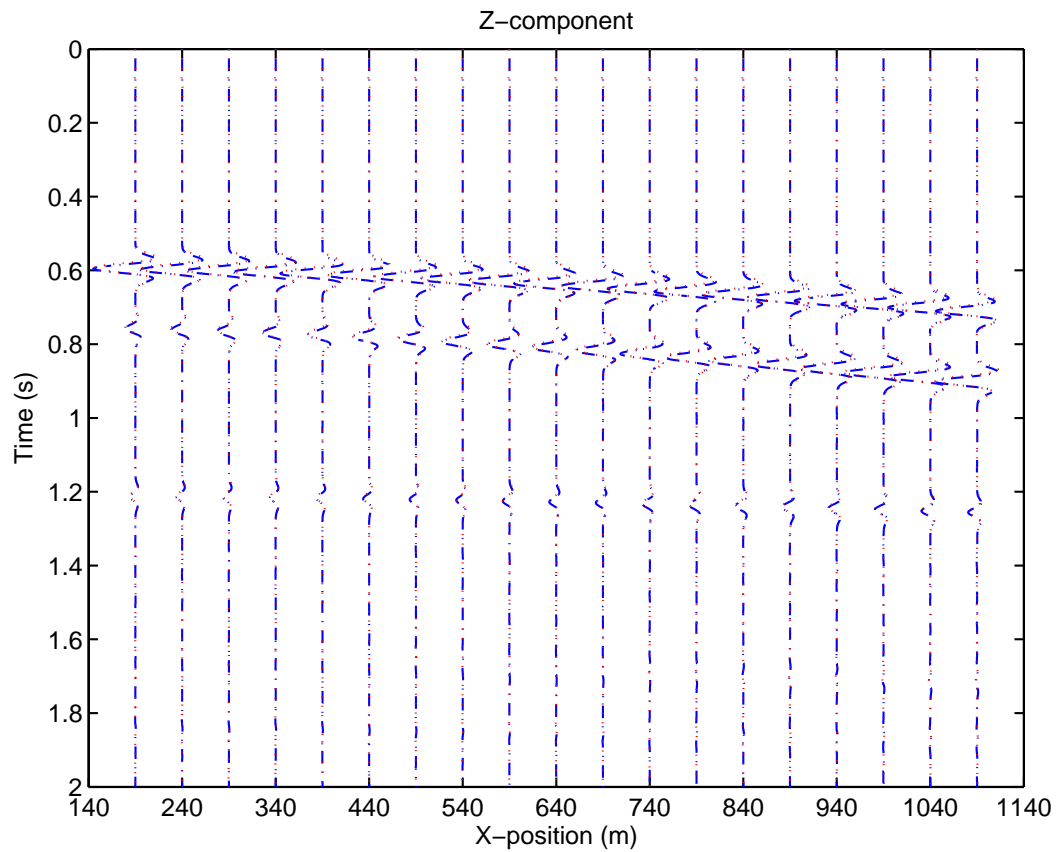


Figure 2.12: Comparison between the  $z$ -component of seismic data generated by the finite-difference method and by the reflectivity method for a whole seismic line: The line is 400 m away from the source in  $y$ -direction. The traces plotted in blue and red were generated by the finite-difference and the reflectivity methods, respectively.



### 2.4.3 Seismic data generated for a complex subsurface model

I generated synthetic seismograms for a large subsurface model with the symmetry varying from isotropic to orthorhombic (figure 2.13) using SSG scheme. Layer 1 is isotropic with P-wave velocity of 2500 m/s, S-wave velocity of 1700 m/s, and density of 1 g/cm<sup>3</sup>. Layer 2 has a VTI symmetry with the following Thomsen's parameters:  $\alpha_0 = 3300$  m/s,  $\beta_0 = 2300$  m/s,  $\varepsilon = -0.2$ ,  $\delta = 0.1$ , and  $\gamma = 0.2$ . The density of the medium is 2 g/cm<sup>3</sup>. Layer 3 has one set of dry fractures with crack density  $e$  of 7%. The background medium has P-wave velocity of 4000 m/s, S-wave velocity of 2700 m/s, and density of 3.0 gm/cm<sup>3</sup>. Layer 4 has an orthorhombic symmetry with anisotropic parameters  $\alpha_0 = 5000$  m/s,  $\beta_0 = 3500$  m/s,  $\varepsilon^{(1)} = 0.25$ ,  $\varepsilon^{(2)} = 0.4$ ,  $\delta^{(1)} = -0.1$ ,  $\delta^{(2)} = 0.2$ ,  $\delta^{(3)} = -0.15$ ,  $\gamma^{(1)} = 0.28$ ,  $\gamma^{(2)} = 0.15$ . The density of the medium is 4.0 gm/cm<sup>3</sup>. Layer 5 (basement) is isotropic having P-wave velocity of 6100 m/s, S-wave velocity of 4100 m/s and density of 6.0 gm/cm<sup>3</sup>. Source type is the same as described in the previous example. The source is buried 10 m in the first layer of the model. Receivers are placed on top of the first layer. Inline and crossline are located at distances of 1940 m and 2340 m from the source. The model has 460, 300, and 605 grids in the  $x$ -,  $y$ - and  $z$ -directions. The grid spacing is kept 10 m in all three directions. Absorbing boundary condition was applied in all the directions. 8000 time steps with sampling interval of 0.5 ms were calculated. Figure 2.14 shows the shot gathers in inline and crossline directions.

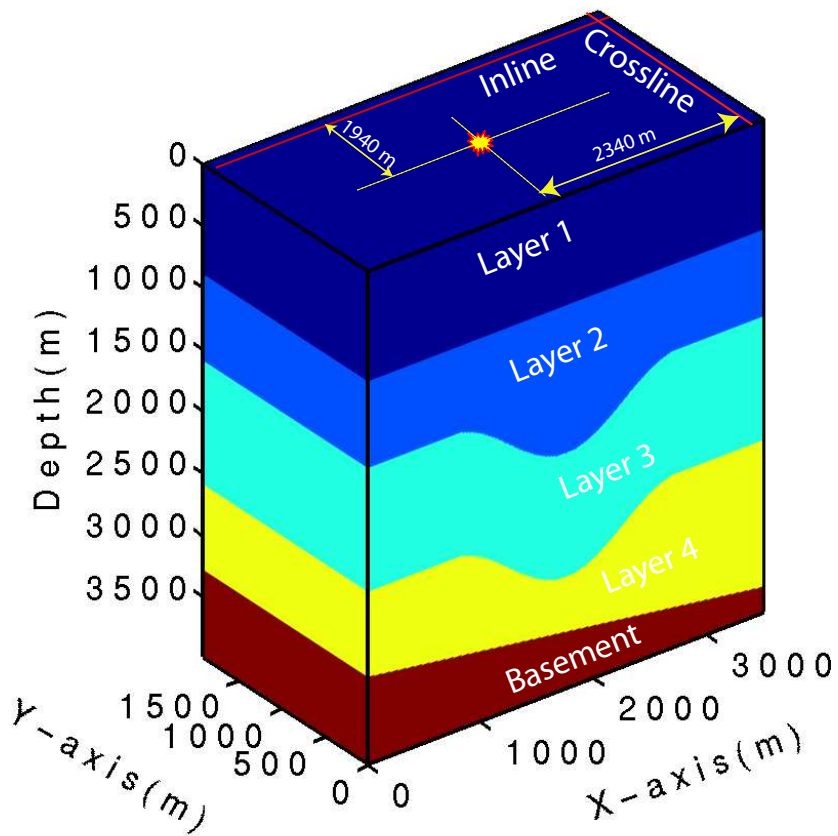
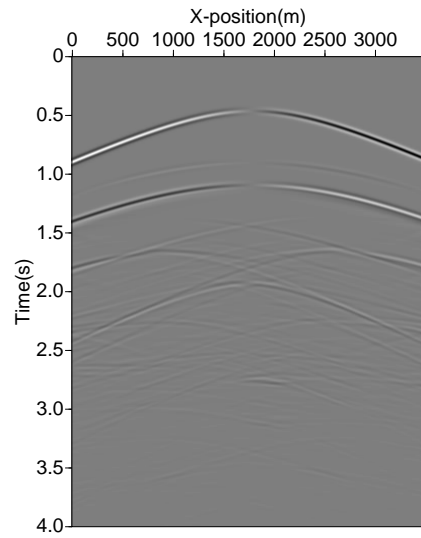
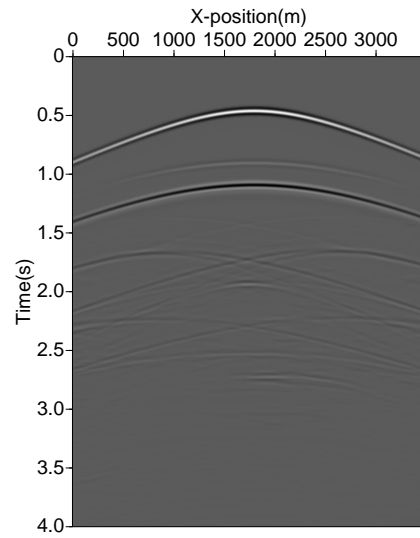


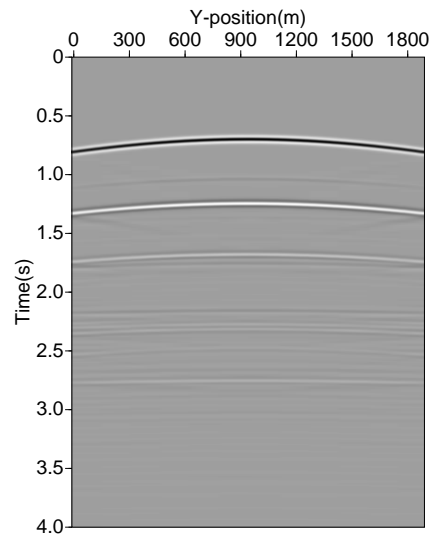
Figure 2.13: 3D model used to generate synthetic seismograms: Layer 1 is isotropic, layer 2 has VTI symmetry, layer 3 has one set of dry fractures, layer 4 has orthorhombic symmetry, and basement is isotropic.



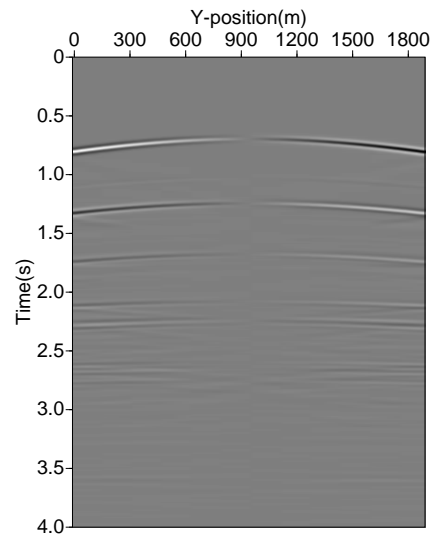
(a)



(b)



(c)



(d)

Figure 2.14: Shot gathers generated for model shown in figure 2.13: (a)  $x$ -component of velocity  $v_x$  in inline direction, (b)  $y$ -component of velocity  $v_y$  in inline direction, (c)  $v_x$  in crossline direction, and (d)  $v_y$  in crossline direction.

## 2.5 Shear-wave splitting study

Closely spaced parallel fractures behave like an anisotropic medium (section 1.3) in the seismic frequency band. The type of anisotropy induced by the fractures depends on a number of factors, namely fracture type (rotationally invariant or corrugated), number of fracture sets present in the medium, fracture orientation and fracture infill (fluid-filled or dry). According to the linear slip theory (section 1.3.1), the compliance matrix  $\mathbf{S}$  of the equivalent medium can be estimated by the following equation:

$$\mathbf{S} = \mathbf{S}_b + \sum_{i=1}^n \mathbf{S}_f^i, \quad (2.14)$$

where  $\mathbf{S}_b$  is the compliance matrix of the background.  $\mathbf{S}_f^i$  is the compliance matrix of the  $i$ th fracture set and  $n$  is the total number of fracture sets. If the fractures have non-zero azimuth  $\phi$  and dip  $\theta$  from the chosen coordinate system, the equivalent fracture compliance matrix  $\mathbf{S}_f^{\phi,\theta}$  can be obtained by applying Bond transformation:

$$\mathbf{S}_f^{\phi,\theta} = \mathbf{M}(\phi, \theta) \mathbf{S}_f \mathbf{M}^T(\phi, \theta), \quad (2.15)$$

where  $\mathbf{M}$  is  $6 \times 6$  Bond transformation matrix (Auld, 1990, p. 75). Equation 2.14 can render equivalent medium which may exhibit symmetry varying from HTI to monoclinic.

### 2.5.1 Background medium and source type

For my modeling experiment, I assume that the background medium is isotropic. A three-layered subsurface model (Figure 2.15) was used for all

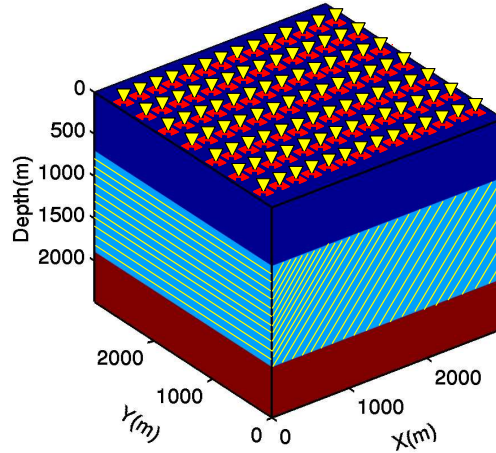


Figure 2.15: Subsurface model used to demonstrate shear wave splitting: In all the experiments, background model remains same. Only the number of fracture sets and fracture orientation changes. A plane-wave source is used. Source is polarized at  $45^\circ$  from  $x$ -axis. Source and receivers are placed at each grid location.

the experiments described here. Although the finite-difference algorithms are capable of handling subsurface models with complex geometry, flat-layered models are used here to study the S-wave splitting. Top and bottom layers are isotropic, and the middle layer can have one or more sets of fractures. The elastic properties of the background are listed in table 2.2.

Thickness (m)	$V_p$ (m/s)	$V_s$ (m/s)	Density (g/cm <sup>3</sup> )
700	3000	2000	1.3
1200	4700	2800	2.3
$\infty$	5000	3200	3.5

Table 2.2: Relevant elastic parameters of the background subsurface model.

To simulate zero-offset S-wave response, a plane-wave shear source is used. A source point is located over each receiver and the source motion is polarized at  $45^\circ$  clockwise from  $x$ -axis; i.e.,  $v_x$  and  $v_y$  are excited in phase with equal amplitudes. Receivers record the data in  $x$ - and  $y$ -directions (figure 2.15).

### 2.5.2 Dipping rotationally invariant fractures

I first consider a set of rotationally invariant fractures (section 1.3.2) embedded in an isotropic background and striking parallel to  $y$ -direction. Wave propagation was simulated in the subsurface model with one set of dry vertical fractures in the middle layer while the crack density was varying from 2% to 10% from left to right. Figure 2.16 shows the  $x$ - and  $y$ -components of the particle velocity. Notice that the arrival time of the  $x$ -component is increasing with increasing fracture density while the arrival time of the  $y$ -component remains unchanged with changing fracture density. The  $x$ -component, which is slower and is polarized perpendicular to the fractures, is conventionally denoted as  $S^\perp$  and the  $y$ -component which is polarized parallel to the fractures is denoted as  $S^\parallel$ .

If the fractures have strike in  $y$ -direction and are making a non-zero dip with vertical, the resultant medium has monoclinic symmetry with a vertical symmetry plane ( $x, z$ ). The resultant stiffness matrix has the same form as written in equation 2.12. A vertically traveling S-wave still splits into faster and slower wave components. However, only one pure mode exists that is  $S^\parallel$

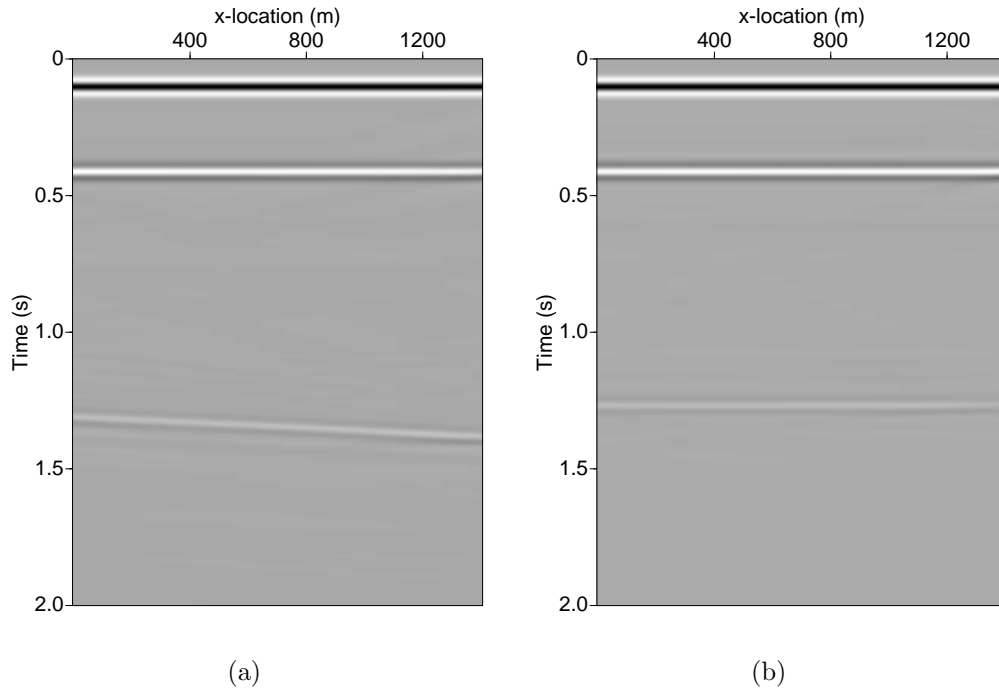


Figure 2.16: Seismic sections generated using a plane-wave source: (a)  $x$ -component of the particle motion ( $S^\perp$ ), and (b)  $y$ -component of the particle motion ( $S^\parallel$ ). There is one set of dry vertical fractures in the middle layer of the subsurface model (figure 2.15) with increasing crack density from left to right of the model. Notice that arrival time of  $S^\perp$  is increasing with increasing fracture density.

which is polarized parallel to the fractures (Grechka and Tsvankin, 2004). The other S-wave is polarized in the  $(x, z)$ -plane. The  $x$ -component of the receiver records only a part of this mode which I still denote as  $S^\perp$ .

For this experiment, I set the crack density  $e$  to be 7% in the middle layer. The fracture set has varying dip with the vertical. The equivalent medium for the middle layer was estimated using equations 2.14 and 2.15. Figure 2.17 shows  $x$ - and  $y$ -components of the particle velocity  $v_x$  and  $v_y$  (or  $S^\perp$  and  $S^\parallel$ , respectively) for dry and fluid-filled fractures dipping  $60^\circ$  from vertical. Notice that for dry fractures  $v_x$  is traveling slower than  $v_y$  while for fluid-filled fractures  $v_y$  is traveling slower than  $v_x$ . Figure 2.18 shows the time-difference between  $S^\perp$  and  $S^\parallel$  for both dry and fluid-filled fractures at varying fracture dip. Notice that at non-zero dip, dry and fluid-filled fractures have different traveltimes-differences which suggests that S-wave splitting can give some indication of fluid type in the dipping fractures. Notice that in case of fluid-filled fractures after a certain dip,  $S^\perp$  becomes faster than  $S^\parallel$ .



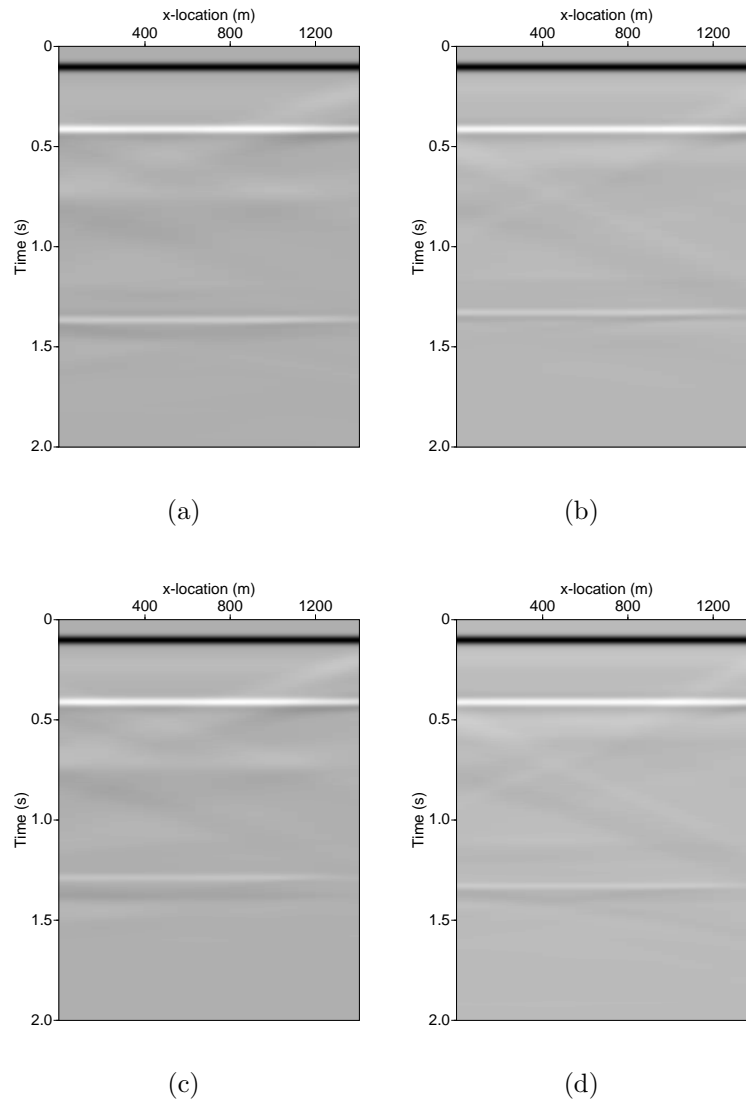


Figure 2.17: Seismic sections generated using a plane-wave source for one set of dry and fluid-filled fractures: Fractures are dipping  $60^\circ$  with vertical. (a)  $x$ -component of velocity ( $v_x$  or  $S^\perp$ ) for dry fractures, (b)  $y$ -component of velocity ( $v_y$  or  $S^\parallel$ ) for dry fractures, (c)  $x$ -component of velocity ( $v_x$  or  $S^\perp$ ) for fluid-filled fractures, and (d)  $y$ -component of velocity ( $v_y$  or  $S^\parallel$ ) for fluid-filled fractures. Notice that for dry fractures  $S^\parallel$  is traveling faster than  $S^\perp$  and opposite is true for fluid-filled fractures.

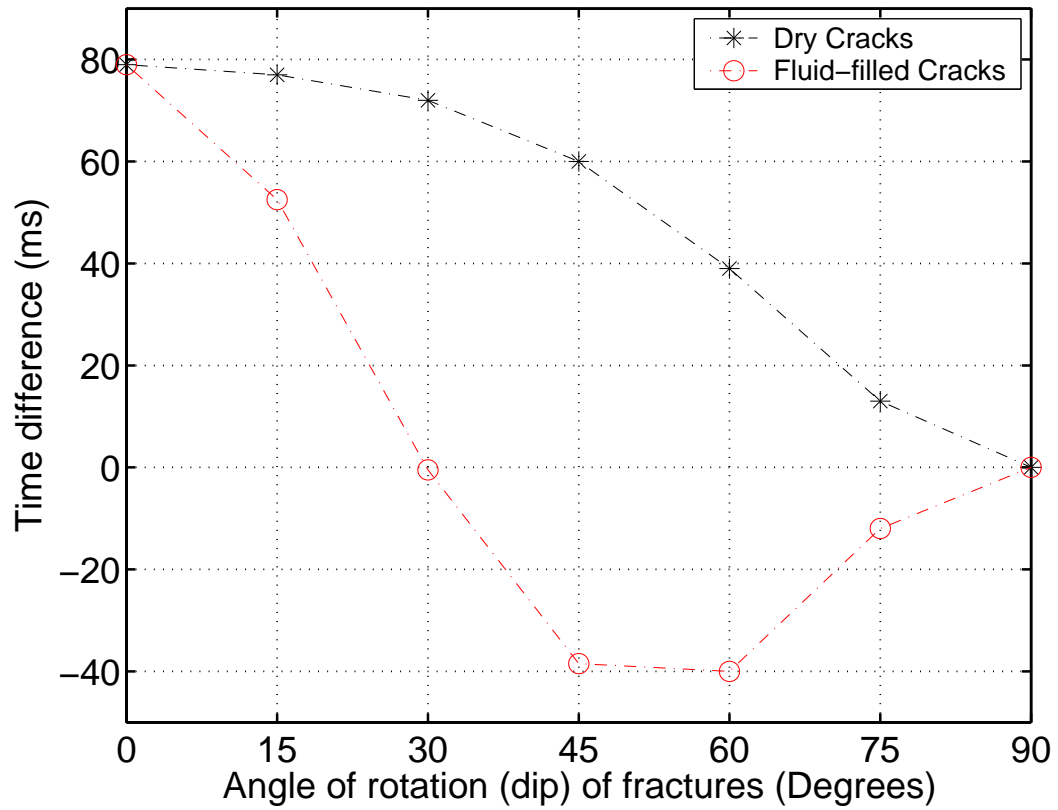


Figure 2.18: Time-difference between  $S^\perp$  and  $S^\parallel$  for both dry and fluid-filled fractures: Time-difference is the largest when the fractures are vertical. As the dip of the fractures is increased, time-difference for fluid-filled fractures starts decreasing and after certain angle,  $S^\parallel$  becomes faster and  $S^\perp$  becomes slower. For dry fractures,  $S^\perp$  and  $S^\parallel$  always remain faster and slower, respectively, but the time-difference between the two starts decreasing after a certain dip.

### 2.5.3 Two rotationally invariant vertical fracture sets

Next two non-orthogonal rotationally invariant fracture sets were considered. If the fracture sets are non-orthogonal the effective medium belongs to monoclinic symmetry with a horizontal plane  $(x, y)$  of symmetry with the following form of stiffness matrix:

$$c = \begin{pmatrix} c_{11} & c_{12} & c_{13} & 0 & 0 & c_{16} \\ c_{12} & c_{22} & c_{23} & 0 & 0 & c_{26} \\ c_{13} & c_{23} & c_{33} & 0 & 0 & c_{36} \\ 0 & 0 & 0 & c_{44} & c_{45} & 0 \\ 0 & 0 & 0 & c_{45} & c_{55} & 0 \\ c_{16} & c_{26} & c_{36} & 0 & 0 & c_{66} \end{pmatrix}. \quad (2.16)$$

For this modeling experiment, one fracture set is always perpendicular to the  $x$ -axis with a crack density of 5% and the second fracture set has a crack density of 7%. The second fracture set is oriented with a varying angle with respect to first fracture set. Equivalent compliance is estimated by using equations 2.14 and 2.15. The recorded  $x$ - and  $y$ -components of particle velocity  $v_x$  and  $v_y$  are mixed mode. A tensor rotation was applied to obtain the pure  $S1$  and  $S2$  modes. The angle of rotation  $\theta$  was estimated as  $\theta = 0.5 \tan^{-1}[2c_{45}/(c_{44} - c_{55})]$  (Helbig, 1994, p. 165).

Figure 2.19 shows  $v_x$ ,  $v_y$  and the pure modes  $S1$  and  $S2$  sections for dry fractures making an angle of  $30^\circ$  with each other. Figure 2.20 shows the time-difference between  $S2$  and  $S1$  waves reflected from the bottom of the fractured layer. Both dry and fluid-filled fractures show the same time-difference. Notice that as the angle between the two fractures is increases,

time-difference decreases. After a certain angle,  $S_1$  becomes slower than  $S_2$ .

#### 2.5.4 Dipping corrugated fractures

Finally, I considered one set of dipping corrugated fractures to observe S-wave splitting. Corrugated fractures occur when, unlike rotationally variant fractures, tangential and normal slips are not decoupled. This condition introduces off-diagonal terms in the fracture compliance matrix. This causes the equivalent medium to be monoclinic even if fractures are vertical. Bakulin et al. (2000c) derived the stiffness matrix of the equivalent medium. They introduced dimensionless compliances  $E_N$ ,  $E_V$ ,  $E_H$ , and  $E_{NV}$  which control the fracture infill. They showed that fractures are dry if  $E_{NV} = 0$ , and are fluid-filled when  $E_{NV}^2 = E_N E_V$ . I used the same conditions here to define dry and fluid-filled fractures. For our modeling purpose, I chose  $E_N = 1.3$ ,  $E_V = 0.25$  and  $E_H = 0.24$ .

As discussed previously, pure  $S^{\parallel}$  exists at all fracture dip, but pure  $S^{\perp}$  exists only when fractures are vertical. This convention can still be used to identify faster and slower S-waves. Figure 2.21 shows the time-difference between faster ( $S^{\parallel}$ ) and slower ( $S^{\perp}$ ) S-waves. Notice that even if the fractures are vertical, S-wave splitting is different for dry and fluid-filled fractures. After certain dip, S-wave splitting starts to decrease for both dry and fluid-filled fractures. Unlike fluid-filled rotationally invariant fractures, in the presence of fluid-filled corrugated fractures  $S^{\parallel}$  always remains faster than  $S^{\perp}$ .

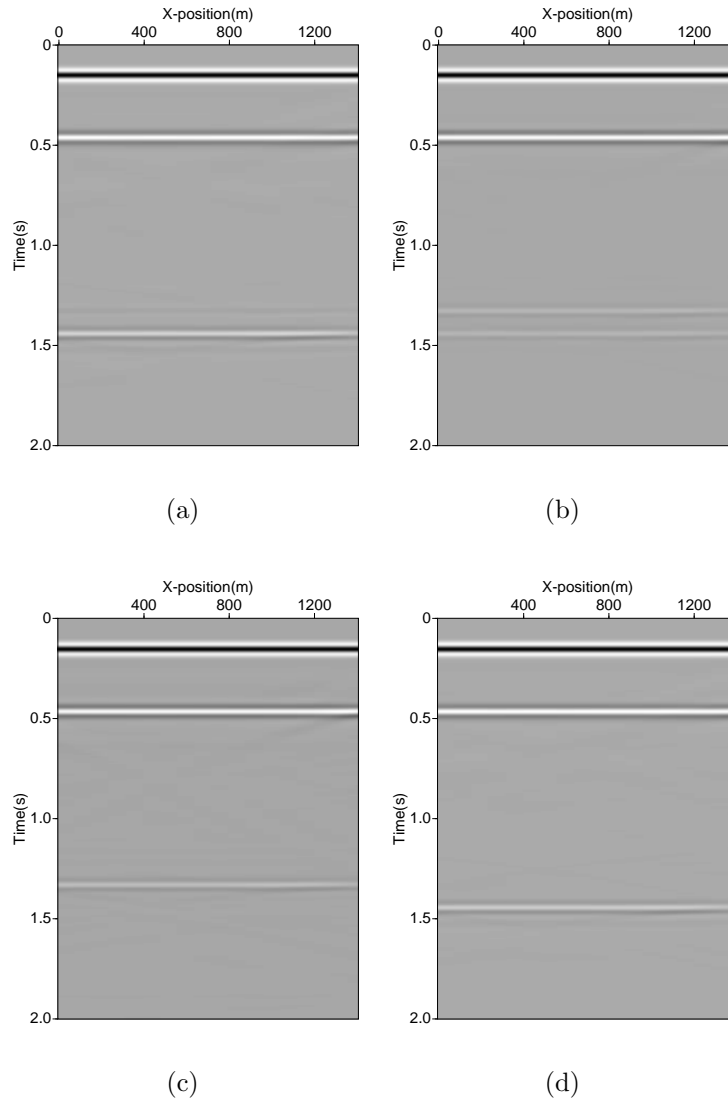


Figure 2.19: S-wave seismic sections for two dry vertical fracture sets making an angle of  $30^\circ$ : (a)  $x$ -component of velocity  $v_x$ , (b)  $y$ -component of velocity  $v_y$ , (c) faster  $S_1$  mode, and (d) slower  $S_2$  mode. Notice the arrival at about 1.5s is reflected from the bottom of the fractured layer. S-wave splitting is evident.

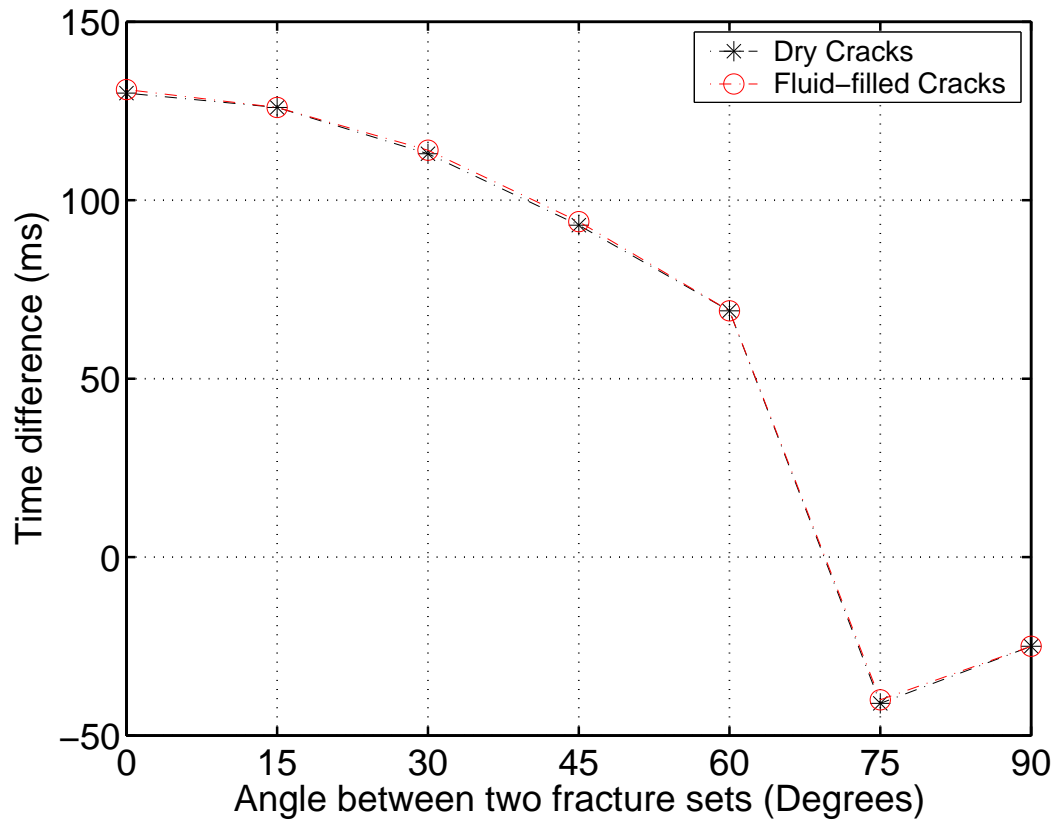


Figure 2.20: Time-difference between  $S_2$  and  $S_1$  waves reflected from the bottom of the fractured layer (two sets of intersecting fractures): Notice that the time-difference for both dry and fluid-filled fractures stays same for all angles. With the angle between the two fracture sets increasing, time-difference is decreasing. After a certain angle pure faster  $S_1$  becomes slower and pure slower  $S_2$  becomes faster.

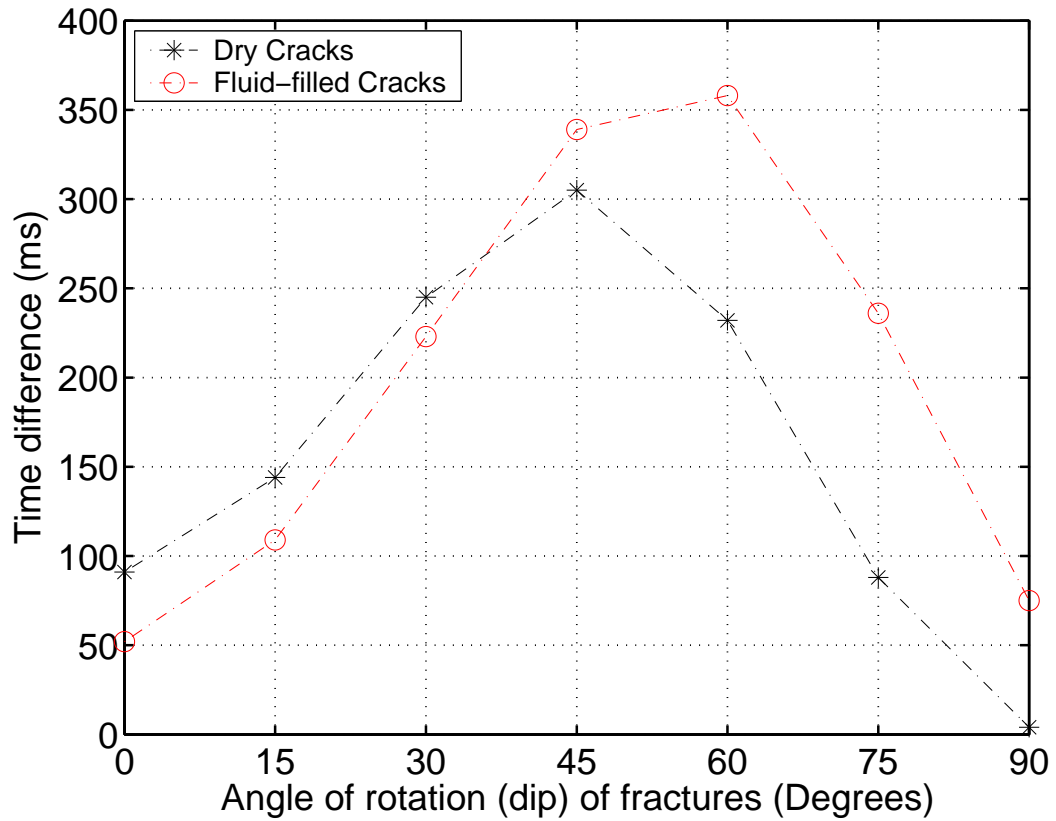


Figure 2.21: Time-difference between  $S^\perp$  and  $S^\parallel$  reflected from the bottom of the fractured layer containing corrugated fractures: Notice that, unlike the case of rotationally variant fractures, vertical dry and fluid-filled fractures have different time-difference. Moreover, dry and fluid-filled fractures show different time-difference as the fractures dip is increased. Dry horizontal fractures, unlike fluid-filled fractures, do not show any shear-wave splitting.

## 2.6 Discussion

I reviewed the finite-difference modeling algorithm for general anisotropic media in standard staggered grid (SSG) and rotated staggered grid (RSG). SSG should be used when the symmetry is higher than or equal to orthorhombic and RSG should be used when the symmetry is lower than monoclinic. I did not use the RSG schemes for all kinds of anisotropic media due to additional computational cost attached to RSG. I simulated wave propagation in a number of homogeneous and complex anisotropic media using both SSG and RSG schemes.

I showed a comparison between the finite-difference generated synthetic seismograms and the synthetic seismograms generated by the reflectivity method in an azimuthally anisotropic medium. There was an excellent match between both the synthetic seismograms. To the best of my knowledge, this is the first time a comparison has been made between the synthetic seismograms generated by the finite-difference method and by the reflectivity method for an azimuthally anisotropic medium.

I have also demonstrated that the S-wave splitting can reveal fracture infill in the presence of dipping fractures. In the presence of two vertical fracture sets, S-wave splitting is affected by the angle between the fractures. This information can be used to get some idea about the angle between the fractures. In case of vertical corrugated vertical fractures, S-wave splitting is sensitive to the fracture infill.



3D forward modeling with the finite-difference scheme is a computationally very expensive procedure. To run a realistic model in a reasonable amount of time, finite-difference codes are usually parallelized. Parallelization is done depending on the type of parallel machines available. Parallel machines can be broadly categorized in two types: (1) Multiple-processors shared-memory systems (MPSM) and (2) multiple-processors distributed-memory systems (MPDM). Common examples of MPSM are Cray SV1, IBM Popwer4 node. CPU clusters and Cray T3E are widely available MPDM machines. MPDM machines are relatively cheaper than MPSM machines; at the same expense more computational power can be bought in MPDM form than in MPSM form. Moreover, MPDM machines are easier to scale to large number of processors. However, it is relatively easier to program on MPSM machines than on MPDM machines. All the variables have the same address space on MPSM systems. On MPDM systems variables may have different address spaces, which requires message passing to exchange the data between the processors. Due to the necessity of passing the data between the processors on MPDM systems, achieving a good performance is not trivial and depends on a number of factors, for example, ingenuity of the programmer and speed of the network. I ran all the models shown here on a four-processor MPSM.

## Chapter 3

### Ray bending in anisotropic media

#### 3.1 Introduction

An accurate estimation of traveltime is needed to map heterogeneity in the earth's subsurface. Traveltimes are also needed for seismic tomography, variants of seismic migration, seismic modeling and inversion. In the past, extensive progress has been made to estimate traveltimes in complex and anisotropic media using a number of schemes. It is not possible to give the details of all the schemes here. However, I will try to give a brief overview of most of the schemes. Most of the traveltime computation schemes fall within one of these two categories: (1) First-arrival traveltime, and (2) Ray-theory based traveltime.

The first-arrival traveltime corresponds to the first arrival of the complete wavefield at a specified receiver position. However, it is not a function of the type of wave (e.g., head wave, direct wave etc.) to arrive first at the receiver. The first-arrival traveltime does not have any shadow zone. However, the traveltime function may not be smooth, especially in case of large velocity contrasts. Most of the schemes, which estimate first-arrival traveltimes, are based on the solution of eikonal equation. Vidale(1988, 1989, 1990)

and van Trier and Symes (1991) proposed different versions of finite-difference solution of the eikonal equation along expanding square (in 2-D) and along an expanding cube (in 3-D) to compute first-arrival traveltimes in isotropic media. Schneider et al. (1992) proposed a method based on Fermat's principle for traveltime computation in isotropic media that uses a local ray-trace solution of the eikonal equation. Faria and Stoffa (1994b) extended this algorithm to compute traveltime in VTI media. Kumar et al. (2004) further extended this scheme to calculate traveltime in tilted TI (TTI) media. Besides finite-difference solution of the eikonal equation, there are various methods of network shortest-path ray tracing that attempt to find the first-arrival traveltime at a receiver position. This type of scheme was first proposed by Moser et al. (1992) and Saito (1989). A very good overview on this kind of method can be found in Nolet and Moser (1993).

The ray-theory traveltime is defined separately for individual elementary waves. Hence, the ray-theory traveltime can be a multivalued function of a receiver location. Ray-theory traveltime is computed by ray tracing. Ray tracing can be broadly classified into two categories: (1) Initial-value ray tracing, and (2) Boundary value ray tracing. In initial-value ray tracing, a fan of rays is shot from the source in the model and some kind of extrapolation scheme is used to estimate the traveltime at a particular point in the model. Paraxial extrapolation (Červený, 1985) is one of the most popular methods of traveltime extrapolation. Figure 3.1 shows an example of initial-value ray tracing. However, these traveltime extrapolation methods fail in case of com-

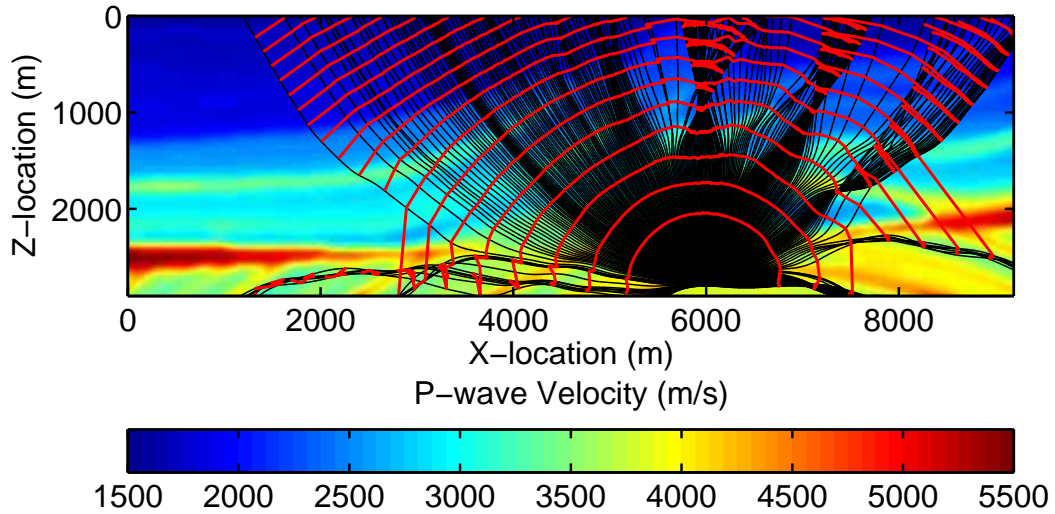


Figure 3.1: Initial-value ray tracing in Marmousi model.

plex media. To overcome the extrapolation problem, Vinje et al. (1993) and Lamba re et al. (1996) proposed wavefront construction scheme to compute the traveltimes. Unlike the previous method, the number of rays in this method is not fixed, but is adjusted at each wavefront using some criteria. Figure 3.2 shows an example of wavefront construction scheme. Notice how the extra rays are being inserted to preserve the ray density. A variant of this method was extended by Kaschwich and Gajewski (1993) for anisotropic media.

The most important case of boundary-value ray tracing is a two-point ray tracing. In a two-point ray tracing, raypath is sought between two fixed points  $\mathbf{S}$  and  $\mathbf{R}$ . The solution of two-point ray tracing may not be unique; multiple rays may connect the points  $\mathbf{S}$  and  $\mathbf{R}$ . Two-point ray tracing can be done by either shooting method or by bending method. In the shooting method, the initial-value ray tracing procedure is put within an iterative loop to find the

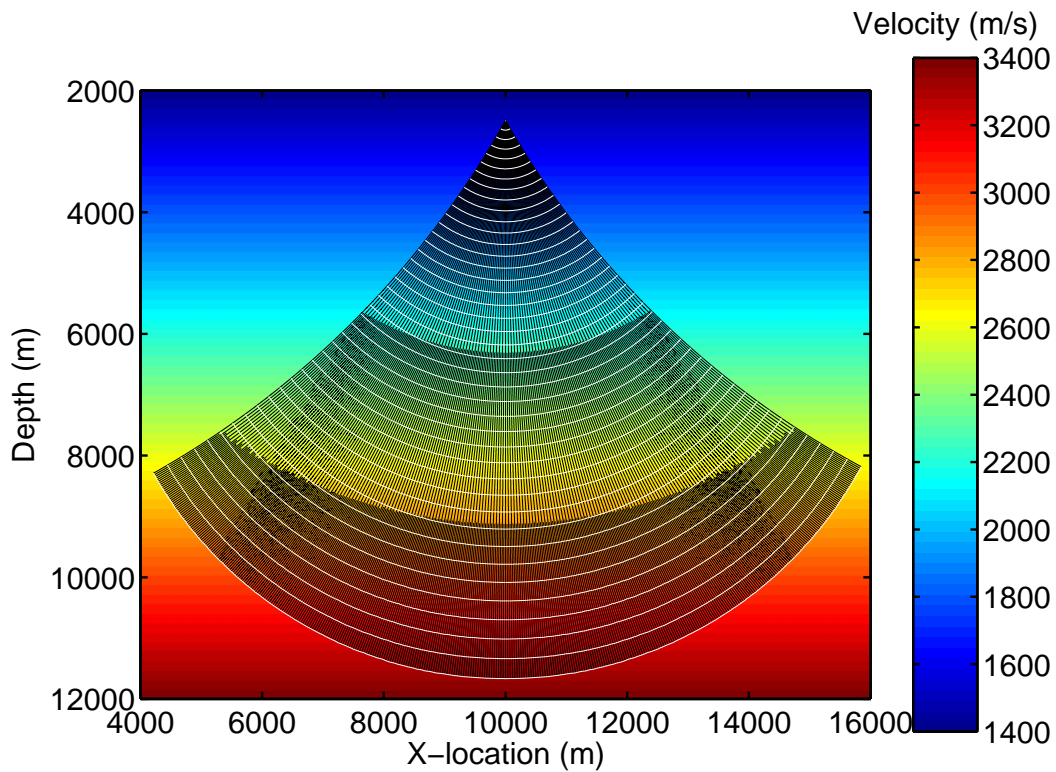


Figure 3.2: An example of wavefront construction technique in a depth-dependent velocity model: Notice that the extra rays are inserted after certain times to maintain the ray density.

ray which starts from  $\mathbf{S}$  and passes through  $\mathbf{R}$ . In a ray bending method, an initial raypath is guessed and then perturbed iteratively until the final solution is attained. Figure 3.3 shows an example of bending method. Boundary-value ray tracing has certain advantages over initial-value ray tracing. To trace rays or to calculate traveltimes using initial-value ray tracing is fast, but it requires some kind of interpolation for a given source-receiver pair (e.g., Červený, 2001, p. 218). On the other hand, a boundary value problem such as a two-point

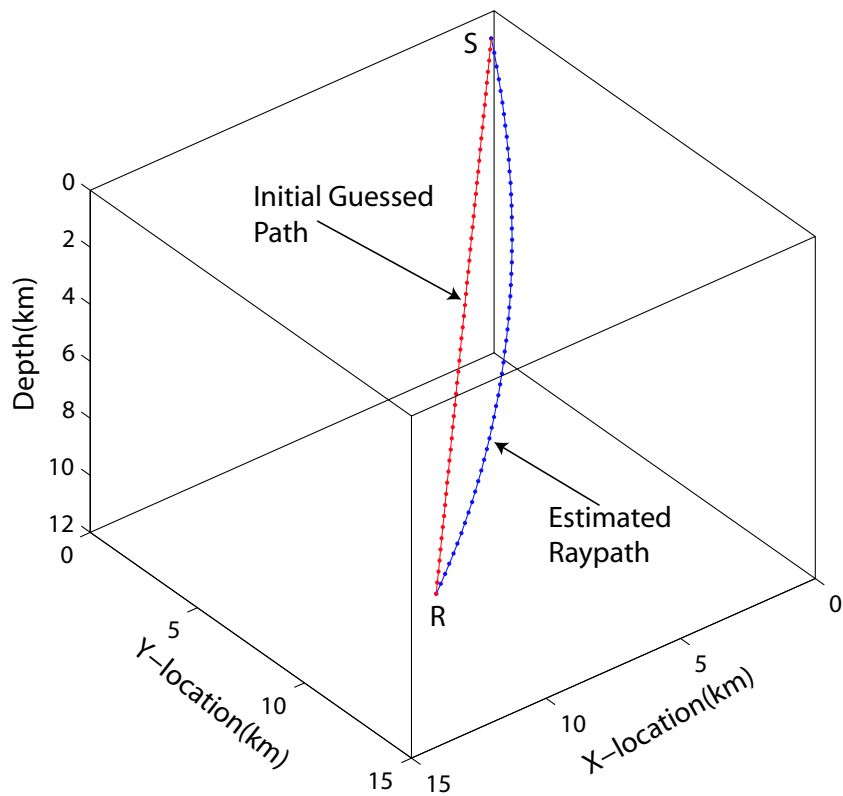


Figure 3.3: The solution of two-point ray tracing by the bending method: The initial guessed raypath is iterated until final solution is attained.

ray tracing does not require any interpolation of the traveltimes. Two-point ray tracing can be used in tomographic and earthquake studies and to image reflectors in oil and gas exploration.

Um and Thurber (1987), Prothero et al. (1988) and Moser et al. (1992) introduced variants of bending schemes for two-point ray tracing based on Fermat's principle. Guiziou et al. (1991) proposed ray bending through complex triangulated surfaces. Farra (1992) developed a bending method using

Hamiltonian formulation. Pšenčík and Farra (2005) and Farra (2005) derived first-order ray tracing equations for qP- and qS-waves, respectively, in weakly anisotropic media. Vesnaver (1996) applied ray bending to do two-point ray tracing on irregular grids. Velis and Ulrych (2001) used a global optimization scheme (simulated annealing) to determine minimum travelttime path between two points in complex structures. Grechka and McMechan (1996) introduced a two-point ray tracing for smoothly varying weak TI media. They approximated the raypaths and the medium by Chebyshev polynomials which limited its applicability only in smoothly varying medium. Moreover, they estimated group velocities in the medium, which are essential for two-point ray tracing, by further linearizing the expressions given by Thomsen (1986) for weak TI media. Surprisingly, I did not find numerous literature on two-point ray tracing in anisotropic media.

Here I follow an approach similar to that of Moser et al. (1992). However, my algorithm addresses some of the fundamental stumbling blocks inherent to two-point ray tracing in anisotropic media. I compute group velocities using Fourier expansion (Byun et al., 1989) for weak VTI media which was modified by Kumar et al. (2004) to estimate group velocities in the symmetry plane of TTI media. I extend it to compute group velocities in any plane of HTI and TTI media. For strong TI media and arbitrary anisotropy, I employ a search method to estimate the phase direction for a particular group direction, which eventually yields the desired group velocity. Similar approach was mentioned in Grechka and McMechan (1996), but to the best of my knowledge

no one has applied it so far in arbitrary anisotropy.

### 3.2 Methodology of ray bending

Here I briefly outline the approach to ray bending. A comprehensive overview can be found in Moser et al. (1992). Fermat's principle states that a raypath from a source to a receiver is stationary i.e., travelttime taken by a ray from the source to the receiver is minimum or

$$T(\mathbf{r}) = \int_{\mathbf{r}} \frac{ds}{V} \longrightarrow \min, \quad (3.1)$$

where  $\mathbf{r}$  denotes the raypath. I define the raypath as a polygonal path consisting of  $k + 1$  points, numbered from 0 to  $k$  and connected by straight line segments. If the location of these points in space is given by  $x$ ,  $y$ , and  $z$ , we can write  $\mathbf{r}$  as an  $n$ -dimensional vector; i.e.

$$\mathbf{r} = (x_0, y_0, z_0, x_1, y_1, z_1, \dots, x_k, y_k, z_k), \quad (3.2)$$

where  $n = 3(k+1)$ . The goal of any two-point ray tracing scheme is to estimate (or to invert) the vector  $\mathbf{r}$ . Many optimization schemes have been applied over the years to estimate  $\mathbf{r}$ . The most popular and robust scheme is to apply a method of conjugate gradient to estimate  $\mathbf{r}$ .

The line integral in equation 3.1 can be approximated using trapezoidal rule as

$$T(\mathbf{r}) = \sum_{i=1}^k \frac{1}{2} \left( \frac{1}{V_i} + \frac{1}{V_{i-1}} \right) |\mathbf{x}_i - \mathbf{x}_{i-1}|, \quad (3.3)$$



where  $\mathbf{x}_i$  stands for  $(x_i, y_i, z_i)$  and  $V_i$  is medium velocity. The integral in equation 3.1 can be evaluated by more sophisticated schemes, for example, Simpson's rule or composite Simpson's rule for better accuracy (e.g., Burden and Faires, 1989, p. 175). The traveltime  $T(\mathbf{r})$  is minimized using a conjugate gradient scheme (e.g., Press et al., 1987) which uses the gradient of time  $\nabla T$ . The gradient of time  $\nabla T$  is also an  $n$ -dimensional vector and is evaluated at each supporting point of the ray:

$$\nabla T(\mathbf{r}) = \left( \frac{\partial T}{\partial x_0}, \frac{\partial T}{\partial y_0}, \frac{\partial T}{\partial z_0}, \frac{\partial T}{\partial x_1}, \frac{\partial T}{\partial y_1}, \frac{\partial T}{\partial z_1}, \dots, \frac{\partial T}{\partial x_k}, \frac{\partial T}{\partial y_k}, \frac{\partial T}{\partial z_k} \right). \quad (3.4)$$

For ray bending, we need to keep the end points fixed, and hence, the corresponding components of time gradient  $\nabla T$  need not be calculated. The rest of the components of  $\nabla T$  can be calculated by a central finite-difference scheme; i.e.,

$$\nabla T(\mathbf{r}) = \frac{T(\mathbf{r} + \delta\mathbf{r}) - T(\mathbf{r} - \delta\mathbf{r})}{2\delta\mathbf{r}}. \quad (3.5)$$

In an isotropic medium, the above scheme can be implemented very easily. However, its implementation in anisotropic media is not trivial since we need to know the group velocity at each  $\mathbf{x}_i$  in direction of  $(\mathbf{x}_i - \mathbf{x}_{i-1})$ . In anisotropic media, evaluation of the group velocity in the desired group direction is not trivial. Next, I explain how to evaluate group velocity in a desired direction in anisotropic media.

### 3.3 Estimation of Group Velocity

#### 3.3.1 Weak TI media

Here I discuss how to, accurately, estimate the group velocity in the desired direction. This issue was first addressed by Thomsen (1986). He showed that in weak TI media, although a particular group direction is not the same as its corresponding phase direction, group velocity is equal to its corresponding phase velocity. Hence, the phase direction corresponding to the particular group direction needs to be estimated to calculate the group velocity. One needs to solve nonlinear equations (see equation 22 in Thomsen, 1986) to estimate the phase direction related to a particular group direction. Grechka and McMechan (1996) made further linearized approximation to obtain the expressions for the group slownesses in a form similar to the one given by Byun et al. (1989), although they followed a different approach to derive their group slowness formulae.

Byun et al. (1989) proposed to express the group velocity in TI media by the following Fourier expansion:

$$\frac{1}{V_g^2(\psi)} = a_0 + a_1 \cos^2 \psi + a_2 \cos^4 \psi, \quad (3.6)$$

where  $\psi$  is the angle between the ray (group direction) and the symmetry axis. Constants  $a_0$ ,  $a_1$ ,  $a_2$  can be solved using group velocity information at  $\psi = 0^\circ$ ,  $\psi = 90^\circ$ , and at some other arbitrary angle where group velocity can be found by any search scheme (section 3.3.2). The approximation in equation 3.6 is known to work for weakly anisotropic or a nearly elliptically

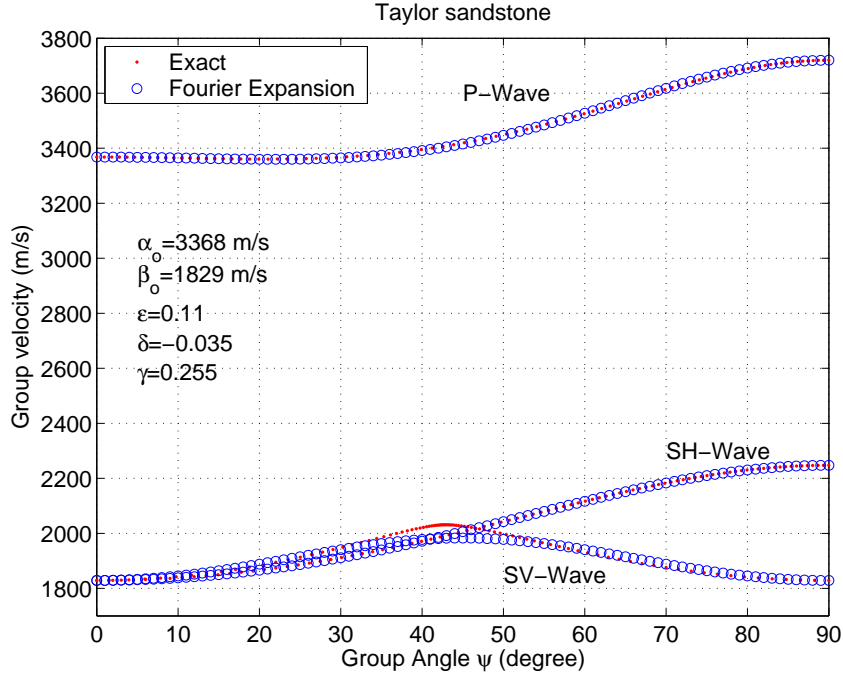


Figure 3.4: Comparison of group velocity computed with Fourier expansion (equation 3.6) and the exact group velocity in Taylor sandstone: For P- and SH-waves, the approximate curves closely follow the exact curves of velocity. But for SV-wave, approximate group velocity curve deviates from the exact velocity curve, especially at the oblique angles.

anisotropic medium (Byun et al., 1989). It should be mentioned that P-wave group velocity surface is not perfectly elliptical, SV-wave group velocity surface is rarely elliptical, and SH-wave group velocity surface is always elliptical. Hence, we can expect the equation 3.6 to yield good results only in case of P- and SH-waves.

Figure 3.4 shows the comparison between the exact and the Fourier expansion (equation 3.6) group velocities for all three modes in Taylor sandstone

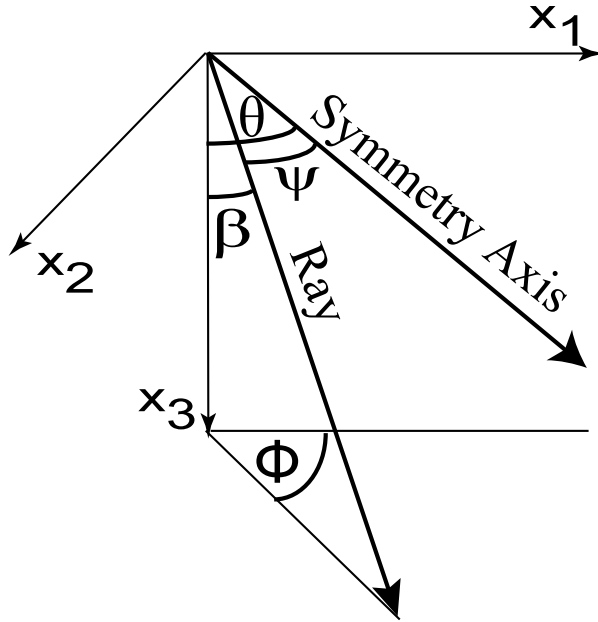


Figure 3.5: The angle  $\psi$  between a ray and symmetry axis can be expressed in terms of the azimuth  $\phi$  and the incidence angle  $\beta$  of the ray with vertical and the tilt  $\theta$  of the symmetry axis with vertical.

(Thomsen, 1986) with Thomsen parameters  $\alpha_0 = 3368 \text{ m/s}$ ,  $\beta_0 = 1829 \text{ m/s}$ ,  $\varepsilon = 0.110$ ,  $\delta = -0.035$ ,  $\gamma = 0.255$ . Notice that for P- and SH-waves, the group velocities calculated by Fourier expansion closely follows the exact group velocities. For SV-wave, the result is not very satisfactory as the velocity surface for SV-wave is non-elliptical.

To implement the equation 3.6 in a TI media with symmetry axis of arbitrary orientation, the angle  $\psi$  between the ray and the symmetry axis is needed. If the symmetry axis makes an angle  $\theta$  with vertical and is confined in  $x_1$ - $x_3$  plane and the azimuth and the incidence angles of a ray are  $\phi$  and  $\beta$ ,

respectively (Figure 3.5), we have

$$\cos \psi = \sin \theta \sin \beta \cos \phi + \cos \theta \cos \beta. \quad (3.7)$$

In the special case of HTI media  $\theta$  becomes  $90^\circ$  and equation 3.7 reduces to  $\cos \psi = \sin \beta \cos \phi$ . If the azimuth  $\phi$  of the ray is  $0^\circ$ , equation 3.7 yields  $\psi = \beta - \theta$ . If the azimuth of the symmetry axis is  $\phi_0$ ,  $\phi$  in equation 3.7 needs to be replaced by  $(\phi - \phi_0)$ . Equations 3.6 and 3.7 can be used together to estimate group velocities in any type of TI media.

Dog Creek shale (Thomsen, 1986), rotated by  $45^\circ$  about  $y$ -axis, with Thomsen parameters  $\alpha_0 = 1875 \text{ m/s}$ ,  $\beta_0 = 826 \text{ m/s}$ ,  $\varepsilon = 0.225$ ,  $\delta = 0.110$ ,  $\gamma = 0.345$  was used as a TTI medium to calculate the group velocities. Figures 3.6(a) and 3.6(c) show group velocities for P- and SV-waves at various azimuths  $\phi$  and incidence angles  $\beta$  calculated using equations 3.6 and 3.7. For P-wave, Fourier expansion scheme yields group velocities close to the exact group velocities; the maximum difference (Figure 3.6(b)) between the exact and approximated group velocities is less than  $5 \text{ m/s}$ . For SV-wave, the Fourier solution does not produce a very good match with the exact group velocity. But error (Figure 3.6(d)) is still less than  $10 \text{ m/s}$  at most of the places. For better computation of the group velocity, I propose to calculate the group velocities for SV-wave using the search scheme discussed next.

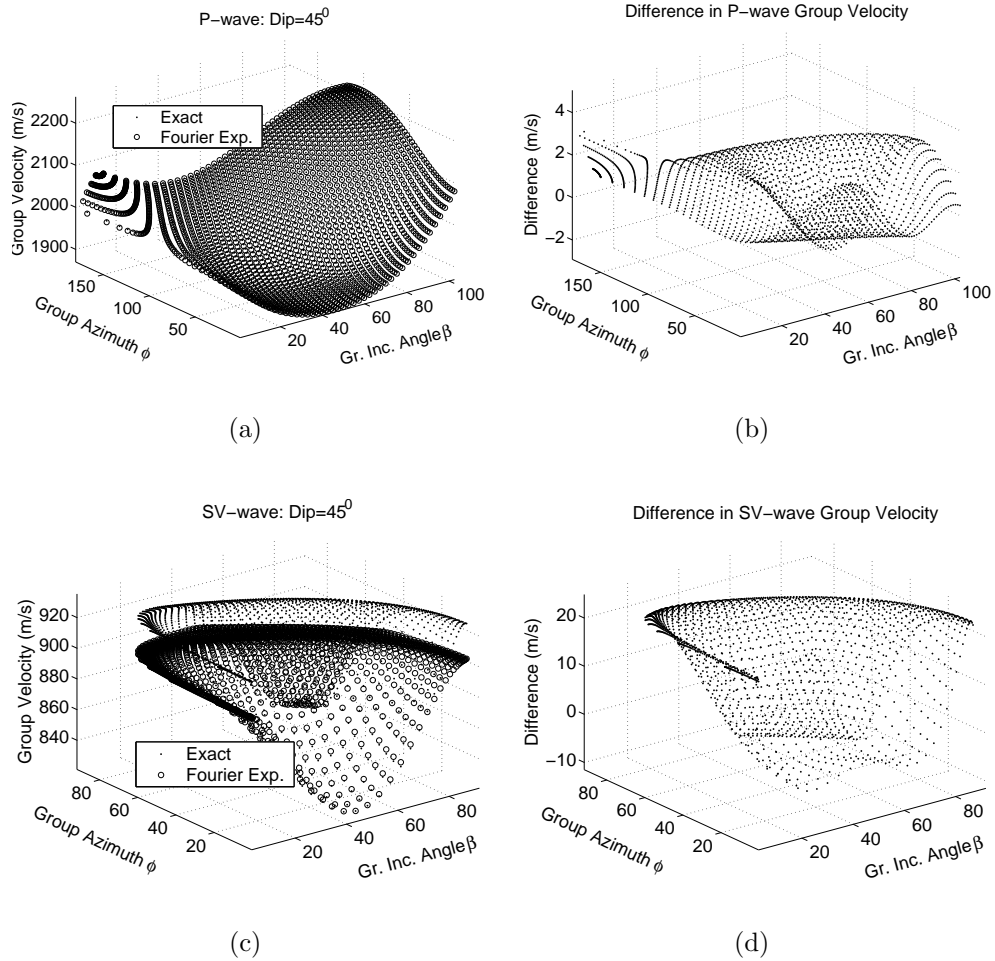


Figure 3.6: P- and SV-waves group velocities calculated using equations 3.6 and 3.7 for a TTI medium (Dog Creek shale rotated by 45° about  $y$ -axis) with azimuth  $\phi$  and incidence angle  $\beta$  of the group velocity vector (Figure 3.5): (a) Group velocities for P-wave, (b) Difference between the exact and the Fourier expansion group velocities for P-wave. (c) Group velocities for SV-wave, and (d) Difference between the exact and the Fourier expansion group velocities for SV-wave. Notice that velocities are varying both with  $\beta$  and  $\phi$ .

### 3.3.2 Strong TI media

Exact group velocities were calculated using the following formulae (e.g., Auld, 1990, p. 212) by a constant increment in the phase angle:

$$[c_{ijkl}l_j l_l - \rho v^2 \delta_{ik}]U_k = 0, \quad (3.8)$$

$$V_j = \frac{1}{\rho v} c_{ijkl} U_i U_k l_l, \quad (3.9)$$

where  $c_{ijkl}$  is the fourth-order stiffness tensor,  $v$  is the phase velocity in phase direction  $l_l$ ,  $U_j$  is the polarization vector of particles,  $\rho$  is the medium density, and  $V_j$  is the group velocity vector. The procedure to compute the group velocity is very straightforward. Phase velocity  $v$  is first estimated in phase direction  $l_l$  by solving equation 3.8, and then equation 3.9 is used to estimate the group velocity in phase direction  $l_l$ . Therefore, estimation of group velocity in arbitrary phase direction does not pose any problem in any kind of anisotropy. Here, it is worth mentioning that in singular directions, polarization vectors  $U_j$  become degenerated (eigenvectors in equation 3.8 cannot be uniquely defined when two or more than two of the eigenvalues are nonunique) which hampers the determination of group velocity in equation 3.9. Fortunately, in exploration seismology S-wave singularity is the most common type of singularity (both S-modes have the same phase velocity), but there are crystals in which P-S singularity is also possible such as Calcium Formate. An elaborate description of S-wave singularity can be found in Crampin and Yeldin (1981). I discuss the problems caused by the S-wave singularity later in the text.

For ray bending purpose, group velocity is needed in a particular ray direction. Estimation of the group velocity in the desired ray direction requires the evaluation of equations 3.8 and 3.9 in various phase directions  $l_i$  until we find the desired group direction (the group direction after each iteration can be found using group velocity components  $V_1$ ,  $V_2$ , and  $V_3$ ). This can be achieved by a table lookup. However, I employed a more efficient scheme in which I use an optimization scheme to minimize the following objective function

$$e = (\phi - \phi_c)^2 + (\beta - \beta_c)^2, \quad (3.10)$$

where  $\phi$  and  $\beta$  are the azimuth and incidence angles of group vector, respectively (Figure 3.5).  $\phi_c$  and  $\beta_c$  are computed using group velocity components which are derived at each iteration until an optimum set is found. For fast convergence of the solution, starting value of the phase direction  $l$  can be set to be the same as the desired group direction. I use a conjugate gradient scheme to minimize the error function  $e$ . It was noticed that the convergence is attained in 2 to 3 iterations. If there is a triplication in the group velocity surface, choice of the group velocity will be determined by the starting phase direction.

Group velocity in TI media depends only on the angle  $\psi$  between ray and the symmetry axis. Therefore, one has to minimize only the difference between the desired  $\psi$  and computed  $\psi_c$  after each iteration. This reduces the computational cost of group velocity estimation. For TI media with arbitrary symmetry axis orientation, equation 3.7 is used to compute equivalent



$\psi$ . Moreover, in TI media all three modes P-, SV-, and SH-waves are completely decoupled which helps handle the S-wave singularity. To compute the group velocity for SV-wave in the singular direction, I simply use the SV-wave polarization vector, and for SH-wave, SH-wave polarization is used. This approach was successfully applied by Shearer and Chapman (1989) to trace rays in TI media using the analytical expressions for polarization vectors of SV- and SH-waves.

Since in TI media all the planes containing the symmetry axis are equivalent, I decided to apply the search scheme in  $[x_1, x_3]$ -plane for any type of TI media. In  $[x_1, x_3]$ -plane  $l_2 = 0$  and  $l_1 = \sin \varphi$  and  $l_3 = \cos \varphi$ , where  $\varphi$  is the starting value of the angle between the symmetry axis and the phase direction (for quick convergence, I set  $\psi$  for  $\varphi$ ). Moreover, for TI media I use the following expression to calculate phase velocities for P- and SV-waves (e.g., Thomsen, 1986; Tsvankin, 2001, p. 17)

$$\begin{aligned} \rho v^2(\varphi) = & (c_{11} + c_{55}) \sin^2 \varphi + (c_{33} + c_{55}) \cos^2 \varphi \\ & \pm \sqrt{[(c_{11} - c_{55}) \sin^2 \varphi - (c_{33} - c_{55}) \cos^2 \varphi]^2} \\ & + 4(c_{13} + c_{55})^2 \sin^2 \varphi \cos^2 \varphi. \end{aligned} \quad (3.11)$$

Here, + stands for P-wave while – stands for SV-wave. Following are the formulae to calculate the particle vibration direction  $U_i$  and the group velocity components  $V_j$ .

$$\frac{U_1}{U_3} = \frac{(c_{13} + c_{55}) \sin \varphi \cos \varphi}{\rho v^2 - c_{11} \sin^2 \varphi + c_{55} \cos^2 \varphi}, \quad (3.12)$$

$$U_1^2 + U_3^2 = 1, \quad (3.13)$$

$$\begin{aligned}
V_1 &= [c_{11}U_1^2l_1 + c_{13}U_1U_3l_3 + c_{55}U_3^2 + c_{55}U_3U_1l_3]/(\rho v), \\
V_2 &= 0,
\end{aligned} \tag{3.14}$$

$$V_3 = [c_{13}U_3U_1l_1 + c_{55}U_1U_3l_1 + c_{55}U_1^2l_3 + c_{33}U_3^2l_3]/(\rho v).$$

For SH-wave,  $U_1 = U_3 = 0$  and  $U_2 = 1$ . Phase velocity  $v$  is given as

$$v = \sqrt{\frac{c_{66} \sin^2 \varphi + c_{55} \cos^2 \varphi}{\rho}}, \tag{3.15}$$

and the components of group velocity are given as

$$\begin{aligned}
V_1 &= c_{66}l_1/(\rho v), \\
V_2 &= 0,
\end{aligned} \tag{3.16}$$

$$V_3 = c_{55}l_3/(\rho v).$$

Estimated group direction  $\psi_c$  is given as  $\tan^{-1} \frac{V_1}{V_3}$  and the error function to minimize is  $(\psi - \psi_c)^2$ .

Figure 3.7 shows the comparison between the exact group velocity, group velocity computed by equation 3.6 and the group velocity derived by search scheme for all three modes in Green River shale (Thomsen, 1986), with Thomsen parameters  $\alpha_0 = 3292 \text{ m/s}$ ,  $\beta_0 = 1768 \text{ m/s}$ ,  $\varepsilon = 0.195$ ,  $\delta = -0.220$ ,  $\gamma = 0.180$ . Fourier expansion completely fails to estimate group velocity of SV-wave at oblique angles. In case of P-wave, Fourier expansion is unable to deliver the satisfactory results at oblique angles. However, Fourier expansion is predicting the accurate group velocity of SH-wave. The search scheme is

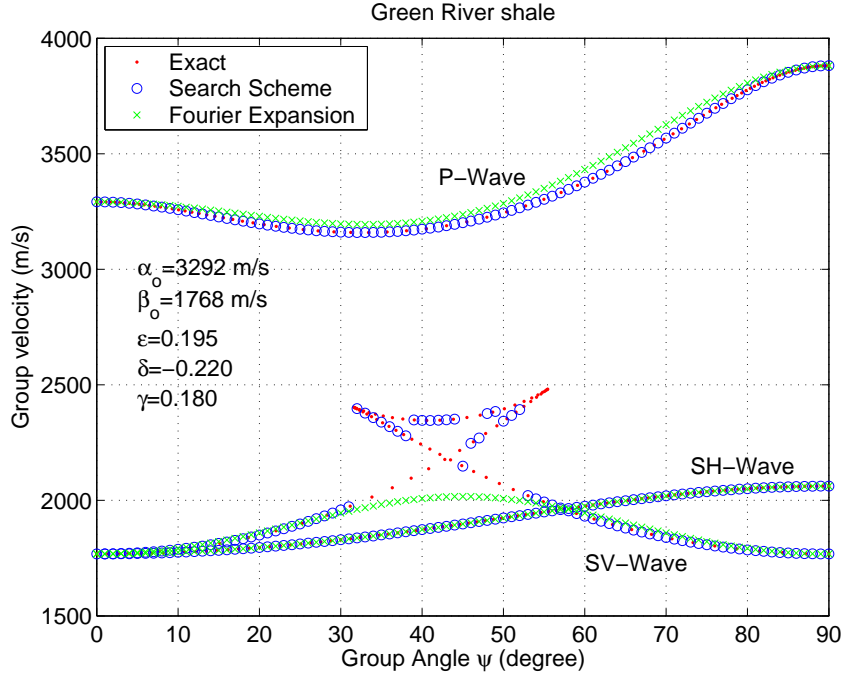


Figure 3.7: Comparison between the exact group velocity, group velocity computed by the Fourier expansion (equation 3.6), and the group velocity derived by search scheme for P-, SV-, and SH-waves in Green River shale: Notice that for P-wave, Fourier expansion solution is deviating from exact group velocity trend at oblique angles. For SV-wave, the Fourier expansion solution completely fails to predict the right group velocity at oblique angles. Search scheme is predicting the group velocity precisely for all three modes. For SV-wave, we get one of the three solutions at triplication.

predicting the perfect solutions for all three modes. However in case of SV-wave, search scheme, as expected, is estimating the group velocity of only one of the three branches of the triplication. This can be explained by the fact that any of the three branches can minimize  $(\psi - \psi_c)^2$ . The solution converges to one of the branches depending on the starting guess.

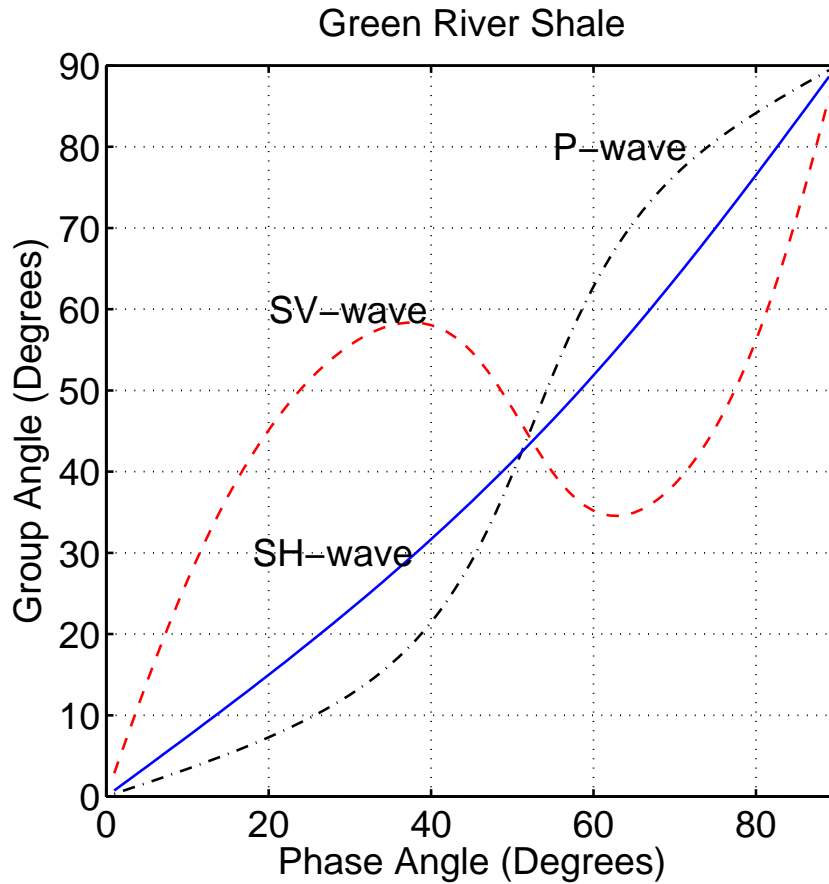


Figure 3.8: Phase and Group angles in Green River shale for P-, SV- and SH-waves: Notice that for SV-wave, three different phase angles have the same group angle which causes the triPLICATION in group velocity surface. The search scheme solves for only one of the phase angles associated with a group direction. Hence, the search scheme yields only one of the branches of the triPLICATION in figure 3.7.

Figure 3.8 shows the relationship between phase and group angles in Green River shale. Notice that for SV-wave, three different phase angles exist for some of the group angles. However, the search scheme solves only for one of the phase angles associated with a particular group angle. However, if there

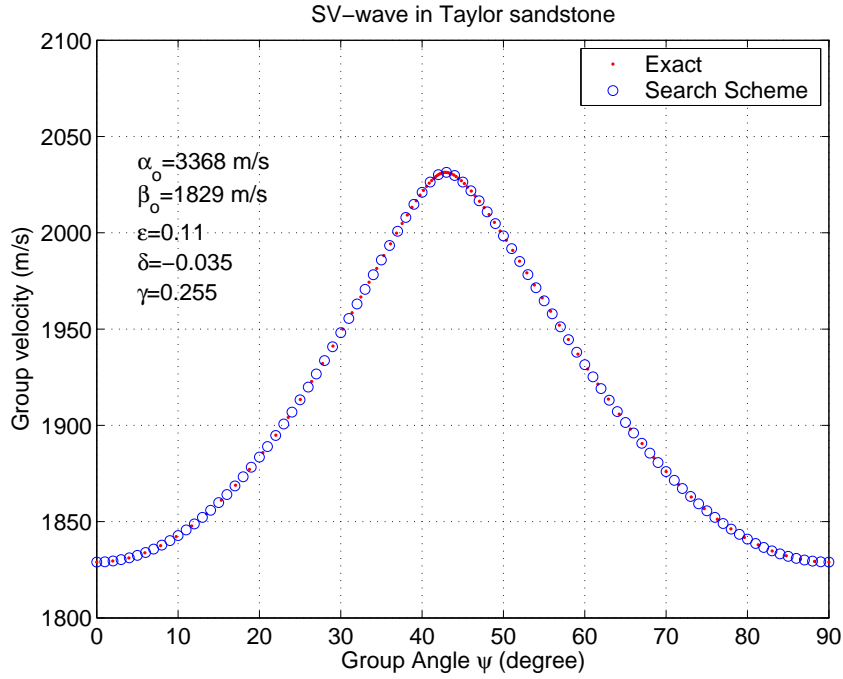


Figure 3.9: Comparison between the exact group velocity and the group velocity computed by search scheme for SV-wave in Taylor sandstone: In the absence of triplication, the search scheme accurately reproduces the whole group velocity curve. Exact group velocity curve was computed by constant increment in phase angle, but we can see that group velocity vectors are unevenly distributed due to focusing and defocusing of the energy. This is not the case in group velocity curve produced by the search scheme.

is no triplication in SV-wave, the search scheme yields a unique solution.

Figure 3.9 shows the comparison for SV-wave between the exact group velocities and the group velocities computed by the search scheme in Taylor sandstone. The search scheme is able to reproduce the entire group velocity curve. Exact group velocity curve was computed by a constant increment in phase angle, but we can see that group velocity vectors are unevenly dis-

tributed due to focusing and defocusing of the energy (Tsvankin, 2001, p. 32). This is not the case in group velocity curve produced by the search scheme.

### 3.3.3 Arbitrary anisotropy

For anisotropic media with symmetry lower than TI, equations 3.8 and 3.9 can be directly used. Due to non-planar nature of the phase vector corresponding to a particular group direction, both the angles defining the orientation of the phase vector need to be inverted for. If the initial guesses of azimuth and incidence angle are  $\phi_{in}$  and  $\beta_{in}$ , respectively, initial components of the phase vector can be written as  $l_1 = \cos \phi_{in} \sin \beta_{in}$ ,  $l_2 = \sin \phi_{in} \sin \beta_{in}$ , and  $l_3 = \cos \beta_{in}$ .

Although the presented algorithm can produce group velocity in arbitrary anisotropy, for the sake of simplicity I employed this scheme in an orthorhombic medium. Since in orthorhombic media, S-waves are decoupled into SH- and SV-waves only in the symmetry plane, I decided to distinguish the two S-wave modes as faster (S1) and slower (S2) waves. The orthorhombic medium was taken from Tsvankin (2001, p. 48), and is defined by the following Thomsen-style parameters introduced by Tsvankin (1997b) for orthorhombic media:  $\alpha_0 = 3000 \text{ m/s}$ ,  $\beta_0 = 2000 \text{ m/s}$ ,  $\varepsilon^{(1)} = 0.25$ ,  $\varepsilon^{(2)} = 0.15$ ,  $\delta^{(1)} = 0.05$ ,  $\delta^{(2)} = -0.1$ ,  $\delta^{(3)} = 0.15$ ,  $\gamma^{(1)} = 0.28$ ,  $\gamma^{(2)} = 0.15$ .

Figure 3.10 shows the phase and group velocity surfaces in the symmetry planes of the orthorhombic medium. Notice the S-wave singularity present in the  $yz$ -plane. Figure 3.11 shows the inverted group velocity with respect to

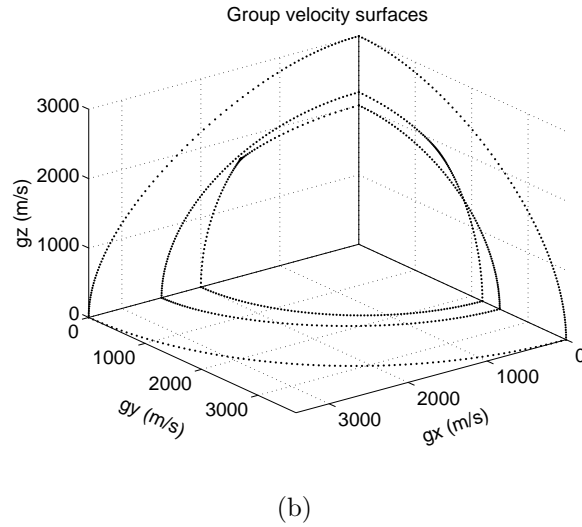
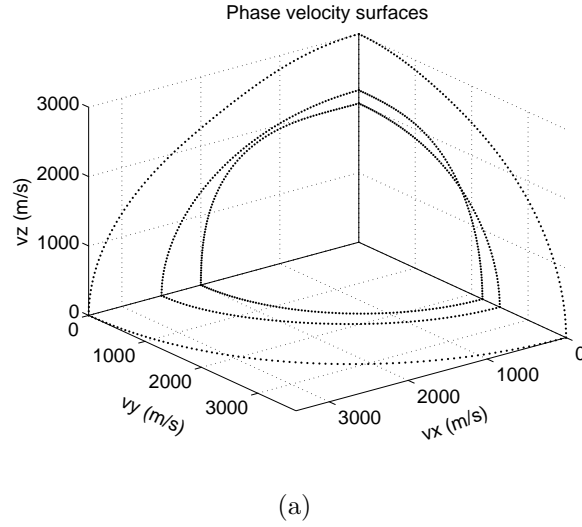


Figure 3.10: Phase (a) and group (b) velocity surfaces of the orthorhombic medium which was used as the test model to invert group velocities using search scheme: Thomsen-style anisotropic parameters are  $\alpha_0 = 3000$  m/s,  $\beta_0 = 2000$  m/s,  $\varepsilon^{(1)} = 0.25$ ,  $\varepsilon^{(2)} = 0.15$ ,  $\delta^{(1)} = 0.05$ ,  $\delta^{(2)} = -0.1$ ,  $\delta^{(3)} = 0.15$ ,  $\gamma^{(1)} = 0.28$ ,  $\gamma^{(2)} = 0.15$ .

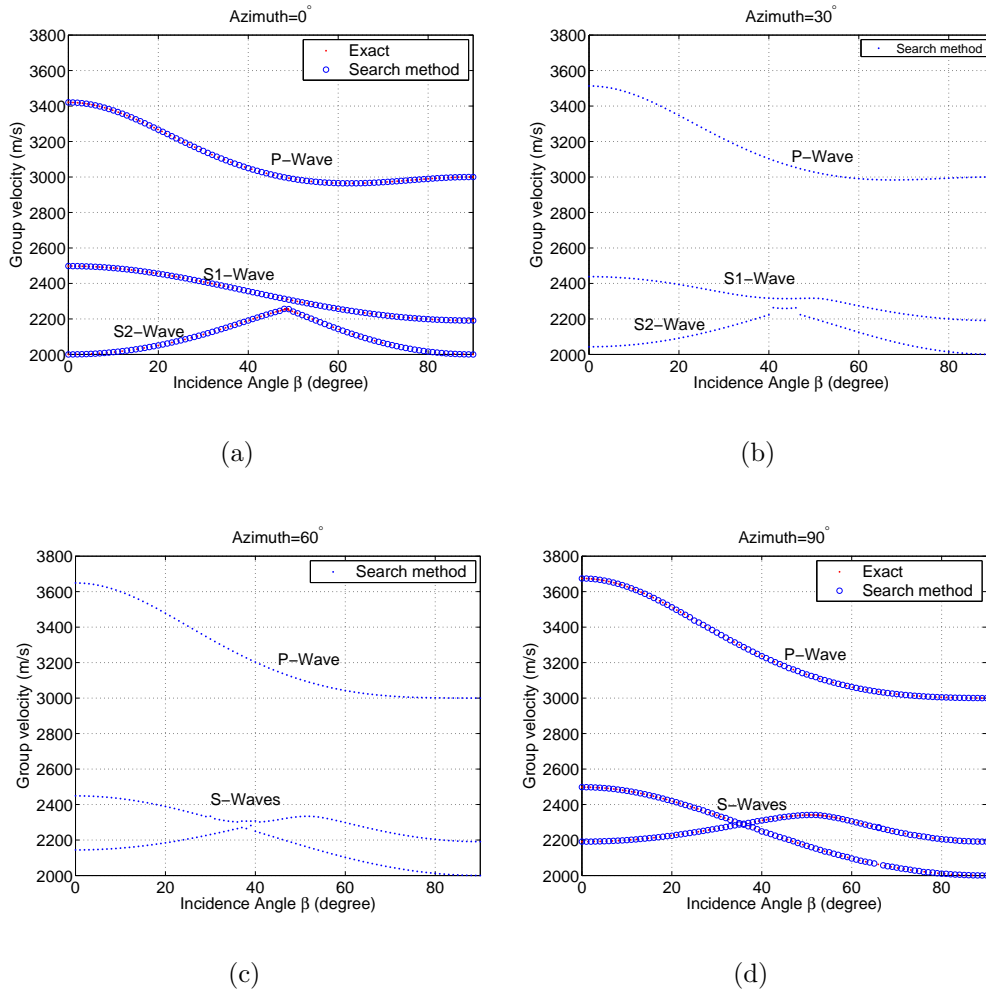


Figure 3.11: Comparison between the exact and the group velocities computed by search scheme at various azimuths: Exact group velocity curves for 30° and 60° were not calculated due to the non-planar phase vector. Notice the problems in estimation of group velocity close to S-wave singularity at oblique azimuth 60°.



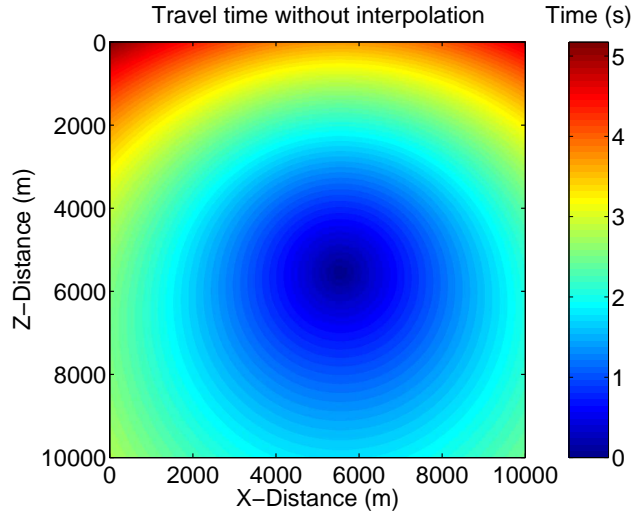
the ray incidence angle  $\beta$  (Figure 3.5) in the vertical planes oriented at various azimuths  $\phi$ . Notice that only at azimuths  $0^\circ$  ( $xz$ -plane) and  $90^\circ$  ( $yz$ -plane), I have the exact group velocity curves to compare with the inverted group velocity curves. This is due to the non-planar orientation of the phase vectors in the non-symmetry planes. Also notice that in the  $yz$ -symmetry plane (azimuth  $90^\circ$ ), we see better results at the S-wave singularity than at the oblique azimuths. The reason behind this is that in the symmetry planes SV- and SH-waves are decoupled, and hence, continuity in the polarization vector is maintained while calculating group velocities using equation 3.9. However, this was not done at the oblique azimuths hence, we see problems at the singularity. Although Vavryčuk (2001) suggested a scheme to maintain the continuity in the polarization vector while tracing rays in anisotropic media to avoid problems at or near the S-wave singularity, I did not apply it here due to the complexity associated with it in bending method.

### 3.4 Interpolation of Traveltime

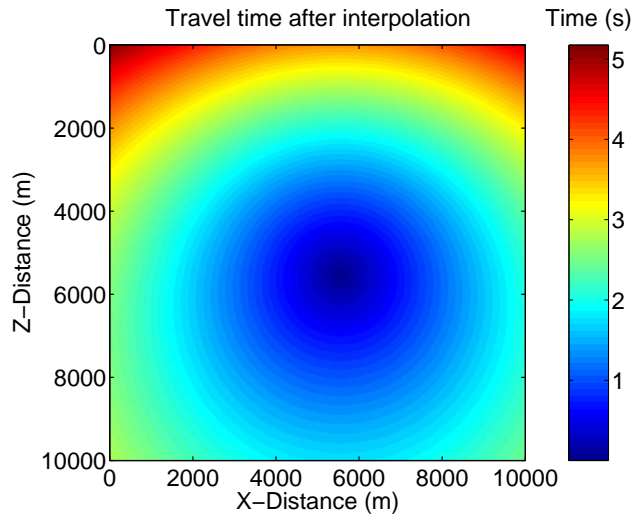
Two-point ray tracing is inherently more expensive than the conventional methods such as eikonal solver or wavefront construction. For practical application of two-point ray tracing for migration or forward modeling, we can compute traveltime on a coarse grid and then interpolate to a finer grid. We can either do interpolation without taking into account of the wavefront curvature such as trilinear and Fourier (sinc-) interpolation, or we may use more sophisticated interpolation schemes taking into account the wavefront curvature

such as parabolic (paraxial) or hyperbolic interpolation. It is well established that the latter class of interpolation schemes yields far superior results than the former class of interpolation techniques (e.g., Brokešová, 1996; Gajewski, 1998). Vanelle and Gajewski (2002), later, established the superiority of the hyperbolic interpolation over the parabolic interpolation. Gajewski (1998) showed how to compute hyperbolic interpolation coefficients from traveltime itself avoiding expensive dynamic ray tracing. But his algorithm was restricted to only horizontal interpolation. Vanelle and Gajewski (2002) extended later this scheme for vertical interpolation as well. This scheme produces excellent results for any type of heterogeneous media. I give a short description of this interpolation scheme in the appendix C.

To test the accuracy of this interpolation scheme, I implemented it on a slowly varying anisotropic medium. The medium has  $1001 \times 1001$  gridpoints with 10 m of grid spacing in either direction. The vertical P-wave velocity  $\alpha_0$  at any depth  $z$  is given as  $1000 + z/5$  m/s. Other anisotropic (Thomsen) parameters are kept constant with depth and are given as  $\varepsilon = 0.3$  and  $\delta = 0.1$ . Traveltime was computed by a brute force scheme developed by Faria and Stoffa (1994b) for VTI media. This traveltime was resampled back to a coarse grid spacing of 100 m and interpolation was implemented to estimate the traveltime at a finer grid of 10 m (figure 3.12). Figure 3.13 shows the relative error (%) in interpolated traveltime compared to the traveltime directly computed at the fine grid. The relative error close to the source (100 m in each direction) was set to zero due to very small traveltime values near the source which may



(a)



(b)

Figure 3.12: Traveltimes estimated with brute force scheme (Faria and Stoffa, 1994b) in a VTI medium with (a) and without (b) hyperbolic interpolation.

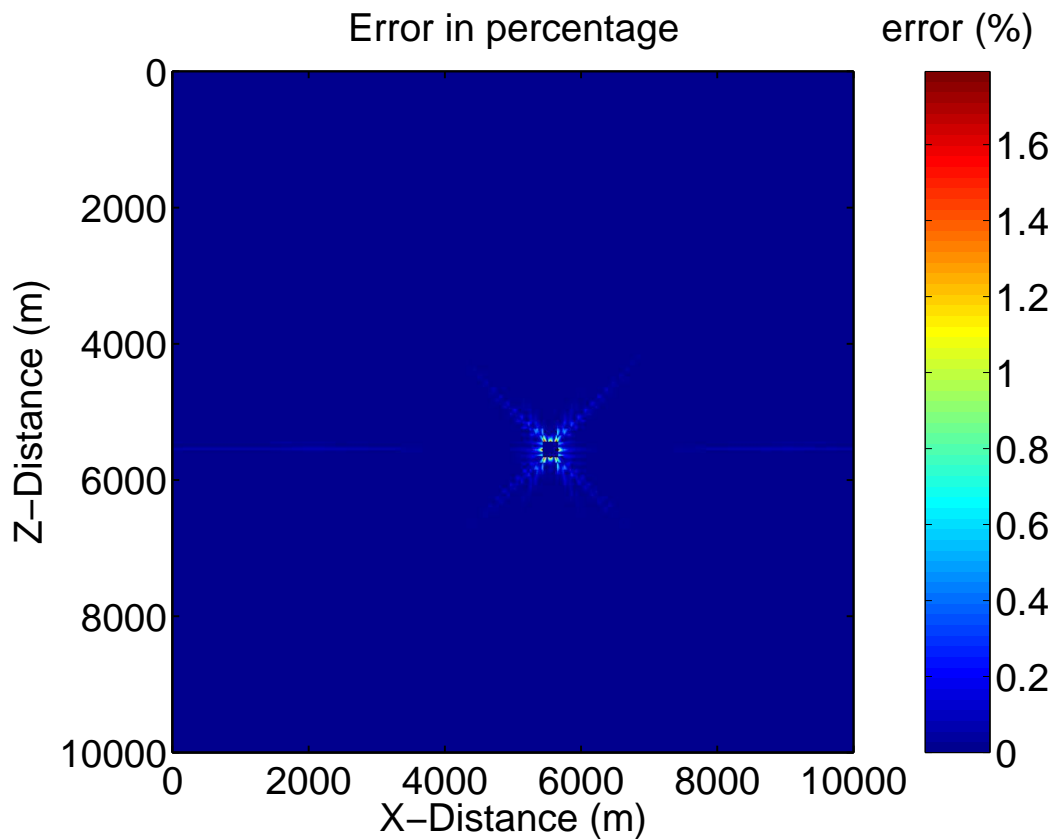


Figure 3.13: Relative absolute error (%) caused by hyperbolic interpolation for a VTI medium with vertical velocity  $\alpha_0$  gradually increasing with depth.

cause a large relative error. It should be noted that the errors are very small other than in the close vicinity of the source.

### 3.5 Ray Tracing Examples

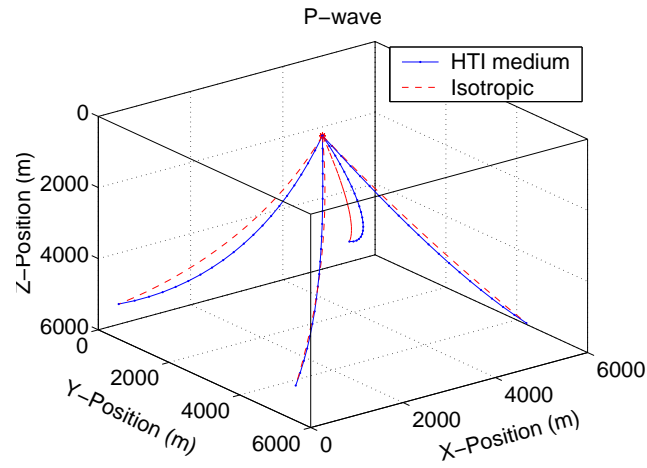
I applied ray bending code in a 3D anisotropic model. The source coordinates (in meters) are  $[2750, 2750, 250]$ , and four receivers are located at  $[250, 250, 5250]$ ,  $[250, 5250, 5250]$ ,  $[5250, 250, 5250]$ , and  $[5250, 5250, 5250]$ . The

subsurface is modeled as a heterogeneous HTI medium with symmetry axis oriented towards  $x_1$ -direction and described by the following generic Thomsen parameters:

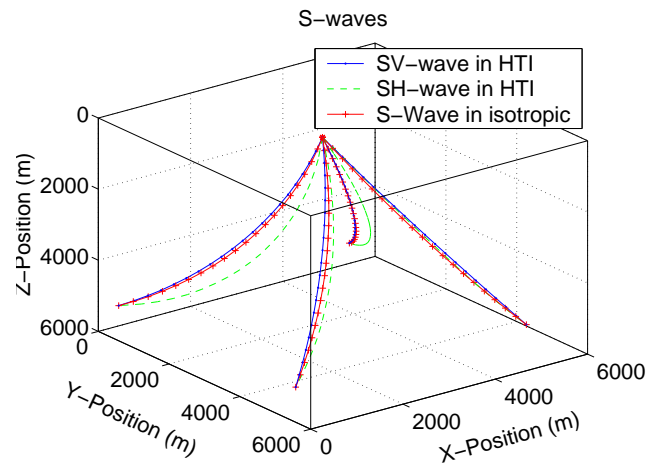
$$\begin{aligned}\alpha &= 1800 + 0.2(x_2 + x_3), \\ \beta &= 870 + 0.2(x_2 + x_3), \\ \varepsilon &= 0.25 + 2x_3 \times 10^{-4}, \\ \delta &= -0.10 + 4x_3 \times 10^{-5}, \\ \gamma &= 0.1 + (x_1 + x_2 + x_3) \times 10^{-4}.\end{aligned}$$

The model has 110 grids in each direction with the grid spacing of 50 m. Medium properties were linearly interpolated in the middle of the grid. Moser et al. (1992) used a beta-spline (e.g., Newman and Sproull, 1981) algorithm for interpolation purposes which, of course, increases the accuracy of computation. Group velocities were calculated using the search scheme. The initial raypath for each ray was guessed as a straight line with 20 equidistant points. The convergence of the relative change in travel time to the machine precision was used as the stopping criterion. All the traveltimes calculations converged in less than 40 iterations. I traced the rays in a comparable isotropic medium also. Medium properties were defined by setting all the anisotropic parameters ( $\varepsilon$ ,  $\delta$ ,  $\gamma$ ) to zero in equations 3.17. Figure 3.14 displays the raypaths for all three kinds of waves. Figure 3.15 displays the traveltimes of all modes in HTI and isotropic medium.

Next, I applied ray bending on a subsurface model (Figure 3.16) to compute traveltimes on each grid point with the hyperbolic interpolation (Vanelle and Gajewski, 2002). The subsurface model contains a TI thrust sheet with



(a)



(b)

Figure 3.14: Raypaths for (a) P-, SV-, and SH-waves in a smoothly varying HTI media (equation 3.17) with symmetry axis in  $x_1$ -direction: Initial raypaths were guessed as a straight line joining source and receivers. Most of the results converged in about 40 iterations. Raypaths for equivalent isotropic medium are also displayed.

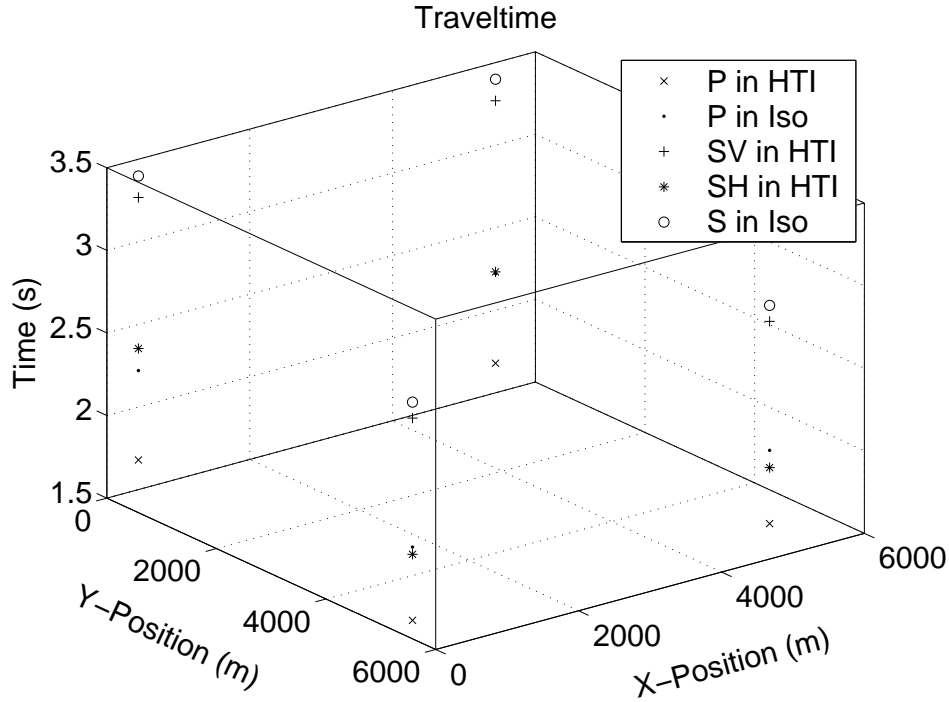


Figure 3.15: Traveltime of P-, SV-, and SH-waves in HTI model. Traveltimes in equivalent isotropic medium are also displayed.

variable tilt ( $0^\circ$ ,  $30^\circ$ ,  $50^\circ$ , and  $60^\circ$ ) embedded in a homogeneous isotropic medium. Thomsen parameters for the thrust sheet are  $\alpha_0 = 3800$  m/s,  $\varepsilon = 0.195$ ,  $\delta = -0.1$ . Other anisotropic parameters ( $\beta_0$ ,  $\gamma$ ) were not considered because I show the result here only for P-wave. The P-wave velocity of the background is 2740 m/s. The model has 411 and 221 grids in  $x$ - and  $z$ -directions, respectively with a grid size of 10 m in each direction. Source is located at [250 m, 250 m]. P-wave traveltime was computed at every 10th grid in both the directions. Group velocities were computed using Fourier expansion. Hyperbolic interpolation was used to compute the traveltime at other grid loca-

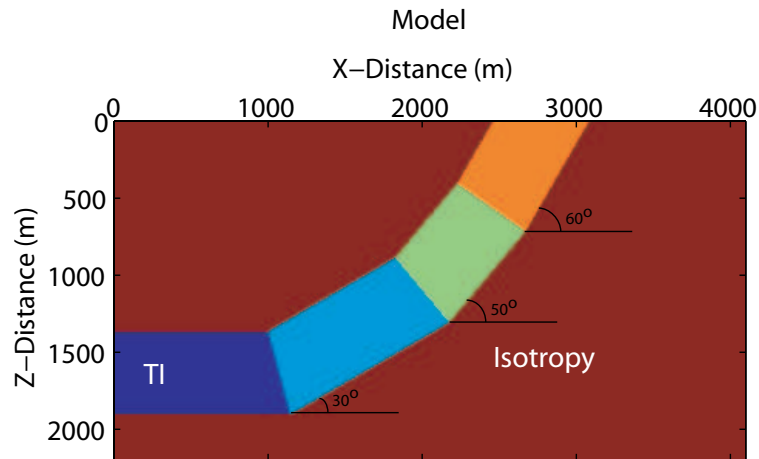
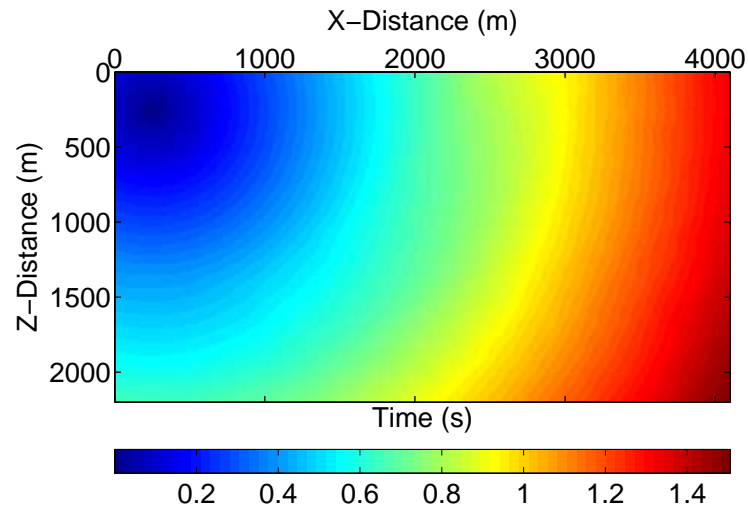


Figure 3.16: The subsurface model with TI thrust sheet embedded into an isotropic background: The thrust sheet is divided into four TI blocs with varying angle of axis of symmetry with respect to the vertical axis.

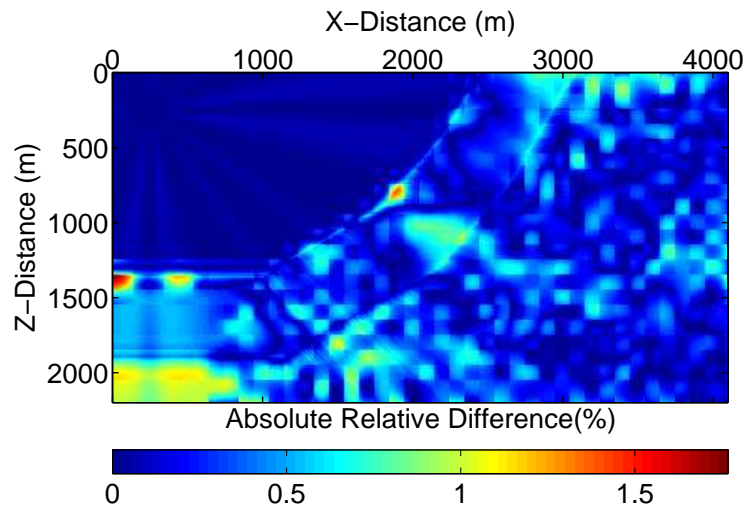
tions (Figure 3.17(a)). For comparison, the traveltimes were also computed by the scheme developed by Kumar et al. (2004).

Figure 3.17(b) shows the relative difference in percentage in traveltimes estimated by both the schemes. At most of the places, relative difference is much less than 1%. Relative difference was set to zero close to the region near the source (100 m in either direction) due to very small traveltimes which causes apparently a large relative difference. Figure 3.18 shows the traveltimes in 3D for the thrust model. The model was kept unchanged in the  $y$ -direction. A source is located at [250 m, 750 m, 250 m]. Traveltimes were again computed on a gridsize of 100 m and then interpolated to the gridsize of 10 m.





(a)



(b)

Figure 3.17: (a) Traveltime computed by two-point ray tracing and interpolation, (b) Absolute relative difference in traveltime computed by ray bending scheme and by method proposed Kumar et al. (2004).

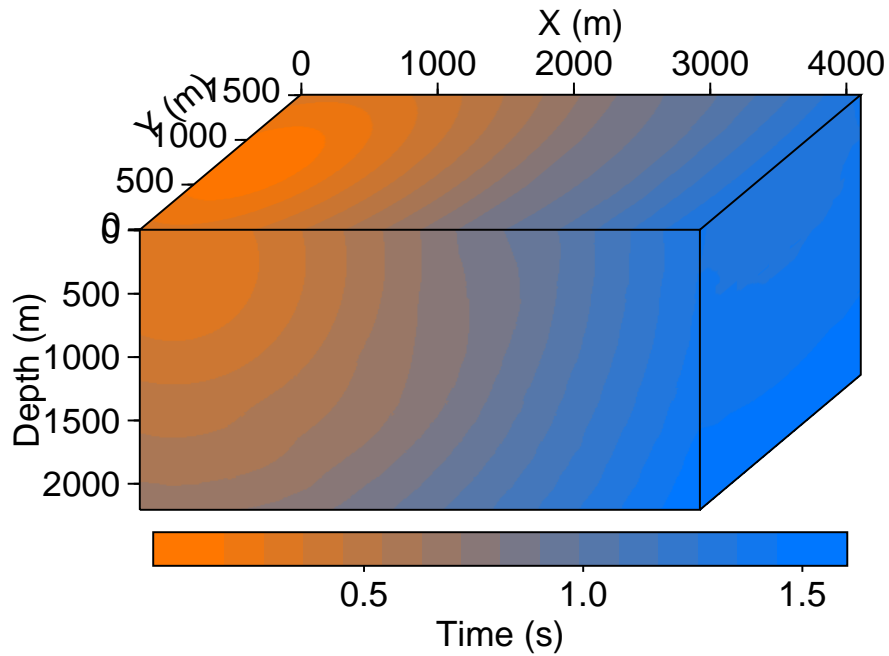


Figure 3.18: Traveltime for the thrustsheet model (figure 3.16) in 3D: The model is not varying in  $y$ -direction.

### 3.6 Discussion

The ray bending algorithm can calculate traveltime and trace rays in a general anisotropic medium. In the presence of multiplicity, ray bending does not guarantee that the solution will converge to a particular arrival. The shortest ray path technique (e.g., Moser, 1991) can provide a good initial guess which almost guarantees that the algorithm converges to the global minima (first-arrival). Another alternative is to use a computationally expensive global optimization scheme (Velis and Ulrych, 2001) to minimize the travel time to obtain the first arrival. Nonetheless, one has to be careful while applying a

two-point ray tracing scheme in a complex structure.

The search scheme uses a method of conjugate gradient to estimate group velocity. I applied this method because it is known to be robust and reasonable in terms of computation costs (Fletcher, 1980). However, one can apply any other optimization scheme such as Newton-Raphson, method of steepest descent or 2nd order Newton's algorithm (e.g., Burden and Faires, 1989, p. 49). The same is true while minimization of travel time is sought.

Precise estimation of group velocity has always been sought in many application of exploration geophysics. For example, schemes to estimate first-arrival travel time in anisotropic media, those proposed by Faria and Stoffa (1994b) and Kumar et al. (2004), can be applied to strongly anisotropic media by precise estimation of group velocities by the search scheme, although it will make those schemes more expensive.

Care must be taken while tracing rays in media with symmetry lower than TI. Due to the sudden change in the polarization vectors in S-wave modes (right after the singularities), one may obtain false bending (Vavryčuk, 2001) and sudden jumps in traveltimes curves. The next step in improving this method can be incorporation of an algorithm to maintain the continuity of the S-wave polarization vectors while tracing the rays. However, I must mention that this correction will pose some technical difficulties. One of the few that stands out is that it will need a large number of supporting points to guarantee that the algorithm does not miss the singular point in space.

## Chapter 4

### Ray-Born inversion for fracture parameters

#### 4.1 Introduction

As I discussed in chapter 1, the conventional methods of AVOA analysis for the inversion of fracture parameters fail in the case of laterally varying media. Shaw and Sen (2004) showed that the linearized reflection coefficients, which are used for AVOA analysis, are equivalent to a first-order Born approximation. Using the first-order Born approximation, Shaw and Sen (2006) derived analytical expressions for the sensitivity matrices for flat layers. These matrices were then used to invert for the fracture parameters (in which AVOA was parameterized by normal and tangential weaknesses  $\Delta_N$  and  $\Delta_T$ , respectively; see section 1.5.3). However, the Born approximation is not limited to only laterally uniform media, and in the past, it has been used to invert for the acoustic and elastic properties of the scatterers from the background (e.g., Stolt and Weglein, 1985; Beydoun and Mendes, 1989; Jin et al., 1992).

Clayton and Stolt (1981), Keys and Weglein (1983) and Cohen et al. (1986) used the Born approximation to invert for the acoustic properties. Beydoun and Mendes (1989) introduced the theoretical basis of inversion for isotropic elastic properties using a Born formulation. They used a single-step

conditioned-gradient algorithm to minimize a misfit function between the observed data and the synthetic data. Beylkin and Burridge (1990) proposed linearized-inversion schemes for both acoustic and elastic media. Their inversion scheme is based on an asymptotic inversion formula developed by Beylkin (1985). Jin et al. (1992) developed a theory using the ray-Born approach to invert for the elastic properties. They proposed using iterative quasi-Newton inversion method to minimize the error function between the data and the scattered wavefield. They also showed, using condition numbers of a Hessian matrix, that this kind of inversion is ill-conditioned if only one scattering mode is available. Thierry et al. (1999) used the ray-Born approach to migrate/invert the true amplitude and the velocity of a 2D complex medium (Marmousi model). Lambaré et al. (2003) and Operto et al. (2003) extended this approach to 3D. Chapman and Coates (1994) generalized the concept of Born scattering to anisotropic media. Eaton and Stewart (1994) developed theoretical basis for ray-Born inversion in TI media. Using some very simple test cases, they showed that their inversion scheme could estimate the locations of the anisotropic scatterers. They cast the inversion as a discrete generalized  $L_2$  optimization problem, which they solved using an iterative quasi-Newton method. They also proposed choosing suitable model parameter which depend on the type of TI media one is inverting for.

In this chapter, I develop the theoretical basis for a ray-Born inversion of fracture parameters ( $\Delta_N$  and  $\Delta_T$ ) in laterally varying media. I implement the inversion in the symmetry plane of the fractured media. I outline the

inversion procedure and propose a regularization scheme that reduces the non-uniqueness from the inversion. I also demonstrate, using numerical examples, that all the frequencies are not needed for a desired inversion result; in fact, a very small number of frequency samples covering the whole spectrum is enough for a good inversion result. I outline the foreseeable problems in the application of this technique to a field dataset. I also detail the application of an asymptotic expansion of the Born integral, which considerably reduces the computation time (appendix E). I demonstrate application of the asymptotic expansion on the forward modeling and the inversion using numerical examples (appendix E).

## 4.2 Methodology

### 4.2.1 The linearized forward problem

Green's tensor  $G_{mk}$  which satisfies the equation of motion can be written as (Červený, 2001, p. 15)

$$(c_{ijkl}G_{ml,k} + \rho\omega^2G_{mi}) = -\delta_{mi}\delta(\mathbf{x} - \mathbf{s}), \quad (4.1)$$

where  $c_{ijkl}$  is the stiffness tensor and  $\rho$  is the density.  $\omega$  is the frequency associated with the Green's tensor  $G_{mk}$ .  $\delta(\mathbf{x})$  is the Dirac delta function, and  $\delta_{mi}$  is the Kronecker delta. The Green's tensor  $G_{mk}$  has the arguments  $(\mathbf{s}, \mathbf{x}, \omega)$ ; this notation signifies the  $k$ -component of particle displacement at  $\mathbf{x}$  due to a unit impulse at time zero (with the dimensions of force per unit volume) in the  $m$ -direction at point  $\mathbf{s}$  (Eaton and Stewart, 1994). Equation 4.1

can be solved using any standard numerical technique (e.g., finite-difference). However, an approximate solution can be obtained about a reference medium using a first-order Born approximation.

The medium parameters and the Green's tensor can be written as a sum of two parts:

$$c_{ijkl} = c_{ijkl}^0 + \Delta c_{ijkl}, \quad (4.2)$$

$$\rho = \rho^0 + \Delta\rho, \quad (4.3)$$

and

$$G_{mk} = G_{mk}^0 + U_{mk}, \quad (4.4)$$

where  $c_{ijkl}^0$  and  $\rho^0$  are the stiffness tensor and the density of the reference medium (or background), respectively.  $\Delta c_{ijkl}$  and  $\Delta\rho$  are the stiffness tensor and the density of the scatterer or the heterogeneity embedded in the background.  $G_{mk}^0$  is the Green's tensor in the reference medium.  $U_{mk}$ , the difference between the exact Green's tensor and the reference Green's tensor is referred to as the scattered wavefield (due to an impulsive source). The parameters for the reference medium,  $c_{ijkl}^0(\mathbf{x})$  and  $\rho^0(\mathbf{x})$ , have to be smooth (differentiable) and continuous. The reference or background Green's tensor satisfies the following equation of motion:

$$(c_{ijkl}^0 G_{ml,k}^0 + \rho^0 \omega^2 G_{mi}^0) = -\delta_{mi} \delta(\mathbf{x} - \mathbf{s}). \quad (4.5)$$

After some algebra and making the assumption that  $G_{mk}(\mathbf{s}, \mathbf{x}, \omega) = G_{mk}^0(\mathbf{s}, \mathbf{x}, \omega)$

(first-order Born approximation, see Červený, 2001, p. 93–95), we get

$$U_{mn}(\mathbf{s}, \mathbf{r}, \omega) \approx \int_D [\Delta\rho\omega^2 \tilde{G}_{mi}^0(\mathbf{x}, \mathbf{r}, \omega) \hat{G}_{ni}^0(\mathbf{x}, \mathbf{r}, \omega) + \Delta c_{ijkl} \tilde{G}_{mk,l}^0(\mathbf{s}, \mathbf{x}, \omega) \hat{G}_{ni,j}^0(\mathbf{x}, \mathbf{r}, \omega)] d\mathbf{x}. \quad (4.6)$$

The tilde ( $\tilde{\phantom{x}}$ ) and hat ( $\hat{\phantom{x}}$ ) denote the quantities associated with the incident and scattered wavefields, respectively. Equation 4.6 is the first-order Born, or single-scattering approximation—multiple interactions between heterogeneities are not considered—for general anisotropic media. For equation 4.6 to be valid;  $|\Delta C_{ijkl}/c_{ijkl}| \ll 1$  and  $|\Delta\rho/\rho| \ll 1$ . It should be noted here that  $U_{mk}$  is the superposition of all single-scattered arrivals from all scatterers embedded in the reference medium.

To solve equation 4.6, we need an analytical expression for the reference Green's tensor  $G_{mi}^0$  which is not available for most of the non-trivial cases. Hence, zeroth-order asymptotic ray theory is used to estimate the reference Green's tensor. In the ray-method, for each type of body wave denoted by  $\Omega$ , an approximate Green's tensor can be written as (Eaton and Stewart, 1994)

$$\Gamma_{mk}^\Omega(\mathbf{s}, \mathbf{x}, \omega) \approx A g_m(\mathbf{s}) g_k(\mathbf{x}) e^{i\omega\tau}, \quad (4.7)$$

where  $\tau$  and  $A$  are the traveltime (from source to scatterer) and the amplitude terms.  $g_m(\mathbf{s})$  and  $g_k(\mathbf{x})$  are the orientations of the source and the receiver, respectively. Using equation 4.7, we can rewrite equation 4.6 as

$$U_{mn}(\mathbf{s}, \mathbf{r}, \omega) \approx \omega^2 \sum_{\Omega} \tilde{g}_m(\mathbf{s}) \hat{g}_n(\mathbf{r}) \int_D d\mathbf{x} [\Delta\rho\delta_{ik} + \Delta c_{ijkl} \tilde{p}_l \hat{p}_j] A \tilde{g}_k \hat{g}_i e^{i\omega\tau}, \quad (4.8)$$



where  $A = \tilde{A}\hat{A}$  and  $\tau = \tilde{\tau} + \hat{\tau}$ , respectively. Vectors  $p_i$  and  $g_i$  represent the polarization and slowness of the particular wave type (P- or S-wave) at the scatterer location. It should be noted that there is, in general anisotropic media, full elastic coupling of the incident and scattered wavefields (i.e., nine possible combinations of three incident and three scattered wave types).

The scalar quantity,

$$R(\mathbf{m}_0, \tilde{\mathbf{p}}, \hat{\mathbf{p}}, \tilde{\mathbf{g}}, \hat{\mathbf{g}}) \equiv [\Delta\rho\delta_{ik} + \Delta c_{ijkl}\tilde{p}_l\hat{p}_j]\tilde{g}_k\hat{g}_i \quad (4.9)$$

that appears in equation 4.8 is called the scattering function. It should be noted that the scattering function for anisotropic media is dependent on the properties of the background media through the slowness and polarization vectors.  $\mathbf{m}_0$  represents a model parameter vector, the components of which are perturbations relative to the background medium expressed in terms of the elastic coefficients and density. The goal of any inversion scheme is to estimate  $\mathbf{m}_0$ .

If we assume that the background medium is isotropic, and if the medium is not varying in one of the horizontal directions (say in the  $y$ -direction), we can apply a two-and-half dimensional correction. After applying two-and-half dimensional correction (or stationary phase approximation, e.g., Bleistein et al., 1987) on equation 4.8 in the  $y$ -direction, we get

$$U_{mn}(\mathbf{s}, \mathbf{r}, \omega) \approx |\omega|^{3/2}(2\pi)^{1/2}e^{\text{sign}(\omega)i\pi/4} \sum_{\Omega} \tilde{g}_m(\mathbf{s})\hat{g}_n(\mathbf{r}) \times \int_{x_1}^{x_2} \int_{z_1}^{z_2} R(\mathbf{m}_0, \tilde{\mathbf{p}}, \hat{\mathbf{p}}, \tilde{\mathbf{g}}, \hat{\mathbf{g}})(\tau, yy)^{-1/2} A e^{i\omega\tau} dx dz. \quad (4.10)$$

### 4.2.2 Inversion scheme

Equation 4.10 can be rewritten as

$$\mathbf{u} = \mathbf{G}\mathbf{m}, \quad (4.11)$$

where  $\mathbf{u}$  is the scattered wavefield,  $\mathbf{G}$  describes the kernel of integral equation 4.10, and  $\mathbf{m}$  is the model vector which contains all the model parameters in the region of interest.

The objective of any inversion scheme is to estimate  $\mathbf{m}$ . Although a direct least squares solution of equation 4.11 exists, it is not used due to several reasons. The large dimensions of the data and model vectors require the calculation of the inverses of very large matrices. Moreover, due to insufficient data and the presence of noise in the data, the inversion may become ill-posed. To circumvent this problem, I use an indirect inversion scheme which tries to minimize the error iteratively until some threshold is reached. The error function is given as

$$E = \frac{1}{2} \Delta \mathbf{u}^T \Delta \mathbf{u} + \epsilon f(\mathbf{m}), \quad (4.12)$$

where  $\Delta \mathbf{u} = \mathbf{u}_{data} - \mathbf{u}_{syn}$ . Function  $f(\mathbf{m})$  is used to constrain the values of the inverted model parameters (see section 4.3.1). The error function can be minimized by either using a global optimization scheme such as genetic algorithm or simulated annealing, or using a local optimization scheme such as Gauss-Newton or conjugate gradient. I used the method of conjugate gradient for the inversion because it is known to be robust and reasonably costly (Press

et al., 1987). The conjugate gradient scheme needs the derivative of the error function at each iteration which is given as

$$\mathbf{c}^j = \frac{\partial E}{\partial \mathbf{m}^j} = -\mathbf{G}^T \Delta \mathbf{u}^j + \epsilon \frac{\partial f(\mathbf{m})^j}{\partial \mathbf{m}^j}, \quad (4.13)$$

where  $\mathbf{c}^j$  is the derivative of the error function at iteration  $j$ . See appendix D for a derivation of equation 4.13.

### 4.3 Implementation of inversion

Before implementing any inversion, it is very important that a suitable model parameterization of the inverse problem has been carried out. Eaton and Stewart (1994) proposed a transformation operator  $\mathbf{L}^q$  such that

$$\mathbf{m}_0 = \mathbf{L}^q \mathbf{m}_q, \quad (4.14)$$

where  $\mathbf{m}_0$  represents the fundamental model parameter vector, the elements of which are the perturbations relative to the background expressed in terms of elastic stiffnesses and density.  $\mathbf{m}_q$  is the new model vector in the desired parameterization. If the medium is transversely isotropic,  $\mathbf{m}_0$  can be written as

$$\mathbf{m}_0 = [\Delta c_{11}, \Delta c_{33}, \Delta c_{13}, \Delta c_{44}, \Delta c_{66}, \Delta \rho]^T. \quad (4.15)$$

However, if the elastic properties of the background of the fractured medium are known, the remaining unknown model parameters which need to be inverted are  $\Delta_N$  and  $\Delta_T$  or  $\mathbf{m}^q = [\Delta_N, \Delta_T]^T$ . It can be shown that for such a model

parameterization  $\mathbf{L}^q$  is given as (appendix D)

$$\mathbf{L}^q = \begin{bmatrix} -(\lambda_b + 2\mu_b) & 0 \\ -\frac{\lambda_b^2}{\lambda_b + 2\mu_b} & 0 \\ -\lambda_b & 0 \\ 0 & -\mu_b \\ 0 & 0 \end{bmatrix}, \quad (4.16)$$

where  $\lambda_b$  and  $\mu_b$  are the background isotropic elastic coefficients. Moreover, the scattering function given in equation 4.9 can be rewritten as

$$R(\mathbf{m}_0, \tilde{\mathbf{p}}, \hat{\mathbf{p}}, \tilde{\mathbf{g}}, \hat{\mathbf{g}}) = \mathbf{h}\mathbf{m}_0 = \mathbf{h}\mathbf{L}^q\mathbf{m}^q. \quad (4.17)$$

For P- and SV-wave scattering (PP, PSV, SVSV, SVP), in the symmetry plane of an HTI medium, vector  $\mathbf{h}$  can be written as (Eaton and Stewart, 1994)

$$\begin{aligned} \mathbf{h} = & (\hat{p}_1\tilde{p}_1\hat{g}_1\tilde{g}_1, \hat{p}_3\tilde{p}_3\hat{g}_3\tilde{g}_3, \hat{p}_1\tilde{p}_3\hat{g}_1\tilde{g}_3 + \hat{p}_3\tilde{p}_1\hat{g}_3\tilde{g}_1, 0, \\ & \hat{p}_1\tilde{p}_1\hat{g}_3\tilde{g}_3 + \hat{p}_3\tilde{p}_3\hat{g}_1\tilde{g}_1 + \hat{p}_1\tilde{p}_3\hat{g}_3\tilde{g}_1 + \hat{p}_3\tilde{p}_1\hat{g}_1\tilde{g}_3, -\hat{g}_i\tilde{g}_i). \end{aligned} \quad (4.18)$$

In the inversion program, there is a choice of inverting only a single component or both the vertical and horizontal components simultaneously. All the data (all the shot gathers) are inverted simultaneously. The data vector  $\mathbf{u}$  is stored

as follows:

$$\mathbf{u} = \begin{bmatrix} \Re U_V^{sr}(\omega_0) \\ \Im U_V^{sr}(\omega_0) \\ \Re U_V^{sr}(\omega_1) \\ \Im U_V^{sr}(\omega_1) \\ \vdots \\ \Re U_V^{sr}(\omega_n) \\ \Im U_V^{sr}(\omega_n) \\ \Re U_V^{s(r+1)}(\omega_0) \\ \Im U_V^{s(r+1)}(\omega_0) \\ \vdots \\ \Re U_V^{sr_n}(\omega_n) \\ \Im U_V^{sr_n}(\omega_n) \\ \vdots \\ \Re U_V^{s_n r_n}(\omega_n) \\ \Im U_V^{s_n r_n}(\omega_n) \\ \Re U_H^{sr}(\omega_0) \\ \Im U_H^{sr}(\omega_0) \\ \vdots \\ \Re U_H^{s_n r_n}(\omega_n) \\ \Im U_H^{s_n r_n}(\omega_n) \end{bmatrix}, \quad (4.19)$$

where  $\Re$  and  $\Im$  represent the real and the imaginary parts of data element  $U$ , respectively. Subscripts  $V$  and  $H$  represent the vertical and horizontal components of the seismic data, respectively. Superscripts  $s$  and  $r$  are the indices for the sources and the receivers, respectively.  $r_n$  is the total number of receivers in each shot gather and  $s_n$  is the total number of shots. Total number of frequency samples used for the inversion depends on the source wavelet. In section 4.3.3, I show that only a limited number of frequency samples are sufficient to obtain satisfactory inversion results.

If there are  $n$  scatterers in the region of interest, the model vector is

given as

$$\mathbf{m} = [\Delta_N^1, \Delta_T^1, \Delta_N^2, \Delta_T^2, \dots, \Delta_N^i, \Delta_T^i, \dots, \Delta_N^{n-1}, \Delta_T^{n-1}, \Delta_N^n, \Delta_T^n]^T. \quad (4.20)$$

Notice that the total number of parameters that needs to be inverted is  $2n$ .

The matrix  $\mathbf{G}$  (equation 4.11) is arranged as

$$\mathbf{G} = [\mathbf{G}_1^1, \mathbf{G}_2^1, \mathbf{G}_1^2, \mathbf{G}_2^2 \dots \mathbf{G}_1^i, \mathbf{G}_2^i \dots \mathbf{G}_1^{n-1}, \mathbf{G}_2^{n-1}, \mathbf{G}_1^n, \mathbf{G}_2^n]. \quad (4.21)$$

$\mathbf{G}_1^i$  and  $\mathbf{G}_2^i$  are computed using equations 4.10, 4.14 and 4.16. Following is the flow diagram to compute  $\mathbf{G}_1^i$  and  $\mathbf{G}_2^i$  when a vertical force is used as the source:

- Loop over all the shots
  1. Calculate  $\tilde{p}_i$  and  $\tilde{g}_i$ .
  2. Calculate  $\tilde{A}$  and  $\tilde{\tau}$  for all incident wave types ( $\tilde{A}_P, \tilde{A}_S, \tilde{\tau}_P, \tilde{\tau}_S$ ).
- Loop over all the receivers
  - i. Calculate all  $\hat{p}_i$  and  $\hat{g}_i$ .
  - ii. Calculate all  $\hat{A}$  and  $\hat{\tau}$ .
  - iii. Calculate Vector  $\mathbf{h}$  (using equation 4.18) for all the scattered wave types ( $\mathbf{h}_{PP}, \mathbf{h}_{PS}, \mathbf{h}_{SS}, \mathbf{h}_{SP}$ ).
  - iv. Compute a temporary variable  $\mathbf{temp}_{PP}$  as  $\tilde{A}_P \hat{A}_P \tilde{g}_3(\mathbf{s}) \mathbf{h}_{PP} * \mathbf{L}^q$ . Similarly, compute  $\mathbf{temp}_{PS}$ ,  $\mathbf{temp}_{SS}$ , and  $\mathbf{temp}_{SP}$ . All these variables have a dimension of  $2 \times 1$ .

- v. Compute the quantity  $\mathbf{V}\mathbf{V}_{PP}$  ( $VV$  stands for vertical force as source and vertical receivers) as  $\mathbf{V}\mathbf{V}_{PP} = \mathbf{temp}_{PP}\hat{g}_3(\mathbf{r})$ . Similarly, compute  $\mathbf{V}\mathbf{V}_{PS}$ ,  $\mathbf{V}\mathbf{V}_{SS}$ , and  $\mathbf{V}\mathbf{V}_{SP}$ . If the horizontal component data are also being used for the inversion, compute  $\mathbf{V}\mathbf{H}_{PP}$ ,  $\mathbf{V}\mathbf{H}_{PS}$ ,  $\mathbf{V}\mathbf{H}_{SS}$ , and  $\mathbf{V}\mathbf{H}_{SP}$  ( $V$  stands for a vertical force as the source and  $H$  stands for the horizontal receivers). For example,  $\mathbf{V}\mathbf{H}_{PP}$  can be computed as  $\mathbf{V}\mathbf{H}_{PP} = \mathbf{temp}_{PP}\hat{g}_1(\mathbf{r})$ .
- \* Loop over all the frequencies
  - a. Compute the quantity  $\mathbf{C}\mathbf{V}\mathbf{V}_{PP}$  as  $\mathbf{C}\mathbf{V}\mathbf{V}_{PP} = \mathbf{V}\mathbf{V}_{PP}e^{i\omega(\hat{\tau}_P+\hat{\tau}_P)}$ . Similarly, compute  $\mathbf{C}\mathbf{V}\mathbf{V}_{PS}$ ,  $\mathbf{C}\mathbf{V}\mathbf{V}_{SS}$ ,  $\mathbf{C}\mathbf{V}\mathbf{V}_{SP}$ , and add them all together to get  $\mathbf{C}\mathbf{V}\mathbf{V}$ . Likewise,  $\mathbf{C}\mathbf{V}\mathbf{H}$  can be calculated for the horizontal component.
  - b. Store the first and second columns of  $\mathbf{C}\mathbf{V}\mathbf{V}$  and  $\mathbf{C}\mathbf{V}\mathbf{H}$  in the column vectors  $\mathbf{G}_1$  and  $\mathbf{G}_2$ , respectively.
- \* End loop over frequency
- End loop over receiver
- End loop over shots

#### 4.3.1 Applied constraint

Inversion of elastic parameters using seismic data is known to yield nonunique solutions. To reduce nonuniqueness in the solutions, a suitable regularization or constraint is applied to the model vector or error function while

performing the inversion. The most popular way to introduce a constraint in the inversion is to define  $f(\mathbf{m})$  in equation 4.12 appropriately. A common way to define  $f(\mathbf{m})$  is as  $f(\mathbf{m}) = [\mathbf{m} - \mathbf{m}_{pr}]^T \mathbf{W}_m [\mathbf{m} - \mathbf{m}_{pr}]$ , where the prior model vector  $\mathbf{m}_{pr}$  and weighting matrix  $\mathbf{W}_m$  are chosen according to the inversion problem and the type of constraint one wants to put in the inversion (e.g., Menke, 1984, p. 53). For example, if one wants the inverted model vector to be close to an a priori model vector  $\mathbf{m}_{pr}$ ,  $\mathbf{W}_m$  needs to be defined as the Identity matrix. Similarly, other types of constraints such as the smoothness or flatness of model vectors can also be easily introduced in the inversion.

Another way to introduce constraint or bias in the inversion is through preconditioned gradient methods. These methods are applicable only when a gradient-based inversion scheme is used (e.g., conjugate gradient, Gauss-Newton). In these techniques, the gradient of the error function is multiplied with a suitable numerical value  $\chi$  at each iteration, which forces the convergence in a particular direction (e.g., Tarantola, 2005, p. 78).  $\chi$  is determined by trial and error and can be fixed for an entire inversion or can be updated at each iteration. These methods have been successfully applied to many geophysical inverse problems (Tarantola, 2005, p. 203–223).

Finally, there are schemes where the function  $f(\mathbf{m})$  in equation 4.12 is defined as an analytical function to introduce constraint or bias. The main criterion for defining  $f(\mathbf{m})$  is that there must exist an analytical expression for the slope of  $f(\mathbf{m})$ . In the gradient-based schemes, the slope of the error or objective function needs to be calculated at each iteration. In the absence



of an analytical expression for the slope of  $f(\mathbf{m})$ , the slope of  $f(\mathbf{m})$  needs to be calculated by finite-difference which will likely introduce additional error in the inversion as well as additional computation time.

While testing my inversion algorithm with various types of models, I noticed that the inverted model parameters  $\Delta_N$  and  $\Delta_T$  were negative at various locations which is not physically possible. I needed to introduce a type of constraint in the inversion which would impose a very high penalty (or yield a very large error) on the error as defined in equation 4.12 when model parameters  $\Delta_N$  and  $\Delta_T$  become negative. Furthermore, I also needed to make sure that there was no or very little penalty on the error when model parameters  $\Delta_N$  and  $\Delta_T$  were greater than or equal to zero. Logarithmic barrier function (e.g., Farguharson et al., 2003) is widely used to impose various types of constraint on the model parameters. However, I could not use it in my inversion algorithm because the log function is not defined for negative arguments. I found that the following expression for  $f(\mathbf{m})$  to be suitable to constrain the inverted model parameters:

$$f(\mathbf{m}) = \sum_{i=1}^n (1 - m_i)^4 e^{-m_i}. \quad (4.22)$$

A suitable value of multiplier  $\epsilon$  (equation 4.12) is chosen by trial and error. I call  $f(\mathbf{m})$  the positivity constraint. Figure 4.1(a) shows the plot of  $f(\mathbf{m})$  with  $\mathbf{m}$ . Only one model parameter  $m$  was used to plot  $f(m)$ . Notice that as  $m$  goes below zero,  $f(m)$  increases sharply, and as  $m$  goes above zero,  $f(m)$  decreases rapidly. There exists an analytical form for the derivative of  $f(\mathbf{m})$

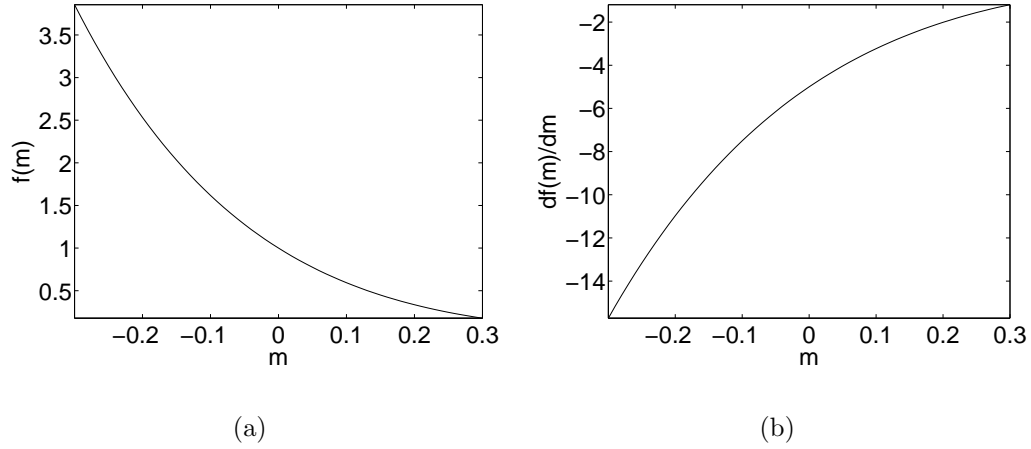


Figure 4.1: (a) Plot of  $f(m)$  against  $m$ : Notice that as the  $m$  goes below zero,  $f(m)$  increases rapidly. (b) Plot of  $df(m)/dm$  against  $m$ : As  $m$  goes below zero, the absolute value of  $df(m)/dm$  increases rapidly which indicates that  $f(m)$  is increasing sharply as  $m$  turns more negative.

that is given by

$$\frac{df(\mathbf{m})}{d\mathbf{m}} = \sum_{i=1}^n -e^{-m_i}(1 - m_i)^3(5 - m_i). \quad (4.23)$$

Figure 4.1(b) illustrates the slope  $df(m)/dm$  of  $f(m)$  for one model parameter  $m$ . Notice the large absolute value of  $df(m)/dm$  when  $m$  is less than zero, which suggests that  $f(m)$  is rapidly increasing when  $m$  is less than zero.

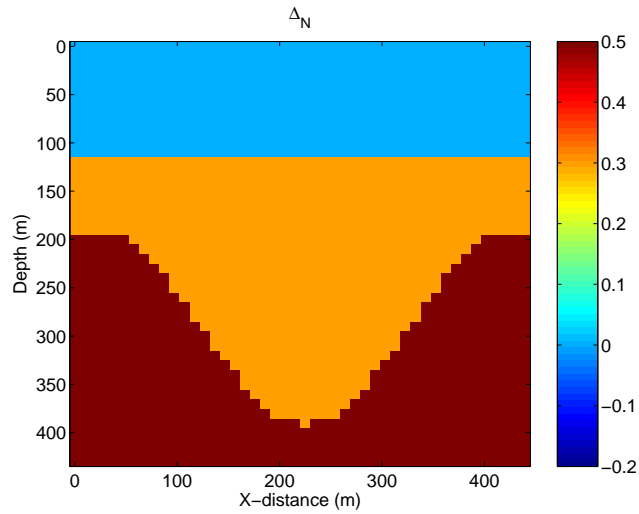
The following example exhibits the importance of the application of the constraint function explained above. Figures 4.2(a) and 4.2(b) show the input model parameters  $\Delta_N$  and  $\Delta_T$ , respectively. Notice the syncline in the model; an AVOA scheme will fail to invert the fracture parameters here. The top layer does not have any fractures, and hence,  $\Delta_N = 0$  and  $\Delta_T = 0$  for it. The middle and the bottom layers have one set of vertical fractures oriented normal

to the  $x$ -direction. The  $\Delta_N$  and  $\Delta_T$  values in the middle layer are 0.3 and 0.1, respectively, while those in the bottom layer are 0.5 and 0.2, respectively. The background medium is kept isotropic and homogeneous. Background P- and S-wave velocities are 3700 m/s and 2300 m/s. There are 46 receivers to collect the data placed at intervals of 10 m. Three sources are used—placed at the  $x$ -locations of 130 m, 230 m and 330 m. The source type is a vertical force. Notice that the receivers are not moved when the source location is changed. Both the vertical and horizontal components of the seismic data are used in the inversion. Input seismic data for the inversion is generated by the ray-Born modeling (using equation 4.10). All the possible modes (PP, PS, SS, SP) were incorporated in the modelled data. Figure 4.3 shows the vertical and horizontal component of the data for a shot located at the  $x$ -location of 230 m. A 40 Hz Ricker wavelet is used as the source pulse. 512 time samples with 2 ms interval were used for the inversion. All the frequencies up to the Nyquist were employed in the inversion (i.e., 256 frequency samples were used). The total scatterers inverted for in the  $x$ - and  $z$ -directions are 46 and 36, respectively. Hence, the total number of model parameters inverted for is  $2 \times 46 \times 36 = 3312$ . 1000 iterations were performed on the inversion before it was stopped; the final error was less than 0.1% of the original error. Figure 4.4 shows the inverted  $\Delta_N$  and  $\Delta_T$  without the positivity constraint  $f(\mathbf{m})$ . Notice that even though the subsurface structure has been recovered by the inversion, at many locations  $\Delta_N$  and  $\Delta_T$  are less than zero or far from the actual value. Next, the inversion was performed using the constraint function  $f(\mathbf{m})$  defined in equation 4.22.

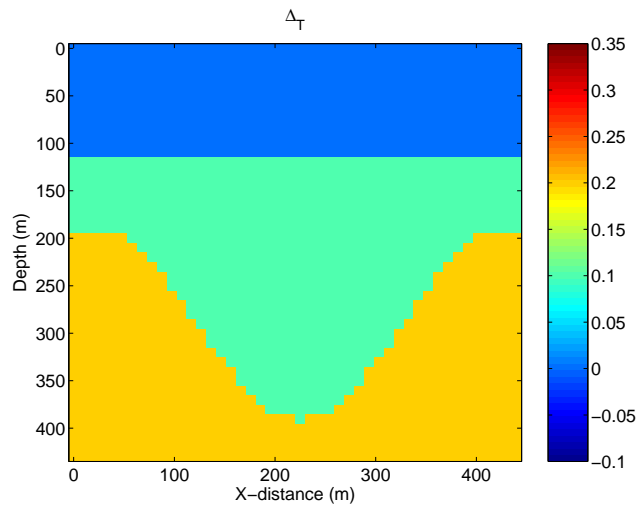
By trial and error, I found the suitable values of multiplier  $\epsilon$  to be 0.007 and 0.002 for  $\Delta_N$  and  $\Delta_T$ , respectively. Again, 1000 iterations were performed before the inversion was stopped. The final error was less than 0.1% of the initial error. Figure 4.5 displays the inverted model parameters. Notice that the inversion results have improved;  $\Delta_N$  and  $\Delta_T$  values at all the locations are positive or zero. Moreover, the values of the inverted model parameters are closer to the original model parameters.

However, we do not always need to use the positivity constraint for a good inversion result. To demonstrate this point, I implemented my inversion algorithm on a flat-layered model with laterally varying fracture parameters. Figure 4.6 illustrates the subsurface model. The top layer does not have any fractures ( $\Delta_N = 0$ ,  $\Delta_T = 0$ ). The middle layer has one set of vertical fractures oriented normal to the  $x$ -direction. Fracture parameters  $\Delta_N$  and  $\Delta_T$  are smoothly increasing from the left of the model to the right of the model. The bottom layer has one set of vertical fractures oriented normal to the  $x$ -direction with constant fracture parameters ( $\Delta_N = 0.5$ ,  $\Delta_T = 0.2$ ). All the inversion parameters and the acquisition geometry were kept identical to those used in the previous model. A 15 Hz Ricker wavelet was used as the source pulse. Figure 4.7 shows the vertical and horizontal component of the data for a shot located at the  $x$ -location of 230 m. I did not apply the positivity constraint (i.e.,  $\epsilon = 0$  in equation 4.12) while performing the inversion. Figure 4.8 shows the inversion results. Notice that the inversion algorithm is yielding  $\Delta_N$  and  $\Delta_T$  that are very close to the original model parameters (figure 4.6). At very

few locations, we notice  $\Delta_N$  and  $\Delta_T$  are less than zero. Here, we can apply the positivity constraint while performing inversion to suppress negative values of  $\Delta_N$  and  $\Delta_T$ . However, it may lead to overestimation of  $\Delta_N$  and  $\Delta_T$  at other locations.



(a)



(b)

Figure 4.2: Input model parameters: (a)  $\Delta_N$  and (b)  $\Delta_T$ . Note that the first layer does not have any fractures, and hence  $\Delta_N = 0$  and  $\Delta_T = 0$ . The middle and bottom layers have one set of vertical fractures oriented normal to the  $x$ -direction.

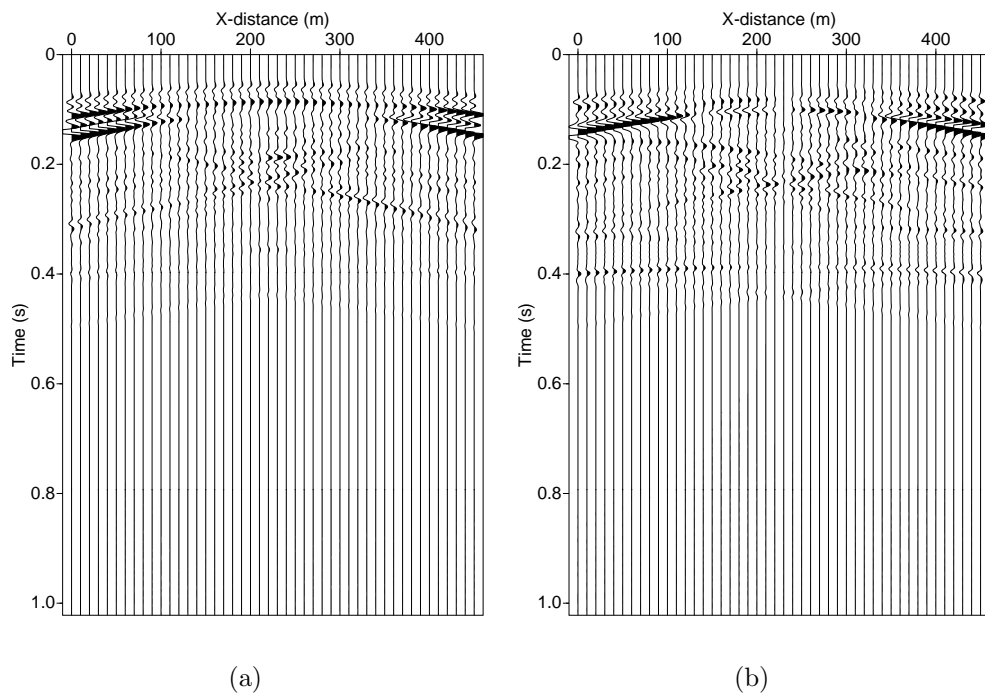
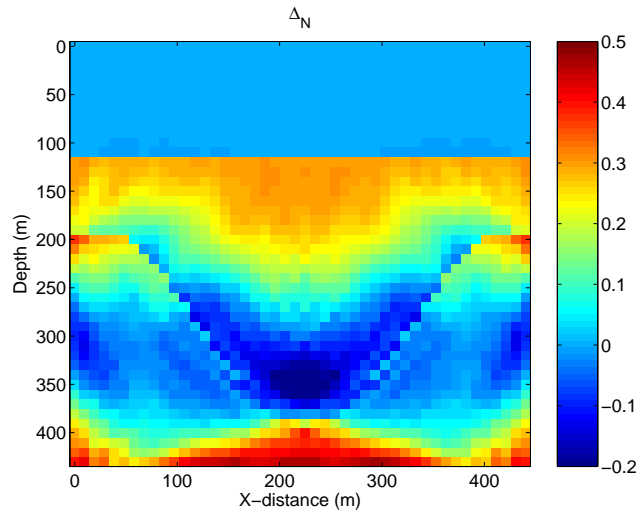
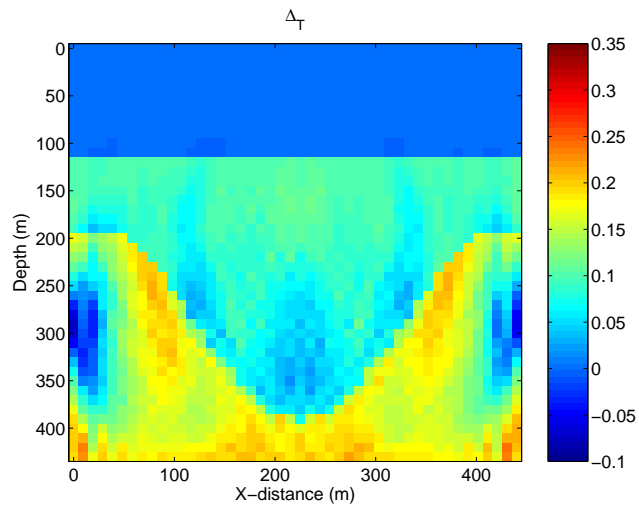


Figure 4.3: (a) Vertical and (b) horizontal components of the data (shot gather) for the model shown in figure 4.2. The shot is located at the  $x$ -location of 230 m. All the scattering modes (PP, PS, SS, SP) were incorporated in the modeling.



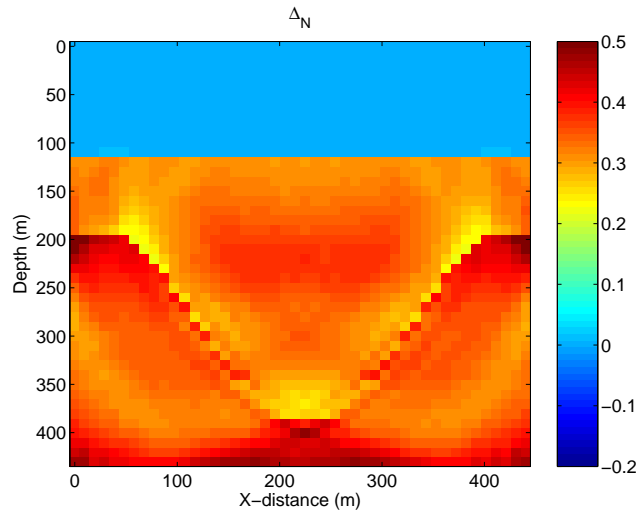
(a)



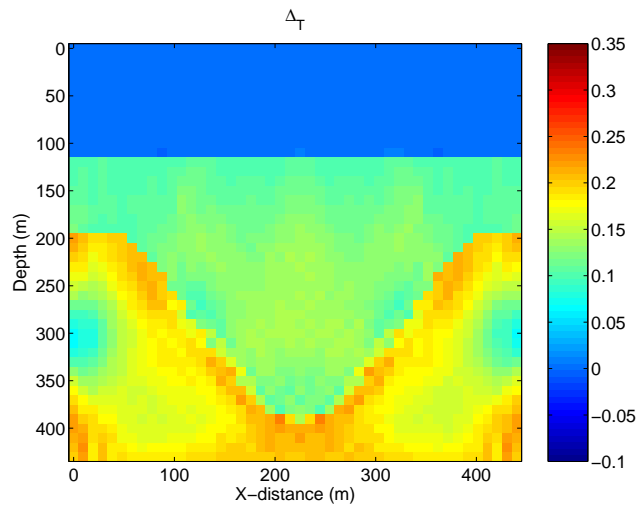
(b)

Figure 4.4: Inverted model parameters without using any constraints in the error function: (a)  $\Delta_N$  and (b)  $\Delta_T$ . Notice that at several locations  $\Delta_N$  and  $\Delta_T$  are less than zero which is not physically possible. Moreover, the inverted model values are not close to the input model values (figure 4.2).



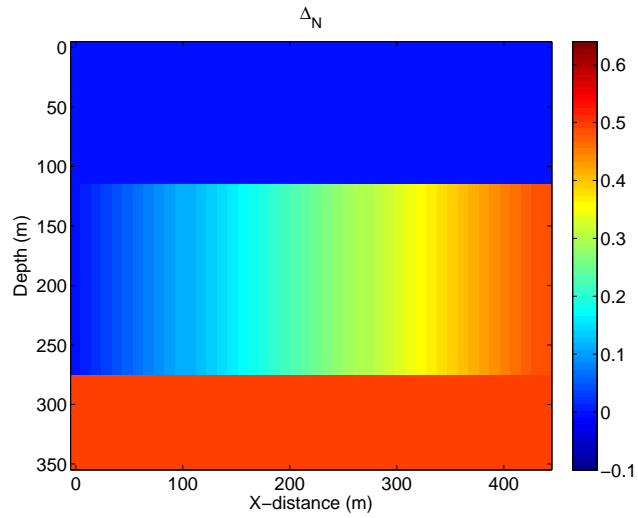


(a)

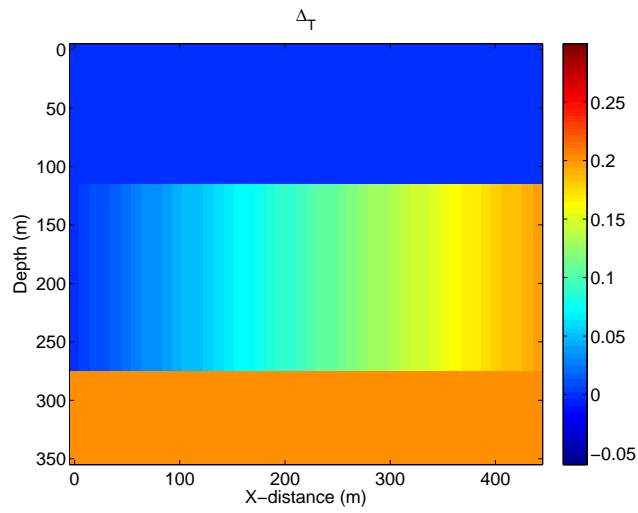


(b)

Figure 4.5: Inverted model parameters with constraint function  $f(\mathbf{m})$  (equation 4.22) added in the error function: (a)  $\Delta_N$  and (b)  $\Delta_T$ . Notice that  $\Delta_N$  and  $\Delta_T$  are no longer less than zero at any location. Moreover, the values of the inverted model parameters are closer to the values of the input model parameters (figure 4.2).



(a)



(b)

Figure 4.6: Subsurface model with laterally varying fracture parameters: (a)  $\Delta_N$  and (b)  $\Delta_T$ . The top layer does not have any fractures, the middle layer has one set of vertical fractures oriented normal to the  $x$ -direction with smoothly varying fracture parameters. The bottom layer also has one set of vertical fractures oriented normal to the  $x$ -direction with constant  $\Delta_N$  and  $\Delta_T$ .

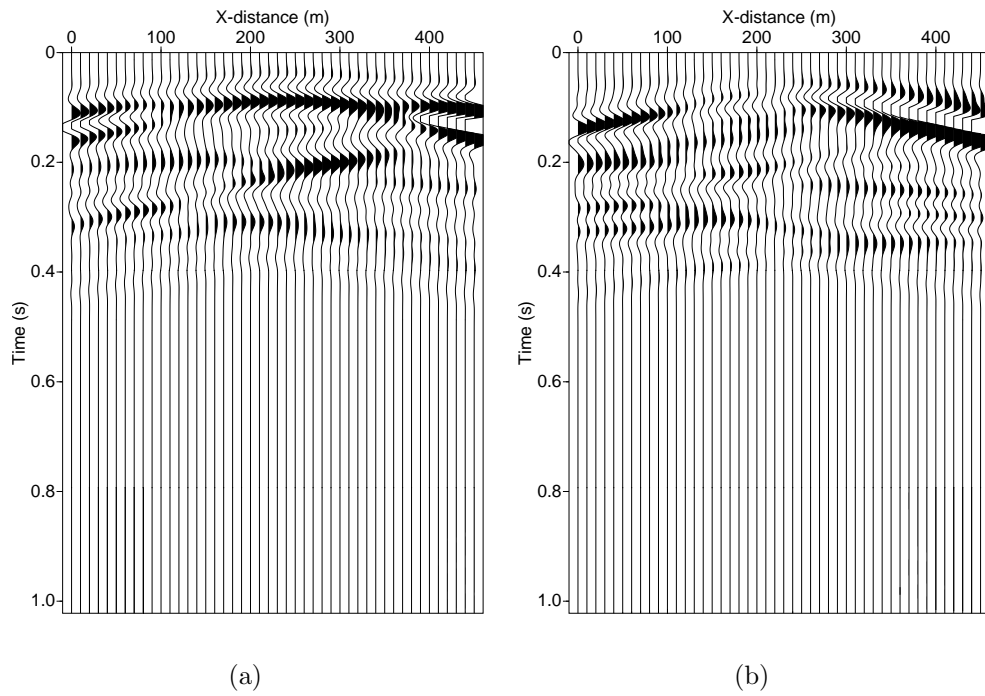
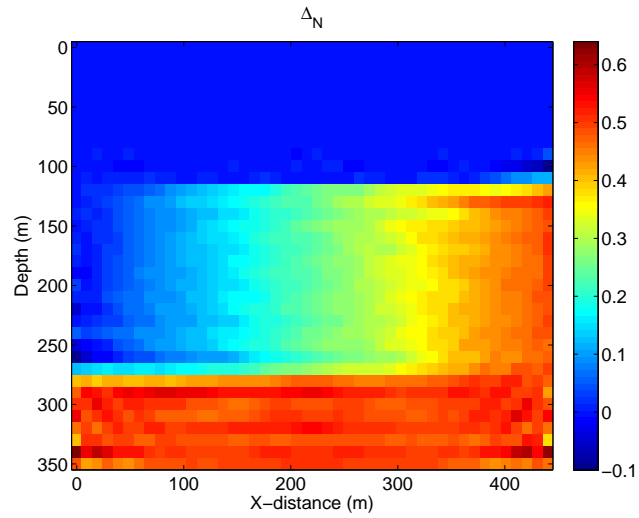
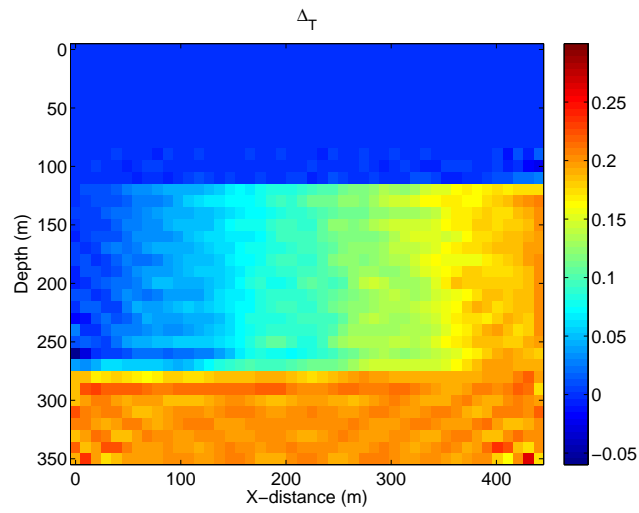


Figure 4.7: (a) Vertical and (b) horizontal components of the data (shot gather) for the model shown in figure 4.6. The shot is located at the  $x$ -location of 230 m. All the scattering modes (PP, PS, SS, SP) were incorporated in the modeling.



(a)



(b)

Figure 4.8: Inverted model parameters for the subsurface model displayed in figure 4.6: (a)  $\Delta_N$  and (b)  $\Delta_T$ . Notice that the inverted  $\Delta_N$  and  $\Delta_T$  values are very close to the original  $\Delta_N$  and  $\Delta_T$ . The constraint function was not used in the inversion.

### 4.3.2 Inversion using single component of seismic data

In most seismic experiments, only single component (mostly vertical) seismic data is collected. To check the feasibility of inverting the fracture parameters using only single component seismic data, I carried out some numerical tests. Figure 4.9 shows the inversion results when only vertical component data was inverted. Notice that the single component inversion results are inferior to the inversion results obtained from the simultaneous inversion of both components (figure 4.5). Figure 4.10 displays the inverted results when only the horizontal component data was used. Again, the inverted results are inferior.

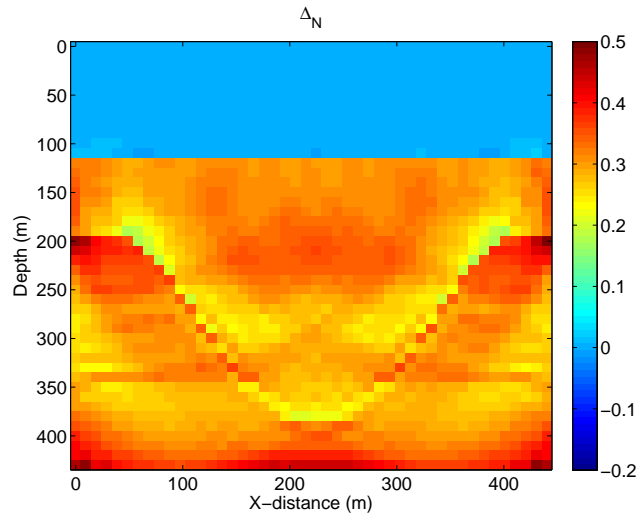
These observations can be explained by the analysis of covariances of the inverted solutions. The solution of an inverse problem is well determined if the estimated solution has small variance (Menke, 1984, p. 58). The covariance of a least squares solution  $\mathbf{m}$ , assuming uncorrelated data with equal variance  $\sigma_d^2$ , can be written as

$$[cov\mathbf{m}] = \sigma_d^2[\mathbf{G}^T\mathbf{G}]^{-1}. \quad (4.24)$$

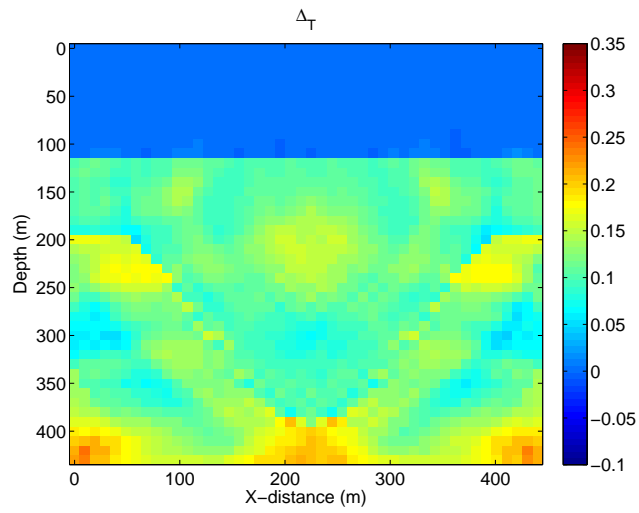
Figure 4.11 displays the diagonal elements of the covariance matrices of  $\Delta_N$  and  $\Delta_T$  in the region of interest when the vertical and horizontal components of data are inverted simultaneously. Figures 4.12 and 4.13 show the covariances when only the vertical and horizontal components of the data are separately inverted. Covariance matrices were determined by calculating matrix  $\mathbf{G}$  (using equation 4.21) for each case and then by multiplying it with its transpose. Variance  $\sigma_d^2$  in the data was calculated assuming a normal distribution. The

covariances of  $\Delta_N$  and  $\Delta_T$  are at minimum when both the components of data are inverted simultaneously. Also note that the covariances are the largest when only the vertical component of data is inverted. Hence, we should expect the least resolved  $\Delta_N$  and  $\Delta_T$  when only the vertical component data is inverted.

Figure 4.14 shows the inversion results for the subsurface model shown in figure 4.6; only the vertical component data was inverted. Figure 4.15 displays the inversion results when only the horizontal component data was inverted. Notice that, in both cases the inversion results have deteriorated compared to the inversion results obtained by inverting both of the components of the data simultaneously (figure 4.8).

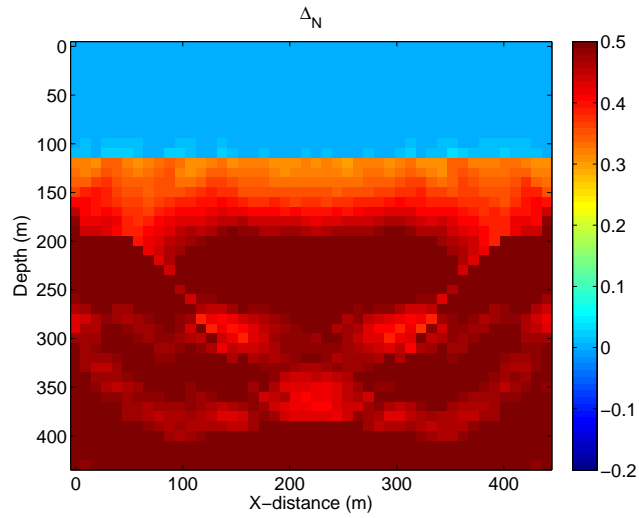


(a)

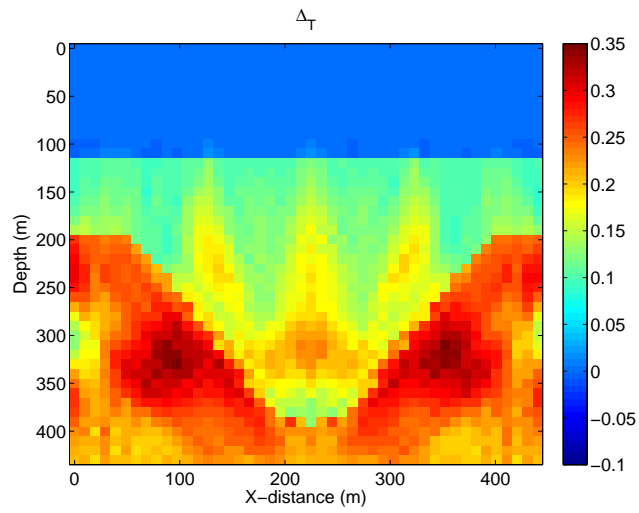


(b)

Figure 4.9: Inverted model parameters (a)  $\Delta_N$  and (b)  $\Delta_T$  using only vertical component seismic data: Note that the inversion results have deteriorated compared to the inversion results when both of the components of the data are inverted simultaneously (figure 4.5). However, the syncline layer has been imaged in both the sections.



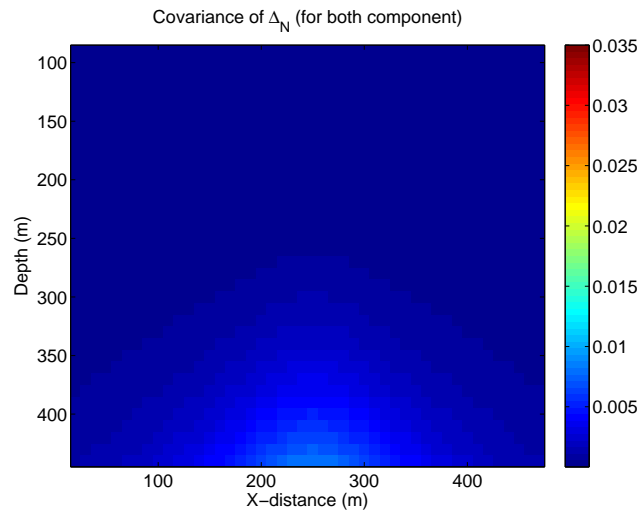
(a)



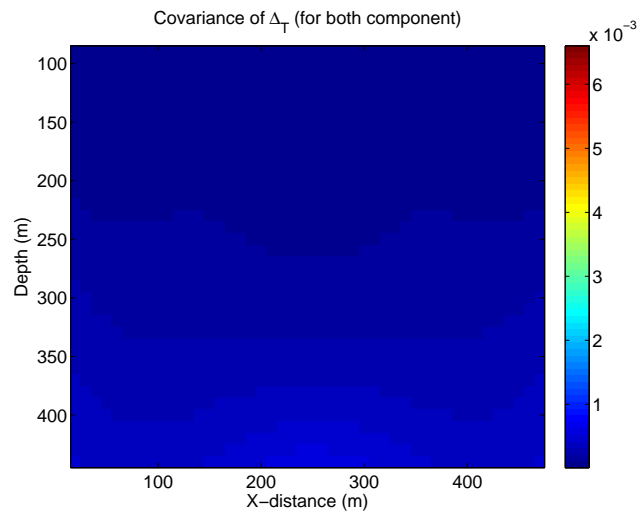
(b)

Figure 4.10: Inverted model parameters (a)  $\Delta_N$  and (b)  $\Delta_T$  using only horizontal component seismic data: Notice that the inversion results have deteriorated compared to the inversion results when both of the components of the data are inverted (figure 4.5); the values of  $\Delta_N$  and  $\Delta_T$  have been overestimated in second layer.



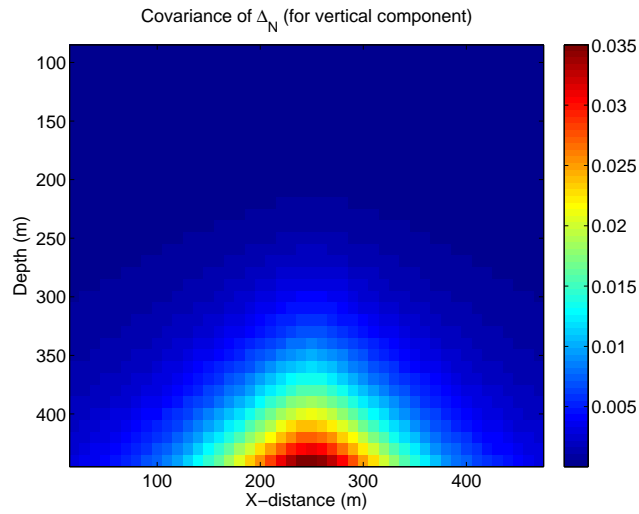


(a)

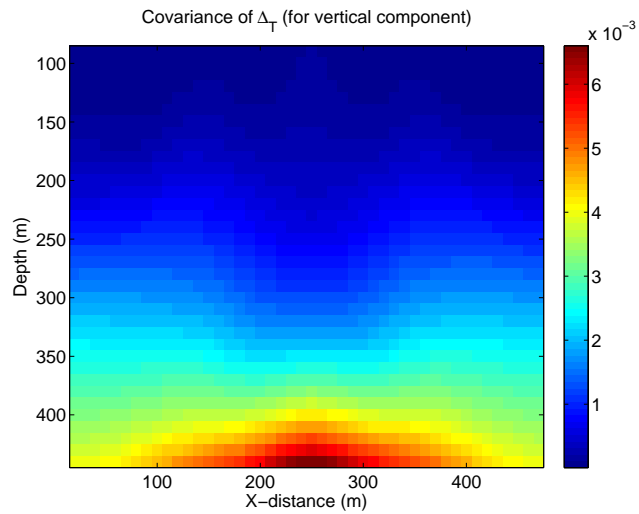


(b)

Figure 4.11: Diagonal elements of the covariance matrices of  $\Delta_N$  and  $\Delta_T$  in the region of interest when the vertical and horizontal components of the data are inverted simultaneously.

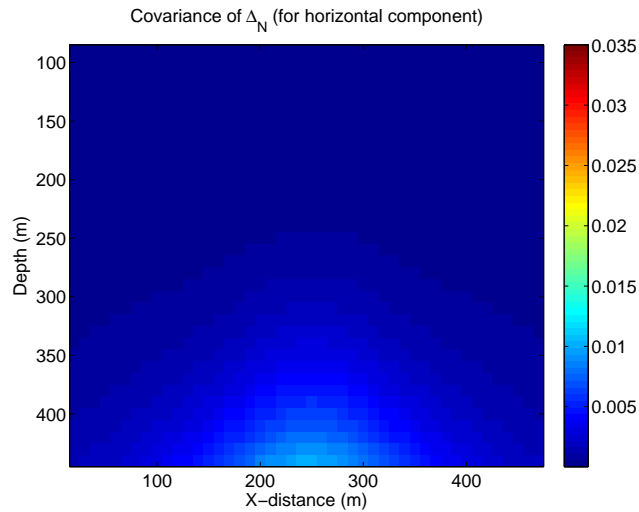


(a)

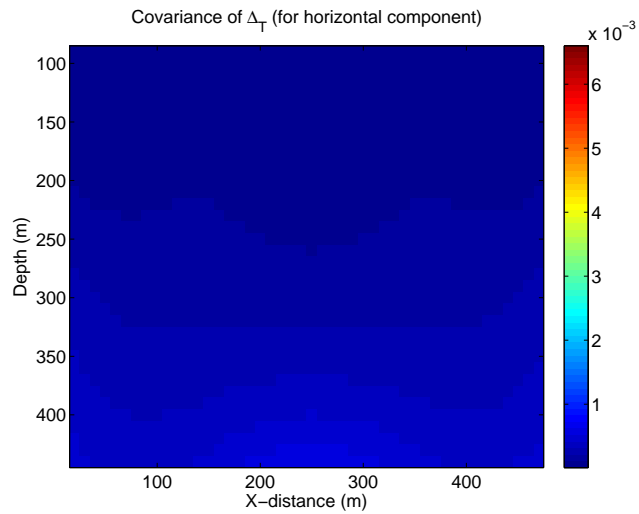


(b)

Figure 4.12: Diagonal elements of the covariance matrices of  $\Delta_N$  and  $\Delta_T$  in the region of interest when only the vertical component data is inverted. The covariances have increased many fold compared to the case when both of the components of the data are inverted simultaneously.

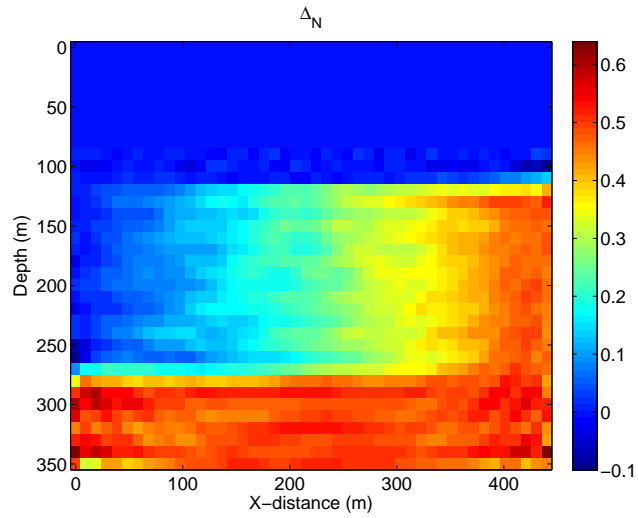


(a)

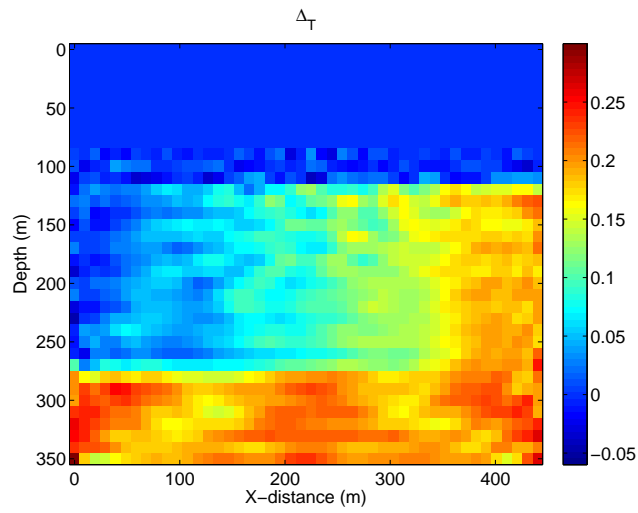


(b)

Figure 4.13: Diagonal elements of the covariance matrices of  $\Delta_N$  and  $\Delta_T$  in the region of interest when only the horizontal component data is inverted. The covariances are larger compared to the case when both of the components are inverted simultaneously. However, the covariances are smaller than those from the case in which only the vertical component is inverted.

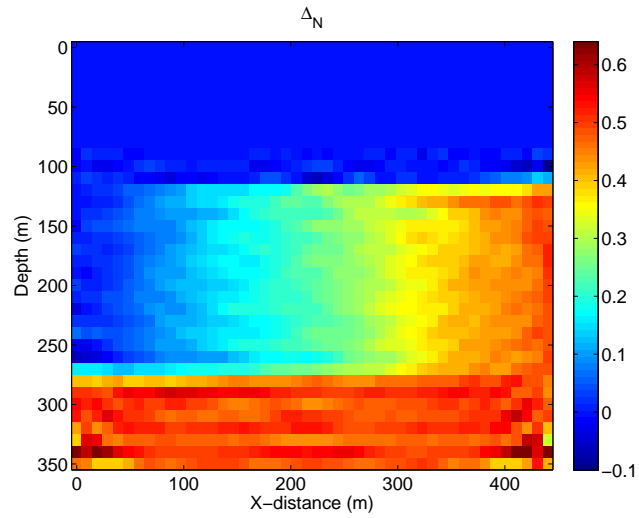


(a)

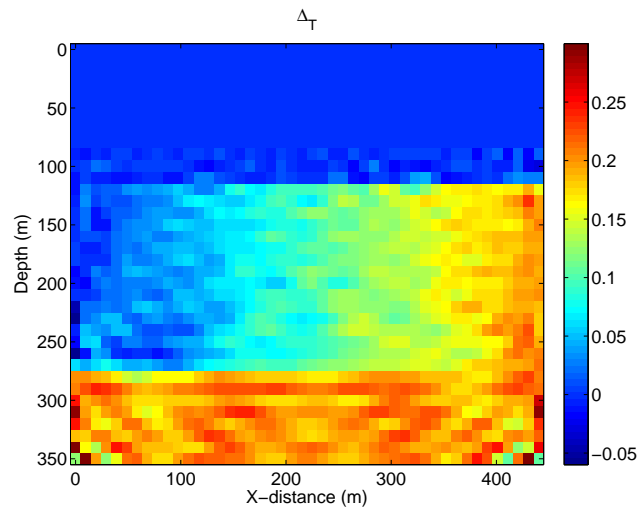


(b)

Figure 4.14: Inverted model parameters (a)  $\Delta_N$  and (b)  $\Delta_T$  using only the vertical component data for the subsurface model shown in figure 4.6. The inverted values are slightly deteriorated when compared to those values inverted from both of the components of the data simultaneously.



(a)



(b)

Figure 4.15: Inverted model parameters (a)  $\Delta_N$  and (b)  $\Delta_T$  using only horizontal component data for the subsurface model shown in figure 4.6. The inverted values are slightly deteriorated when compared to those values inverted from both of the components of the data simultaneously.

### 4.3.3 Sensitivity of the inversion to the frequency content in the data

I implemented the ray-Born inversion scheme in the frequency domain. This gives us the flexibility of choosing only a limited number of frequencies for the inversion. An inversion scheme implemented in the frequency-domain is similar to the time-domain inversion if all of the frequencies are inverted simultaneously (Pratt et al., 1998). In the past, a number of researchers have demonstrated that reasonable inversion results can be obtained by using a small number of frequencies. Pratt (1988) and Lo et al. (1988) used single-frequency data to obtain seismic images through diffraction tomography. Pratt and Worthington (1990) developed a non-linear inversion scheme to derive seismic images using single-frequency wide-aperture cross-hole data. Liao and McMechan (1996) studied multi-frequency viscoacoustic modeling and inversion and demonstrated that a limited number of frequency samples can be used to invert for the quality factor  $Q$  and the seismic velocity. Pratt (1999) applied and evaluated a frequency-space domain approach to waveform inversion on a physical scale model.

The inversion results I have shown in the previous sections were inverted using all of the frequency samples up to the Nyquist. Using all of these frequency samples in the inversion requires a large amount of the memory (number of rows in matrix  $\mathbf{G}$  are directly proportional to the number of frequencies used in the inversion) and renders the inversion process very computationally expensive. To check the feasibility of inversion using only a

limited number of frequencies, I carried out a number of numerical tests each with a smaller number of frequency samples. The tests were performed on the subsurface model shown in figure 4.2. All of the inversion parameters, regularization coefficients and the acquisition geometry were kept identical to those which were used in the previous examples (section 4.3.1). A 40 Hz Ricker wavelet was used as the source pulse. Instead of using all of the frequency samples up to the Nyquist (250 Hz), I discarded all of the frequency samples beyond 130 Hz; i.e. the maximum value of frequencies used for the inversion was 130 Hz—amplitude spectrum of the 40 Hz Ricker wavelet is zero beyond 130 Hz (figure 4.16).

Figure 4.17 shows the inversion results when every other frequency sample up to 130 Hz was used in the inversion. The total number of frequency samples employed was only 67. Whereas, 256 frequency samples were used to obtain the results shown in figure 4.5. Notice that the results are comparable. Next, the inversion was performed using every third and fourth frequency sample up to 130 Hz; 45 and 34 frequency samples were used, respectively. Figures 4.18 and 4.19 show the inversion results. Notice that the inverted values are still very close to the results shown in figure 4.5.

I also inverted  $\Delta_N$  and  $\Delta_T$  using a 30 Hz Ricker wavelet as a source pulse. Of course, a lower frequency band would render the inversion results with a lower spatial resolution. Figure 4.20 shows the amplitude spectrum of a 30 Hz Ricker wavelet. Notice that beyond 96 Hz, the amplitude spectrum is zero. Hence, I discarded all of the frequency samples beyond 96 Hz. Figure 4.21

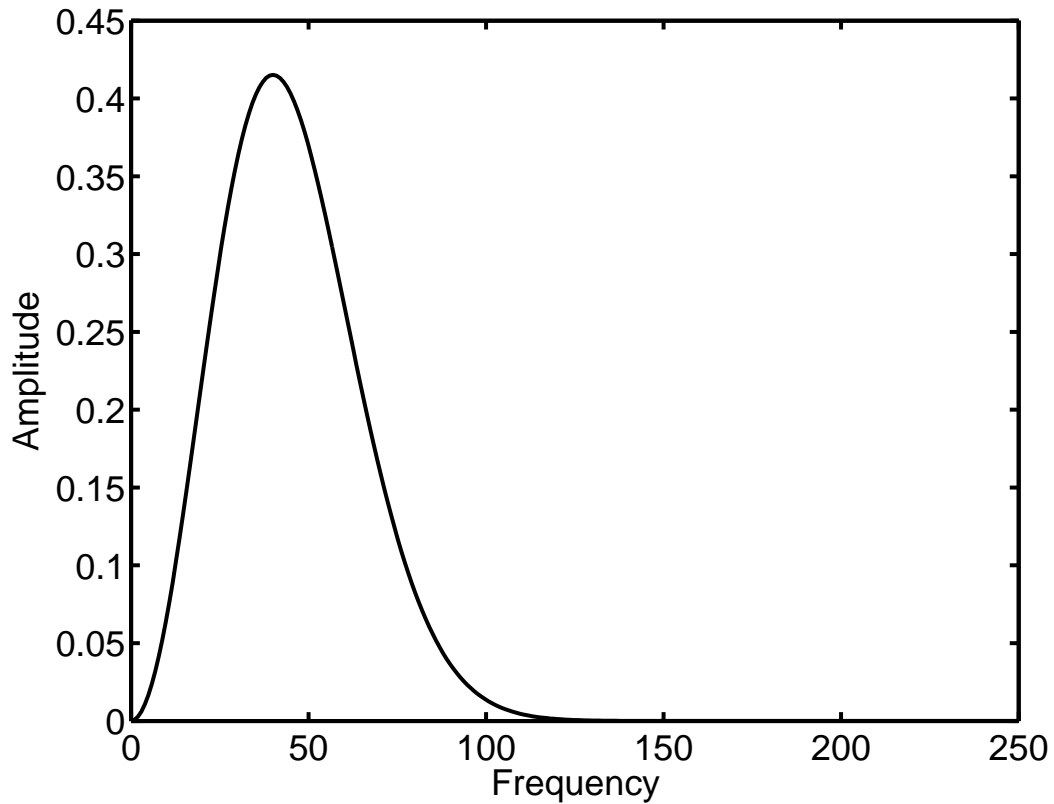
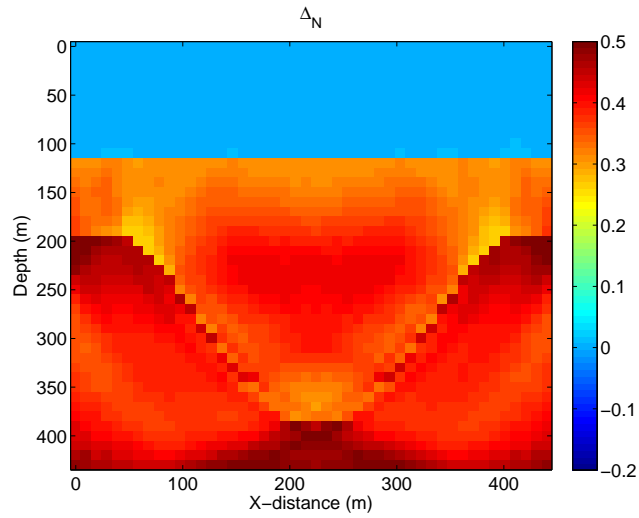


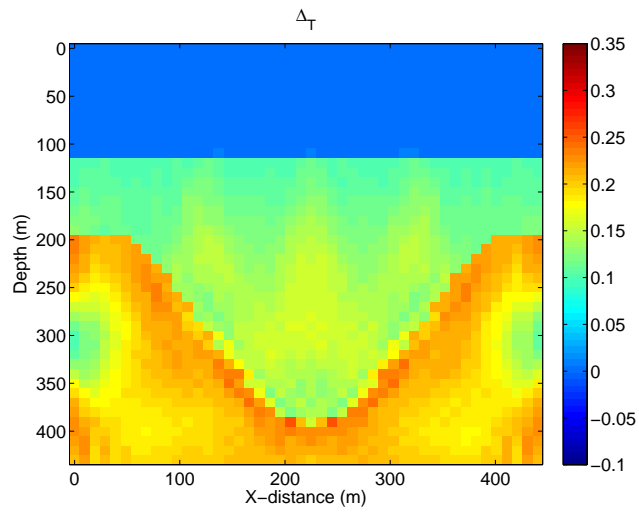
Figure 4.16: Amplitude spectrum of a 40 Hz Ricker wavelet: Notice that beyond 130 Hz, the amplitude spectrum is zero.

displays the inverted models when every frequency sample up to 96 Hz was used for the inversion. Notice that the spatial resolution of both  $\Delta_N$  and  $\Delta_T$  is reduced. Figure 4.22 shows the inverted models when every other frequency sample up to 96 Hz was used in the inversion. Notice that the spatial resolution is further reduced. Moreover,  $\Delta_N$  and  $\Delta_T$  values have been overestimated for the second layer. Figure 4.23 displays the inversion result when every third frequency sample was employed in the inversion; the results have deteriorated



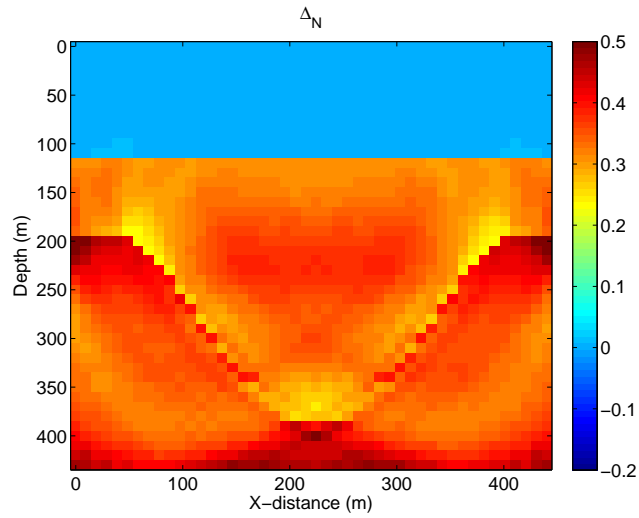


(a)

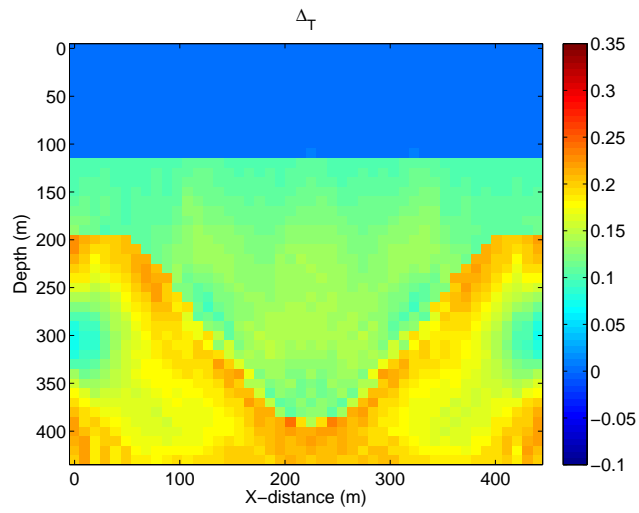


(b)

Figure 4.17: Inverted (a)  $\Delta_N$  and (b)  $\Delta_T$  using every other frequency sample up to 130 Hz: Source pulse is a 40 Hz Ricker wavelet. Notice that the results are very similar to the results shown in figure 4.5 which was generated using all of the frequency samples up to the Nyquist.

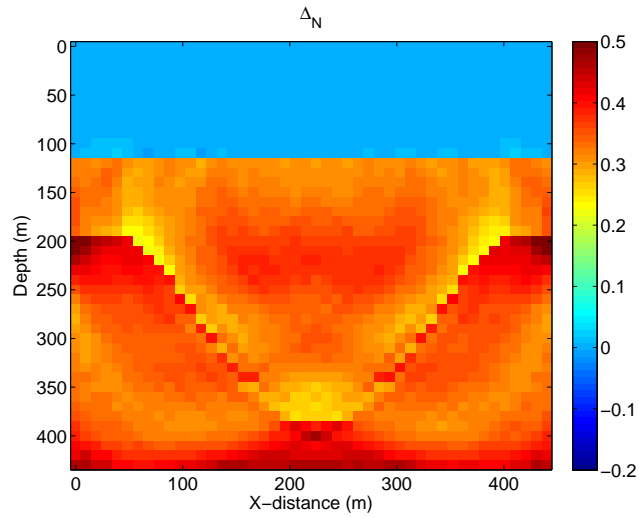


(a)

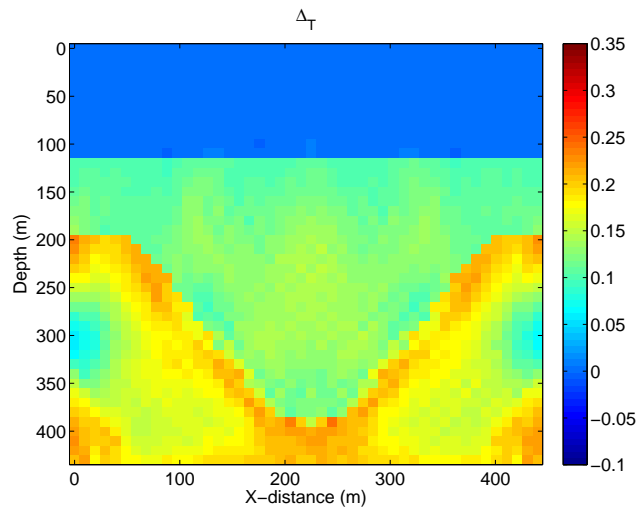


(b)

Figure 4.18: Inverted (a)  $\Delta_N$  and (b)  $\Delta_T$  using every third frequency sample up to 130 Hz: Source pulse is a 40 Hz Ricker wavelet. Notice that the results are very similar to the results shown in figure 4.5 which was generated using all of the frequency samples up to the Nyquist.



(a)



(b)

Figure 4.19: Inverted (a)  $\Delta_N$  and (b)  $\Delta_T$  using only every fourth frequency sample up to 130 Hz: Source wavelet is a 40 Hz Ricker wavelet. Notice that the inverted results have slightly deteriorated when compared to the results shown in figure 4.5.

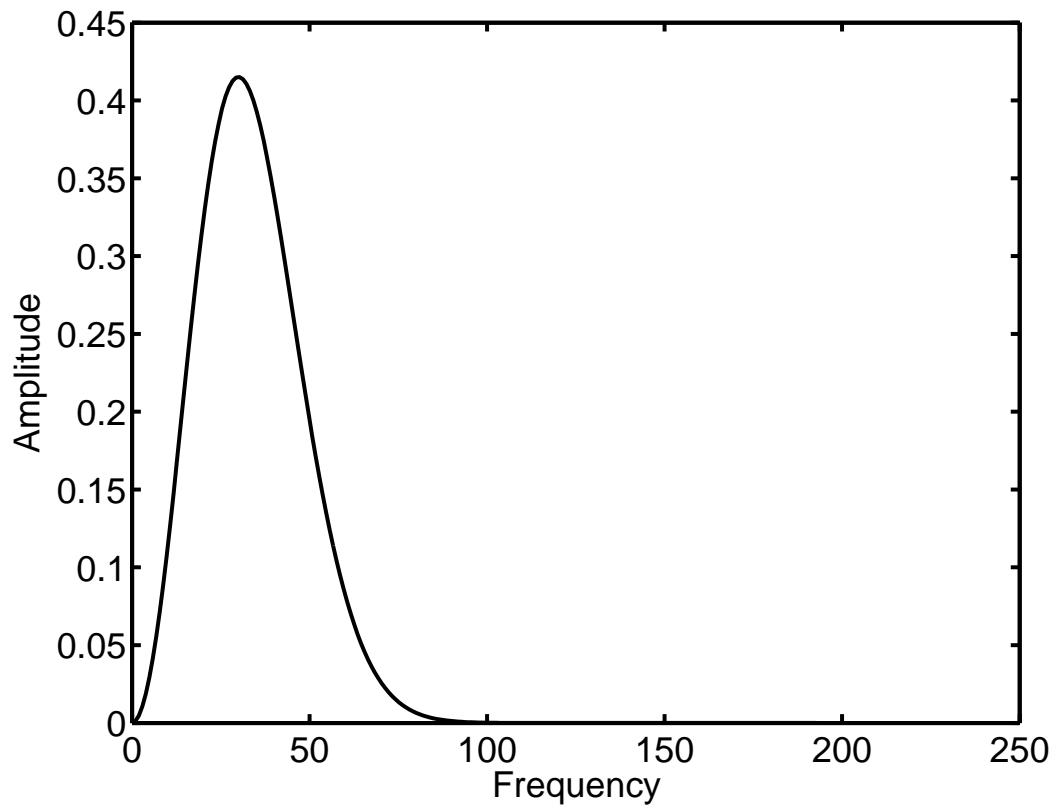
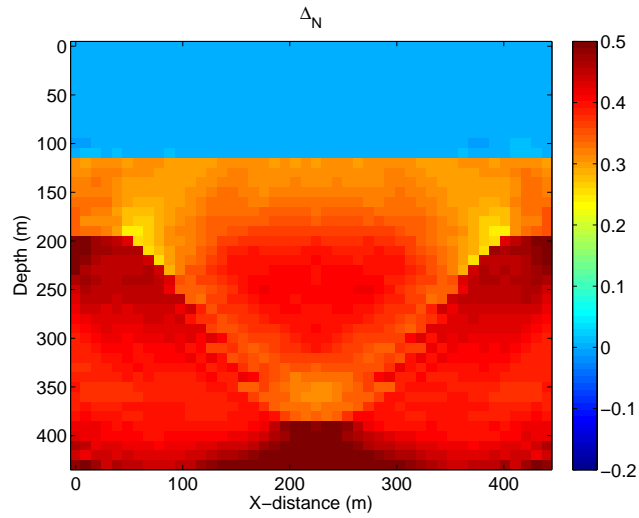
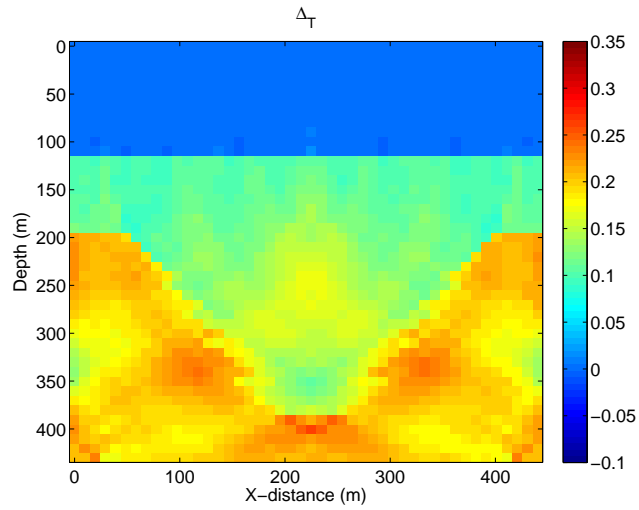


Figure 4.20: Amplitude spectrum of a 30 Hz Ricker wavelet: Notice that beyond 96 Hz, the amplitude spectrum is zero.

further when compared to the results shown in figure 4.21.

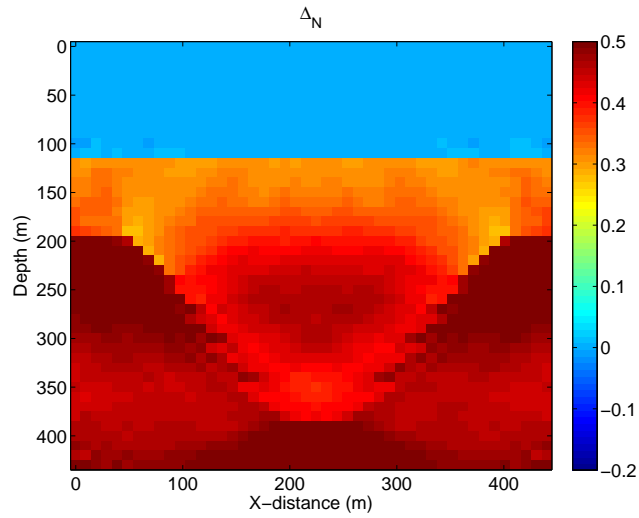


(a)

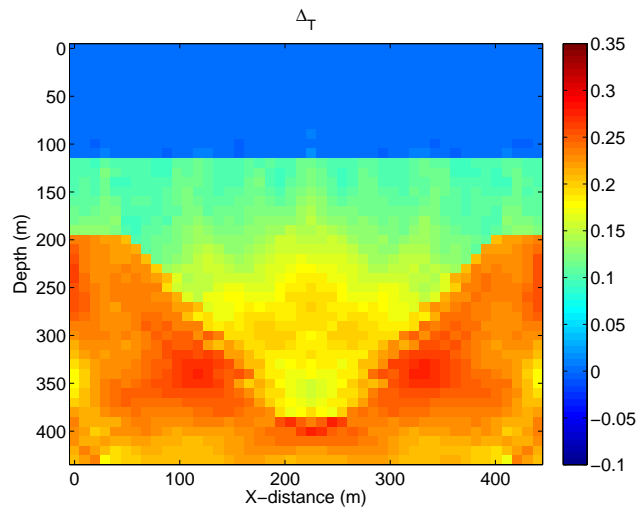


(b)

Figure 4.21: Inverted (a)  $\Delta_N$  and (b)  $\Delta_T$  using every frequency sample up to 96 Hz: Source pulse is a 30 Hz Ricker wavelet. Notice that the spatial resolution of the inverted models has gone down.

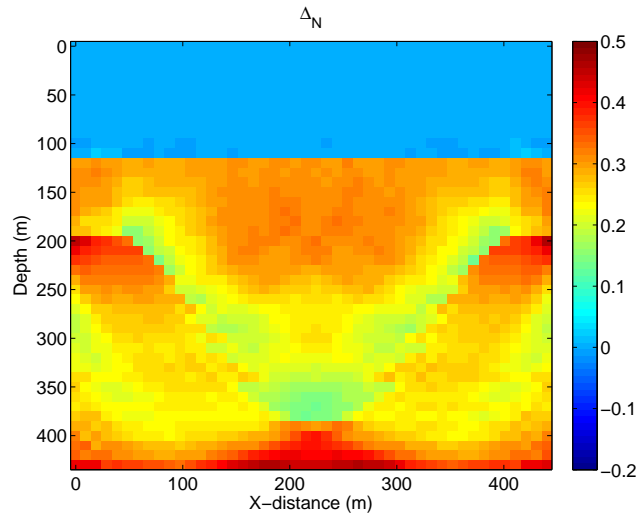


(a)

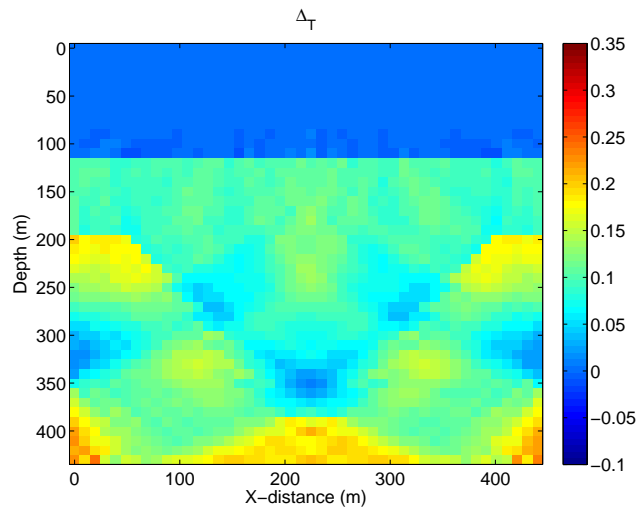


(b)

Figure 4.22: Inverted (a)  $\Delta_N$  and (b)  $\Delta_T$  using every other frequency sample up to 96 Hz: Source pulse is a 30 Hz Ricker wavelet. Notice that the spatial resolution has further gone down. Moreover,  $\Delta_N$  and  $\Delta_T$  values have been overestimated for the second layer.



(a)



(b)

Figure 4.23: Inverted (a)  $\Delta_N$  and (b)  $\Delta_T$  using every third frequency sample up to 96 Hz: Source pulse is a 30 Hz Ricker wavelet; the results have worsened when compared to the results shown in figure 4.21.

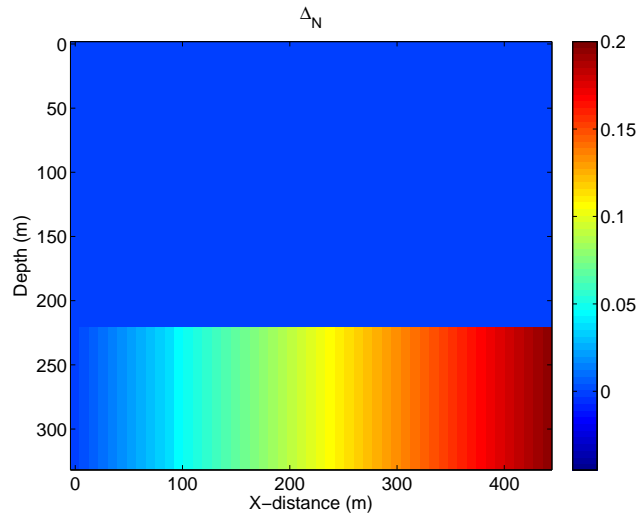
#### 4.3.4 Application of inversion on a finite-difference generated dataset

I implemented the ray-Born inversion on a dataset which was generated using the 3D finite-difference code written for arbitrary anisotropy (chapter 2). Figure 4.24 shows the subsurface model used for the experiment. The model has two flat layers. The top layer does not have any fractures; whereas, the bottom layer has one set of vertical fractures oriented normal to the  $x$ -direction with the fracture parameters smoothly increasing from the left of the model to the right of the model. The background properties of the model and the survey parameters are similar to those used in the first example in section 4.3.1. The source wavelet is a 15 Hz Ricker; a vertical force was used as the source. It must be mentioned here that the synthetic seismograms generated by my finite-difference code represent particle velocity instead of particle displacement (I implemented finite-difference algorithm using a velocity-stress formulation; see chapter 2). Hence, while performing the inversion, I multiplied the ray-Born data  $U_{mn}$  (equation 4.10), which represents particle displacement, by  $i\omega$  to convert to particle velocity. Figure 4.25 displays one of the shot gathers generated by the finite-difference code. Direct waves were muted out. For comparison, I also generated synthetic data using the ray-Born scheme before performing the inversion. Figure 4.26 shows a comparison between the finite-difference data and the ray-Born generated data at various offsets; there is a reasonable match. We cannot expect a perfect match because the first-order Born approximation generates the linearized reflection coefficients (Shaw and Sen, 2004) while the finite-difference algorithm generates the true reflection

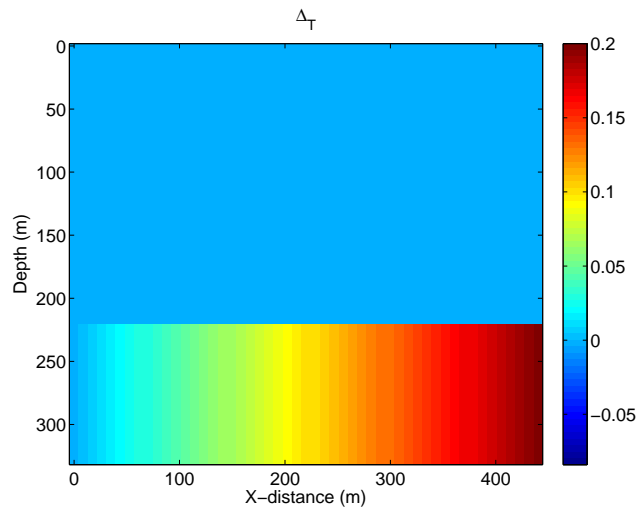


coefficients and includes multiple scattering.

Figure 4.27 shows the inversion results. The inversion has recovered the general trend of  $\Delta_N$  and  $\Delta_T$  of the original model. While performing the inversion, the positivity constraint was applied; I found the suitable value of multiplier  $\epsilon$  to be 0.15 for both  $\Delta_N$  and  $\Delta_T$ . At a few locations, the inversion has predicted negative values of  $\Delta_N$  and  $\Delta_T$ . A higher value for multiplier  $\epsilon$  will prevent the inversion from yielding negative  $\Delta_N$  and  $\Delta_T$  at these locations. However, it may cause an overestimation of  $\Delta_N$  and  $\Delta_T$  at other locations. I also applied second-order Tikhonov regularization (or flatness constraint; Menke, 1984, p. 53) in the  $z$ -direction to eliminate discontinuities from the solution. Every other frequency sample up to 70 Hz (15 Hz Ricker wavelet has zero amplitude beyond 70 Hz) was used in the inversion. 1000 iterations were performed on the inversion before it was stopped. The final error was about 10% of original error.



(a)



(b)

Figure 4.24: Subsurface model used to generate finite-difference data: (a)  $\Delta_N$  and (b)  $\Delta_T$ . The top layer does not have any fractures. The bottom layer has one set of vertical fractures oriented normal to the  $x$ -direction.  $\Delta_N$  and  $\Delta_T$  are smoothly increasing from the left to the right in the model.

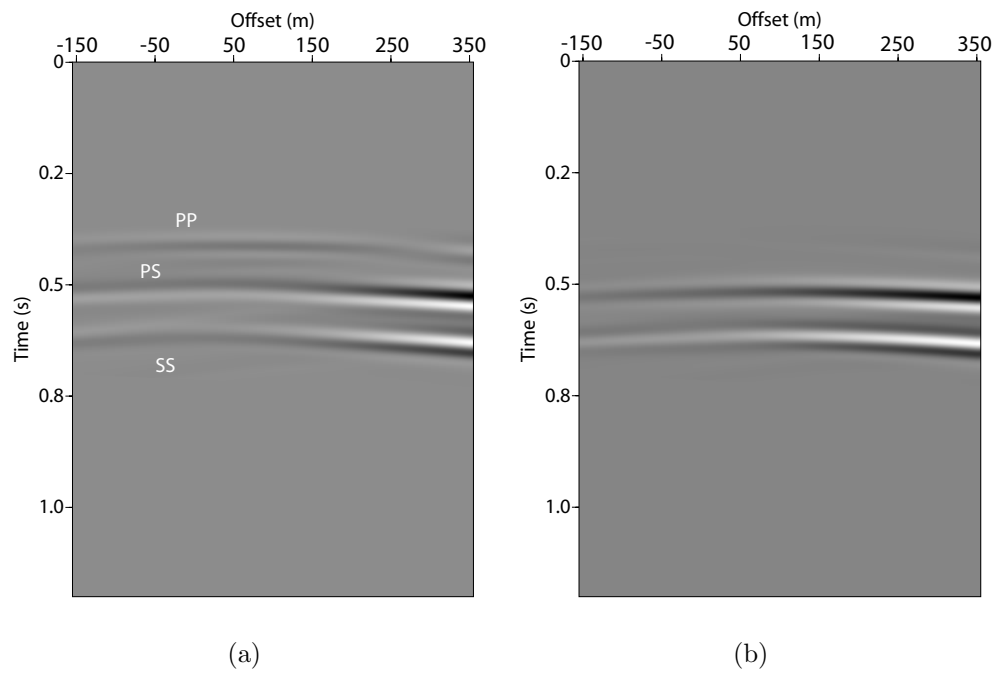
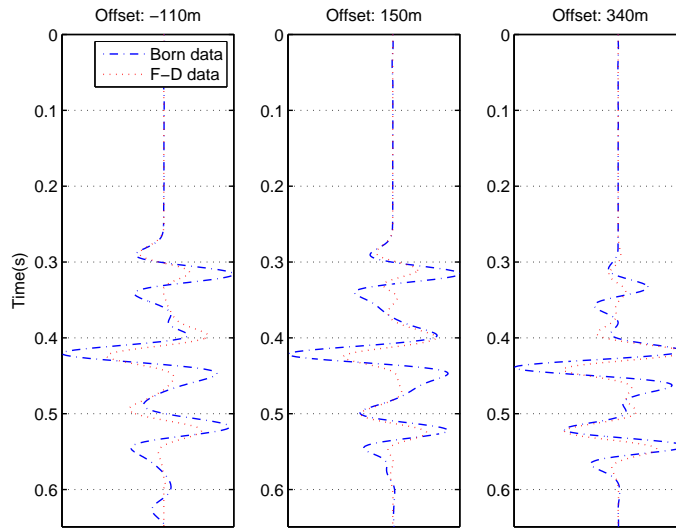
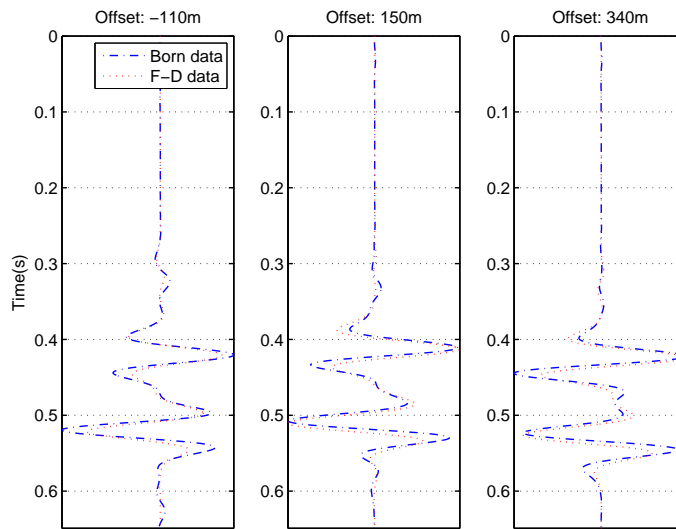


Figure 4.25: One of the shot gathers generated by 3D finite-difference code: (a) Vertical component (b) Horizontal component. The direct waves have been muted out. The source type is a vertical force. Hence, in addition to the PP and the PS arrivals, the SS arrival is also present.

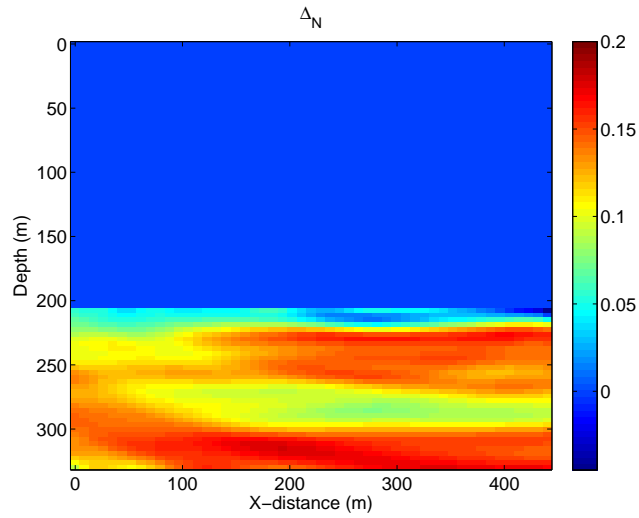


(a)

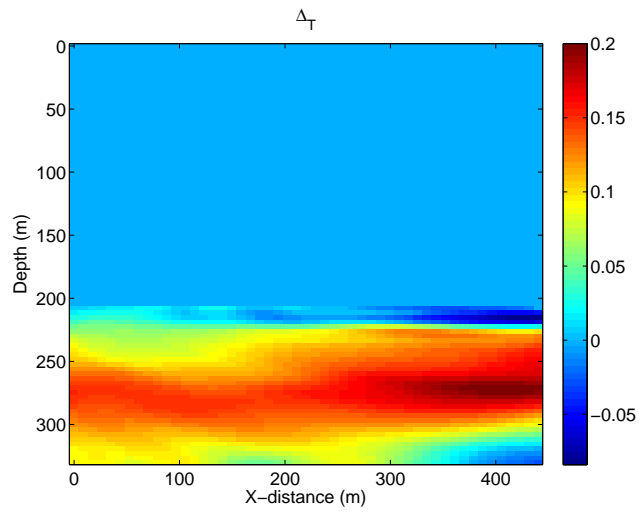


(b)

Figure 4.26: Comparison between finite-difference data (red) and ray-Born generated data: (a) Vertical component (b) Horizontal component. There is a reasonable match between these two data sets.



(a)



(b)

Figure 4.27: Inverted model parameters (a)  $\Delta_N$  (b)  $\Delta_T$ : The general trend in  $\Delta_N$  and  $\Delta_T$  has been recovered. At a few locations, the values of  $\Delta_N$  and  $\Delta_T$  are less than zero which can be avoided by setting a larger value for multiplier  $\epsilon$ . However, this may cause over estimation of  $\Delta_N$  and  $\Delta_T$  at other locations.

## 4.4 Discussion and conclusions

I reviewed ray-Born modeling and inversion for general anisotropic media and derived new equations needed to implement these techniques in HTI media. The main advantage of a ray-Born inversion is that it can be implemented in laterally varying media where a conventional AVOA scheme is not applicable. The main drawback of this inversion scheme is that an a priori estimate of the background medium is needed before it can be implemented. However, AVOA analysis also requires a priori knowledge of the background. I also demonstrated that the best estimate of  $\Delta_N$  and  $\Delta_T$  is possible when both the vertical and the horizontal component data are inverted simultaneously. Furthermore, a positivity constraint function (or regularization) may be needed to obtain good inversion results. I also demonstrated by numerical examples that a small number of frequency samples are sufficient to obtain desired inversion results. Depending upon the peak frequency in the data, every third or fourth frequency samples are sufficient for satisfactory results.

I also implemented an asymptotic expansion of the Born integral in the depth domain (appendix E). Asymptotic expansion renders the ray-Born modeling and inversion computationally far less expensive than the one that is implemented without the asymptotic approximation. However, it requires the knowledge of the precise location of the reflectors before the inversion can be performed.

A real dataset will require some conditioning before the ray-Born approximation can be implemented on it—all the multiples present in the data

will have to be eliminated since the first-order Born approximation does not account for multiple scattering (or multiples). Moreover, true amplitudes of the data will have to be preserved while processing it. An exact source wavelet will also need to be derived before the inversion can be performed. A good estimate of the background medium is also required to estimate traveltimes and amplitude of the rays which are essential for the computation of Green's function (equation 4.7).

The inversion scheme discussed in this chapter assumes that orientation of the fractures is known. Moreover, the inversion was performed in the symmetry plane of the fractured medium. However, fracture orientation is rarely known before the seismic data is collected over a region. Hence, there is no guarantee that a seismic line will be passing through the symmetry plane of the fractured media. Therefore, a practical application of this inversion scheme will require that multiazimuth data be inverted simultaneously which will invert for the fracture orientation as well. This will also eliminate the requirement that a seismic data line is available over the symmetry plane. I did not perform an inversion with multiazimuth data due to the excessive computational cost of a simultaneous inversion of such a large number of parameters. It would also require enormous computer memory to store the matrix  $\mathbf{G}$ . In the inversion algorithm, I assumed that the reference medium (or background) is isotropic for the purpose of the computation of the traveltimes and the divergence losses—traveltimes and divergence losses are essential for estimating the Green's function for the reference medium. This is a reasonable approx-

imation if the anisotropy is weak. However, in the case of strong anisotropy one will have to treat the reference medium as anisotropic. It should also be noted that all of the Green's functions, and hence, the modeling and inversion schemes were derived for a point force—a vertical or horizontal force used as a source function. However, to apply the inversion scheme on a marine dataset, the Green's function for an explosion source should be used to derive the expression for the scattered data  $\mathbf{u}_{syn}$  (equation 4.10).



## Chapter 5

### Summary and Future Work

#### 5.1 Summary

In chapter 1, I provided an overview of equivalent media theories for cracks and fractures, and defined the fracture parameters which need to be inverted for, in order to characterize a naturally fractured reservoir. I also discussed the state of the art methods available to invert for the fracture parameters.

In chapter 2, I implemented standard and rotated staggered grid finite-difference schemes to simulate wave propagation in 3D general anisotropic media. The anisotropic media up to orthorhombic symmetry were modeled using Standard Staggered Grid scheme (SSG) and beyond (monoclinic and triclinic) using Rotated Staggered Grid scheme (RSG). The rationale of not using RSG for all types of anisotropic media is that the RSG schemes are slightly more expensive than SSG schemes. For a 1D azimuthally anisotropic medium, I showed comparison between the seismic data generated by my finite-difference code and by the reflectivity algorithm; they are in excellent agreement. I also conducted a study on zero-offset shear-wave splitting using the finite-difference modeling algorithm in a rotated staggered grid. Wave propagation

was simulated for both rotationally invariant and corrugated fractures embedded in isotropic background for one or more than one set of fluid-filled and dry fractures. S-wave splitting was studied for dipping fractures, two vertical non-orthogonal fractures and corrugated fractures. My modeling results confirm that S-wave splitting can reveal the fracture infill for the case of dipping fractures. S-wave splitting analysis also has the potential to reveal the angle between the two vertical fractures. I also noticed that in case of vertical corrugated fractures, S-wave splitting is sensitive to the fracture infill.

I developed an efficient ray bending scheme in 3D general anisotropic media (chapter 3). The accuracy of the method is dictated by the accuracy in computing group velocity in the group (ray) direction. I developed two schemes for achieving this: one is based on a Fourier series expansion valid essentially in weak TI media while the other scheme uses a conjugate gradient algorithm to relate a group direction to its phase direction. Although the latter scheme is valid for arbitrary anisotropy, the estimated phase direction for the desired group direction is dependent on the starting phase direction. Finally, the raypaths are calculated by using Fermat's principle of minimum time. Starting with a straight raypath I find the stationary path using a conjugate gradient scheme. For practical application to modeling and migration, I implemented a hyperbolic interpolation scheme resulting in an efficient scheme for travel time computation in finely gridded models.

Chapter 4 is focused on the inversion for the fracture parameters in laterally varying media. I developed the theoretical basis to invert for fracture

parameters using a ray-Born approximation. I showed using numerical examples that the ray-Born approximation has the potential to invert the fracture parameters in laterally varying media. I also demonstrated that both horizontal and vertical components of seismic data are needed for desired inversion results. Furthermore, I also showed that all the frequency samples up to the Nyquist need not to be inverted for a good inversion results. In fact, inversion of a very small number of frequency samples yields satisfactory results. I also expanded Born integral in depth using asymptotic approximation. This renders the ray-Born based modeling and inversion algorithms computationally very cheap.

## 5.2 Future work

Ray-Born inversion scheme can be extended to invert multiazimuth data. However, the inversion will be very slow and one may run into severe memory problem as there will be too many model parameters to be inverted for simultaneously. However, one of the advantages is that the fracture orientation can also be posed as a model parameter. This will eliminate the necessity of knowing the fracture orientation prior to the inversion. In the inversion scheme, I also assumed that the background medium is isotropic, which is a reasonable approximation if the anisotropy is weak. However in the presence of strong anisotropic media, background media need to be treated as anisotropic media for the purpose of Green's function estimation in the background. In my inversion scheme, background information is a priori information. However,

as a future work it should be tested if the background elastic properties can also be inverted using ray-Born inversion scheme.

The ray bending algorithm, which I developed to estimate traveltime in anisotropic media, does not pick a desired branch at a triplication (the fastest or the most energetic one) rather the code selects a particular branch of triplication depending on the given initial ray path. The code can be modified, which would choose a particular branch at the triplication.

As a future work, 3D finite-difference code for general anisotropic media can be modified to account for anisotropic attenuation. However, this will render the modeling code computationally very expensive.

Most of the methods proposed in the past to invert the fracture parameters are based in the  $x-t$  domain. However in the  $x-t$  domain, in case of anisotropic media, phase and group directions are different which renders the analysis and the inversion of seismic data very difficult. Moreover, we need to make certain approximations to implement most of the inversion techniques in the  $x-t$  domain. For example, amplitude vs. offset and azimuth (AVOA) analysis assumes that phase and group direction are same in the fractured reservoirs which is a reasonable approximation if the anisotropy is weak. However, in presence of strong anisotropy, it may lead to the wrong analysis. A better domain to handle anisotropic media is plane-wave or  $\tau-p$  domain. Sen and Mukherjee (2003) used  $\tau-p$  domain to nmo-correct the seismic data recorded over a transversely anisotropic subsurface with a vertical axis of symmetry (VTI). They also derived a convenient form of vertical slowness  $q$  as a func-

tion of horizontal slowness  $p$  which in turn was used to compute  $\tau$ - $p$  curve for VTI media. Baan and Kendall (2003) gave an exact expression for  $q(p)$  for HTI media. However, due to its complexity it has not been used anywhere for the modeling or inversion purposes.

I have modified the expressions for  $q(p)$  for HTI media which were derived by Sen and Mukherjee (2003) originally for VTI media. These equations have a more convenient form and can be used to invert for the fracture parameters. The first approximated equation (approximation 1) for  $q(p)$  for HTI media is as follows:

$$q^2(p_x) = \frac{1}{\alpha_{vert}^2} \left( 1 - \frac{p_x^2 \alpha_{el}^2}{1 - 2\eta^{(V)} p_x^2 \alpha_{el}^2} \right) - p_y^2. \quad (5.1)$$

Another equation (approximation 2) for  $q(p)$  can be written as

$$q^2(p_x) = \frac{1}{\alpha_{vert}^2} (1 - p_x^2 \alpha_{el}^2) \left( 1 - \frac{2\eta^{(V)} p_x^4 \alpha_{el}^4}{1 - p_x^2 \alpha_{el}^2} \right) - p_y^2, \quad (5.2)$$

where  $\alpha_{vert}$  is vertical P-wave velocity,  $p_x$  and  $p_y$  are slownesses in  $x$ - and  $y$ -directions, respectively.  $\eta^{(V)} = (\varepsilon^{(V)} - \delta^{(V)}) / (1 + 2\delta^{(V)})$  and  $\alpha_{el}^2 = \alpha_{vert}^2 (1 + 2\delta^{(V)})$ . Notice that  $\varepsilon^{(V)}$  and  $\delta^{(V)}$  are Thomsen-style parameters for HTI media given by Tsvankin (1997a). These parameters can be easily written in terms of fracture parameters ( $\Delta_N$  and  $\Delta_T$ ) or fracture density (Bakulin et al., 2000a).  $\tau$ - $p$  curve can be computed by using the equation  $\tau(p) = 2zq(p)$ . I tested the accuracy of these equations in an HTI medium—background of the medium is isotropic with one set of vertical dry fractures embedded in it. Crack density of the fracture set is 7%. P-wave velocity of the background medium is

4 km/s. Thickness of the medium is 1 km. Figure 5.1 shows the comparison between the exact  $\tau$ - $p$ -curve,  $\tau$ - $p$ -curves computed by using approximation1 and approximation2 at various azimuths. We see an excellent match between the exact curve and the curve generated by the approximation1 whereas there is a reasonably good match between the exact curve and the curve generated by the approximation2. Notice that  $\phi = 0^\circ$  represents the symmetry plane and  $\phi = 90^\circ$  represents the isotropic plane of the HTI medium. One still needs to find out which of the approximations is more suitable for the inversion purposes.

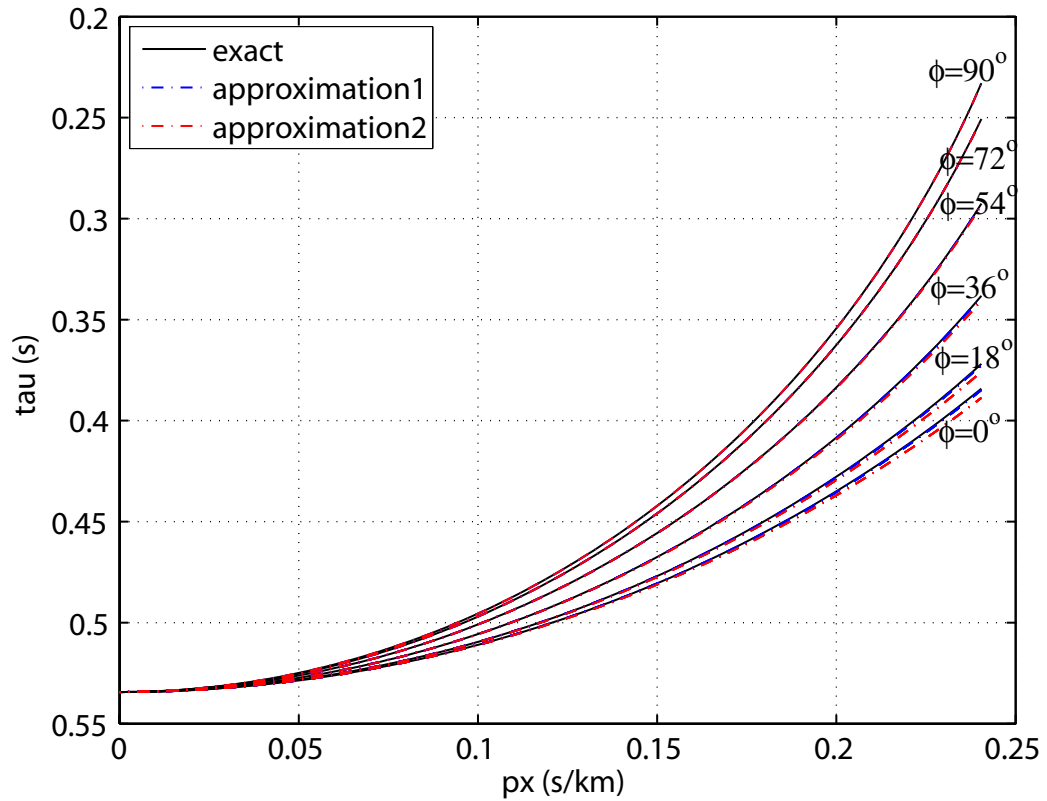


Figure 5.1: Comparison between the exact  $\tau$ - $p$  curve and  $\tau$ - $p$  curves generated by using the  $q(p)$  given in equations 5.1 and 5.2 which I call approximation1 and approximation2, respectively.

## Appendices



## Appendix A

### Phase and group velocity calculation

Phase velocity  $v$  is calculated using the following Christoffel equation (Musgrave, 1970) by a constant increment in the phase angle:

$$[c_{ijkl}l_jl_n - \rho v^2\delta_{ik}]U_k = 0, \quad (\text{A.1})$$

where  $c_{ijkl}$  is the fourth-order stiffness tensor,  $v$  is the phase velocity in phase direction  $l_n$ ,  $U_j$  is the polarization vector of particles,  $\rho$  is the medium density. Equation A.1 is a typical eigenvalue equation whose solution yields three eigen values corresponding with corresponding eigen vectors. The three eigen values correspond to square of slownesses of three wave types and the corresponding eigen vectors coincide with the polarization of particles with the respect to the phase direction. In general anisotropic media, the most common way to classify a wave type is by it's speed. The three wave types are P, S1 and S2. P is the fastest while the S2 is the slowest. If the medium is TI or isotropic, waves can be classified as P-, SV-, and SH-waves which are distinguished by polarization of particles with respect to the phase direction.

The Group Velocity vector  $V_j$  is computed by the following equation (Musgrave, 1970):

$$V_j = \frac{1}{\rho v} c_{ijkl} U_i U_k l_n, \quad (\text{A.2})$$

The procedure to compute the group velocity is straightforward. Phase velocity  $v$  is first estimated in phase direction  $l_n$  by solving equation A.1, and then equation A.2 is used to estimate the group velocity in the phase direction  $l_n$ .

## Appendix B

### Thomsen's model of fractured porous media

The effect of equant porosity (i.e., isometric pores that are not characterized as being ‘thin and flat’ and not having any particular orientation) was not considered while explaining equivalent media theories (section 1.3). At first glance, it seems that the equant porosity should not introduce any further anisotropy in a fractured or cracked medium due to their non-orientation in a particular direction. However, Thomsen (1995) showed that there is an effect on equivalent stiffness tensor of the rocks due to the fluid-flow between the cracks and pores. He derived an expression called **fluid influence factor**  $D_{cp}$  for hydraulically connected pores and cracks for ‘low’ and ‘moderately high’ frequencies. It is given as

$$D_{cp}(lo) = \left[1 - \frac{k'}{k} + \frac{k'}{k(\phi_c + \phi_p)}(A_p\phi_p + A_c e)\right]^{-1}, \quad (\text{B.1})$$

and

$$D_{cp}(mh) = \left[1 - \frac{k'}{k} + \frac{k'}{k\phi_c}A_c e\right]^{-1}, \quad (\text{B.2})$$

for ‘low’ and ‘moderately high’ frequencies, respectively. Here  $k$  and  $k'$  are the bulk moduli of the background medium and the fluid filling the cracks, respectively.  $\phi_p$  and  $\phi_c$  are the fractions of volume occupied by pores and cracks, respectively. Coefficients  $A_p$  and  $A_c$  are given as  $A_p = (3 - 2g)/(2g)$

and  $A_c = (4/9) \times [(2 - 3g)/(1 - g)]$  where  $g = V_s/V_p$ . Note that the above formulae is valid only when  $\phi_p < 10\%$ .

Here ‘low frequency’ means low enough for the fluid pressure to have time to equilibrate. In other words, under the application of stress (i.e., during wave-propagation) the fluid can flow from the cracks to the equant pores. In the seismic experiment, most of the frequency fall below this ‘low frequency’. Hudson (1981) did not consider this phenomena in his derivation for the equivalent stiffness coefficients for the fluid-filled cracks (equations 1.18 and 1.19). The ‘Moderately high’ frequency implies that fluid in the cracks did not have enough time to flow to the pores during the wave-propagation. This approximation is useful to analyse the ultrasonic data. In the limiting case of zero equant porosity, equations B.1 and B.2 become identical, and hence, in the seismic frequency range, equation B.2 can be used to analyse fluid-effect on the anisotropy of the medium. Crack porosity  $\phi_c$  can be expressed as  $\phi_c = (4\pi ec)/(3a)$ . It should be noted that for very low aspect ratio ( $c/a$ ) of the cracks (i.e., very low  $\phi_c$ ), ‘fluid influence factor’ for moderately high frequencies  $D_{cp}(mh)$  goes to zero. Hence, the Hudson’s model for fluid-filled cracks in the ultra-sonic range turns out to be valid.

Bakulin et al. (2000a) showed that  $\Delta_N$  and  $\Delta_T$  can be related to the ‘fluid influence factor’ in the following way:

$$\Delta_N = q\Delta_N^{Hudson,dry}, \quad (\text{B.3})$$

$$\Delta_T = \frac{16}{3} \frac{e}{(3 - 2g)}, \quad (\text{B.4})$$

where  $q = (1 - \frac{k'}{k})D_{cp}(l\omega)$ . The very first thing that can instantly be noticed is that  $\Delta_T$  is immune to the fluid influence factor. Equations 1.9 and 1.18 suggest that in the absence of fluid influence factor, P-wave velocities across and parallel to fluid-filled cracks in an isotropic background are equal which is rarely the case (Thomsen, 1995) (Christoffel equation give P-wave velocities perpendicular and parallel to fractures in an HTI as  $\sqrt{c_{11}/\rho}$  and  $\sqrt{c_{33}/\rho}$ , respectively. In case of fluid-filled fractures, equation 1.18 deduce  $\Delta_N = 0$ , which implies  $c_{11} = c_{33}$ ).

## Appendix C

### Hyperbolic interpolation of travelttime

Here, we follow Vanelle and Gajewski (2002) for hyperbolic interpolation of travelttime. Taylor expansion of  $\tau^2$  is carried out near the source position vector  $\mathbf{s}_0 = (s_1, s_2, s_3)^T$  and receiver position vector  $\mathbf{g}_0 = (g_1, g_2, g_3)^T$ . Let the variations in source and receiver positions be  $\Delta\mathbf{s}$  and  $\Delta\mathbf{g}$  such that  $\mathbf{s} = \mathbf{s}_0 + \Delta\mathbf{s}$  and  $\mathbf{g} = \mathbf{g}_0 + \Delta\mathbf{g}$ . After expanding  $\tau^2(\mathbf{s}, \mathbf{g})$  upto second order, we get

$$\begin{aligned} \tau^2(\mathbf{s}, \mathbf{g}) &= (\tau_0 - \mathbf{p}_0^T \Delta\mathbf{s} + \mathbf{q}_0^T \Delta\mathbf{g})^2 + \tau_0(-2\Delta\mathbf{s}^T \mathbf{N} \Delta\mathbf{g} - \Delta\mathbf{s}^T \mathbf{S} \Delta\mathbf{s} \\ &\quad + \Delta\mathbf{g}^T \mathbf{G} \Delta\mathbf{g}) + O(3). \end{aligned} \tag{C.1}$$

In index notation, above equation can be written as ( $i, j = 1, 2, 3$ )

$$\begin{aligned} \tau^2(s_i, g_i) &= (\tau_0^2 - p_{0i} \Delta s_i + q_{0i} \Delta g_i)^2 + \tau_0(-2\Delta s_i \Delta g_j N_{ij} - \Delta s_i \Delta s_j S_{ij} \\ &\quad + \Delta g_i \Delta g_j G_{ij}) + O(3), \end{aligned} \tag{C.2}$$

where,

$$p_{0i} = \left. \frac{\partial \tau}{\partial s_i} \right|_{\mathbf{s}_0, \mathbf{g}_0} \quad \text{and} \quad q_{0i} = \left. \frac{\partial \tau}{\partial g_i} \right|_{\mathbf{s}_0, \mathbf{g}_0} \tag{C.3}$$

are the slowness vectors at  $\mathbf{s}_0$  and  $\mathbf{g}_0$ , respectively. The matrices  $\mathbf{S}$ ,  $\mathbf{G}$ , and  $\mathbf{N}$  are given as

$$\begin{aligned}
 S_{ij} &= - \left. \frac{\partial^2 \tau}{\partial s_i \partial s_j} \right|_{\mathbf{s}_0, \mathbf{g}_0} = S_{ji}, \\
 G_{ij} &= \left. \frac{\partial^2 \tau}{\partial g_i \partial g_j} \right|_{\mathbf{s}_0, \mathbf{g}_0} = G_{ji}, \\
 N_{ij} &= - \left. \frac{\partial^2 \tau}{\partial s_i \partial g_j} \right|_{\mathbf{s}_0, \mathbf{g}_0} \neq N_{ji}
 \end{aligned} \tag{C.4}$$

All interpolation coefficients ( $p_{0i}$ ,  $q_{0i}$ ,  $S_{ij}$ ,  $G_{ij}$ ,  $N_{ij}$ ) are computed at every grid location. If interpolation for source location is not required then only  $q_{0i}$  and  $G_{ij}$  need to be computed. Input traveltimes which are given on a coarse grid are used to compute interpolation coefficients. For details, see Vanelle and Gajewski (2002).

## Appendix D

### Derivation of some of the formulas used in chapter 4

#### D.1 Derivation of equation 4.13

Error function is written as

$$E = \frac{1}{2} \Delta \mathbf{u}^T \Delta \mathbf{u} + \epsilon f(\mathbf{m}), \quad (\text{D.1})$$

where  $\Delta \mathbf{u} = \mathbf{u}_{data} - \mathbf{u}_{syn}$ . Using equation 4.11, we can write D.1 as

$$\begin{aligned} E &= \frac{1}{2} (\mathbf{u}_{data} - \mathbf{G}\mathbf{m})^T (\mathbf{u}_{data} - \mathbf{G}\mathbf{m}) + \epsilon f(\mathbf{m}) \\ &= \frac{1}{2} [\mathbf{u}_{data}^T \mathbf{u}_{data} - (\mathbf{G}\mathbf{m})^T \mathbf{u}_{data} - \mathbf{u}_{data}^T (\mathbf{G}\mathbf{m}) + (\mathbf{G}\mathbf{m})^T (\mathbf{m})] + \epsilon f(\mathbf{m}) \\ &= \frac{1}{2} [\mathbf{u}_{data}^T \mathbf{u}_{data} - 2(\mathbf{G}\mathbf{m})^T \mathbf{u}_{data} + (\mathbf{G}\mathbf{m})^T (\mathbf{G}\mathbf{m})] + \epsilon f(\mathbf{m}) \end{aligned}$$

taking the derivative with respect to  $\mathbf{m}$

$$\begin{aligned} \frac{\partial E}{\partial \mathbf{m}} &= [-\mathbf{G}^T \mathbf{u}_{data} + \mathbf{G}^T (\mathbf{G}\mathbf{m})] + \epsilon \frac{\partial f(\mathbf{m})}{\partial \mathbf{m}} \\ &= -\mathbf{G}^T [\mathbf{u}_{data} - \mathbf{G}\mathbf{m}] + \epsilon \frac{\partial f(\mathbf{m})}{\partial \mathbf{m}} \\ &= -\mathbf{G}^T \Delta \mathbf{u} + \epsilon \frac{\partial f(\mathbf{m})}{\partial \mathbf{m}} \quad (\text{D.2}) \end{aligned}$$



## D.2 Derivation of $\mathbf{L}^q$ for vertical fractures (equation 4.16)

In the symmetry plane of HTI media,  $\mathbf{m}_0$  is given as (equation 4.15)

$$\mathbf{m}_0 = [\Delta c_{11}, \Delta c_{33}, \Delta c_{13}, \Delta c_{66}, \Delta \rho]^T. \quad (\text{D.3})$$

If the background is isotropic, equation D.3 can be rewritten as (using equation 1.9)

$$\mathbf{m}_0 = \left[ (\lambda_b + 2\mu_b)\Delta_N, \frac{\lambda_b^2}{\lambda_b + 2\mu_b}\Delta_N, \lambda_b\Delta_N, \mu_b\Delta_T, \Delta\rho_b \right]^T, \quad (\text{D.4})$$

where  $\lambda_b$  and  $\mu_b$  are background elastic coefficients and  $\rho_b$  is background density. In my inversion scheme, I assume that  $\lambda_N$ ,  $\mu_b$  and  $\rho_b$  are known. Hence the unknowns are  $\Delta_N$  and  $\Delta_T$ , i.e.  $\mathbf{m}^q = [\Delta_N, \Delta_T]^T$ . Following equation need to be solved to obtain  $\mathbf{L}^q$ :

$$\mathbf{m}_0 = \mathbf{L}^q \mathbf{m}^q, \quad (\text{D.5})$$

where  $\mathbf{m}_0$  and  $\mathbf{m}^q$  are known. By simple algebra, it can be shown that the following expression of  $\mathbf{L}^q$  satisfy the equation D.5 (equation D.5 can have many solutions as it is an underdetermined problem):

$$\mathbf{L}^q = \begin{bmatrix} -(\lambda_b + 2\mu_b) & 0 \\ -\frac{\lambda_b^2}{\lambda_b + 2\mu_b} & 0 \\ -\lambda_b & 0 \\ 0 & -\mu_b \\ 0 & 0 \end{bmatrix}, \quad (\text{D.6})$$

## Appendix E

### A useful asymptotic approximation of Born integral

Evaluation of equation 4.10 is computationally very expensive which renders both forward modeling and inversion very time consuming. However, an asymptotic expansion of equation 4.10 in depth allows one to evaluate it only at the layer boundaries instead of computing it for the entire zone of interest.

Here I follow Bleistein (1984, p. 73–76) for explaining the asymptotic expansion of Fourier integrals with monotonic phase. Suppose that an integral is given in the following form:

$$I(\omega) = \int_a^b f(z)e^{i\omega\phi(z)} dz. \quad (\text{E.1})$$

By asymptotic expansion of zero-order equation E.1 can be rewritten as

$$I(\omega) = \frac{1}{i\omega} \frac{f(z)}{\dot{\phi}(z)} e^{i\omega\phi(z)} \Big|_{z=b} - \frac{1}{i\omega} \frac{f(z)}{\dot{\phi}(z)} e^{i\omega\phi(z)} \Big|_{z=a}. \quad (\text{E.2})$$

If there are discontinuities in the integral E.1, it needs to be evaluated piecewise; i.e.,

$$\begin{aligned} I(\omega) &= \int_a^b f(z)e^{i\omega\phi(z)} dz = \int_a^{l_1} f(z)e^{i\omega\phi(z)} dz \\ &+ \int_{l_1}^{l_2} f(z)e^{i\omega\phi(z)} dz + \dots + \int_{l_n}^b f(z)e^{i\omega\phi(z)} dz. \end{aligned} \quad (\text{E.3})$$

Equation E.2 can be applied at each segment of integral in equation E.3. Equation 4.10 has the same form as that of equation E.1; equivalent  $\phi(z)$  and  $f(z)$  are given as

$$\phi(z) \equiv \tau, \quad (\text{E.4})$$

and

$$\begin{aligned} f(z) \equiv & |\omega|^{3/2} (2\pi)^{1/2} e^{\text{sign}(\omega)i\pi/4} \sum_{\Omega} \tilde{g}_m(\mathbf{s}) \hat{g}_n(\mathbf{r}) \\ & \times \int_{x_1}^{x_2} R(\mathbf{m}_0, \tilde{\mathbf{p}}, \hat{\mathbf{p}}, \tilde{\mathbf{g}}, \hat{\mathbf{g}})(\tau, yy)^{-1/2} A dx. \end{aligned} \quad (\text{E.5})$$

Hence, the relationship E.2 can be used in equation 4.10 to compute the scattered field  $U_{mn}$ . Figure E.1 shows a subsurface model with a number of layers ( $l_1, l_2, \dots, l_n$ ). Instead of calculating equation 4.10 for each scatterer in the subsurface which is computationally very expensive, one can implement equation E.3 on equation 4.10 to compute the scattered wavefield or synthetic seismic data in a relatively much shorter time. Here layer boundaries ( $l_1, l_2, \dots, l_n$ ) will act as discontinuities in the integral E.3.

To demonstrate the applicability of the asymptotic approximation, I generated synthetic seismic data with and without the asymptotic approximation of equation 4.10. Figure E.2 displays the subsurface model used for modeling. Layer 1 does not have any fractures in it whereas layer 2 and layer 3 have one set of vertical fractures.  $\Delta_N$  and  $\Delta_T$  values of the fracture set embedded in layer 2 are 0.3 and 0.1, respectively, and those in layer 3 are 0.5 and 0.2. Background medium is homogeneous with P- and S-wave velocities

of 3700 m/s and 2300 m/s, respectively. Density of the background is 2.3 g/cc. The model has 400 and 350 scatterers in  $x$ - and  $z$ -directions, respectively. The source type is a vertical force and the source pulse is a 40 Hz Ricker wavelet. A single line of receivers was used to collect the data. Both vertical and horizontal components were modelled, and all the wave modes (PP, PS, SS, SP) were incorporated in the modeling. A taper was applied on the edges of the model to suppress truncation phases from the edges. Figure E.3 shows the synthetic seismograms generated with and without implementing the asymptotic approximation (equation E.3) of equation 4.10. Figures E.3(a) and E.3(c) display the vertical and horizontal components of synthetic data generated without the asymptotic approximation. Figures E.3(b) and E.3(d) show vertical and horizontal components of the synthetic data generated by applying the asymptotic approximation. Notice that the synthetic data generated with and without asymptotic approximation appear very similar. Figure E.4 displays the comparison between the seismic data generated with and without the asymptotic approximation at various offsets; they are in excellent agreement. It is worth mentioning here that the computation of synthetic data with asymptotic approximation was about 300 times faster than the one which was computed without asymptotic approximation.

Asymptotic approximation can also be used for the inversion purposes. The computation time for such an inversion will be very cheap and less memory intensive. However, we will need to know the exact location of the reflectors before inversion can be implemented. Theoretically, it is possible to know

the exact location of the reflectors once the depth imaging has been applied on the data. Inversion procedure remains exactly the same as I described in the previous sections. The only difference is that the model parameters are defined only at the top of each layer (hence, a very small number of parameters needs to be inverted). Furthermore, the forward model  $\mathbf{u}_{syn}$  after each iteration is generated using asymptotic approximation (equation E.3) of equation 4.10. I demonstrate the applicability of this method on a three layer model. Figure E.5 shows the model used to demonstrate the inversion. Top layer does not have any fractures. Layer 2 has one set of vertical fractures oriented normal to  $x$ -direction with  $\Delta_N = 0.3$  and  $\Delta_T = 0.1$ . Layer 3 also has one set of vertical fractures oriented normal to  $x$ -direction with  $\Delta_N = 0.5$  and  $\Delta_T = 0.2$ . Inversion was performed using two types of survey geometries. First survey had a single shot placed in the middle of survey line (at  $x$ -location of 500 m). Receivers were placed in a split-spread fashion at a spacing of 10 m. In the second survey, three shots were used;  $x$ -location of shots were 200 m, 400 m and 600 m. There were 100 receivers placed at an interval of 10 m. Receiver locations were not changed when the shots were moved. Source pulse used was a 40 Hz Ricker wavelet and a vertical force was used as the source. Both vertical and horizontal components data were inverted simultaneously. Figures E.6(a) and E.6(b) show the inverted model parameters ( $\Delta_N$  and  $\Delta_T$ ) for top of second layer (flat layer) and third layer (syncline), respectively. As expected, better inversion results are obtained when multiple shots are used.

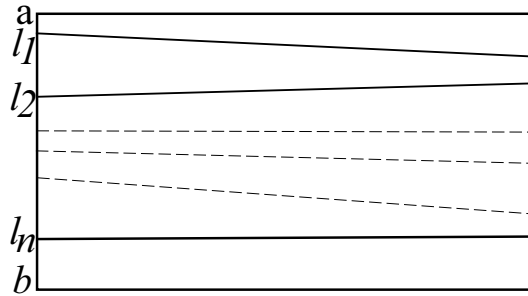


Figure E.1: A typical subsurface with a number of layers ( $l_1, l_2, \dots, l_n$ ).

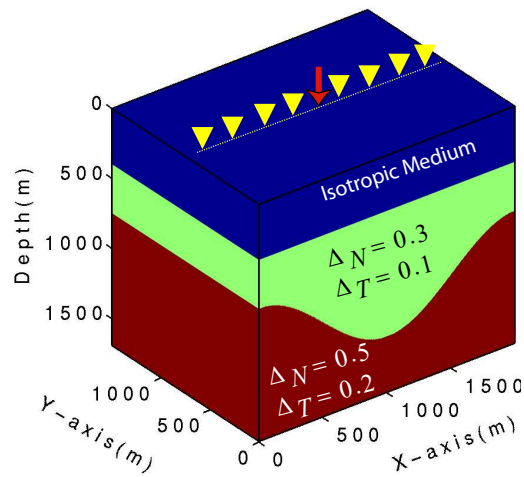


Figure E.2: Subsurface model used to generate synthetic seismic data. A vertical force was used as the source. A single line of receivers was used to collect the data. First layer is isotropic while second and third layers have one set of vertical fractures oriented normal to  $x$ -direction.

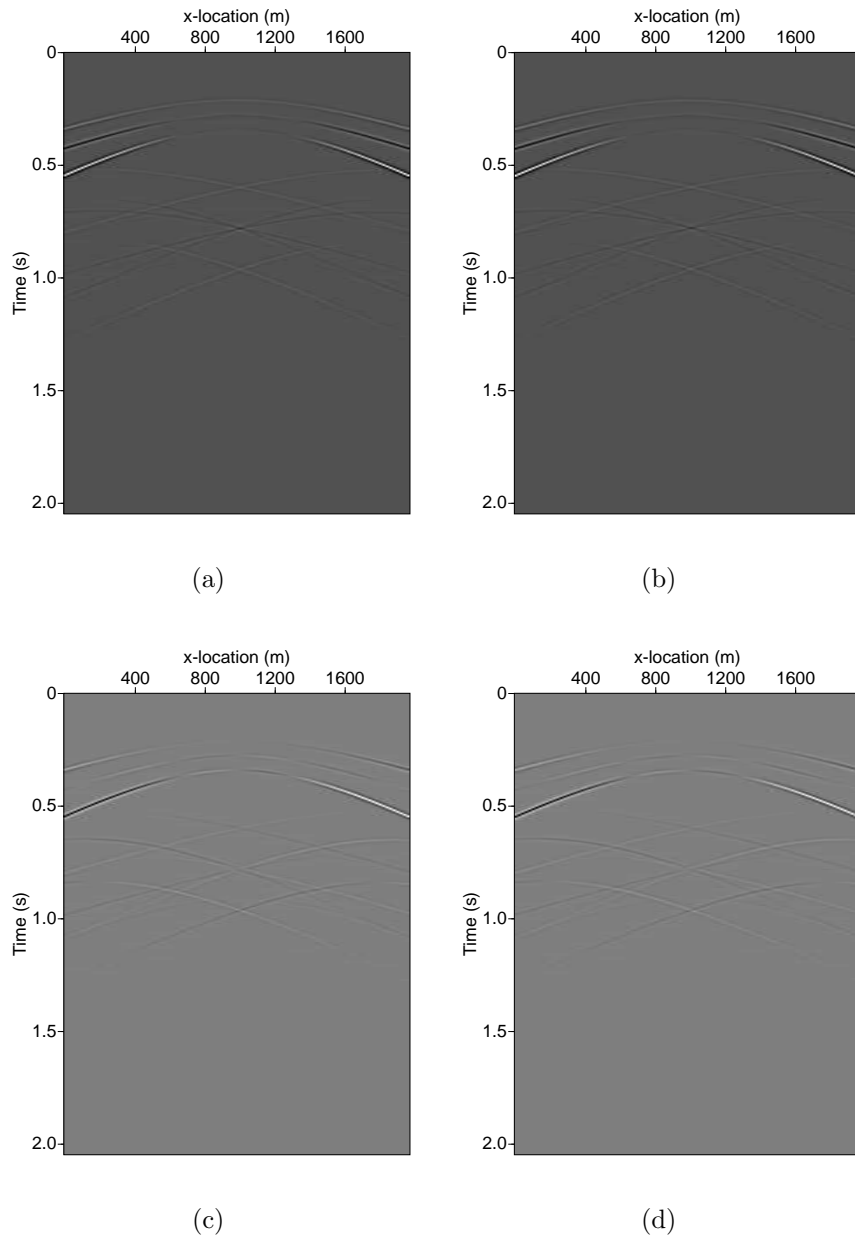
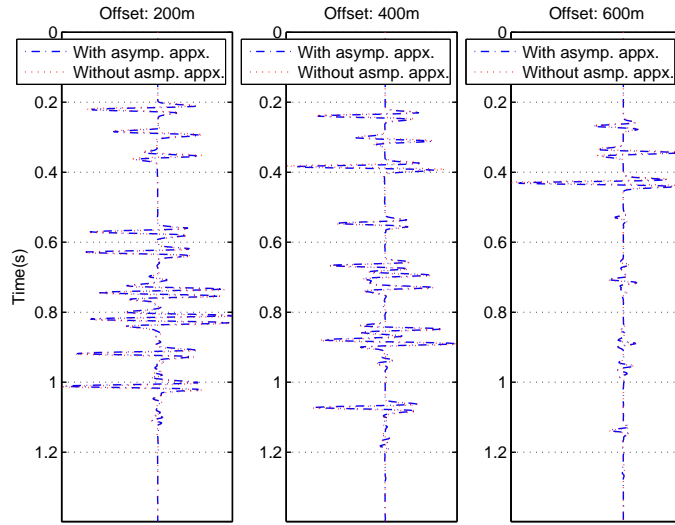
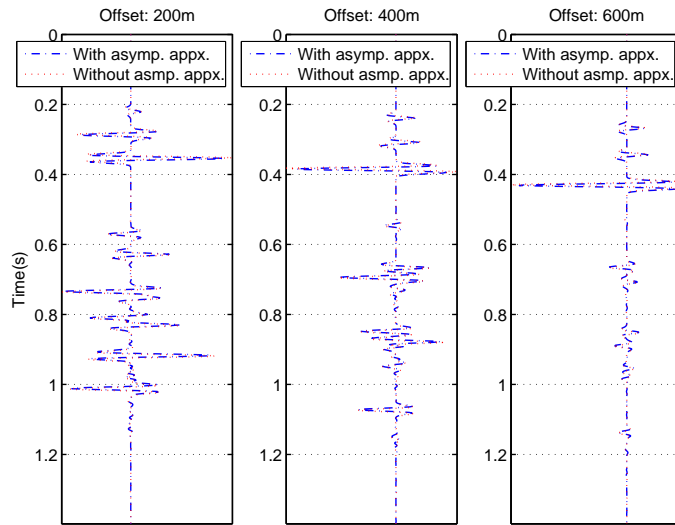


Figure E.3: Seismic sections generated for model shown in figure E.2: (a) Vertical component generated without asymptotic expansion, (b) Vertical component generated after applying asymptotic expansion, (c) Horizontal component generated without asymptotic expansion, and (d) Horizontal component generated after applying asymptotic expansion.



(a)



(b)

Figure E.4: Comparison between the synthetic data generated with and without asymptotic approximation of equation 4.10: (a) Vertical component, (b) Horizontal component. Notice that the synthetics are in excellent match.



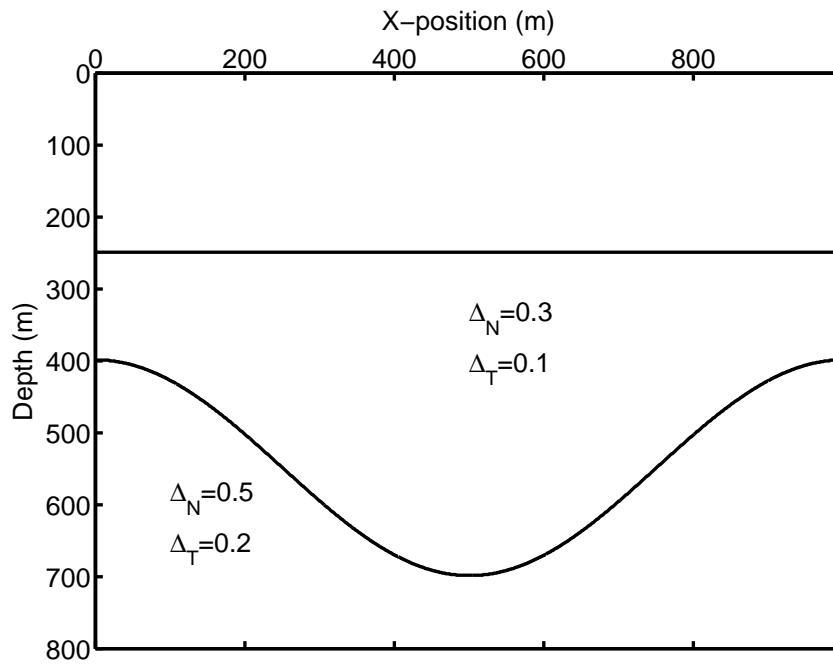
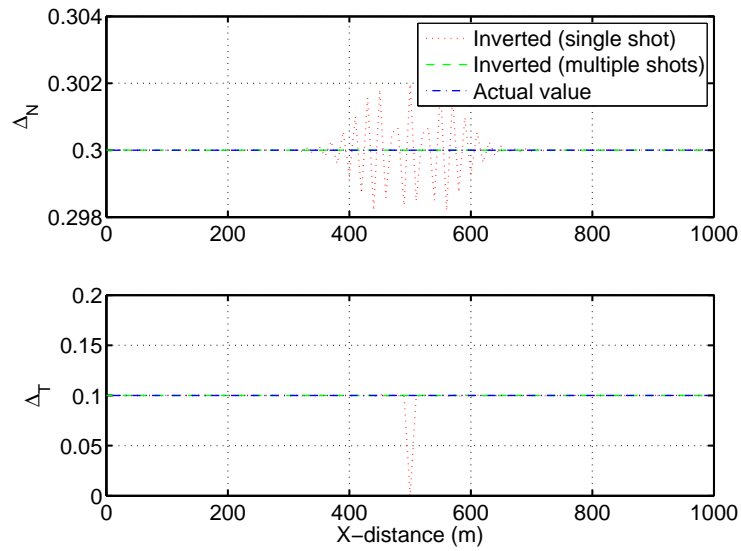
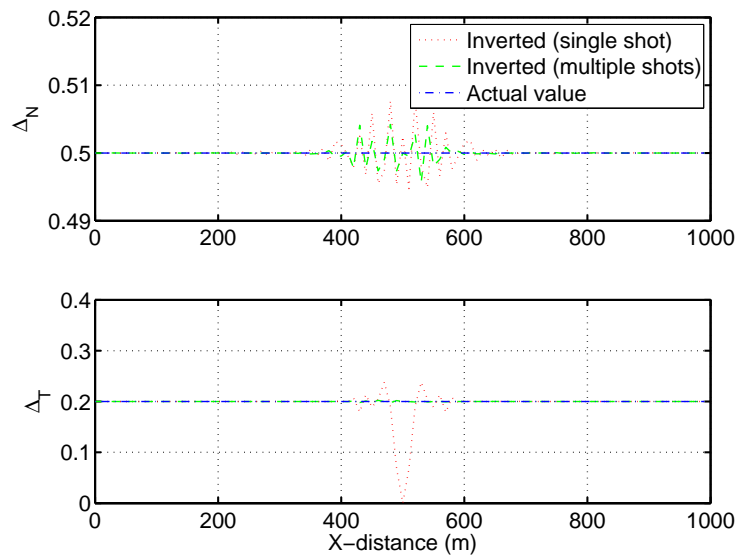


Figure E.5: A three layer model used to demonstrate the inversion by asymptotic approximation: First layer does not have any fractures in it. Layer 2 has one set of vertical fractures oriented normal to  $x$ -direction with  $\Delta_N = 0.3$  and  $\Delta_T = 0.1$ . Layer 3 also has one set of vertical fractures oriented normal to  $x$ -direction with  $\Delta_N = 0.5$  and  $\Delta_T = 0.2$ .



(a)



(b)

Figure E.6: Inverted models  $\Delta_N$  and  $\Delta_T$  for top of (a) layer 2 (flat layer) and (b) layer 3 (syncline) of the model shown in figure E.6. Notice that the inversion results are much better when multiple shots are used.

## Bibliography

- Aguilera, R., 1995, Naturally fractured reservoirs: PennWell Books, Tulsa, OK.
- Aguilera, R., 1998, Geologic aspects of naturally fractured reservoirs: The Leading Edge, **17**, 1667–1670.
- Aki, K., and Richards, P. G., 2002, Quantitative seismology: University Science Books, Sausalito, California.
- Alford, R. M., 1986, Shear data in the presence of azimuthal anisotropy: Dilley, Texas:, *in* 56th Ann. Internat. Mtg. Soc. of Expl. Geophys., 476–479.
- Assad, J. M., Tatham, R. H., McDonald, J. A., and Jech, J., 1993, A physical model study on scattering of waves by aligned cracks: Comparison between experiment and theory: Geophysical Prospecting, **41**, 323–339.
- Auld, B. A., 1990, Acoustic fields and waves in solids: Krieger Publ. Co., Malabar, Florida.
- Baan, M., and Kendall, J. M., 2003, Traveltime and conversion-point computations and parameter estimation in layered, anisotropic media by  $\tau$ - $p$  transform: Geophysics, **68**, 210–224.
- Backus, G. E., 1962, Long-wave elastic anisotropy produced by horizontal layerings: J. Geophys. Res., **67**, 4427–4440.
- Bakulin, A., Grechka, V., and Tsvankin, I., 2000a, Estimation of fracture parameters from reflection seismic data—part I: HTI model due to a single fracture set: Geophysics, **65**, 1788–1802.
- Bakulin, A., Grechka, V., and Tsvankin, I., 2000b, Estimation of fracture parameters from reflection seismic data—part II: Fractured models with monoclinic symmetry: Geophysics, **65**, 1803–1817.

- Bakulin, A., Grechka, V., and Tsvankin, I., 2000c, Estimation of fracture parameters from reflection seismic data—part III: HTI model due to a single fracture set: *Geophysics*, **65**, 1788–1802.
- Bansal, R., Enhancement of potential fracture signals on surface seismic data:, MS thesis, Virginia Tech, 2003.
- Beydoun, W. B., and Mendes, M., 1989, Elastic ray-Born  $l_2$  migration/inversion: *Geophys. J. Int.*, **97**, 151–160.
- Beylkin, G., and Burridge, R., 1990, Linearized inverse scattering problems in acoustics and elasticity: *Wave Motion*, **12**, 15–52.
- Beylkin, G., 1985, Imaging of discontinuities in the inverse scattering problem by inversion of a causal generalized Radon transform: *J. math. Phys.*, **26**, 99–108.
- Bleistein, N., Cohen, J. K., and Hagin, F., 1987, Two-and-half dimensional Born inversion with an arbitrary reference: *Geophysics*, **52**, 26–36.
- Bleistein, N., 1984, *Mathematical methods for wave phenomena*: Academic Press, Orlando, Florida.
- Booth, D. C., and Crampin, S., 1983, The anisotropic reflectivity technique—theory: *Geophys. J. Roy. Astr. Soc.*, **72**, 755–766.
- Brokešová, 1996, Construction of ray synthetic seismogram using interpolation of travel times and ray amplitude: *Pure and Applied Geophysics*, **48**, 503–538.
- Burden, R. L., and Faires, J. D., 1989, *Numerical analysis*: PWS-KENT Publ. Co., Boston.
- Byun, B. S., Corrigan, D., and Gaiser, J. E., 1989, Anisotropic velocity analysis for lithology discrimination: *Geophysics*, **54**, 1564–1574.
- Carcione, J. M., Herman, G. C., and ten Kroode, A. P., 2002, Seismic modeling: *Geophysics*, **67**, 1304–1325.

- Carcione, J. M., 1994, The wave equation in generalized coordinates: *Geophysics*, **59**, 1911–1919.
- Červený, V., 1985, The application of ray tracing to the numerical modeling of seismic wavefields in complex structures: *Handbook of Geophys. Expl.: Geophysical Press*.
- Červený, V., 2001, *Seismic ray theory*: Cambridge University Press, Cambridge, UK.
- Chapman, C. H., and Coates, R. T., 1994, Generalized Born scattering in anisotropic media: *Wave Motion*, **19**, 309–341.
- Cheng, C. H., 1978, *Seismic velocities in porous rocks: Direct and inverse problems*: Ph.D. thesis, MIT, Cambridge, Massachusetts.
- Christensen, R. M., 1979, *Mechanics of composite materials*: JOHN WILEY & SONS.
- Clayton, R. W., and Stolt, R. H., 1981, A Born-WKBJ inversion method for acoustic reflection data: *Geophysics*, **46**, 1559–1567.
- Cohen, J. K., Haglin, F. G., and Bleistein, N., 1986, Three-dimensional Born inversion with an arbitrary reference: *Geophysics*, **51**, 1552–1558.
- Contreras, P., Grechka, V., and Tsvankin, I., 1999, Moveout inversion of P-wave data for horizontal transverse isotropy: *Geophysics*, **64**, 1219–1229.
- Crampin, S., and Yeldin, M., 1981, Shear-wave singularities of wave propagation in anisotropic media: *J. Geophys.*, **49**, 43–46.
- De Hoop, A. T., 1995, *Handbook of radiation and scattering of waves*: Academic Press.
- Dong, Z., and McMechan, A. G., 1995, 3-D viscoelastic anisotropic modeling of data from a multicomponent, multiazimuth seismic experiment in northeast Texas: *Geophysics*, **60**, 1128–1138.
- Eaton, D. W. S., and Stewart, R. R., 1994, Migration/inversion for transversely isotropic media: *Geophys. J. Int.*, **119**, 667–683.

- Eshelby, J. D., 1957, The determination of the elastic field of an ellipsoidal inclusion, and related problems: Proc. Royal Soc. London, **A241**, 376–396.
- Farguharson, C. G., Oldenburg, D. W., and Routh, P. S., 2003, Simultaneous 1D inversion of loop-loop electromagnetic data for magnetic susceptibility and electrical conductivity: Geophysics, **68**, 1857–1869.
- Faria, E. L., and Stoffa, P. L., 1994a, Finite-difference modeling in transversely isotropic media: Geophysics, **59**, 282–289.
- Faria, E. L., and Stoffa, P. L., 1994b, Traveltime computation in transversely isotropic media: Geophysics, **59**, 272–281.
- Farra, V., 1992, Bending method revisited: A Hamiltonian approach: Geophys. J. Int., **109**, 138–150.
- Farra, V., 2005, First-order ray tracing for qS waves in inhomogeneous weakly anisotropic media: Geophys. J. Int., **161**, 309–324.
- Fletcher, R., 1980, Practical methods of optimization, Volume 1: Unconstrained optimization: John Wiley Inc.
- Fornberg, B., 1988, The pseudospectral method: Accurate representation of interfaces in elastic wave calculations: Geophysics, **53**, 625–637.
- Frankel, A., 1993, Three-dimensional simulations of ground motions in the San Bernardino Valley, California, for hypothetical earthquakes on the San Andreas fault: Bull. Seism. Soc. Am., **83**, 1020–1041.
- Fryer, G. J., and Frazer, L. N., 1984, Seismic wave propagation in stratified anisotropic media: Geophys. J. Roy. Astr. Soc., **78**, 691–710.
- Gajewski, D., 1998, Determining the ray propagator from traveltimes:, *in* 68th Ann. Internat. Mtg. Soc. of Expl. Geophys., 1900–1903.
- Graves, R. W., 1996, Simulating seismic wave propagation in 3D elastic media using staggered-grid finite difference: Bull. Seism. Soc. Am., **86**, 1091–1106.

- Grechka, V. Y., and McMechan, G. A., 1996, 3-D two-point ray tracing for heterogeneous, weakly transversely isotropic media: *Geophysics*, **61**, 1883–1894.
- Grechka, V., and Tsvankin, I., 2004, Characterization of dipping dipping fractures in a transversely isotropic background: *Geophysical Prospecting*, **52**, 1–10.
- Grechka, V., 2003, Effective media: A forward modeling view: *Geophysics*, **68**, 2055–2062.
- Guiziou, J. L., Mallet, J. L., Nobili, P., Anandappane, R., and Thisse, P., 1991, 3-D ray-tracing through complex triangulated surfaces:, *in* 61st Ann. Internat. Mtg. Soc. of Expl. Geophys., 1497–1500.
- Hall, S. A., and Kendall, J. M., 2003, Fracture characterization at Valhall: Application of P-wave amplitude variation with offset and azimuth (AVOA) analysis to a 3D ocean-bottom data set: *Geophysics*, **68**, 1150–1160.
- Helbig, K., 1994, Foundations of anisotropy for exploration seismics: Handbook of geophysical explorations: Pergamon Press Inc., Tarrytown, NewYork.
- Hudson, J. A., 1980, Overall properties of a cracked solid: *Math. Proc. Camb. Phil. Soc.*, **88**, 371–384.
- Hudson, J. A., 1981, Wave speeds and attenuation of elastic waves in material containing cracks: *Geophys. J. Roy. Astr. Soc.*, **64**, 133–150.
- Hudson, J. A., 1991, Overall properties of heterogeneous material: *Geophys. J. Int.*, **107**, 505–511.
- Igel, H., and Crampin, S., 1990, Extracting shear wave polarizations from different source orientations: Synthetic modelling: *J. Geophys. Res.*, **95**, 11,283–11,292.
- Igel, H., Mora, P., and Bruno, R., 1995, Anisotropic wave propagation through finite-difference grids: *Geophysics*, **60**, 1203–1216.

- Jin, S., Madariaga, R., Virieux, J., and Lambaré, G., 1992, Two-dimensional asymptotic iterative elastic inversion: *Geophys. J. Int.*, **108**, 575–588.
- Kachanov, M., 1992, Effective elastic properties of cracked solids: critical review of some basic concepts: *Appl. Mech. Rev.*, **45**, 304–335.
- Kaschwich, T., and Gajewski, D., 1993, Wavefront-oriented ray tracing in 3D anisotropic media:, *in* 65th Conference and Exhibition EAGE.
- Kelly, K. R., Ward, R. W., Treitel, S., and Alford, R. M., 1976, Synthetic seismograms: a finite-difference approach: *Geophysics*, **41**, 2–27.
- Kennett, B. L. N., 1983, *Seismic wave propagation in stratified media*: Cambridge University Press, Cambridge.
- Keys, R. G., and Weglein, A. B., 1983, Generalized linear inversion and the first-order Born theory for acoustic media: *J. math. Phys.*, **24**, 1444–1449.
- Kumar, D., Sen, M. K., and Ferguson, R. J., 2004, Traveltime calculation and prestack depth migration in tilted transversely isotropic media: *Geophysics*, **69**, 37–44.
- Lambaé, G., Lucio, P. S., and Hanyga, A., 1996, Two-dimensional multivalued traveltime and amplitude maps by uniform sampling of a ray field: *Geophys. J. Int.*, **125**, 584–598.
- Lambaré, G., Operto, S., Podvin, P., and Thierry, P., 2003, 3D ray+Born migration/inversion-Part1: Theory: *Geophysics*, **68**, 1348–1356.
- Laubach, S. E., Marrett, R. A., and Scott, A. R., 1998, Characteristics and origins of coal cleat: A review: *International Journal of Coal Geology*, **35**, 175–207.
- Laubach, S. E., 2003, Practical approaches to identifying sealed and open fractures: *AAPG Bulletin*, **87**, 561–579.
- Levander, A. R., 1988, Fourth-order finite-difference P-SV seismogram: *Geophysics*, **49**, 1933–1957.



- Liao, Q., and McMechan, G. A., 1996, Multifrequency viscoacoustic modeling and inversion: *Geophysics*, **61**, 1371–1378.
- Liu, E., Crampin, S., and Hudson, J. A., 1997, Diffraction of seismic waves by cracks with application to hydraulic fracturing: *Geophysics*, **62**, 253–265.
- Lo, T., Toksöz, M. N., Xu, S. H., and Wu, R. S., 1988, Ultrasonic laboratory test of geophysical tomographic reconstruction: *Geophysics*, **53**, 947–956.
- MacBeth, C., and Crampin, S., 1991, Comparison of signal processing techniques for estimating the effects of anisotropy: *Geophysical Prospecting*, **39**, 357–386.
- Mallick, S., and Frazer, L. N., 1990a, Reflection/Transmission coefficients and azimuthal anisotropy in marine seismic studies: *Geophys. J. Int.*, **105**, 241–252.
- Mallick, S., and Frazer, L. N., 1990b, Computation of synthetic seismograms for stratified azimuthally anisotropic media: *J. Geophys. Res.*, **95**, 8513–8526.
- Marfurt, K. J., 1984, Accuracy of finite-difference and finite-element modeling of the scalar and elastic wave equations: *Geophysics*, **49**, 533–549.
- Menke, W., 1984, *Geophysical data analysis: Discrete inverse theory*: Academic Press, Orlando.
- Minkoff, S. E., 2002, Spatial parallelism of a 3D finite difference velocity-stress elastic wave propagation code: *SIAM J. Sci. Comput.*, **24**, 1–19.
- Moczo, P., Kristek, J., and Halada, L., 2000, 3D fourth-order staggered-grid finite-difference schemes: Stability and grid dispersion: *Bull. Seism. Soc. Am.*, **90**, 587–603.
- Moczo, P., Kristek, J., Vavryčuk, V., and Halada, L., 2002, 3D heterogeneous staggered-grid finite-difference modeling of seismic motion with volume harmonic and arithmetic averaging of elastic moduli and densities: *Bull. Seism. Soc. Am.*, **92**, 3042–3066.

- Moser, T. J., Nolet, G., and Snieder, R., 1992, Ray bending revisited: *Bull. Seism. Soc. Am.*, **82**, 259–288.
- Moser, T. J., 1991, Shortest path calculation of seismic rays: *Geophysics*, **56**, 59–67.
- Musgrave, M. J. P., 1970, *Crystal acoustics*: Holden Day.
- Naville, C., 1986, Detection of anisotropy using shear-wave splitting in VSP surveys: requirements and applications:, *in* 56th Ann. Internat. Mtg. Soc. of Expl. Geophys., 391–394.
- Nelson, R. A., 2001, *Geologic analysis of naturally fractured reservoirs*: Gulf Publishing Company, Houston, Texas.
- Neves, F. A., Al-Marzoug, and Nebrija, E. L., 2003, Fracture characterization of deep tight gas sands using azimuthal velocity and AVO seismic data in Saudi Arabia: *The Leading Edge*, **22**, 469–475.
- Newman, W. M., and Sproull, R. F., 1981, *Principles of interactive computer graphics*: McGraw-Hill, New York.
- Nolet, G., and Moser, T. J., 1993, Teleseismic delay times in a 3-D Earth and a new look at the s discrepancy: *Geophys. J. Int.*, **114**, 185–195.
- Olson, J., and Pollard, D. D., 1989, Inferring paleostresses from natural fracture patterns: A new method: *Geology*, **17**, 345–348.
- Operto, S., Lambaré, G., Podvin, P., and Thierry, P., 2003, 3D ray+Born migration/inversion-Part2: Application to the SEG/EAGE overthrust experiment: *Geophysics*, **68**, 1357–1370.
- Padovani, E., Priolo, E., and Seriani, G., 1994, Low- and high-order finite-element method: experience in seismic modeling: *J. Comp. Acoust.*, **2**, 371–422.
- Pratt, R. G., and Worthington, M. H., 1990, Inverse theory applied to multi-source cross-hole tomography. Part 1: Acoustic wave-equation method: *Geophysical Prospecting*, **38**, 287–310.

- Pratt, R. G., Shin, C. S., and Hicks, G. J., 1998, Gauss-Newton and full Newton methods in frequency-space seismic waveform inversion: *Geophys. J. Int.*, **133**, 341–362.
- Pratt, R. G., 1988, Frequency-domain elastic wave modeling by finite difference: A tool for crosshole seismic imaging: *Geophysics*, **55**, 626–632.
- Pratt, R. G., 1999, Seismic waveform inversion in the frequency domain, Part 1: Theory and verification in a physical scale model: *Geophysics*, **64**, 888–901.
- Press, H. P., Flannery, B. P., Teukolsky, S. A., and Vetterling, W. T., 1987, *Numerical recipes: The art of scientific computing*: Cambridge University Press.
- Prothero, W. A., Taylor, W. J., and Eickemeyer, J. A., 1988, A fast, two-point, three-dimensional raytracing algorithm using a simple step search method: *Bull. Seism. Soc. Am.*, **78**, 1190–1198.
- Pšenčík, I., and Farra, V., 2005, First-order ray tracing for qP waves in inhomogeneous, weakly anisotropic media: *Geophysics*, **70**, D65–D75.
- Ramos-Martínez, J., Ortega, A. A., and McMechan, G. A., 2000, 3-D seismic modeling for cracked media: Shear-wave splitting at zero-offset: *Geophysics*, **65**, 211–221.
- Rüger, A., and Tsvankin, I., 1997, Using AVO for fracture detection: Analytic basis and practical solutions: *The Leading Edge*, **16**, 1429–1434.
- Rüger, A., 1997, P-wave reflection coefficients for transversely isotropic models with vertical and horizontal axis of symmetry: *Geophysics*, **62**, 713–722.
- Saenger, E. H., and Bohlen, T., 2004, Finite-difference modeling of viscoelastic and anisotropic wave propagation using the rotated staggered grid: *Geophysics*, **69**, 583–591.
- Saenger, E. H., Gold, N., and Shapiro, S. A., 2000, Modeling the propagation of elastic waves using a modified finite-difference grid: *Wave Motion*, **31**, 77–92.

- Saito, H., 1989, Travel times and ray paths of first arrival seismic waves: Computation method based on Huygen's principle., *in* 59th Ann. Internat. Mtg. Soc. of Expl. Geophys., 244–247.
- Schneider, W. A., Ranzinger, K. A., Balch, A. H., and Kruse, C., 1992, A dynamic programming approach to first arrival travelttime computation in media with arbitrarily distributed velocities: *Geophysics*, **57**, 39–50.
- Schoenberg, M., and Douma, J., 1988, Elastic wave propagation in media with parallel fractures and aligned cracks: *Geophysical Prospecting*, **36**, 571–590.
- Schoenberg, M., and Helbig, K., 1997, Orthorhombic media: Modeling elastic wave behavior in a vertically fractured earth: *Geophysics*, **62**, 1954–1974.
- Schoenberg, M., and Sayers, C., 1995, Seismic anisotropy of fractured rock: *Geophysics*, **60**, 204–211.
- Schoenberg, M., 1980, Elastic wave behavior across linear slip interfaces: *J. Acoust. Soc. Am.*, **68**, 1516–1521.
- Sen, M. K., and Mukherjee, A., 2003,  $\tau$ - $p$  analysis in transversely isotropic media: *Geophys. J. Int.*, **154**, 647–658.
- Sen, M. K., and Stoffa, P. L., 1991, Nonlinear one-dimensional seismic waveform inversion using simulated annealing: *Geophysics*, **56**, no. 10, 1624–1638.
- Serón, F. J., Badal, J., and Sabadell, F. J., 1996, A numerical laboratory for simulation and visualization of seismic wavefields: *Geophysical Prospecting*, **44**, 603–642.
- Shaw, R. K., and Sen, M. K., 2004, Born integral, stationary phase and linearized reflection coefficients in weak anisotropic media: *Geophys J. Int.*, **158**, 225–238.
- Shaw, R. K., and Sen, M. K., 2006, Use of AVOA data to estimate fluid indicator in a vertically fractured medium: *Geophysics*, **71**, C15–C24.

- Shearer, P. M., and Chapman, C. H., 1989, Ray tracing in azimuthally anisotropic media: I. Results for models of aligned cracks in the upper crust: *Geophys. J. Int.*, **96**, 51–64.
- Shen, F., Sierra, J., Burns, D. R., and Toksöz, M. N., 2002, Azimuthal offset-dependent attributes applied to fracture detection in a carbonate reservoir: *Geophysics*, **67**, 355–364.
- Sheriff, R. E., 2002, *Encyclopedia dictionary of applied geophysics*: Soc. of Expl. Geophys.
- Shuck, E. L., Davis, T. L., and Benson, R. D., 1996, Multicomponent 3-D characterization of a coalbed methane reservoir: *Geophysics*, **61**, 315–330.
- Stearns, D. W., 1994, *AAPG fractured reservoir school notes*: AAPG, Great Falls, Montana.
- Stolt, R. H., and Weglein, A. B., 1985, Migration and inversion of seismic data: *Geophysics*, **50**, 2458–2472.
- Tarantola, A., 2005, *Inverse problem theory and methods for model parameter estimation*: Society for Industrial and Applied Mathematics, Philadelphia.
- Tessmer, E., and Kosloff, D., 1994, 3-D elastic modeling with surface topography by a Chebychev spectral method: *Geophysics*, **59**, 464–473.
- Thierry, P., Operto, S., and Lambaré, G., 1999, Fast 2-D ray+Born migration/inversion in complex media: *Geophysics*, **64**, 162–181.
- Thomsen, L., Tsavkin, I., and Mueller, M. C., 1999, Coarse-layer stripping of vertically variable azimuthal anisotropy from shear-wave data: *Geophysics*, **64**, 357–386.
- Thomsen, L., 1986, Weak elastic anisotropy: *Geophysics*, **51**, 1954–1966.
- Thomsen, L., 1995, Elastic anisotropy due to aligned cracks in porous rock: *Geophysical Prospecting*, **43**, 805–830.
- Tsvankin, I., 1997a, Reflection moveout and parameter estimation for horizontal transverse isotropy: *Geophysics*, **62**, 614–629.

- Tsvankin, I., 1997b, Anisotropic parameters and P-wave velocity for orthorhombic media: *Geophysics*, **62**, 1292–1309.
- Tsvankin, I., 2001, *Seismic signatures and analysis of reflection data in anisotropic media*: Elsevier Science Ltd., Oxford, UK.
- Um, J., and Thurber, C., 1987, A fast algorithm for two-point seismic ray tracing: *Bull. Seism. Soc. Am.*, **77**, 972–986.
- van Trier, J., and Symes, W. W., 1991, Upwind finite-difference calculation of traveltimes: *Geophysics*, **56**, 812–821.
- Vanelle, C., and Gajewski, D., 2002, Second-order interpolation of traveltimes: *Geophysical Prospecting*, **50**, 73–83.
- Vavryčuk, V., 2001, Ray tracing in anisotropic media with singularities: *Geophys. J. Int.*, **145**, 265–276.
- Velis, R. D., and Ulrych, T. J., 2001, Simulated annealing ray tracing in complex three-dimensional media: *Geophys. J. Int.*, **145**, 447–459.
- Vesnaver, A. L., 1996, Ray tracing based on Fermat’s principle in irregular grids: *Geophysical Prospecting*, **44**, 741–760.
- Vidale, J. E., 1988, Finite-difference calculation of travel times: *Bull. Seism. Soc. Am.*, **78**, 2062–2076.
- Vidale, J. E., 1989, Finite-difference calculation of traveltimes in 3-D: *in* 59th Ann. Internat. Mtg. Soc. of Expl. Geophys., 1096–1098.
- Vidale, J. E., 1990, Finite-difference calculation of traveltimes in three dimensions: *Geophysics*, **55**, 521–526.
- Vinje, V., Iversen, E., and Gjoystdal, H., 1993, Traveltime and amplitude estimation using wavefront construction: *Geophysics*, **58**, 1157–1166.
- Virieux, J., 1984, SH-wave propagation in heterogeneous media: Velocity-stress finite-difference method: *Geophysics*, **49**, 1933–1957.

Virieux, J., 1986, P-SV wave propagation in heterogeneous media: Velocity-stress finite-difference method: *Geophysics*, **51**, 889–901.

Winterstein, D. F., and Meadows, M. A., 1991, Shear-wave polarization and subsurface stress directions at Lost Hills field: *Geophysics*, **56**, 1331–1348.

## Vita

Reeshidev Bansal was born at Betiah, Bihar, India, on July 28, 1978, to Sr. Mahiman Kr. Tulsian and Smt. Kiran Devi. He completed his primary school from Sarasavati Shishu Mandir, Gorakhpur, and high school from M. G. Inter College, Gorakhpur in 1996. He entered the department of Geology and Geophysics at the Indian Institute of Technology, Kharagpur, India in 1997. He completed his BSc in Geological Sciences in 2000 and the first year of MSc in Exploration Geophysics in 2001. He enrolled in the Geophysics MS program at Virginia Tech in August 2001 and graduated from there in 2003. In fall of 2003, he started working on his PhD at UT Austin in the Jackson school of Geosciences. During the summers of 2005 and 2006, he worked for WesternGeco, Houston and Chevron's Energy Technology Company, Houston, respectively. Upon graduation, he will join Integrated Seismic Research team at ExxonMobil Upstream Research Company, Houston, Texas. He is a member of SEG and SPG.

Permanent address: Medico Surgicals, Gandhi Park  
Gorakhpur, India 273001

This dissertation was typeset by the author.